

**AIR-TO-AIR REFUELLING
AERODYNAMIC INTERACTION**

by

Patrick F. Landry

B.Sc., The University of Ottawa, 1989

**THESIS SUBMITTED IN PARTIAL FULFILMENT
OF THE REQUIREMENTS FOR A
MASTER'S DEGREE OF APPLIED SCIENCE**

in

THE FACULTY OF GRADUATE STUDIES

Department of Mechanical Engineering

We accept this thesis as conforming
to the required standard

THE UNIVERSITY OF BRITISH COLUMBIA

June 1997

© Patrick F. Landry, 1997

In presenting this thesis in partial fulfilment of the requirements for an advanced degree at the University of British Columbia, I agree that the Library shall make it freely available for reference and study. I further agree that permission for extensive copying of this thesis for scholarly purposes may be granted by the head of my department or by his or her representatives. It is understood that copying or publication of this thesis for financial gain shall not be allowed without my written permission.

Department of Mechanical Engineering
The University of British Columbia
Vancouver, Canada

Date 4 July, 1997

ABSTRACT

With the advent of the CC-130(H)T (Hercules) aircraft in the role of air tanker in support of the CF-18A fighter aircraft, a flight testing programme was initiated in order to establish the compatibility of the two aircraft for *Air-to-Air Refuelling* (AAR). Concurrently, scale testing was conducted in a low speed wind tunnel at the University of British Columbia to investigate the effect of the CC-130H(T)'s wing-tip vortex on the CF-18A aircraft in the AAR pre-contact position.

The scale testing was accomplished by subjecting a 1/12 scale model of the CF-18A to the tip vortex of a generating wing placed upstream in a wind tunnel. Custom-designed mounts allowed for variation of the model's vertical position and of the generating wing's lateral position inside the wind tunnel. Force and pressure sensors installed on the model served to measure the positional effects of the vortex for three AAR conditions defined by tanker vortex strength and CF-18A angle-of-attack.

The present study has shown that, when considering the wing-tip vortex exclusively, the optimal AAR pre-contact region is far inboard of and below the tanker wing tip, while the most unstable region of the tip vortex is just outboard of and roughly level with the tanker's wing tip. Furthermore, the magnitude of the aerodynamic forces on the model was observed to be proportional to the strength of the generated vortex, and insignificant Reynolds number effects were observed between half-speed and full-speed tests.

ACKNOWLEDGEMENTS

This project would undoubtedly not have been seen through to successful completion without the contribution of several people. First and foremost, the author wishes to express his gratitude to his advisor, Professor Sheldon I. Green, for his most valued guidance and support throughout the course of this thesis. Professor Green's useful advice and unwavering enthusiasm often granted the author the motivation to move forward in the face of adversity.

Technical assistance provided by Mr. Andre Bidaud was instrumental in the design and construction of the 10-channel amplifier, in the writing of the data acquisition program, and in resolving many problems related to instrumentation.

The author would like to express his appreciation to the UBC Mechanical Engineering Department faculty and staff for the efficient and timely support provided throughout the course of his studies, and in particular to Professors I. Gartshore and G. Parkinson, as well as to Dean Leonard and Jan Marsden.

A special thanks to the supervisors and technicians of the UBC Metal Workshops for many building deadlines met and for helpful design advice, as well as to Matt Findlay, for his invaluable tutoring in using Tecplot.

The research was funded by the Canadian Department of National Defence under DSS contract 07SV.W8477-2-AC37. The CF-18A 1/12 scale model was built by Aldrige, Pears & Associates (APA) Models Inc., of Vancouver, BC.

Last but not least, the author wishes to express his utmost gratitude to his family and friends for their incessant moral support and patience throughout this process, and especially to Karen Jamison for being the pillar of it all.

TABLE OF CONTENTS

Abstract	ii
Acknowledgements	iii
Table of Contents	iv
List of Figures	vi
List of Tables	viii
CHAPTER 1 - INTRODUCTION	
1.1 Research Description	1
1.2 Literature Review	8
1.3 Modelling Considerations	28
1.4 Thesis Report Overview	33
CHAPTER 2 - EXPERIMENTAL APPARATUS AND PROCEDURE	
2.1 Experimental Apparatus	35
2.2 Experimental Procedure	47
CHAPTER 3 - RESULTS	
3.0 General	61
3.1 Aerodynamic Force Data	70
3.2 Pressure Data	98
3.3 Uncertainty Analysis	107
CHAPTER 4 - DISCUSSION	
4.1 Force Data	117
4.2 Pressure Data	135

CHAPTER 5 - CONCLUSIONS AND RECOMMENDATIONS

5.1	Conclusions	140
5.2	Recommendations	144
REFERENCES		147
APPENDIX A	Determination of AAR Conditions to be Investigated	148
APPENDIX B	Force and Pressure Data Plots	167
APPENDIX C	Code Listing and Specifications	211
APPENDIX D	Generating Wing Downwash Velocity Analysis	217

LIST OF FIGURES

Figure 1.1	CF-18A Aircraft	3
Figure 1.2	CC-130H(T) Aircraft	4
Figure 1.3	AAR Contact Position	6
Figure 1.4	Flows Around an Airfoil (With and Without Circulation)	10
Figure 1.5	Concept of Circulation	11
Figure 1.6	Prandtl's Horseshoe Vortex System	13
Figure 1.7	Shear Layer Theory Interpretation	14
Figure 1.8(a)	Aerodynamic Lift Distribution (Rectangular Wing in a Subsonic Flow)	14
Figure 1.8(b)	Vorticity Distribution and Trailing Vortex System	15
Figure 1.9	Effects of wing Downwash	17
Figure 1.10	Tangential Velocity Distribution in a Vortex	20
Figure 1.11	Axial Velocity in a Vortex Flow	22
Figure 1.12	Pressure and Tangential Velocity Relation in a Vortex	25
Figure 1.13	Effect of Mach Number on the Lift Coefficient	31
Figure 2.1	CF-18A 1/12 Scale Model	41
Figure 2.2	CF-18A Model Mount Diagram	42
Figure 2.3	Sting, Mount and Model Structural Interface (Top View)	48
Figure 3.1	Variation of Model MAC Leading Edge z -Position with α_m	63
Figure 3.2	Principal Image Vortices due to BLWT Walls	65
Figure 3.3	Least and Most "Position-Sensitive" Region for the Lift Force	76
Figure 3.4	Angle-of-Lean of the Model Mount	78
Figure 3.5	Least and Most "Position-Sensitive" Regions for the Side Force	84
Figure 3.6	Schematic for the Analysis of Three Similar Cases	91

Figure 3.7	Least and Most “Position-Sensitive” Regions for the Rolling Moment	94
Figure 4.1	Hypothetical Flow Pattern Explaining Non-Intuitive Side Forces	125
Figure 4.2	Least and Most “Overall-Stable” AAR Pre-Contact Regions	132

LIST OF TABLES

Table 2.1	Channel Characteristics for the Sting Balance Force Transducer	38
Table 2.2	Sting Balance Channel Interaction Characteristics	38
Table 2.3	BLWT Calibration Data	52
Table 2.4	Maximum Estimated Aerodynamic Loads on the Model	54
Table 2.5	Maximum Anticipated Loads on the Sting Balance	54
Table 2.6	Sting / Amplifier Calibration Results	56
Table 2.7	Pressure Transducers Calibration Data	58
Table 2.8	AAR Cases Investigated	59
Table 2.9	Wind Tunnel Conditions for the Three AAR Cases	59
Table 3.1	Actual z-Location of the Model MAC Leading Edge w.r.t. the Vortex Centerline)	64
Table 3.2	Ground and Formation Effects on the Generating Wing's Lift and Circulation	66
Table 3.3	Generating Wing Circulation (Accounting for BLWT Wall Effects)	67
Table 3.4	Displacement of the Generated Vortex Core due to BLWT Wall Effects	68
Table 3.5	Relative Position of the Model w.r.t. the Vortex Core (After BLWT Wall Effect Corrections and for $ZPOS/c_m=0$)	69
Table 3.6	Induced Lift Force Variation With Position	76
Table 3.7	Side Force-to-Lift Ratios (for Reference Data)	79
Table 3.8	Side Force Direction Reversal Ranges for $YPOS=0$	82
Table 3.9	Induced Side Force Variation With Position	83
Table 3.10	Calculated and Obtained Inherent Rolling Moments ($\psi=3.5$ degrees)	88
Table 3.11	Induced Forces and Rolling Moments for Three Similar Cases	91

Table 3.12	Induced Rolling Moment Variation With Position	93
Table 3.13	Aerodynamic Force Uncertainties Due to Model Geometry	111
Table 3.14	Sting-Induced Force Uncertainties on the Model	113
Table 3.15	Summary of Uncertainties for Wind Tunnel Tests	115
Table 4.1	CC-130H(T)'s Tip Vortex Vertical Location in the AAR Pre- Contact Position	122

CHAPTER 1

INTRODUCTION

1.1 Research Description

1.1.1 Project Background

Many military aircraft are now able to replenish their fuel tanks in-flight by receiving fuel from a tanker aircraft. This process is known as *Air-to-Air Refuelling* (AAR). During this process, the aircraft to be refuelled (the *receiver* aircraft) must fly in close proximity to and downstream of a larger *tanker* aircraft in order to connect to the tanker's refuelling drogue. There are many advantages associated with the capability of refuelling an aircraft in flight: time and fuel savings, operational flexibility and reduction in the risk of accidents are but a few. Conversely, there exists a potential for disaster due to the precarious position of the receiver aircraft during AAR: notwithstanding the inherent risk of close proximity flying, the receiver aircraft's pilot must also continually fight the strong aerodynamic wake of the tanker, a combination of complex turbulent flows capable of "tossing" a smaller aircraft in any direction.

For the purpose of this thesis, two aircraft types are of interest: the CF-18 (Hornet), a modern jet fighter aircraft (the *receiver*), and the CC-130H(T) (Hercules), a larger tactical tanker aircraft (the *tanker*). A brief description of these aircraft is necessary to fully understand the nature of this research.

CF-18 aircraft: Built by McDonnell Aircraft Company, the CF-18 (also referred to as the CF188) is now the only fighter aircraft operated by the Canadian Forces. This multi-purpose, all-weather fighter assumes the roles of air superiority, interdiction and ground attack. Two variants are used by the Canadian Forces: the CF-18A (single seat) and the CF-18B (dual seat). Note that even though both variants are capable of AAR, the dual seat model is primarily used for training and thus operational AAR is mainly performed with the CF-18A aircraft (although results from this research will apply to both versions since their external dimensions are identical).

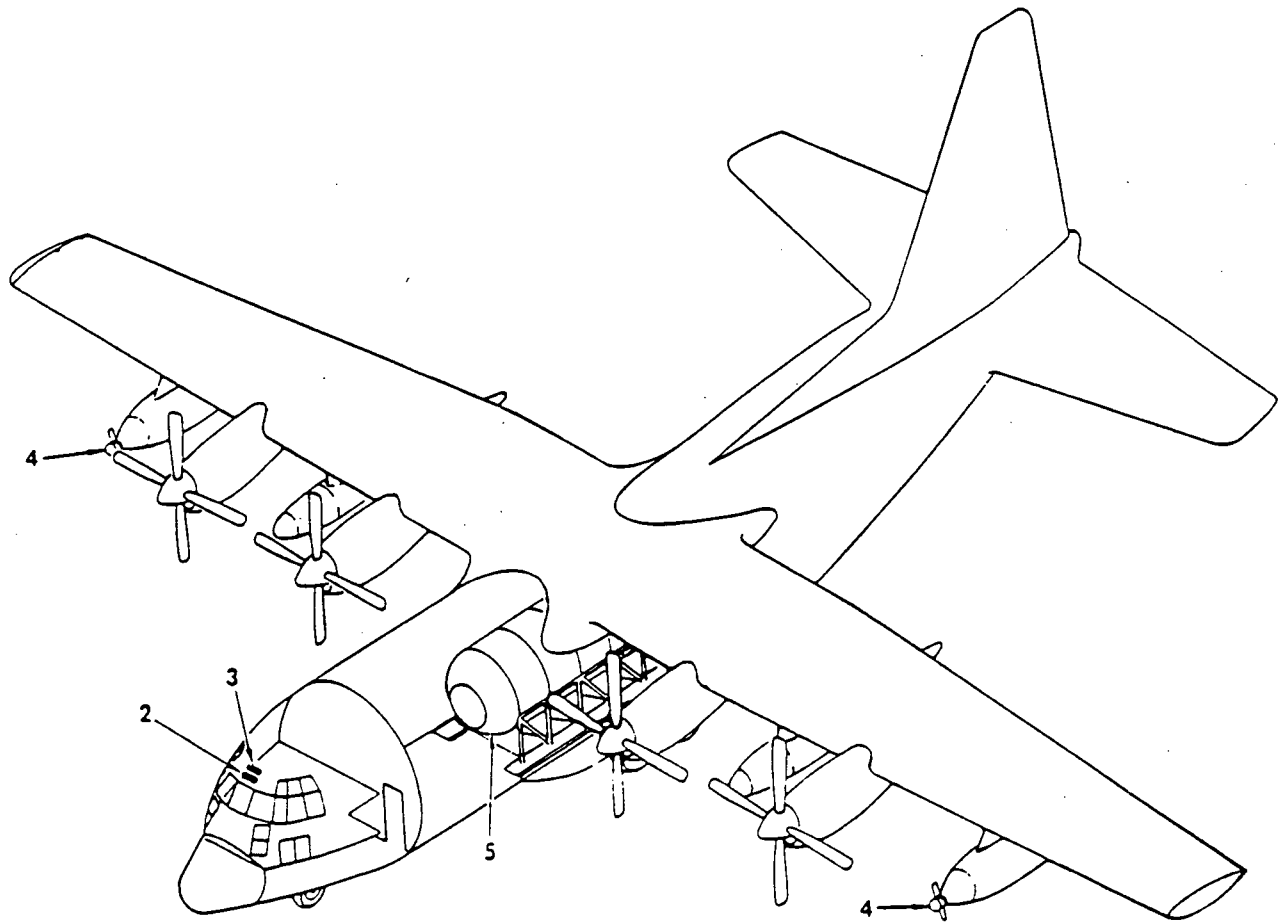
The aircraft possesses a full-authority control augmentation system for which the primary control surfaces are the ailerons, the twin rudders, the differential leading and trailing edge flaps, and the differential stabilators. The CF-18A has a modified NACA-65A (supersonic) wing with an aspect ratio of 3.5, a geometric twist of -4.0 degrees, a dihedral of -3.0 degrees and a thickness ratio varying between 3.5% (wing tip) and 5.0% (exposed root). Albeit a supersonic aircraft, the CF-18A's powerful flaps and leading edge extensions (LEX's) allow it to fly at relatively low speeds, and at angles of attack up to 50 degrees. The aircraft operating weight for AAR varies from 31,300 lbs to 40,000 lbs. Figure 1.1 shows the CF-18A aircraft.



Figure 1.1: CF-18 Aircraft

CC-130H(T) aircraft: The CC-130H (Hercules) is an all-metal, high wing, long range monoplane built by Lockheed Aerospace Systems Corporation (LASC). The fuselage comprises a large cargo compartment (located aft) and a flight deck (located in the nose). The aircraft is powered by four constant-speed turboprop engines mounted below the wings, while its primary control surfaces are governed by mechanical systems with hydraulic boost. The roles of the CC-130H include military transport, Search and Rescue (SAR), open-skies verification, support to peacekeeping and disaster-relief missions. Recent configuration

modifications made by LASC have given birth to the CC-130H(T), a tanker version of the heavy cargo aircraft. In this last version, the aircraft was modified to accommodate a cargo fuel tank, two wing-mounted fuel dispenser pods and associated fuel lines. The operational gross weight of the CC-130H(T) varies between 130,000 lbs and 155,000 lbs. Figure 1.2 shows the CC-130H(T) aircraft as well as the location of the refuelling pods.



- 2. Fuel control panel
- 3. Auxiliary fuel and pod control panels
- 4. AAR pods
- 5. Fuselage fuel tank

Figure 1.2: CC-130H(T) Aircraft

In 1992, the Canadian Department of National Defence (DND) purchased five CC-130H(T) aircraft for the purpose of providing an airborne refuelling capability to the CF-5 and the CF-18 aircraft. The Aerospace Engineering Test Establishment (AETE) located in Cold Lake, Alberta, was tasked to conduct acceptance testing of the CC-130H(T) prototype through a program of full scale flight testing. The program showed that both the CF-5 and the CF-18 were compatible with the CC-130H(T) for the purpose of AAR, each within a specific flight envelope (as specified in [1]). However, only broad qualitative results were obtained. The inability to take accurate position, force or pressure measurements in flight and the high cost associated with full-scale testing have limited the acquisition of quantitative data regarding the aerodynamic interaction between the tanker and the receiver aircraft.

1.1.2 Rationale for AAR Research

As shown in Figure 1.2, the CC-130H(T)'s refuelling pods are located on the wings, outboard of the outboard engines, thus near the wing tips. Because the receiver aircraft must make contact with the refuelling drogue trailing from a pod, it must fly almost directly behind (and below) the wing tip of the tanker, in a region characterized by a strong tanker wing-tip vortex. Figure 1.3 shows the refuelling drogue contact position (note that all dimensions shown are in feet).

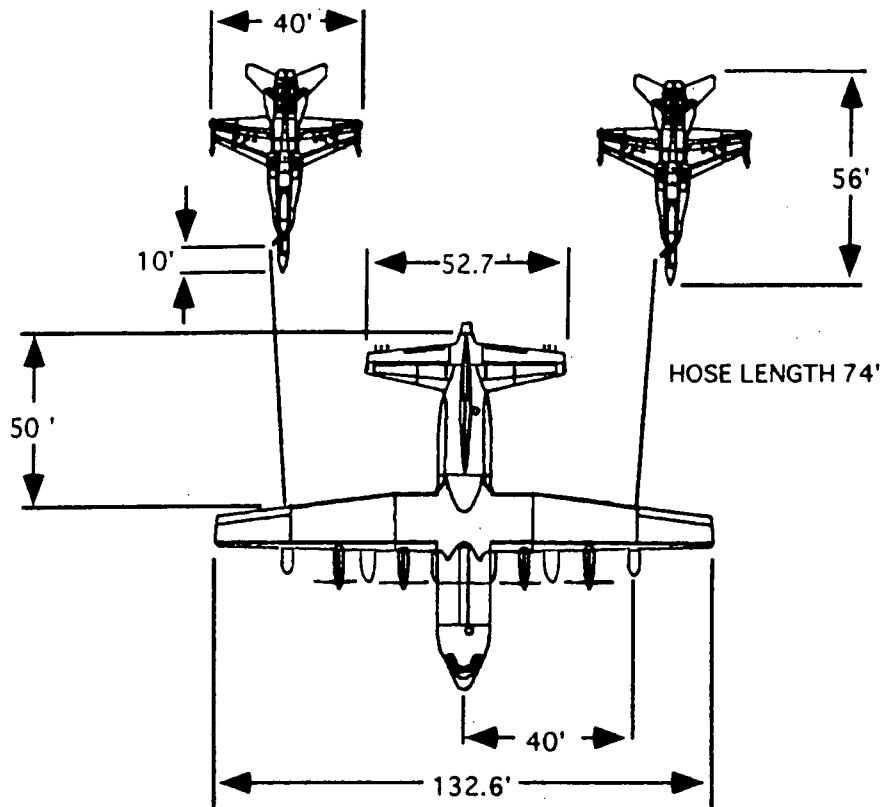


Figure 1.3: AAR Contact Position

The expected rolling effects induced by the tanker aircraft's wing-tip vortex combined with the close proximity of the tanker and receiver aircraft during AAR were felt to constitute a safety concern and to bear potential for an air catastrophe.

The tanker wake was briefly investigated during full-scale testing, and the test pilots reported that the strong wing-tip and fuselage vortices tended to roll the receiver aircraft towards the tanker on either side of it. These effects were most noticeable in the pre-contact position (i.e., one receiver aircraft length directly behind the refuelling drogue). Since the refuelling drogue's position dictates the relative position of the two aircraft in the contact phase, the wing-tip vortex influence at that position is critical to establishing drogue contact

in a safe and efficient manner.

Concurrently to the full-scale testing, a 1/12 scale-model wind tunnel test program was conducted at the University of British Columbia (UBC) in order to gain a better understanding of the aerodynamic forces involved during AAR, thus the purpose of this thesis. This method was deemed a reasonable and cost effective alternative for the quantitative investigation of tanker/ receiver aerodynamic interaction.

There are however serious considerations to be made when wind tunnel testing becomes the method of choice. Among others, wall effects and other flow disturbances should be minimized. Dimensional analysis requirements are also often difficult (or impossible) to satisfy. These concerns are discussed with more detail in sections 1.3 and 3.0 of this report. For operational and financial reasons (mainly due to the fact that the CF-5 was scheduled for retirement from Service in 1995), the wind tunnel testing was limited to studying the effects of the CC-130H(T) wing-tip vortices on the CF-18A aircraft.

1.1.3 Research Method Summary

The UBC Boundary Layer Wind Tunnel was selected as the testing facility. With a test section measuring five feet in height and eight feet in width, this wind tunnel allows for relatively large scale modelling at wind velocities up to 20 m/s (72 km/h).

Simulation of the aerodynamic interaction was achieved by mounting a 1/12 scale model of a CF-18A aircraft on a force and moment transducer (the *Sting balance*) at some

distance downstream from a generating wing intended to simulate the wing-tip vortex of the CC-130H(T). The CF-18A model was also pressure-tapped in 72 strategic locations, namely, on the top surface of both LEX's, as well as on the top and bottom surfaces of both wings. The scope of the scale test program is to investigate the forces and pressure distribution on the lifting surfaces of the CF-18A in the AAR pre-contact phase, for various relative aircraft positions and specific flight conditions. The results of this research could be used to amend the CF-18A/ CC-130H(T) AAR envelope, to determine the critical areas of the pre-contact zone, or to establish a better location for the AAR pods on the CC-130H(T).

By varying the relative position of the receiver aircraft with respect to the tanker, it is possible to determine best and worst AAR pre-contact relative positions. The mount of the CF-18A allows for the model's vertical movement (defined as *ZPOS*) in the wind tunnel while the generating wing's mount allows for lateral movement (defined as *YPOS*). Furthermore, the angle of attack (AOA) on both the model and the generating wing can easily be varied independently to simulate the desired flight condition.

1.2 Literature Review

Although often invisible to the naked eye, vortices are nonetheless an crucial reality of aerodynamics. Due of the broadness of the subject, we will limit our study to the analysis of *tip vortices*, which occur wherever a lifting surface terminates in a fluid.

1.2.1 History of Vortex Research

The history of aerodynamic vortices associated with generation of lift by airfoils began early in the history of heavier-than-air flight. Although earlier practical tests had proven the existence of lift and drag, mid-eighteenth century mathematical theory of fluid flow still predicted that a body in a steady two-dimensional flow in a perfect fluid would not produce any lift or drag. This is known as D'Alembert's Paradox and was not resolved until 1905. In 1902, Kutta, a leading German mathematician, made the assumption that a two-dimensional, steady flow over both surfaces of an airfoil with a sharp trailing edge must leave the airfoil smoothly at the trailing edge, since infinite flow accelerations would be required otherwise (and thus this would not constitute a realistic model). Kutta further assumed that a superimposed circulatory flow had to be generated around the airfoil in order to keep the stagnation point back at the trailing edge for any angle of attack (as shown in Figure 1.4). The outcome was the well known *Kutta-Joukowski condition* (1905) which states that “one of the stagnation points on an airfoil with a sharp trailing edge must be located at the trailing edge”, implying that circulation must be present around any two-dimensional lift-generating surface.

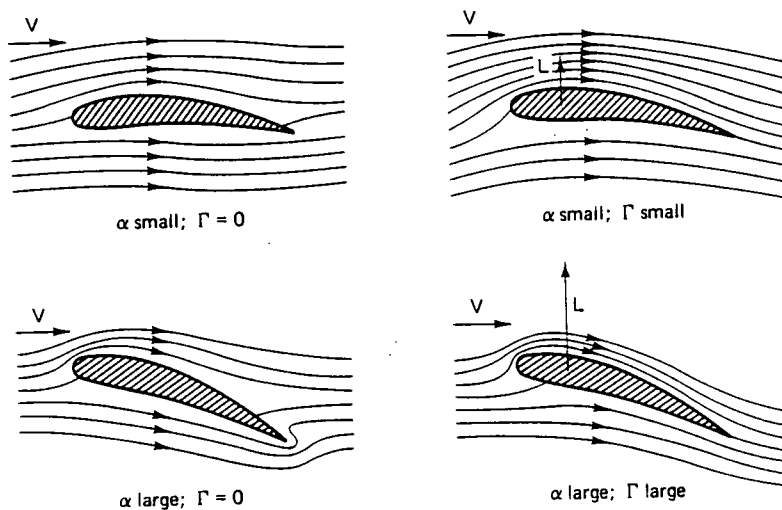


Figure 1.4: Flows Around an Airfoil (With and Without Circulation)

Furthermore, Kutta and Joukowski developed a mathematical relationship between lift and circulation, known as the *Kutta-Joukowski Law*. It states that “the lift generated from a two-dimensional body is directly proportional to the circulation around this body”. Mathematically:

$$L = \rho V \Gamma b \quad (1.1)$$

Experiments have shown the structure of the aerodynamic vortex to be more complex than the predictions of early models. Lanchester was seemingly the first to explain the role of vortex formation in the generation of lift by an airfoil. The first analytical treatment by Ludwig Prandtl (1904) was relatively simple but each subsequent theoretical or experimental study added some complexity to the problem. Further investigations (such as in-flight measurements by McCormick et al., as well as analysis by Batchelor) have shown the wing-tip vortex to have a complex, three-dimensional structure. More recent considerations such as

vortex stability led to the categorization of aircraft wake turbulence into several major areas such as formation and decay of trailing vortices.

1.2.2 Circulation and Lift

In order to begin the study of wing tip vortices, it is imperative to review the principles of circulation and lift. Circulation is defined as the line integral of velocity along a closed path and is a measure of the strength of a circulatory flow. Referring to the closed curve C in Figure 1.5:

$$\Gamma = -\oint_C \vec{V} \cdot d\vec{r} \quad (1.2)$$

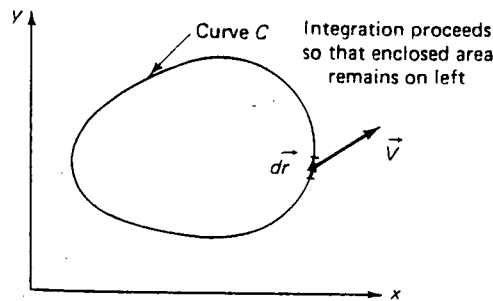


Figure 1.5: Concept of Circulation

The subscript C denotes the integral around a closed contour (e.g. the cross-section of a lifting surface) and V is the local velocity vector along the infinitesimal element dr . Note that a negative sign is used in order to be consistent with the sign convention (i.e., the path of the integration is *counterclockwise* while positive circulation is defined as being *clockwise*). The total circulation is the sum of the contributions of all the elements on the closed contour.

It can be shown from Bernoulli's principle that circulation around a lifting surface in a uniform, linear flow causes lift in the direction perpendicular to the direction of the freestream. This is however a two-dimensional model and thus neglects body end-effects. For practical reasons, this discussion will be limited to the analysis of airfoils (or aircraft wings) as lifting bodies, although the theory applies to any body in any fluid freestream.

1.2.3 Formation of Wing Tip Vortices

Three theories can explain the formation of wing-tip vortices. The most physical explanation (the *Tip Pressure theory*) stems from the difference in pressure between the top and bottom surfaces of a wing in a freestream flow. At the wing tips, the air "leaks" from the high pressure surface (usually the bottom surface) to the low pressure surface (the top surface), creating a *roll-up* of the flow behind the wing: the trailing vortex.

Bernoulli's principle, Helmholtz vortex laws and William Thompson's theorem provide a second (and more complex) explanation for formation of tip vortices: the *Lifting Line theory*. According to Prandtl, the circulation at each infinitesimal location along the span of a wing can be represented by a point vortex. When all these points are linked spanwise, the resulting line formed is termed a *vortex filament* (also termed *lifting line* or *bound vortex*). Prandtl thus concluded that the physical wing could be mathematically modelled by a vortex filament properly placed along the span of the wing. *Helmholtz vortex laws*, first defined in 1858, can be summarized as follows:

- i) *a vortex filament cannot end in a fluid: it must extend to infinity or form a*

closed path;

- ii) *the strength of a vortex filament is constant along its length; and,*
- iii) *vortices in a fluid always remain attached to the same particles of fluid.*

William Thompson further established that “circulation around any path in a vortex always enclosing the same particles of fluid is independent of time”. These theorems led Prandtl to the conclusion that the bound vortex could not disappear at the wing tips, but rather must continue in the fluid and produce *free vortices* at the wing tips. Since the vortices must remain attached to the same particles of fluid initially involved at the wing tips, these free vortices trail behind the wing (thus termed *trailing vortices*) and form, with the bound vortex, the well known Prandtl's horseshoe vortex model. Figure 1.6 illustrates Prandtl's horseshoe vortex system with characteristic lifting line and trailing vortex system.

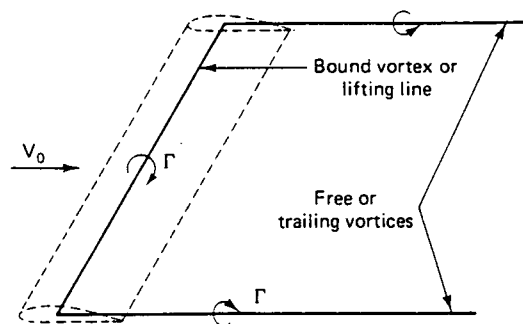


Figure 1.6: Prandtl's Horseshoe Vortex System

A third explanation to the formation of tip vortices is the *Shear Layer theory*. Taking an inboard view of a finite wing in a freestream flow (see Figure 1.7), the (non-separated) flow near the wing surface is represented by vectors parallel to the wing, while the undisturbed

freestream flow some spanwise distance away from the wing is represented by parallel vectors in the direction of U_∞ . The non-parallelism between the wing surface flow vectors and the freestream flow outside of the wing tip implies a downwash velocity component near the wing tip, which in turn implies vorticity oriented in the streamwise direction.

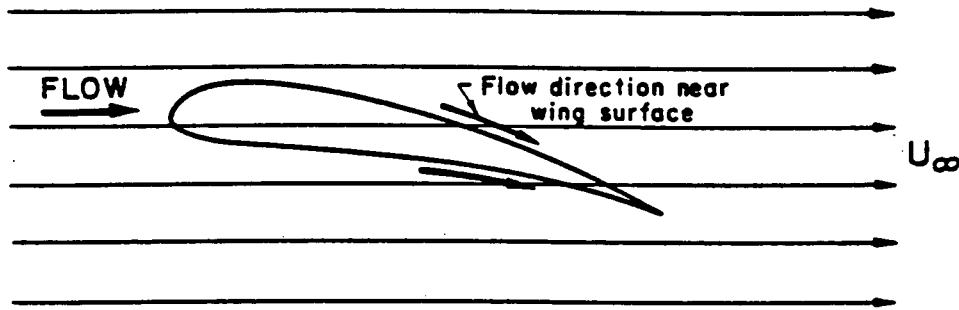


Figure 1.7: Shear Layer Theory Interpretation

Typically, on a finite (three-dimensional) wing, lift decreases towards the wing tips (Figure 1.8 (a)) and flow patterns over the wings vary with position along the span. As a result, circulation generation will be maximized at mid-span and zero at the wing tips (Figure 1.8(b)).

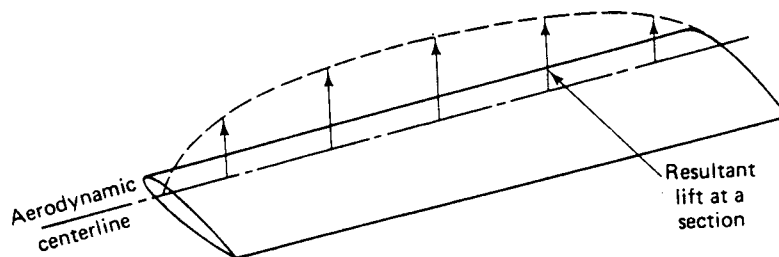


Figure 1.8(a): Aerodynamic Lift Distribution (for a Rectangular Wing in a Subsonic Flow)

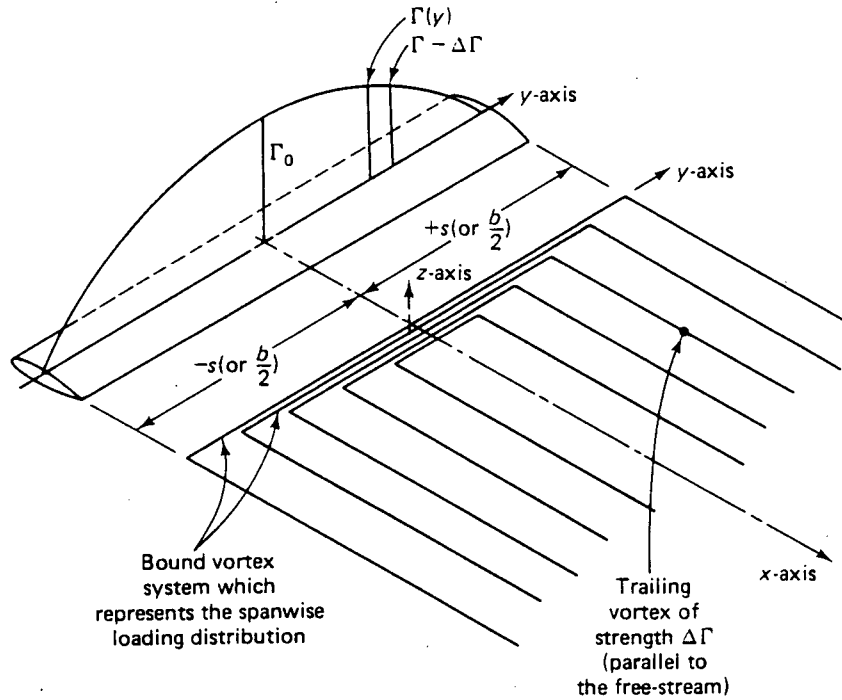


Figure 1.8(b): Vorticity Distributions and Trailing Vortex System

In practice, it has been shown that most of the trailing vortex system displayed in Figure 1.8(b) initiates at the wing tip, where the lift per unit span decreases most rapidly. As each tip vortex moves downstream, it rolls up more and more of the wing's wake until its circulation is equal to that of the bound vortex from the midspan to the wing tip (the other tip vortex accounting for the opposite half of the wing span). At roughly three chord lengths downstream from the wing, the trailing vortices are said to be fully *rolled-up* [8]. Since vortices cannot end in a fluid (Helmholtz), the trailing vortices must in theory also connect somewhere downstream. This occurs at the *starting vortex* location, or the location where the wing was impulsively started. The starting vortex has the same strength as the bound vortex and lies downstream at infinity, which justifies the approximation of the horseshoe vortex

model. In practice, however, the trailing vortices extend downstream until the action of fluid viscosity completely dissipates them.

Downwash Effect: A secondary effect due to the direction and pattern of the trailing vortices is a downward flow of air at and directly behind the wing, called *downwash*. Considering the circulation distribution $\Gamma(y)$ illustrated in Figure 1.8(b) and an arbitrary point y along the wing span, it can be shown that the semi-infinite trailing vortex at y induces a downwards velocity δw_{y_1} at a point y_1 located on the aerodynamic centerline (x -axis). The magnitude of this velocity is equal to one-half the velocity that would be induced by an infinitely long vortex filament, or:

$$\delta w_{y_1} = \frac{1}{2} \left[\frac{d\Gamma}{dy} dy \frac{1}{2\pi(y-y_1)} \right] \quad (1.3)$$

Integrating for the total wing span, this equation yields the downwash velocity at any point y_1 , and given $\Gamma(y)$ for the wing, one can obtain the downwash velocity distribution $w(y)$.

The downwash velocity at a given point y_1 on the aerodynamic centre (i.e., at the quarter-chord) decreases the effective angle of attack of the wing by the *downwash angle* $\epsilon(y)$, calculated as:

$$\epsilon(y_1) = \tan^{-1}\left(\frac{w_{y_1}}{U_\infty}\right) \approx \frac{w_{y_1}}{U_\infty} \quad (1.4)$$

Note that the approximation in Equation (1.4) assumes that w_{yi} is small compared to U_∞ (i.e., the downwash angle is small), which is true in most cases. Thus the wing's *effective angle of attack* (α_e) at any point along the span is the geometric angle of attack reduced by the downwash angle. Incidentally, this in turn causes the lift vector L' to be "tilted" back by the downwash angle, inducing a reduction in the lift force (always defined as perpendicular to the freestream: $L = L' \cos \epsilon$) and a new drag component (the "induced drag": $D_i = L' \sin \epsilon$) on the wing. Figure 1.9 illustrates the effects of the downwash on effective angle of attack, lift and drag (note that L' is the lift vector representing the downwash-free case).

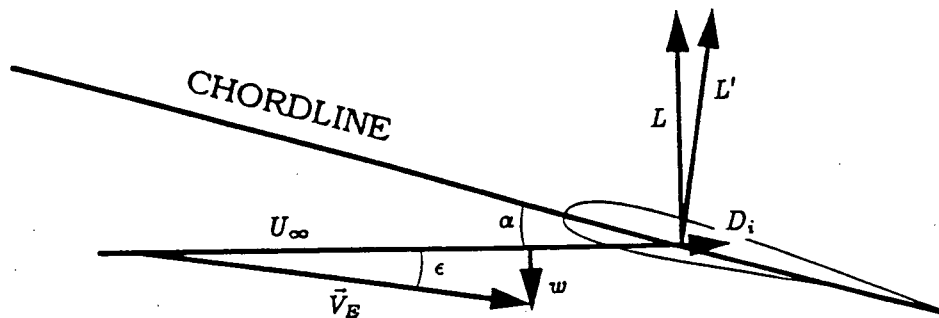


Figure 1.9: Effects of Wing Downwash

1.2.4 Vortex Roll-Up

Although Lifting Line theory explains how a wing sheds a sheet of vorticity (and not concentrated wing-tip vortices), well-defined wing-tip vortices have been observed immediately downstream of wings. This apparent contradiction was first explained by Prandtl (1919), who claimed that the sheet of vorticity shed by a wing will roll-up due to its own velocity. Further investigations have shown that the vast majority of the bound circulation on a wing is shed near the tips, and thus that midspan-shed circulation could be neglected. Thus,

the concentration of shed vorticity at the wing tips will roll-up the remainder of the wing's vorticity sheet within a few chords downstream of the tips. Furthermore, Betz (1932) has shown that, for an elliptically loaded wing, the resultant trailing vortex will be located at $\pi/4$ times (i.e., about 80% of) the semi-span from the wing root ¹.

This last observation seemingly contradicts one of the Lifting Line theory's fundamental assumptions (ie. that the shed vortex sheet lies in a semi-infinite plane downstream of the wing), and thus one could expect poor results from this theory. However, this discrepancy surprisingly has little effect on the accuracy of the Lifting Line theory, likely because of the small change in orientation of the vortex sheet during roll-up.

Further experimentation revealed that vortex roll-up develops very quickly downstream of the wing tip. Studies by Green and Acosta (1991), Arndt et al. (1991), Stinebring et al. (1991) and Shekarriz et al. (1992, 1993) all concur in showing that the completion of vortex roll-up occurs 2-3 chords downstream of the wing, for various wing geometries (rectangular with rounded tip, elliptical, rectangular with square tip and swept-back trapezoidal). Computational Fluid Dynamics (CFD) techniques have also been used to attempt modelling of the wing-tip vortex roll-up. The results obtained by such methods unanimously predict complete vortex roll-up (i.e., 95% of the bound vorticity is in the tip vortex) within 1-2 wing spans downstream of the wing. Although CFD methods are improving, they still fail to reproduce details of near-field tip vortex flow adequately.

¹ Arndt et al. (1991) have subsequently shown that elliptic wings' tip vortices actually do not roll-up at this location (presumably due to three-dimensional effects not accounted for in the Lifting Line theory), but closer to 95% of the wing span.

1.2.5 Velocity and Pressure Distribution in a Vortex

Once the vortex is fully rolled up, a quantitative analysis becomes relatively simple (compared to the roll-up process itself). There has been several experimental studies of the fully developed vortex. Due to the nature of our investigation, we shall focus our study to the *near field tip vortex*, that is, the region of the vortex immediately downstream (i.e., within 20 chord lengths) from the wing tip.

The vortex velocity field can be simplified into two components: tangential (U_θ) and axial (U_x), radial velocity (U_r) being usually negligible. Two coordinates are required to fully describe the flow: x , the streamwise distance downstream from the wing's leading edge, and R , the radial distance from the vortex centerline.

Tangential Velocity: Figure 1.10(a) illustrates theoretical tangential velocity distribution in a vortex, while Figures 1.10(b) and 1.10(c) show experimental results ² obtained at downstream distances of two and ten chord lengths, respectively (Green, 1995).

² Experimental results were obtained using holographic particle image velocimetry in the tip-vortex of a NACA 64-309 rectangular planform, untwisted hydrofoil with $c = 15.2$ cm and $AR = 2.3$, and fitted with a rounded tip.

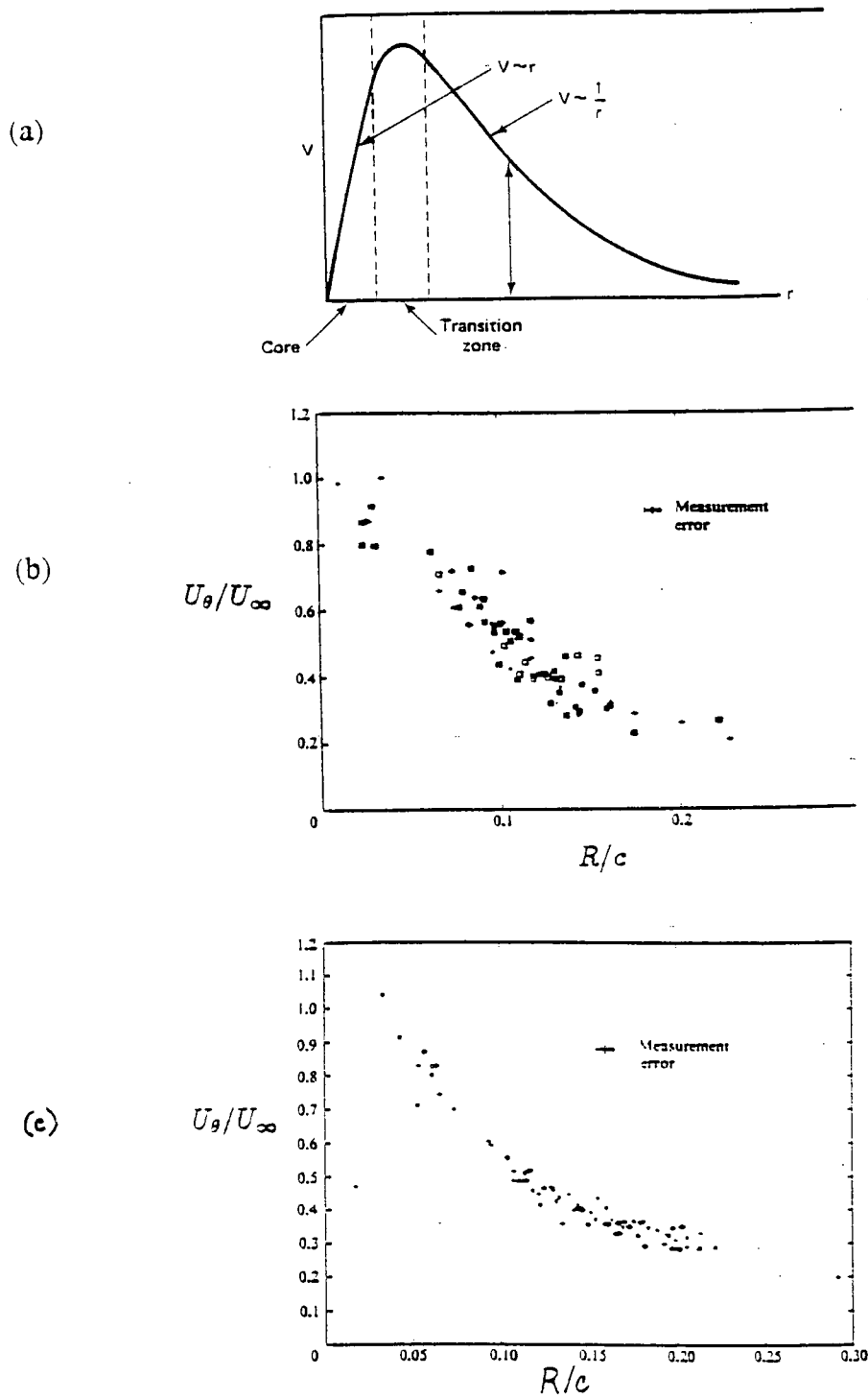


Figure 1.10: Tangential Velocity Distributions in a Vortex:
 (a) Theoretical; (b) Experimental Results at $x/c=2$; and (c) Experimental Results at $x/c=10$

Note that in Figures 1.10(b) and 1.10(c), the tangential velocity (U_θ) is normalized by the freestream velocity (U_∞), and that the radial distance from the vortex centerline (R) is normalized by the chord length (c).

The radius at which peak tangential velocity is attained delimits the inner core and is thus called *vortex core radius* (R_c). For $R \leq R_c$, viscous forces are dominant ($Re < 1$) and tangential velocity increases almost linearly with radius. For $R > R_c$, inertia forces are dominant ($Re > 1$) and tangential velocity decreases monotonically approximately with the inverse of the radial distance from the vortex centerline. The above experimental data indicates that the vortex core radius is very small (in the order of $0.03c$) and that U_θ rises very sharply to a value near U_∞ at R_c . Other experiments (Arndt et al., 1991) have shown similar values of peak tangential velocities. Another reported (and important) feature of the tangential velocity field is its unsteadiness (Green reports peak-to-peak fluctuations of $0.15U_\infty$, with experimental error of only $\pm 0.01U_\infty$), attributable to *core stripping* (Bandyopadhyay et al., 1990, and Sarpkaya, 1992). Note also that the vortex tangential velocity distribution is essentially unchanged from Figure 1.10(b) to figure 1.10(c), which implies that there is very little difference in the vortex structure (dimension, shape and velocity distribution) between $x=2c$ and $x=10c$.

Green (1990) has shown that the mean tangential velocity, when normalized by the wing mid-span bound circulation, does not vary with angle of attack and downstream distance for $2 \leq x/c \leq 10$.

Axial Velocity: Batchelor (1964) was seemingly the first to predict an axial velocity excess in the trailing vortex, indeed not an intuitive concept. Batchelor's prediction was based on the analysis of a streamline extending from upstream of the wing to the tip vortex centerline. Neglecting elevation changes along the streamline, setting U_R and U_θ to zero along the centerline (by definition), and representing viscous losses by a head drop ΔH , Bernoulli's equation becomes:

$$\frac{U_{xc}}{U_\infty} = \sqrt{1 + \frac{p_s - p_c - \rho g \Delta H}{\rho U_\infty^2 / 2}} \quad (1.5)$$

where U_{xc} is the axial velocity on the centerline. It has been shown that $p_s - p_c$ (the pressure drop in the vortex core) is always positive and on the order of three times the dynamic pressure. If ΔH is small comparatively to $p_s - p_c$ (which it is), we get: $U_{xc} \approx 2U_\infty$. Figures 1.11(a) and 1.11(b) show axial velocity measurements for the vortex flows represented in Figures 1.10(b) and 1.10(c), respectively.

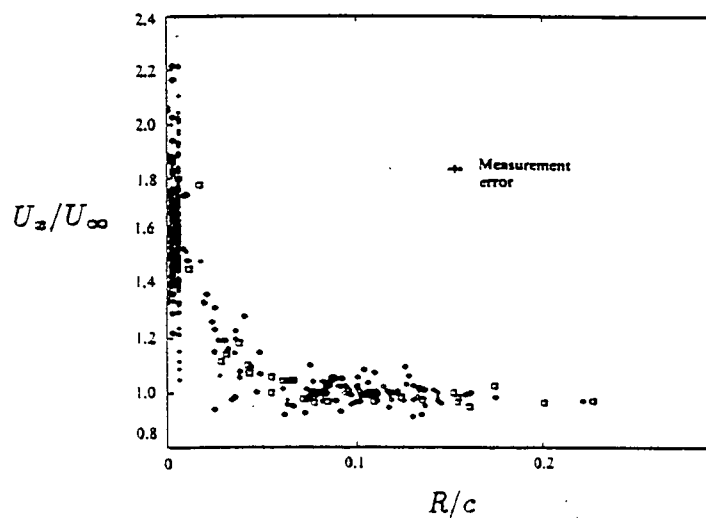


Figure 1.11(a): Axial Velocity in a Vortex Flow: Experimental Results for $x/c=2$

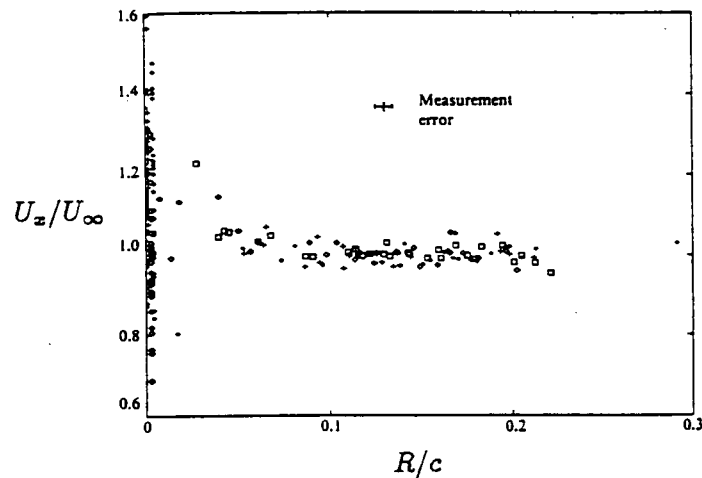


Figure 1.11(b): Axial Velocity in a Vortex Flow: Experimental Results for $x/c=10$

Note once again the normalization of the axial velocity (U_x) by the freestream velocity, and that of the radial dimension (R) by the chord length.

Figures 1.11(a) and 1.11(b) clearly display the excess axial velocity within the vortex core and confirm the relatively small size of the vortex core radius. The rapid decrease in U_x (tending towards U_∞) as we move away from the vortex centerline indicates that excess axial velocity is almost exclusively a vortex core phenomena. Furthermore, comparing figures 1.11(a) and 1.11(b), one can appreciate the loss in core axial velocity between $x=2c$ and $x=10c$, indicating that the head loss between these two points is substantial.

Vortex core axial velocity is equally characterized by unsteadiness rising monotonically as the core is approached. Peak-to-peak fluctuations of the order of U_∞ have been recorded near the core centerline. The general effect of increasing α is an increase in mean axial

velocity (mainly because $p_\infty - p_c$ increases as α increases).

Pressure Distribution: Pressure and velocity fields within a vortex are related by Bernoulli's principle, usually neglecting body forces, and thus once the velocity field is understood, the pressure field becomes relatively simple. For a fully rolled-up vortex (which can be considered axisymmetric), the assumption of negligible radial velocity justifies the use of a simple form of the radial momentum equation to relate the pressure field to the velocity field, or:

$$\frac{\partial p}{\partial r} = \rho \frac{U_\theta^2}{r} \quad (1.6)$$

If $U_\theta(r)$ has been defined, integrating Equation (1.6) yields:

$$p(r) = p_\infty - \rho \int_r^\infty \frac{U_\theta^2}{r} dr \quad (1.7)$$

Note that in order to obtain the vortex core pressure p_c one may set $r=r_c$ in Equation (1.7). This relation applied to a typical vortex tangential velocity distribution yields:

$$p_c = p_\infty - (4.4 \pm 0.8) \frac{\rho U_\infty^2}{2} \quad (1.8)$$

while experimental measurements (Green, 1991) produced similar results with slightly higher core pressures. Experimental results confirmed that the vortex core pressure can be below the

freestream pressure by a factor of four times the dynamic pressure. Similarly to the velocity fields, significantly large fluctuations were observed in the vortex pressure field (on the order of the dynamic pressure). Figure 1.12 illustrates the relation between pressure and tangential velocity distribution in a fully rolled-up vortex.

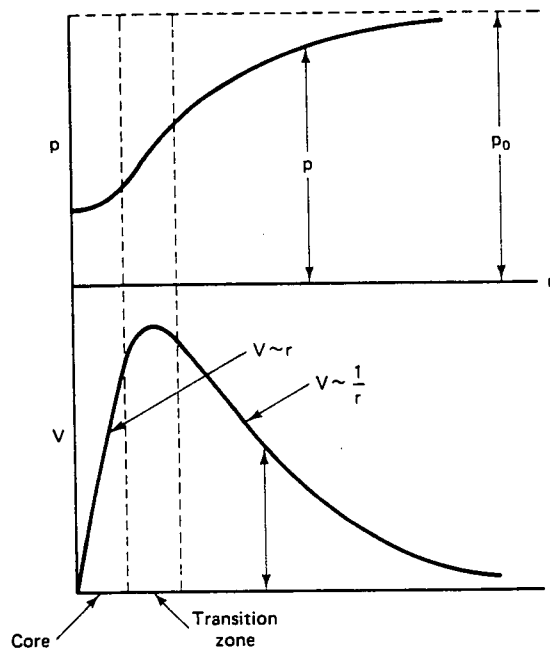


Figure 1.12: Pressure and Tangential Velocity Relation in a Vortex Flow

Tip Vortex Far Field: It is useful to conclude this section with a broad overview of the *far field* of the tip vortex, that is, the region far downstream from the wing tip where decay of the tip vortices is observed.

Tip vortices have been observed to subsist in a fluid several thousand chords downstream of the wing. Furthermore, vortices have been observed to migrate downwards due to their mutually-induced velocities, travelling towards the ground by a factor of four or more

wingspans (a prime concern near airfields, where small aircraft are at risk of encountering the vortex of a larger plane while in a vulnerable position). Vortices equally migrate sideways with wind. According to Sarpkaya (1989), factors affecting the rate of decay include perturbations in the fluid (i.e., wind and other atmospheric disturbances), wing loading and tip shape. Crow (1970) has observed that small perturbations create vortex instability in the form of sinusoidal disturbances that grow until the two trailing vortices “link” far downstream, resulting in the formation of *vortex rings*. The vortex rings subsequently dissipate fairly quickly (Sarpkaya and Daly, 1987).

Because of the great distances involved in natural vortex decay (literally hundreds of thousands of chords downstream of the wing) and of the hazards associated with trailing vortices, vortex wake dissipation has been a major concern in the aerospace industry since the 1970's.

1.2.6 Vortex-Surface Interaction

The interaction of vortices with solid boundaries are of particular interest in helicopter rotor and turbomachinery blade design, topics for which many studies have been conducted. Vortex-airfoil interaction, although less well documented, is crucial in AAR. Low speed wind tunnel experiments were conducted by Seath and Wilson [10] using a vortex generating wing placed upstream of a NACA-64A015 airfoil at zero AOA and for $Re \approx 500,000$. The results showed a spanwise drift of the vortex upon contact with the airfoil, which can be explained by the presence of an image vortex below the airfoil surface (similar to that of a vortex coming

into ground effect). The drift increased with increasing circulation from the generating wing and was found to be most pronounced when the vortex core was located approximately $0.06c$ above the airfoil leading edge (c being the airfoil's constant chord ≈ 25 cm). Maximum spanwise drift was observed to be approximately equal to $0.2c$. Furthermore, the contact of a moderate-strength vortex with the airfoil's top surface was found to decrease C_p on the suction surface (i.e., increasing suction) and to increase it on the pressure side, thus increasing the overall lift on the airfoil.

Other studies by Meier and Timm [11] (1985) have shown that there is nearly no interaction between the vortex and the boundary layer of an airfoil when the vortex passes at a distance greater than approximately $c/3$ from the top or bottom surface of the airfoil (and thus will have no significant effect the airfoil's pressure distribution except for the generation of a small suction region near the stagnation point on the upper surface). Results also show that when the vortex passes within $c/4$ of the airfoil's top surface, the suction surface sees a significant decrease in C_p and the pressure surface remains relatively unaffected. Conversely, when the vortex passes within $c/4$ of the airfoil's bottom surface, the suction surface is still significantly affected (decreasing C_p at the front of the airfoil) while the pressure surface develops regions of decreased C_p . If the vortex is near level with the airfoil's leading edge, only the suction surface seems to be significantly affected (C_p becomes more negative). These results were found to be nearly independent of Mach number for $0.2 \leq M \leq 0.8$.

Though these results are likely to explain some of the pressure distribution trends experienced for this research, factors such as the shape of the model's wings (i.e., low aspect

ratio and thickness, twist and sweepback) as well as the relatively high AOA's used for the testing are expected to produce somewhat different aerodynamic behaviour. It is speculated that a higher AOA combined with low wing thickness will increase the vertical region of influence of the vortex, and that wing twist combined with a low AR will decrease spanwise drift by creating an adverse pressure gradient along the span.

1.3 Modelling Considerations

Due to the unavailability of a working theory in many fluid mechanics applications, many such engineering problems must be solved by experimentation in order to develop empirical relations, or simply to investigate the effects of design parameter modifications. Because design, construction and testing of full-scale prototypes is a costly and often impractical (if at all possible) alternative, small-scale model testing is the only truly pragmatic solution to these problems.

In the case of AAR aerodynamic interaction investigation, small-scale wind tunnel testing was highly desirable not only because of substantial cost reductions (a CF-18A's operational cost is approximately \$20,000/ hour), but also because it allows for better control of the testing parameters. There are however some drawbacks to small-scale wind tunnel testing, which will be discussed in the following section.

1.3.1 Dimensional Analysis for Aerodynamic Modelling

Wind tunnel testing requires dimensional analysis. For the CF-18A model, the most

important requirement is obviously geometrical similarity (including geometric AOA), followed by Reynolds number (Re), Mach number (M) and specific heat ratio (k).

Geometrical similarity was achieved through the design and construction of a 1/12 scale model for which all dimensions were scaled to the CF-18A aircraft (refer to section 2.1.3). Wing AOA similarity was also easily achievable since the CF-18A model mount was designed for AOA adjustment in the wind tunnel. Unfortunately, as it is often the case in aerodynamic modelling, the other similarity parameters could not be matched given the available means of testing.

Reynolds number: $Re = V_l/v$

In order to match Re of the model (Re_m) with that of the aircraft in flight (Re_a) using the mean aerodynamic chord as the characteristic length, we require:

$$\frac{V_m}{V_a} = \frac{v_m \bar{c}_a}{v_a \bar{c}_m} \quad (1.9)$$

where the subscripts “m” and “a” refer to the model and the full-scale aircraft, respectively.

Since the prototype’s characteristic length is 12 times that of the model, velocities on the order of 12 times that of the aircraft would be required in the wind tunnel (assuming a similar viscosity coefficient). Even in the event that this last requirement was a possibility, supersonic (and hypersonic) velocities would be required, which obviously is not a reasonable

simulation. In practice however, V_a is up to 13 times the maximum airspeed attainable in the UBC Boundary Layer Wind Tunnel (BLWT), and thus matching of Re would require that v_m be on the order of 150 times less than v_a . Such a fluid does not exist, and if it did, it would likely be impractical, at best, for use in a wind tunnel. Consequently, Re_m will be much less than Re_a (typically, by a factor of 100). Fortunately, as shown in figure 192 of [9], the effect of Re on the lift coefficient curve is practically undiscernible for $10^2 < Re < 10^7$, except near C_{Lmax} (which we will not reach in this testing), and thus the discrepancy in Re should be inconsequential³.

Mach number: $M = V/a$

The AAR envelope defined for the CC-130H(T) and the CF-18A is such that Mach number ranges from $M=0.26$ (at 500 ft PA, 170 KIAS) to $M=0.75$ (at 35,000 ft PA, 240 KIAS). The UBC BLWT has a maximum sustainable capacity of $M=0.05$! The Mach number simply cannot be matched for this type of testing. Fortunately, as shown in Figure 1.13, the effect of M on the lift coefficient is small for a thin, symmetrical airfoil ($\alpha_o=0$) and for $M<0.7$, and thus the discrepancy in the Mach number between the model and the prototype is not a major concern in this case.

³ In order to experimentally assess the effect of the Re discrepancy, some wind tunnel tests were conducted at values of Re roughly half of that used for the rest of the testing. Section 3.1.4 summarizes the results.

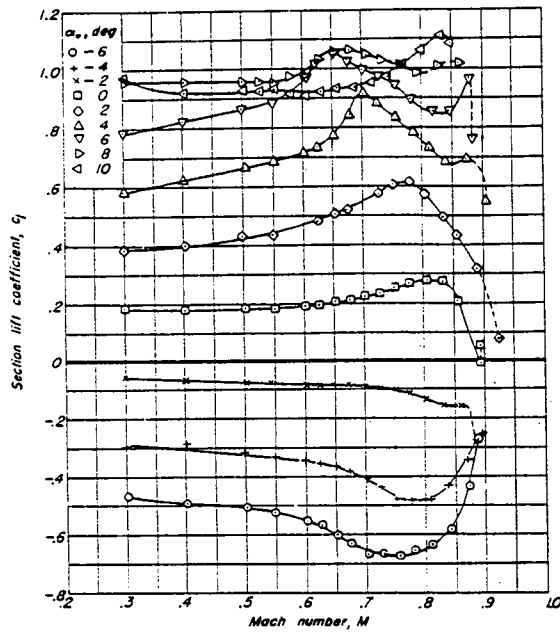


Figure 1.13: Effect of Mach Number on the Lift Coefficient

It is worthwhile to note, however, that according to Prandtl-Glauert and Kármán-Tsien approximations, the pressure coefficient (C_p) is largely affected by Mach number for $M > 0.2$. Accordingly, values of C_p obtained in the BLWT will be somewhat disparate from those of full scale AAR, but trends of pressure distribution on lifting surfaces should be unaffected.

Specific heat ratio:

$$\gamma = \frac{\tilde{p}}{c}$$

The specific heat ratio (γ) is relevant only in compressible flow problems (i.e., for $M > 0.3$) and thus will not be considered for this analysis.

1.3.2 Parameter Scaling

The vortex produced by the generating wing must be set to match the model's dimensions and the wind tunnel's lower airspeed. According to section 1.2.5 of this report, the CC-130H(T) and the generating wing will produce tip vortices with similar velocity and pressure distributions outside the vortex core. The criteria for scaling the circulation of the aircraft (Γ_a) to the BLWT conditions is thus to match the freestream-normalized tangential velocities (U_θ/U_∞) at a normalized radial distance from the vortex centerline (r/c), or:

$$\left(\frac{U_\theta}{U_\infty}\right)_m @ \left(\frac{r}{c}\right)_m = \left(\frac{U_\theta}{U_\infty}\right)_a @ \left(\frac{r}{c}\right)_a \quad (1.10)$$

Since the core radius is small compared to that of the vortex, we can neglect the aerodynamic forces produced by the inner core pressure on the trailing aircraft. Outside of the vortex core, the tangential flow velocity decreases with distance from vortex centerline (r), as described in section 1.2.5. More precisely, for a circular concentric flow:

$$U_\theta = \frac{\Gamma}{2\pi r} \quad (1.11)$$

Substituting this relation into Equation (1.10), we get:

$$\frac{\Gamma_m}{\bar{c}_m U_{\infty m}} = \frac{\Gamma_a}{\bar{c}_a U_{\infty a}} \quad (1.12)$$

where the mean aerodynamic chords are those of the CF-18A model and aircraft, respectively, and thus the circulation required by the CF-18A model (from the generating wing) is:

$$\Gamma_m = \Gamma_a \left(\frac{V_m}{V_a} \right) \left(\frac{\bar{c}_m}{\bar{c}_a} \right) \quad (1.13)$$

Knowing the lift curve slope, zero-lift AOA and the aspect ratio for the generating wing, it is then possible to adjust the wing's geometric AOA inside the wind tunnel (using Equation (1.1)) to obtain the desired circulation for the CF-18A model. Furthermore, since the generating wing's dimensions and shape are almost consistent with the scaling of the CF-18A model (the CC-130H(T) has a slightly tapered wing with a mean aerodynamic chord approximately six times that of the generating wing), one can expect the general size and velocity distribution of the tip vortex core to be reasonably sized for the model.

1.4 Thesis Report Overview

This thesis report presents an orderly description of the investigation of air-to-air refuelling wing-tip vortex interaction between the CC-130H(T) and the CF-18A aircraft. The material included in each chapter is meant to provide a detailed recapitulation of the research undertaken, as well as to reflect the learning experience of the author during the course of this project.

Chapter 2 provides a detailed account of experimental apparatus and procedures. Chapter 3 discloses experimental results and provides an assessment of data measurement

error. The results are further discussed in Chapter 4, yielding final conclusions and recommendations as Chapter 5.

CHAPTER 2

EXPERIMENTAL APPARATUS AND PROCEDURE

The experimental data required for the analysis of AAR aerodynamic interaction was collected inside the University of British Columbia (UBC) Boundary Layer Wind Tunnel (BLWT). A scale model CF-18A was built for the purpose of the testing while the CC-130H(T) wing tip vortex was simulated by installing a vortex-generating wing upstream of the CF-18A model in the wind tunnel. Pressure data on the model was collected through a network of 74 pressure taps linked to a Scanivalve/ solenoid controller combination and pressure transducers. Simultaneously, a six-channel force transducer provided readings of the forces experienced by the model. All pressure and force signals were relayed to a signal conditioning system and recorded in output data files. This chapter provides a detailed description of the equipment and experimental procedures used to model the AAR aerodynamic interaction.

2.1 Experimental Apparatus

2.1.1 Boundary Layer Wind Tunnel

The University of British Columbia (UBC) Boundary Layer Wind Tunnel (BLWT) is an experimental facility that allows relatively large scale aerodynamic modelling. Powered by a single, nine-foot diameter fan, this wind tunnel offers a constant cross-sectional area test section measuring 1.5 metres (5 ft) in height by 2.4 metres (8 ft) in width over a length of approximately 24 metres (80 ft). The maximum attainable wind velocity in the UBC BLWT

is approximately 18 m/s, though the maximum acceptable velocity for sustained operation is limited to approximately 16.8 m/s due to electrical power limitations of the fan motor. The air flow in the test section is longitudinally streamlined through a set of 13 radial flow vanes. A 1.2 metres (4 ft) diameter hole in the wind tunnel floor downstream of the test section allows for the protrusion of the Sting balance mount (refer to section 2.1.2 - *Sting balance*- for more details). A Pitot tube also protrudes from the BLWT test section floor to the left of the main hole, allowing for airflow velocity calibration and reference static pressure measurement.

2.1.2 Sting Balance

The Sting balance is a six-channel force transducer mounted on a cantilever structure. The force transducer houses six load cells, each comprising an arrangement of four 120-Ohm strain gauges, configured to measure vertical forces (also referred to as “normal” forces), side forces, axial force and rolling moments imposed to its outer sleeve. The Sting balance's structure and sensor arrangement provides a robust yet very sensitive force transducer allowing only a negligible amount of interference between its channels.

The force transducer's strain gauges' response is linear within their operating range (roughly from 0 to 1000 microstrains). Thus, the Sting balance provides voltage outputs proportional to the moment applied with respect to each axis. Each of the six channels of the Sting balance force transducer provides a voltage output specific to a reference axis and proportional to a moment or a force. The six channels are as follow:

M_{N1}, M_{N2} : *normal force* moments with respect to points *N1* and *N2*, respectively;

M_{S1}, M_{S2} : *side force* moments with respect to points *S1* and *S2*, respectively;

R : *rolling moment* with respect to the centerline (i.e., the *x*-axis) of the Sting balance; and,

A : *axial force* (compression / tension) along the central axis of the Sting balance.

The Sting balance is designed for maximum values of ± 150 lbs in normal and side forces, ± 75 lbs in axial force and ± 1000 in-lbs for pitching, yawing and rolling moments. The hand-press-fit outer sleeve of the balance is designed to protect the internal strain gauges. The balance provides values of pitching moment at two known gauging points (*N1* and *N2*) along the Sting. Knowing the magnitude of the two moments and their respective location with respect to the electrical centre of the Sting, the resultant vertical force (i.e., the lift force on the model) can be calculated. Similarly, the resulting side force is obtained by reading the moments at points *S1* and *S2*. The rolling moment and the axial force are directly proportional to the voltage readings on the *R*-channel and *A*-channel, respectively.

The Sting balance force transducer operates on a 6.00 volts DC excitation input. Table 2.1 provides more detail on the Sting balance force transducer channels' response and range.

Channel	Response	Range
N1	-6.51	±1000
N2	6.12	±1000
S1	6.51	±1000
S2	5.95	±1000
R	9.07	±1000
A	55.15 ($\mu\text{V/lbf}$)	±75 (lbf)

Table 2.1: Channel Characteristics for the Sting Balance Force Transducer

Furthermore, Table 2.2 provides channel interaction characteristics obtained by comparing the "noise voltage" of the disturbed channel to its potential maximum voltage output. The interaction is specified for the highest loading calibration data available, although noise varies linearly with channel output. Note that channel interactions less than 1/4 percent are neglected and therefore appear as "0".

Interaction on ...	from N1	from N2	from S1	from S2	from R	from A
N1			0	0	0	± 1.5%
N2			0	0	0	± 1.5%
S1	0	0			± 5.0%	± 1.3%
S2	0	0			± 3.0%	± 1.3%
R	0	0	0	0		0
A	± 6.5%	± 0.5%	± 11.5%	± 0.8%	± 18.0%	

Table 2.2: Sting Balance Channel Interaction Characteristics

The Sting balance allows for adjustment of the force transducer's vertical angle to roughly ± 30 degrees from the horizontal (cantilever) position. This feature permits the variation of the angle of attack (AOA) of a cantilever-mounted aircraft model, and was used in this project to adjust the model's AOA.

2.1.3 CF-18A Model

A 1/12 scale model of a CF-18A aircraft was used for the experiment. Designed by the author and built by Aldrige, Pears & Associates (APA) Models Inc., the model demanded several custom features in order to fulfill the requirements of this project. Firstly, a light yet rigid model was required for proper aerodynamic simulation and to avoid exceeding the Sting balance force transducer's stress limits (the balance must be able to support both the aircraft and its mount in a cantilever position). This was accomplished by using a hollow fibreglass body internally stiffened by a thin aluminium structure, which also served to attach the aircraft to its mount (see *CF-18A Model Mount*- section 2.1.4).

The next challenge was the installation of 74 pressure taps, distributed on both leading edge extensions (LEX) and both wings of the model. Wing thickness sometimes not exceeding four millimetres called for careful design and installation in order to properly fit the taps and their respective pressure lines inside the wing structure, while ensuring the structural rigidity of the wings. The method adopted consisted in building the upper and the lower halves of the model separately, then to carefully remove excess material in both halves to install the pressure lines. Finally, the two halves were joined with a combination of epoxy bridges (for structural

rigidity) and glue at the edges. The aircraft's four-degree wing twist was also preserved in the model. In order to minimize flow interference near the pressure taps, the pressure lines run from the wings inside the body cavity and out through the rear end of the model, next to the mount.

Lastly, an engine simulation duct was incorporated to the design in order to model the flow around the wing roots as realistically as possible. The duct runs from both engine intakes to a common rigid plastic tube that extends back to the exhaust area where it is designed to be connected to a high powered vacuum, simulating the engine intake flow around the wing roots.

The design was broken down by aircraft sections, using information provided by McDonnell Aircraft Co. (through the Department of National Defence) and by a 1/30 scale F-18A model which was assembled mainly for visualization purposes and for measuring undefined dimensions. A hard Styrofoam and plastic model was initially built to serve as a template for the mould, which in turn produced the final fibreglass model. The results often exceeded the design requirements for the project.

Due to modelling restrictions (but also due to weight, cost and design limitations), moveable leading and trailing edge flaps could not be incorporated in the model design¹. Consequently, the flaps are always set to the incidence angle of the wing, which will affect the lift of the model. Figure 2.1 shows the 1/12 scale CF-18A model used for the testing.

¹ On the CF-18A aircraft, the leading and trailing edge flaps each operate according to a "schedule" based on current flight conditions (i.e., Mach number and AOA), which proved to be impractical for model testing.



Figure. 2.1 : CF-18A 1/12 Scale Model

The 74 pressure taps are distributed between the wings and the Leading Edge Extensions (LEX's) of the model. More precisely, 18 pressure taps are found on each wing's upper surface (in four rows from wing root to wing tip at 5%, 15%, 30%, 50% and 75% chord), 12 on each wing's lower surface (in the same four rows at 10%, 40% and 70% chord), and seven at regular intervals on the top surface of each LEX.

2.1.4 CF-18A Model Mount

The CF-18A model does not directly mount onto the Sting balance, but is rather attached to it through a rigid mount which allows the model's vertical position to be shifted by ± 38 cm from the Sting's central position (roughly 32 inches, or 0.82 m, above the BLWT floor when horizontally aligned). This feature was incorporated in order to investigate the effects

of relative vertical position between the two aircraft (relative lateral position can be adjusted by moving the generating wing laterally - refer to section 2.1.5). The mount is comprised of a steel cylindrical over-sleeve, which fits snugly over the Sting force transducer, and which is affixed to a slotted, vertically mounted aluminium plate (Figure 2.2). The total weight of the mount is approximately 6.35 kg. The plate measures 37 inches (94.0 cm) in length by 2.0 inches (5.1 cm) in width and has a thickness of ½ inch (1.3 cm). Two ½ inch-wide slots span a total of 36 inches (91.4 cm) along the length of the plate, allowing the model's vertical position to be adjusted by ±15 inches (±38 cm) by sliding its supporting T-brackets up or down the slots.

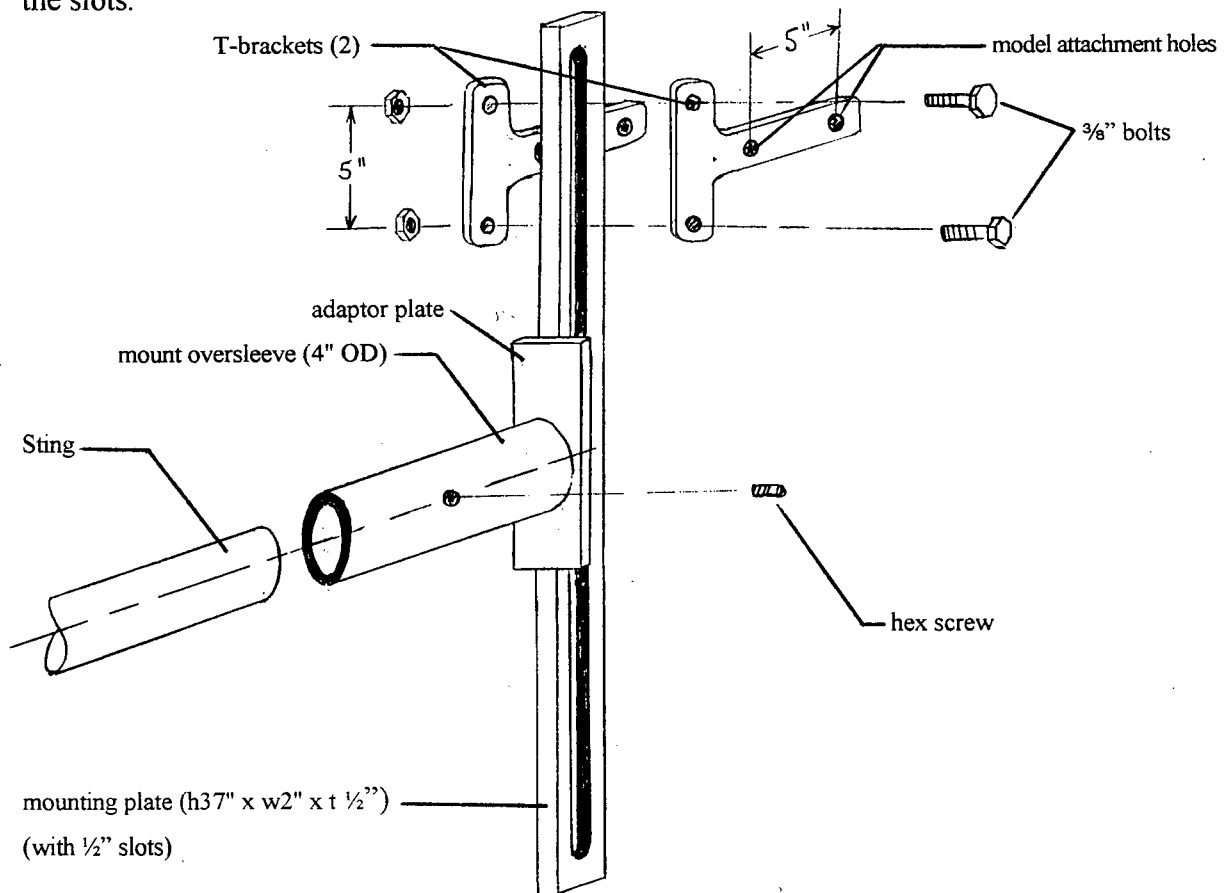


Figure 2.2: CF-18A Model Mount Diagram

2.1.5 Vortex Generating Wing

The wing section used for generating the CC-130H(T)'s scaled tip vortex is a standard Clark Y (14% thickness) untapered airfoil with a 2 ft (0.61 m) chord length and an aspect ratio of 1.49 (including the mount). The zero-lift angle for this airfoil is -3.0 degrees and the lift curve slope is given by the equation:

$$\frac{dC_L}{d\alpha} = \frac{2\pi AR}{(AR+2)} \quad (2.1)$$

The wing is mounted vertically on its right tip using a heavy, metal plate floor mount designed for stability and mobility of the wing in the wind tunnel. The exposed part of the mount was covered by a fibreglassed hard foam airfoil section having an identical profile to that of the wing. The purpose of the mount cover is to prevent vortex generation from the wing-tip closest to the floor of the wind tunnel. The vertical-type mounting of the generating wing is not a concern since it is placed far enough upstream to provide a fully rolled-up vortex for the model (refer to section 1.2.4 - *Vortex Roll-Up*). The generating wing's lateral position and AOA (denoted as α_{GW}) could be varied in order to simulate various relative positions and flight conditions.

In accordance with equation (2.1), increasing α_{GW} also increases the wing's lift coefficient, which in turn (for a constant q) increases the wing's lift force (L_{GW}) and the generated circulation (Γ_{GW}). For the testing, the generating wing was set at specific angles of

attack in order to produce the desired circulation over the model (refer to Appendix A for the selection of the specific conditions) .

2.1.6 Scanivalve and Solenoid Controller

The Scanivalve/ Solenoid Controller combination allows for quick, systematic and automated reading of a number of pressure lines. The Scanivalve is a selector valve whose function is to block *all but* four designated pressure lines when set in any one position, enabling the connection of these four lines to four pressure sensors. A five millisecond, 28 volt pulse to the *step* circuit of the Scanivalve causes its internal solenoid armature to rotate by 1/24 of a full rotation, allowing the next four pressure lines to be connected to the pressure sensors, and so on. Once the armature has completed 24 steps (thus allowing for a total of 96 pressure line connections), it has returned to its original position and is ready to proceed through another cycle, if required. The first (reference) solenoid armature position is called the *home* position. The *step* cycle can be interrupted at any position by sending a five millisecond, 28 volt pulse to the *home* circuit of the Scanivalve, which immediately drives the armature back to the starting position.

The step frequency of the Scanivalve can be adjusted by varying the rate at which the voltage pulses reach the *step* circuit. The CTRL2 model Solenoid Controller produces the voltage pulses that drive the Scanivalve. The pulses can be generated manually by pressing the *step* or the *home* button on the controller front panel, or regulated through a microprocessor-generated digital signal to the Controller. The Controller pulse rate field ranges from 50

min/pulse to 0.04 sec/pulse (i.e., 25 pulses per second, limited by the internal armature of the Scanivalve) under a standard 115 volts AC (50-400 Hz) power source.

Since accurate reading of pressure lines requires a settling time that is much larger than the Controller's minimum pulse delay (in the order of 5 seconds), the Scanivalve/ Solenoid Controller system was deemed more than adequate for the purpose of this project.

2.1.7 Pressure Transducers

Four 160PC Low Pressure Sensors were used as part of the data acquisition system. These thin-diaphragm sensors provide an output voltage proportional to the pressure applied to their diaphragm. The pressure sensors operate from a single, positive supply voltage ranging from +6.0 to +12.0 volts DC (typical excitation is +8.0 volts DC), and provide temperature compensation between -40°C and +85°C. The voltage output ranges linearly from +1.0 volt DC under a pressure of -5.0 inches of water (-1245 Pa) to +6.0 volts DC under a pressure of +5.0 inches of water (+1245 Pa), with a zero-pressure output of +3.5 volts DC. The reference pressure was taken from the static pressure port of the Pitot tube inside the BLWT. Section 2.2.2 provides calibration information for the 160PC Low Pressure Sensors.

2.1.8 Analogue to Digital (A/D) Converter

The use of an A/D converter was necessary to provide an interface with the computer used to drive the data acquisition system. A 12 bit, 1.0 MHz, ISC-16 A/D card was used. This device is used to convert the analogue voltage output from the force and pressure transducers

to a digital signal that can be processed and stored by the computer, as well as to output the voltage required to drive the solenoid controller's *step* and *home* circuits. The ISC-16 A/D card's input voltage range is -10 to +10 volts.

2.1.9 10-Channel Amplifier

In order to reduce the A/D converter's inherent uncertainty when reading very small voltages (and thus to improve data accuracy), the Sting force transducer voltage outputs had to be independently amplified for each channel. This was accomplished through a 10-channel amplifier built for the purpose of this project. The amplifier hosts a power unit, a digital metre and 10 slots for fitting removable integrated circuit boards. Each board is fitted with a combination of potentiometers, resistors and resistor switches to provide an adjustable gain varying between $K=1$ and $K=10^3$. Only six of the 10 channels were needed (for the six force channels) since the four pressure transducer signals did not require amplification.

2.1.10 Data Acquisition Controller

Orchestrating of the data acquisition was the task of the *Data Acquisition Controller*, essentially a micro-computer to which the A/D converter board is linked through the ISC-16 A/D card. A Turbo-C software program controlled the data acquisition, processing and storage. A code listing for the data acquisition program is included in Appendix C.

2.2 Experimental Procedure

2.2.1 Equipment Installation

The Sting balance was installed through a floor opening far downstream in the BLWT. This location enabled the generating wing (located roughly 8 m upstream) to produce a fully rolled-up vortex at the model.

The model mount was then secured to the Sting balance by sliding its over-sleeve onto the Sting's force transducer's outer sleeve. A flat-head hex screw ensured no slippage between the sleeve and the over-sleeve contact surfaces. The model was affixed to the mount by two T-brackets. The base of the T-brackets bolt to each side of the internal aluminium structure of the model through two sets of holes in the model's aft body, thus keeping the bolts and nuts out of the airflow (Figure 2.3). These holes were covered with thin adhesive tape during the testing in order to keep a smooth flow near the tail. The top part of the T-brackets attach to the mount through two 3/8 inch bolts set five inches apart, allowing vertical movement of the brackets along the slotted vertical plate.

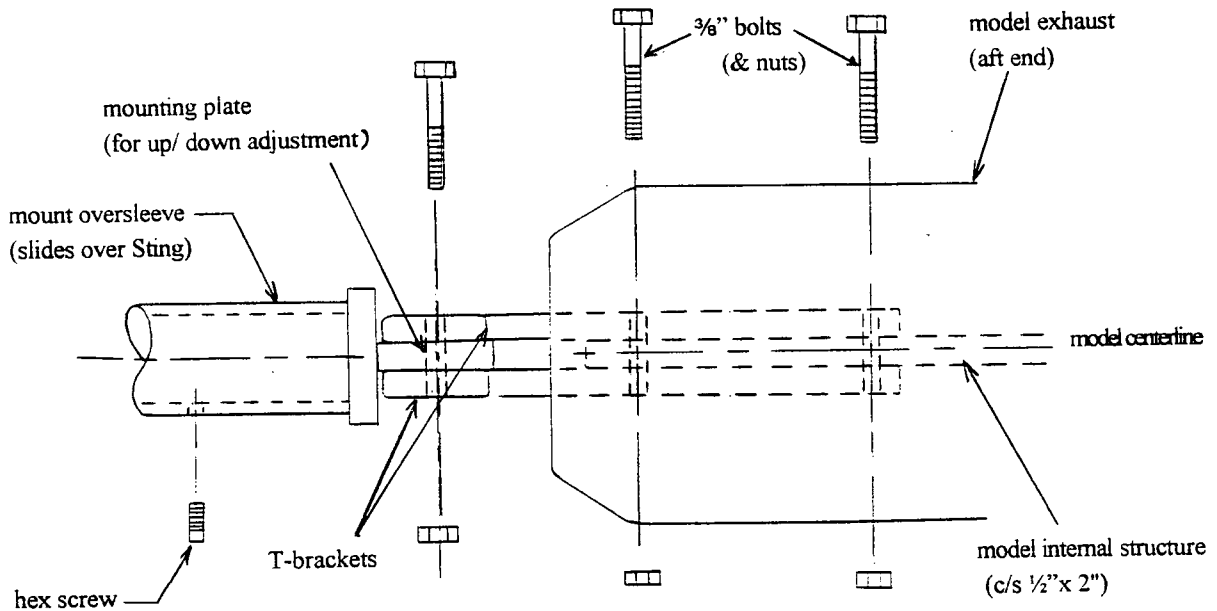


Figure 2.3: Sting, Mount and Model Structural Interface (Top View)

The Scanivalve/ Solenoid Controller arrangement was installed on a shelf located just below the BLWT floor and near the Sting balance, thus keeping the Scanivalve out of the airstream. The pressure lines running from the exhaust of the model were bundled and loosely tied to the Sting balance structure in order to minimize their effect on the airflow. The pressure lines ran along one of the Sting balance's vertical supports down through the BLWT floor hole and to the Scanivalve. The power source used for the Scanivalve was a standard 115V/60Hz wall outlet. The *home* and *step* excitation terminals were relayed to the ISC-16 A/D converter to drive the *home* and *step* circuits from the data acquisition controller. Four output pressure lines ran from the Scanivalve to four pressure transducers, also located below the BLWT floor.

The four pressure transducers shared a common reference pressure line through a four-in-one line adapter. The resulting single pressure line was connected to a BLWT Pitot tube

reference pressure port, thus relaying the static pressure of the airflow in the BLWT simultaneously to all four transducers' reference pressure ports. This ensured standardization of the pressure readings. The reference pressure was measured approximately 30 cm above the BLWT floor, slightly ahead and to the left of the model in order to avoid wall, floor, model and generating wing effects as much as possible. The +8.0 volts excitation voltage for the pressure transducers was provided by the power source.

The vortex-generating wing was installed approximately 24 feet (7.3 m) upstream of the model's nose in the BLWT. With a non-tapered chord of two feet, it was estimated that the wing would provide a fully rolled-up vortex at the model's location (a fully rolled-up vortex is known to develop within three chord lengths downstream of the wing tip - refer to section 1.2.4). The generating wing was held in a vertical position on the bottom of the BLWT by a sturdy steel mount. The upper part of the mount attaches to the wing's protruding steel support through four 1/4" bolts, while the lower part of the mount consists of a cross-shaped thin plate designed to keep the wing from tipping under the aerodynamic forces. Markings made on a wooden plate glued to the lower part of the mount served as an AOA scale for the generating wing. The assembly's sheer weight ensured the stability of the wing in the BLWT, even at maximum wind velocity and maximum α_{GW} . Due to the orientation of its camber, the generating wing produced a counter-clockwise (ccw) vortex for the model.

Finally, the 10-channel amplifier, the ISC-16 A/D converter, the power source and the data acquisition controller were installed on a table in the immediate vicinity of the BLWT.

2.2.2 Equipment Calibration

Sensors and experimental equipment require calibration. The objectives of calibration include determining a suitable scale for measurands, as well as verifying the repeatability of the relation between inputs and outputs for a given measuring instrument. In some cases, this was merely a task of associating an instrument readout with a repeatable test parameter (such as matching fan RPS with BLWT wind velocity), while other sensors required a more extensive calibration process. The equipment requiring calibration for this project were the BLWT, the Sting balance, the 10-channel amplifier and the pressure transducers.

Boundary Layer Wind Tunnel

The BLWT was calibrated through the use of a pitot-static probe and manometer combination. The wind tunnel driving fan was set at specific RPS values between zero and maximum output (60 Hz) and a manometer reading was taken for each setting once all conditions were stabilized. The manometer consists of a glass tube 200 mm long and graduated in 1 mm increments. The *total pressure* (p_T) line from the pitot tube is connected to the lower part of the glass tube (the fluid reservoir), while the pitot *static pressure* (p_s) line is connected to the upper part of the glass tube (above the fluid level). The pitot static pressure is taken inside the wind tunnel and thus the manometer reading yields the freestream *dynamic pressure* (p_d), since:

$$p_d = p_T - p_s \quad (2.2)$$

The manometer's inclination is adjustable to various vertical-to-horizontal ratios (1:2, 1:5, 1:10 and 1:25). For this experiment, the manometer was set at a vertical-to-horizontal ratio of 1:5, corresponding to an inclination (θ) of 11.3 degrees from the horizontal. The manometer fluid is alcohol and has a specific density (γ_f) of 0.80. The freestream dynamic pressure is obtained through the mathematical relation:

$$p_d = \gamma_f \rho_w g D \sin \theta \quad (2.3)$$

where D is the length of the manometer fluid column measured along the manometer tube from the reference point (i.e., when the freestream velocity is zero) and ρ_w is water density. When all constants and units are standard metric, the pressure reading is in Pascals (Pa).

According to Bernoulli's principle, the corresponding freestream velocity (V_∞) is given by the equation:

$$V_\infty = \sqrt{\frac{2p_d}{\rho_a}} \quad (2.4)$$

where ρ_a is the air density under the BLWT atmospheric conditions. Conveniently enough, the atmospheric conditions in the BLWT were approximately those of a standard atmosphere at sea level (15°C and 101.3 kPa). Equations (2.3) and (2.4) can be combined to yield:

$$V_\infty = \sqrt{\frac{2\gamma_f \rho_w g D \sin\theta}{\rho_a}} \quad (2.5)$$

Given that $\gamma_f = 0.80$, $\rho_w = 10^3 \text{ kg/m}^3$, $\theta = 11.3 \text{ deg}$ and $\rho_a = 1.225 \text{ kg/m}^3$, Equation (2.5)

becomes:

$$V_\infty = 50.1 D^{1/2}$$

Although the fan was able to attain an output of 60 Hz for short periods, fan settings above 55 Hz could not be sustained by the fan's electric motor, causing it to automatically shut itself off. Consequently, a maximum fan setting of 50 Hz was used for the wind tunnel testing.

Table 2.3 provides a summary of the BLWT calibration readings. Each reading was taken four times (twice during the crescendo and twice during the de-crescendo of the fan RPS) to verify data repeatability. The average of the four readings is tabulated. It was found that all same-RPS manometer readings were within 2% of each other, confirming repeatability.

Fan Setting (RPS)	D (mm)	p_a (Pa)	V_∞ (m/s)
0	0	0	0
10	2.1	3.2	2.3
15	4.9	7.5	3.5
20	10.2	15.7	5.1
25	18.1	27.8	6.74
30	28.0	43.1	8.38
35	41.7	64.1	10.2
40	59.6	91.7	12.2
45	84.1	129	14.5
50	111.9	172.1	16.8
55	147.7	227.2	19.3

Table 2.3: BLWT Calibration Data

Sting Balance/ Amplifier

After assembly of the Sting balance in the BLWT, calibration of the Sting force transducer/ signal amplifier was required in order to get a suitable signal to the A/D converter. The A/D converter's signal reception range is -10.0 volts to +10.0 volts and thus the amplifier was calibrated to make maximum use of this range with careful attention not to exceed the A/D limits.

Prior to calibrating the Sting/ amplifier apparatus, an estimate of maximum loads anticipated in normal, side and rolling axes was required to determine ranges for the calibration. This in turn required a prior analysis of the anticipated aerodynamic forces acting on the CF-18A model, which can only be obtained by looking at specific AAR conditions (i.e., airspeed, AOA, aircraft weight, tanker circulation, etc.). Three points of the refuelling envelope were investigated for the purpose of this project ². The selected AAR points include a maximum circulation (Γ_{max}) condition, a minimum circulation (Γ_{min}) condition and a typical circulation (Γ_{typ}) condition, as established in [1] (refer to section 1 of Appendix A for details on the selection of these points). The calculations associated with determining the aerodynamic forces on the model are detailed in section 2 of Appendix A. The results are summarized in Table 2.4.

² The selection of these points reflects the overall aim of the thesis, which is to investigate the aerodynamic effects of the CC-130H(T)'s wing-tip vortex on the CF-18A aircraft in the pre-contact position and under various AAR conditions.

PARAMETER	MIN / MAX VALUES
LIFT FORCE ("+" is up)	0 / +56.6 N
SIDE FORCE ("+" is right)	-3.0N / +3.0N
ROLLING MOMENT ("+" is ccw)	-4.3 N·m / +4.3 N·m

Table 2.4: Maximum Estimated Aerodynamic Loads on the Model

Similarly, Table 2.5 provides a summary of the maximum anticipated loads on each of the Sting's channels. Details of the calculations provided in section 3 of Appendix A.

CHANNEL	MIN / MAX VALUES
N1	-57.0 N·m / -19.5 N·m
N2	-87.0 N·m / -40.3 N·m
S1	-2.92 N·m / +2.92 N·m
S2	-3.50 N·m / +3.50 N·m
R	-4.3 N·m / +4.3 N·m
A	(not used)

Table 2.5: Maximum Anticipated Loads on the Sting Balance

The actual calibration of the Sting balance/ amplifier was carried out in two phases: first, a verification phase to confirm the linear characteristics of all channels, followed by a calibration phase in which the amplifier was set to provide a suitable range for each channel (by adjusting the gain potentiometers).

For the verification phase, the model mount was installed on the Sting, which was then subjected to normal forces, side forces and rolling moments of known value and location, using

the maximum anticipated load values determined in Tables 2.4 and 2.5 as guidelines. Normal and side forces were applied by hanging weights from the model mount, either directly (for the case of downward normal force) or using a pulley to direct the force at will (for the case of side forces and upward normal force). Accordingly, normal and side forces were applied at the vertical slot centre location of the mount (i.e., 4.88 inches (12.4 cm) ahead of the *NI* axis). Using forces of -60 lbs to + 40 lbs in the normal direction (in increments of 5 lbs), moments of +302 lb·in to -186 lb·in and -873 lb·in to +387 lb·in were produced at *NI* and *N2*, respectively. Similarly, forces of -20 lbs to +20 lbs were used to produce moments of ± 98 lb·in and ± 252 lb·in at *S1* and *S2*, respectively. Each measurement was performed twice (i.e., during loading and unloading), and the average of the two readings was used. It was observed that any two corresponding readings were within 2% of each other. The results also confirmed the linear response of the Sting for channels *NI*, *N2*, *S1* and *S2* within the verified ranges. The rolling moment channel verification was performed without the model mount and using the Sting torsion bar. This bar is designed to provide pure torsion to the balance by allowing two equal forces of opposite sign to create a moment about the Sting's centerline axis. A combination of equal upwards and downwards normal forces was used to produce rolling moments up to ± 276 lb·in. Once again, each point was measured twice and corresponding readings were within 1% of each other, while the results confirmed the linear response of the Sting for this channel.

The calibration phase was performed with the mount installed on the Sting for all channels. The procedure followed was that of a convergence loop since the two

potentiometers used for calibrating each channel were inter-related (due to the initial load on the Sting). First, the “zeroing” potentiometer was adjusted to obtain a zero-volt reading when no load was applied to the Sting. Then, after applying the largest load used in the verification phase (for a specific channel), the gain potentiometer was adjusted to obtain the correct reading, based on the desired scale for the channel. This would in turn affect the *zero* reading, which had to be re-adjusted, after which the load was re-applied and the gain re-adjusted, repeating this procedure until convergence was obtained (i.e., until the no-load reading was zero and the desired scale was obtained). Finally, a last verification was conducted to ensure the linearity of the new scale and the repeatability of the readings. The results of the Sting/ amplifier calibration are displayed in Table 2.6. Note that the calibration was performed in *lb inches* since the Sting technical manual uses these units (note that *lb inches* can be converted to *Newton metres* by simply dividing by 8.33).

CHANNEL	MIN / MAX MOMENTS (lb·in)	MIN / MAX READINGS (volts)	SCALE (lb·in/ volt)
N1	-195 / +302	-1.95 / +3.02	100
N2	-873 / +387	-8.73 / +3.87	100
S1	-98 / +98	-1.96 / +1.96	50.0
S2	-252 / +252	-5.04 / +5.04	50.0
R	-276 / +276	-5.52 / +5.52	50.0

Table 2.6: Sting/ Amplifier Calibration Results.

Pressure Transducers

Calibration of the pressure transducers was done last. The four transducers were calibrated by subjecting them to a column of water of height $h=0$ to $h=5$ inches (in increments of 1.0 inch), and reading the voltage output through the A/D converter. Clear tigon tubing was used to contain the fluids and water was added with an eye-dropper. Input port P1 (which served as the reference pressure port for the testing) was left open to atmospheric pressure for the first phase of the calibration. In the second phase, the negative pressure range was calibrated by carrying the same procedure using the reference pressure port P1 as the “pressure side” and leaving P2 open to atmospheric pressure. Since each output voltage (V_{out}) reading is the average of 255 readings taken at 0.01 second intervals, each pressure transducer was tested only once. The measurement error was $\pm 0.5\text{mm} \approx \pm 0.02\text{inches}$ (less than 0.02%) and it was found that the difference between the theoretical values (refer to the pressure transducer specs - Appendix C) and calibration readings was less than 3%. It was thus concluded that the pressure transducers needed no additional calibration. The results from the calibration data are displayed in Table 2.7.

h (water column) (inches)	Theoretical V_{out} (volts)	Transducer #1 V_{out} (volts)	Transducer #2 V_{out} (volts)	Transducer #3 V_{out} (volts)	Transducer #4 V_{out} (volts)
-5.00	+1.0	+1.01	+0.98	+1.01	+0.97
-4.00	+1.5	+1.51	+1.48	+1.50	+1.50
-3.00	+2.0	+2.03	+1.99	+2.01	+1.99
-2.00	+2.5	+2.54	+2.47	+2.53	+2.51
-1.00	+3.0	+3.06	+2.96	+3.01	+3.03
0.00	+3.5	+3.54	+3.50	+3.48	+3.52
+1.00	+4.0	+4.08	+4.01	+3.95	+4.05
+2.00	+4.5	+4.57	+4.53	+4.46	+4.53
+3.00	+5.0	+5.04	+5.07	+4.97	+5.02
+4.00	+5.5	+5.53	+5.56	+5.51	+5.49
+5.00	+6.0	+6.01	+6.04	+6.08	+5.96

Table 2.7: Pressure Transducers Calibration Data

2.2.3 Experimental Procedure

Once all experimental equipment was in place and calibrated, the actual testing process involved little more than running the data acquisition program under specific wind tunnel, generating wing and model conditions. A total of 96 such conditions were investigated by combining any of two levels of wind tunnel settings, five generating wing positions, five vertical positions for the model, and three simulated flight conditions (altitude and airspeed dependant). Each of the three AAR points chosen was investigated under 32 different test conditions in order to determine the effects of relative aircraft position as well as those of the Reynolds number on scale testing in the BLWT. The three AAR conditions investigated are summarized in Table 2.8, while wind tunnel modelling specifics corresponding to these AAR

conditions are summarized in Table 2.9. (calculation details for Tables 2.8 and 2.9 can be found in Appendix A).

Flight Condition	Airspeed (KIAS)	Altitude (ft)	CC130H(T) weight (lbs)	CF-18A weight (lbs)	CF-18A AOA (deg)
$\Gamma_{max}=287 \text{ m}^2/\text{s}$	170	35,000	155,000	33,500	12.3
$\Gamma_{typ}=189 \text{ m}^2/\text{s}$	190	20,000	150,000	33,500	9.8
$\Gamma_{min}=96.4 \text{ m}^2/\text{s}$	240	500	135,000	33,500	6.2

Table 2.8 : AAR Cases Investigated

Condition	Airspeed (m/s)	Air density (kg/m³)	(α_g)_{cw} (deg)	(α_g)_m (deg)
$\Gamma_{max} = 2.56 \text{ m}^2/\text{s}$	16.8	1.225	7.7	12.3
$\Gamma_{typ} = 1.98 \text{ m}^2/\text{s}$	16.8	1.225	5.2	9.8
$\Gamma_{min} = 1.09 \text{ m}^2/\text{s}$	16.8	1.225	1.6	6.2

Table 2.9 - Wind Tunnel Conditions for the Three AAR Cases

Aircraft relative position analysis was conducted for all three AAR conditions described in Table 2.9 using five different vertical settings (*ZPOS*) each for five lateral settings (*YPOS*) (i.e., 25 test points for each AAR condition). In order to provide a basis for comparison, reference tests (without generating wing) were also conducted for each of the five vertical settings and for each α_m corresponding to a AAR condition. The testing pattern (i.e., the order in which the tests were performed) was based on ease of parameter variation with the intent of minimum position setting for the model and the generating wing. Consequently, the generating

wing's position ($YPOS$) was kept constant while testing was conducted for five vertical positions of the model ($ZPOS$), each of which in turn tested for the three AAR conditions (by suitably varying α_m and α_{GW}) prior to changing $ZPOS$. Furthermore, half-speed tests (used for Re effects investigation) were conducted immediately following their corresponding full-speed test, wind speed being the only adjustment required between the two.

Although force data were plotted for all three AAR conditions, it was felt that typical AAR pressure data would provide sufficient information on the vortex-wing interaction to be investigated. Furthermore, Re effects were investigated both with and without the generating wing for the condition $YPOS=ZPOS=0$.

CHAPTER 3

RESULTS

The results of the BLWT tests are displayed in Appendix B and comprise model force and pressure distribution data for all test conditions. An objective and systematic description of the results is presented in this chapter, while more in-depth interpretation and analysis will be the focus of Chapter 4.

3.0 General

Throughout the results description and analysis, the terms “interaction” and “reference” are used to distinguish between tests conducted *with* and *without* the generating wing, respectively. The difference between interaction forces and reference forces (i.e., when the reference data has been subtracted from the interaction data to study the effect of the vortex) are referred to as “vortex-induced forces”, or simply “induced forces”. Similarly, the term “ZPOS” refers to the vertical position of the model with respect to that of the generated vortex, while the term “YPOS” refers to the horizontal position of the generating wing (and thus that of the generated vortex) with respect to the model (thus the condition $YPOS=ZPOS=0$ represents the case for which the Sting longitudinal axis is aligned with the vortex centerline, also referred to as the “central position”). Finally, the terms Γ_{min} , Γ_{typ} and Γ_{max} are used throughout the following two chapters to distinguish between the three AAR conditions investigated (refer to section 2.2.3 for specifics on these conditions).

Since the position of the vortex core was not directly measured in this investigation, the vertical distance between the vortex centerline and the model's longitudinal axis could only be estimated (using the results of previous vortex core investigation). The model's longitudinal axis is defined at the leading edge of the mean aerodynamic chord (MAC). Section 1.2.4 reported that for an elliptically loaded wing, vortex roll-up occurs at approximately 90% of the wing's semi-span, outboard from the wing root. For a rectangular, square-tip half-wing, (such as the generating wing used), experiments by Green (1988) have shown that vortex roll-up is also between 88% and 93% of the semi-span. Using 90% of the semi-span as an average, this distance is 0.82 m (from the BLWT floor), thus approximately 0.09 m below the generating wing's free tip. This position nearly coincides with the central position of the Sting (which is less than half a centimetre higher), and thus given the uncertainty in the estimation, we shall approximate the vortex centerline vertical position to correspond with the central position.

The vertical distance between the vortex centerline and the model requires a reference point on the model. For practical reasons and ease of reference, the wings' leading edge at the MAC is defined as the model reference. However, the z -position of the MAC leading edge varies not only with $ZPOS$ but also with α_m , since the point of rotation for varying α_m is point "O" on the Sting (refer to Figure 3.1).

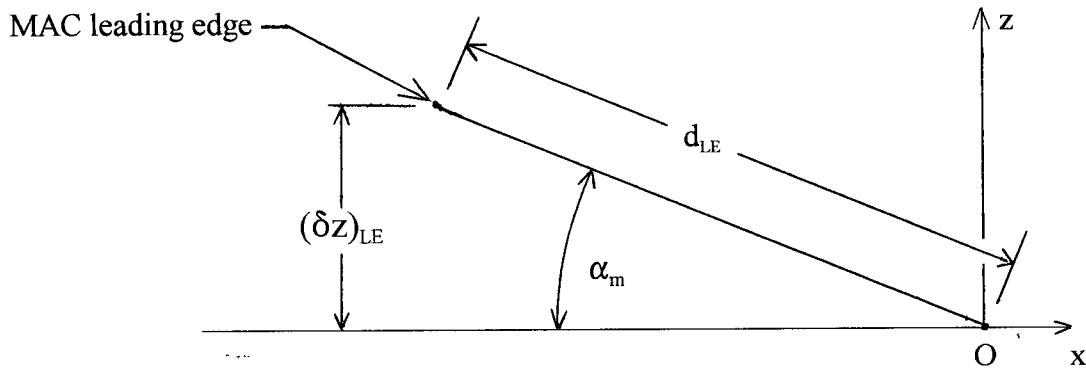


Figure 3.1: Variation of Model's MAC Leading Edge z -Position with α_m

Accordingly, any variation of α_m will translate into a MAC leading edge vertical position change $(\delta z)_{LE}$ given by:

$$(\delta z)_{LE} = d_{LE} \sin \alpha_m \quad (3.1)$$

where $d_{LE} = 0.947$ m, the distance of the MAC leading edge from point "O". Accordingly, the z -location of the MAC leading edge (z_{LE}), using the central position as a reference, is:

$$z_{LE} = ZPOS + (\delta z)_{LE} \quad (3.2)$$

Thus, a more accurate measure of the model's relative z -position with respect to the vortex centerline is z_{LE} , replacing the measure $ZPOS$.

From Equations (3.1) and (3.2), we get:

$$z_{LE} = ZPOS + d_{LE} \sin \alpha_m \quad (3.3)$$

Table 3.1 displays the revised values of relative z -position of the MAC leading edge as

functions of $ZPOS/c_m$ and α_m .

ZPOS/ c_m	z_{LE} (m)		
	@ $\alpha_m = 6.2$ deg	@ $\alpha_m = 9.8$ deg	@ $\alpha_m = 12.3$ deg
-1.3	-0.278	-0.219	-0.178
-0.50	-0.048	+0.011	+0.052
0	+0.102	+0.161	+0.202
+0.50	+0.252	+0.311	+0.352
+1.3	+0.482	+0.541	+0.582

Table 3.1: Actual z-Location of the Model MAC Leading Edge w.r.t. the Vortex Centerline

The strength and the position of the vortex core are affected by BLWT wall effects. These effects are better understood by referring to the *image vortices* created as a result of the BLWT walls. Although an infinity of images of the generated vortex are created by the physical boundaries of the BLWT, only the four nearest images (using each wall as a plane of symmetry) need to be considered since effects from far images are either negligible or tend to cancel each other.

Considering the effect on vortex strength first will allow for a more accurate analysis of the effects on vortex position. In the BLWT, the generating wing experiences “ground effect” from the side walls, as well as “formation effects” from the top and bottom walls. The combined result increases the lift of the generating wing, and thus its tip vortex strength. Considering the four principal images shown in Figure 3.2, ground and formation effects can be estimated from figures 9.10 and 9.11 of [3].

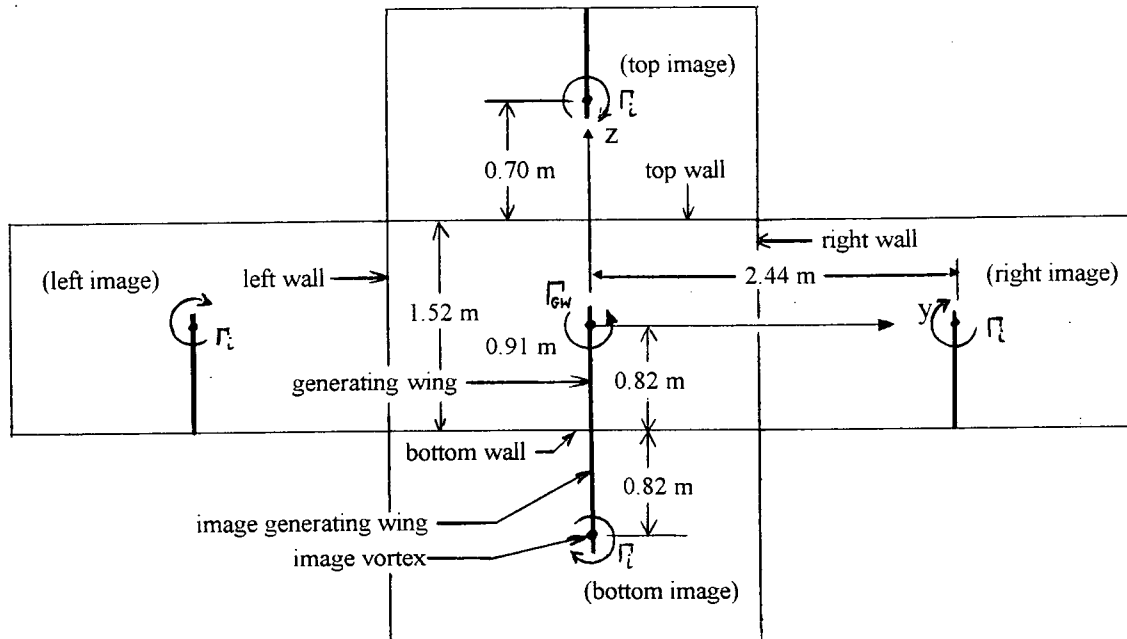


Figure 3.2: Principal Image Vortices due to BLWT Walls

Formation effects are constant for all conditions since the generating wing does not move along the z -axis. For wing spans (b_{GW}) of 1.82 m spaced 1.22 m apart (S), Figure 9.11 of reference [3] yields $(C_D)_{formation}/(C_D)_{solo} \approx 0.92$, which implies generating wing lift and circulation increases of approximately 4 percent¹. Table 3.2 summarizes these effects. Note that for ground effect estimation, the height-to-span ratio (h/b_{GW}) in Figure 9.10 of [3] also yields *induced drag* ratios, which are converted to net lift increases in the same fashion as the formation effects.

¹This is the *induced drag* ratio (K_i). Since $C_L \sim (C_D)^{1/2}$, the net lift (and circulation) increase is:

$$(\Delta L/L) = (\Delta \Gamma/\Gamma) = \sqrt{1/K_i} - 1$$

		GROUND EFFECTS (% increase)		FORMATION EFFECTS	TOTAL EFFECT
		left wall	right wall	(% increase)	(% increase)
YPOS= 0	h (m)	1.22	1.22		
	h/b_{GW}*	0.67	0.67		
	k	0.98	0.98	0.92	
	ΔL (%)	+1.0	+1.0	+4.3	+6.3
	ΔΓ (%)	+1.0	+1.0	+4.3	+6.3
YPOS= +0.305 m	h (m)	0.91	1.52		
	h/b_{GW}*	0.50	0.83		
	k	0.92	1.0	0.92	
	ΔL (%)	+4.1	0	+4.3	+8.4
	ΔΓ (%)	+4.1	0	+4.3	+8.4
YPOS= +0.61 m	h (m)	0.61	1.83		
	h/b_{GW}*	0.33	1.0		
	k	0.83	1.0	0.92	
	ΔL (%)	+9.6	0	+4.3	+13.9
	ΔΓ (%)	+9.6	0	+4.3	+13.9

* $b_{GW} = 0.91$ m

Table 3.2: Ground and Formation Effects on the Generating Wing's Lift and Circulation

Note that the total effects displayed in Table 3.2 are symmetrical for negative values of *YPOS*, the left wall effect simply becoming the right wall effect and vice-versa, yielding identical results to those obtained with positive values of *YPOS*. The final results on the magnitude of the generated circulation are displayed for each case in Table 3.3.

	Γ_{\min} (m ² /s)	Γ_{typ} (m ² /s)	Γ_{\max} (m ² /s)
YPOS = 0	-1.15	-2.09	-2.73
YPOS = ± 0.305 m	-1.17	-2.14	-2.79
YPOS = ± 0.61 m	-1.23	-2.24	-2.93

Table 3.3: Generating Wing Circulation (Accounting for BLWT Wall Effects)

Each image vortex shown in Figure 3.2 imparts a velocity to the generated vortex core, given by:

$$V_0 = -\Gamma_{\text{GW}} / (2\pi r) \quad (3.4)$$

where r is the distance between the centre of the generated vortex and that of the image vortex being considered. The velocities imparted by the image vortices are vectorially added to obtain the resultant velocity of the generated vortex core. Note that Figure 3.2 displays the generating wing in the central position (i.e., for $YPOS=0$), a case for which the left and right image vortices will cancel each other's effect. However, when the generating wing is not centred in the BLWT, the left and right image vortices do not cancel out, resulting in a vertical motion of the vortex core. This effect is most noticeable for $YPOS=\pm 0.61$ m and must be considered in the analysis. The top and bottom image vortices, though acting in opposite directions on the generated vortex, do not cancel out because of their different radius of action. The result is a constant leftwards motion of the generated vortex. The total displacement of the generated vortex (horizontally and vertically) at the model MAC leading edge is shown in Table 3.4 for each of the three cases (using the vortex

strength data from Table 3.3). The horizontal and vertical displacements of the generated vortex due to wall effects will be referred to as $(dy)_w$ and $(dz)_w$, respectively. Note that positive $(dy)_w$ and $(dz)_w$ are along the positive y -axis and the z -axis, respectively.

YPOS	Γ_{\min} case		Γ_{typ} case		Γ_{\max} case	
	$(dy)_w$	$(dz)_w$	$(dy)_w$	$(dz)_w$	$(dy)_w$	$(dz)_w$
-0.61 m	-0.013 m	-0.047 m	-0.024 m	-0.085 m	-0.031 m	-0.111 m
-0.305 m	-0.012 m	-0.018 m	-0.023 m	-0.032 m	-0.029 m	-0.042 m
0	-0.012 m	0	-0.022 m	0	-0.029 m	0
+0.305 m	-0.012 m	+0.018 m	-0.023 m	+0.032 m	-0.029 m	+0.042 m
+0.61 m	-0.013 m	+0.047 m	-0.024 m	+0.085 m	-0.031 m	+0.111 m

Table 3.4: Displacement of the Generated Vortex Core due to BLWT Wall Effects

Table 3.4 shows that the BLWT wall effects are significant, shifting the generated vortex by approximately up to 3 cm horizontally and ± 11 cm vertically. In light of this information, a new vortex centerline position can be estimated. Using the previously established initial position of the vortex core (i.e., the Sting's central position), a new model relative position (w.r.t. the vortex centerline) can be calculated by combining the information of Tables 3.1 and 3.4. More specifically:

$$y_w = - (YPOS + (dy)_w) \quad (3.5(a))$$

$$\text{and:} \quad z_w = z_{LE} - (dz)_w \quad (3.5(b))$$

where y_w and z_w are the horizontal and vertical positions of the model w.r.t. the estimated

location of the generated vortex centerline, after BLWT wall effect corrections. Note the negative sign in Equation 3.5(a) used for consistency to convert $YPOS$ (which is the position of the *generating wing* w.r.t. the model) to the relative position of the *model* w.r.t. the generating wing. Values of y_w and z_w for the three cases are displayed in Table 3.5. For simplicity, values of z_w are given for the condition $ZPOS=0$, and thus z_w can be calculated for other values of $ZPOS$ simply by adding $ZPOS$ to the value displayed in Table 3.5.

YPOS	Γ_{\min} case		Γ_{typ} case		Γ_{\max} case	
	y_w (m)	z_w (m)	y_w (m)	z_w (m)	y_w (m)	z_w (m)
-0.61 m	+0.62	+0.15	+0.63	+0.25	+0.64	+0.31
-0.305 m	+0.32	+0.12	+0.33	+0.19	+0.33	+0.24
0	+0.01	+0.10	+0.02	+0.16	+0.03	+0.20
+0.305 m	-0.29	+0.08	-0.28	+0.13	-0.28	+0.16
+0.61 m	-0.60	+0.05	-0.59	+0.08	-0.58	+0.09

Table 3.5: Relative Position of the Model w.r.t. the Vortex Core
(After BLWT Wall Effect Corrections and for $ZPOS=0$)

The effect of positioning the generating wing vertically (as opposed to horizontally, as for the full-scale case) does not affect the characteristics of the generated vortex (refer to section 1.3) and only insignificantly affects the horizontal component of the downwash velocity by reversing the downwash angle (refer to Appendix D for the details of this analysis). For the model positions considered “valid” data (refer to section 4.1), this discrepancy is within the uncertainty in the model dimensions, and thus can be neglected in the side force analysis.

3.1 Aerodynamic Force Data

3.1.1 Lift Force

Due to the generating wing's camber and AOA, a counter-clockwise vortex flow is "seen" by the model (simulating the left wing-tip vortex of the CC-130H(T)). Accordingly, the model should experience increased lift when the vortex core is located to the left of it (thus creating an upwash on the model), and decreased lift when the vortex core is to the right of it (creating a downwash on the model).

The lift force (also referred to as the "normal force") sustained by the model during testing was plotted against $ZPOS$ for all generating wing positions ($YPOS$) and for the three AAR conditions investigated. Lift forces are non-dimensionalized when divided by $\Gamma_{GW}\rho U_m c_m$, where c_m is the MAC for the model. Plots 1.1 to 1.3 display the non-dimensional lift force (with corresponding reference data) as a function of the relative vertical position of the vortex, for the five relative horizontal positions. Plots 2.1 to 2.3 show the non-dimensional, vortex-induced lift force for the same relative positions, while plot 2.4 is a comparison between non-dimensional reference lift for the three AAR cases. Note that for the sake of consistency in the readings, reference lift forces are also non-dimensionalized by the circulation related to their specific case (although the reference data was obtained without the generating wing).

Reference Data

As expected, the lift curves show lift to increase proportionally with α_m for reference conditions. The magnitude of the lift force was found to be up to 58% larger than that predicted in maximum load estimations, which incidently took into consideration the increased lift produced by the interacting vortex flow (refer to Appendix A). The results also show a general trend of lift increase with $ZPOS$ for all three reference curves. This is at least partially attributable to BLWT wall effects, and will be discussed more in detail in Chapter 4. All three reference data curves show great similarity in shape, which provides a strong basis for comparison with interaction data. Finally, the “dip” in the reference force curves ($ZPOS/c_m=0$) is likely due to a slight misalignment of the two slots on the model mounting plate: as the model is shifted from $ZPOS/c_m=-0.5$ to $ZPOS/c_m=0$, the top bolt of the mount’s T-brackets is moved to the upper slot of the mounting plate. Should the upper slot be slightly misaligned with the bottom slot (by an estimated 0.05 inch), the model’s AOA would be 0.6 degree less at $ZPOS/c_m=0$, thus inducing the lift force “dip” observed.

The Γ_{typ} and Γ_{max} curves are practically superimposed when the data is non-dimensionalized, while the Γ_{min} curve displays values roughly 20% larger than the other two. This is not a data discrepancy and stems from the conditions simulated for each case. More precisely, the full scale conditions simulated differ in altitude, airspeed and tanker weight, yielding a different value of normalized lift for each case ². Incidently, the full-scale Γ_{min}

² Refer to Appendix A for details on the determination of AAR cases.

case also yields a normalized lift value that is 19% larger than that of the full-scale Γ_{max} case, while the full-scale Γ_{yp} case's normalized lift value is very near that of the full-scale Γ_{max} case. The values obtained in the BLWT tests (for the reference data) are on average 6% larger than the full-scale values (due to wall effects, most likely) and reflect them closely, indicating that circulation scaling was successfully accomplished.

Interaction Data

The interaction data also shows the anticipated trend of increasing lift force with α_m (with some obvious effects from the generating wing), as well as the trend of increasing lift force with $ZPOS$. The magnitude of the interaction lift force was also found to be considerably larger than that predicted in maximum load estimations: interaction data figures reached up to 79% in excess of the maximum lift force predictions (up to 70% when neglecting wall effects). This trend will be discussed further in Chapter 4.

The effects of the generating wing on the lift force are considerable and results display trends that are consistent with expectations: for all three AAR conditions, the lift force is increased for negative values of $YPOS$ (i.e., when the model is to the right of the vortex) as well as for most cases where $YPOS=0$. Conversely, a decrease in lift force characterizes most conditions for which $YPOS$ is positive, as the vortex creates a downwash over the model. Exceptions to this trend are observed in plot 2.1, where increases in lift are observed for $YPOS>0$ and $ZPOS/c_m \geq 0$, which is contrary to intuition. These cases will be further discussed in Chapter 4.

Plots 2.1 to 2.3 show, however, that the leftmost-located vortex does not necessarily always yield the largest lift increase (nor does the rightmost-located vortex always yield the largest lift decrease), suggesting that the vertical position of the model has a significant effect on the magnitude of ΔL ³. A closer look at the lift data reveals that ΔL is generally larger for $YPOS=-0.61$ m than for $YPOS=-0.305$ m (both characterized by a vortex flow upwash) when the vortex core is below the model's wings ($ZPOS/c_m \geq -0.5$), while ΔL is generally larger for $YPOS=-0.305$ m than for $YPOS=-0.61$ m when the vortex core is above the model's wings ($ZPOS/c_m = -1.3$)⁴. Conversely, no similar trend exists for the negative induced lift between $YPOS=+0.61$ m and $YPOS=+0.305$ m, as their values of ΔL are closer to each other. For these cases, however, it is possible that the BLWT ceiling may interfere with the vortex flow pattern above the model's wings for $ZPOS/c_m = +1.3$, inhibiting the downward flow on the model and thus yielding a positive ΔL when a negative ΔL would otherwise have been observed.

It can also be observed that the Γ_{max} case does not always yield the largest lift increase or decrease for a given test condition (although it is generally the case), indicating that the effect of the generated vortex is very much dependent on its relative vertical position w.r.t. the model, especially when its core is near wing level (e.g., for $YPOS=-0.305$ m and $ZPOS=-0.15$ m, ΔL is larger for the Γ_{typ} case than for the Γ_{max} case, although the

³ For simplicity throughout Chapters 3 and 4, the symbol ΔL is used to represent a change in lift force caused by the generated vortex.

⁴ Note that the Γ_{min} and the Γ_{max} cases display some exceptions to these trends, mostly for $ZPOS/c_m = \pm 1.3$.

vortex core for the Γ_{max} case is merely 5 cm below that of the Γ_{typ} case).

For all cases where the generating wing is horizontally in-line with the model (i.e., $YPOS=0$), $\Delta L \approx 0$ when the model is below the vortex core (i.e., for $ZPOS/c_m \leq -0.5$)⁵, and becomes strictly positive when the model is roughly even with or located above the vortex core. This observation is supported by pressure distributions on the model LEX's and wings, which will be discussed in section 3.2.1.

It is also worth noting the large positive induced lift for $YPOS < 0$ and when the model's wings are nearly level with (but above) the vortex estimated centerline (i.e., $-0.5 \leq ZPOS/c_m \leq +0.5$ for the Γ_{typ} and the Γ_{max} cases, and $0 \leq ZPOS/c_m \leq +0.5$ for the Γ_{min} case). These are conditions where the vortex is best located to produce an upwash on the model's wings and LEX, thus creating large induced lift forces.

Finally, the non-dimensional lift values are generally largest for the Γ_{min} case and smallest for the Γ_{max} case (which is consistent with the reference data). This trend is least accentuated for $YPOS = -0.305$ m and becomes more accentuated for increasing and decreasing $YPOS$ ⁶, indicating that vortex strength has the least impact on the model's lift for $YPOS = -0.305$ m, and the greatest impact for $YPOS = +0.61$ m. However, since the tanker aircraft wing tip vortex circulation is relatively constant during AAR, it is more practical to

⁵ Assuming that the vortex core location is roughly that calculated in section 3.0.

⁶ Non-dimensional lift forces for the Γ_{typ} case are, on average, between 14% and 27% less than those obtained for Γ_{min} , while the non-dimensional lift forces for the Γ_{max} case are between 15% and 30% less than those obtained for Γ_{min} .

assess the impact of the vortex on the lift force as a function of relative position.

Considering that the receiver aircraft pilot (flying in the wake of the tanker) is looking for a region for which *variations* in forces and moments are minimal with vertical and lateral movement w.r.t. the tip vortex, and for a given vortex strength.

For the purpose of this analysis, we will define the concept of “position-sensitivity” as the variation of a parameter induced by the variation of the model’s position w.r.t. the vortex core. Accordingly, the lift force on the model is most “position-sensitive” when large variations in the lift force are observed for (lateral and vertical) position variations of the model w.r.t. the vortex core, while it is less “position-sensitive” when small variations in the lift force are observed for position variations of the model w.r.t. the vortex core.

In light of this definition, a “position-sensitivity” analysis can be (fairly) simply accomplished by looking at maximum variations in the induced normalized lift force for constant *YPOS* or *ZPOS*. The results are displayed in Table 3.6, where the symbol $((\Delta L')_{max} - (\Delta L')_{min})$ indicates the range of induced, normalized lift for each AAR case.

Table 3.6 shows that there is generally less vortex-induced lift variation as the model is moved up or down when $YPOS \geq 0$, while the largest vortex-induced lift variation seems to occur when $YPOS = -0.61$ m. Similarly, the least and most vortex-induced lift variation for lateral movement occur for $ZPOS/c_m = -1.3$ and $ZPOS/c_m = 0$, respectively.

	$((\Delta L')_{\max} - (\Delta L')_{\min})_{\Gamma_{\min}}$	$((\Delta L')_{\max} - (\Delta L')_{\min})_{\Gamma_{\text{typ}}}$	$((\Delta L')_{\max} - (\Delta L')_{\min})_{\Gamma_{\max}}$
$YPOS = -0.61 \text{ m}$	2.46	1.04	1.62
$YPOS = -0.305 \text{ m}$	1.88	1.07	0.95
$YPOS = 0$	1.20	0.85	0.54
$YPOS = +0.305 \text{ m}$	1.97	0.63	0.74
$YPOS = +0.61 \text{ m}$	1.72	0.51	0.47
$ZPOS/c_m = -1.3$	0.78	1.29	1.45
$ZPOS/c_m = -0.5$	1.51	1.86	2.37
$ZPOS/c_m = 0$	2.26	1.91	2.30
$ZPOS/c_m = +0.5$	1.81	1.93	2.20
$ZPOS/c_m = +1.3$	1.40	1.45	1.26

Table 3.6: Induced Lift Force Variation With Model Position

It is thus reasonable to conclude that the region of the vortex for which the lift force is least “position-sensitive” is to the left and below the vortex core, while the region of the vortex for which the lift force is most “position-sensitive” is outboard of the model’s left wing tip and slightly below its wing level. Figure 3.3 illustrates the least and most position-sensitive regions observed for the lift force on the model.

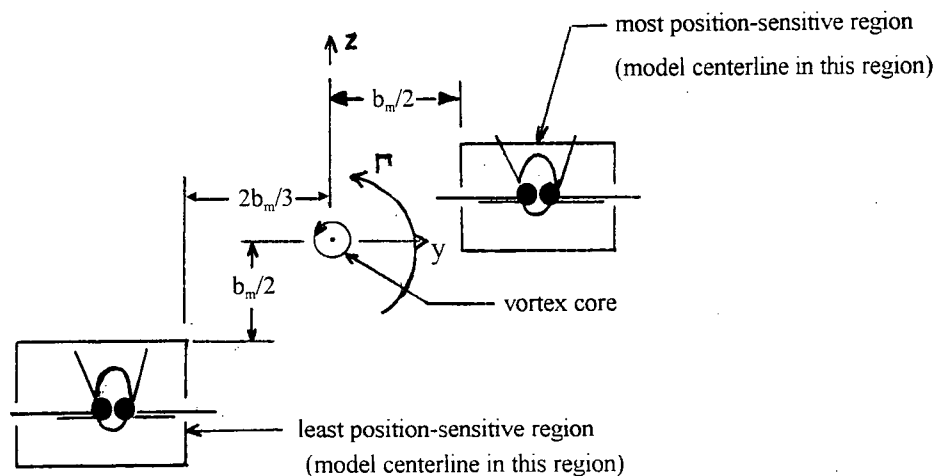


Figure 3.3: Least and Most “Position-Sensitive” Regions for the Lift Force

3.1.2 Side Force

In like fashion to the treatment of the lift force, side force data for the model was plotted against $ZPOS$ for all generating wing positions ($YPOS$) and for the three AAR conditions investigated. Side forces are also non-dimensionalized when divided by $\Gamma_{GW}\rho U_m c_m$. Plots 3.1 to 3.3 display the non-dimensional side force (and corresponding reference data) as a function $ZPOS$ for five relative horizontal positions ($YPOS$). Plots 4.1 to 4.3 show the induced non-dimensional side force for the same relative positions, while plot 4.4 is a comparison between non-dimensional reference data for the three AAR cases. As for the lift force, the reference side forces are also non-dimensionalized by the circulation related to their specific case, although the reference data was obtained without the generating wing.

Reference Data

Although no significant side force reading was expected in reference data, plot 4.4 shows the existence of inherent side forces on the model for all conditions. This is either due to a misalignment of the Sting (thus inducing model yaw), to an existing asymmetry in the model construction, or to a combination of both factors. This observation will be the subject of further discussion. A general trend of rightward (i.e., positive) side force increase with increasing $ZPOS$ is also clearly visible. Plot 4.4 equally shows how side force reference curves for the Γ_{typ} and the Γ_{max} cases neatly superimpose when normalized by their respective values of Γ , while the reference curve representing Γ_{min} does not (this was also

the case for the lift force reference data and stems from the conditions simulated for each case). There is no apparent correlation between the magnitude of the side force readings and α_m . The congruence between the three side force reference data curves confirms the trend of side force variation with *ZPOS* and will serve as a strong basis for comparison with interaction data.

The pattern similarity between the side force and lift force reference curves suggests that there is a relationship between the side and lift forces. A possible explanation for this pattern is that the model mount was not perfectly vertical after installation of the model, but rather leaned at an angle ψ clockwise from the vertical (which we will call “angle-of-lean”), causing a component of the model’s lift to act in the direction of the side force axis, thus creating an apparent positive side force equally increasing with *ZPOS*. Figure 3.4 illustrates this hypothesis.

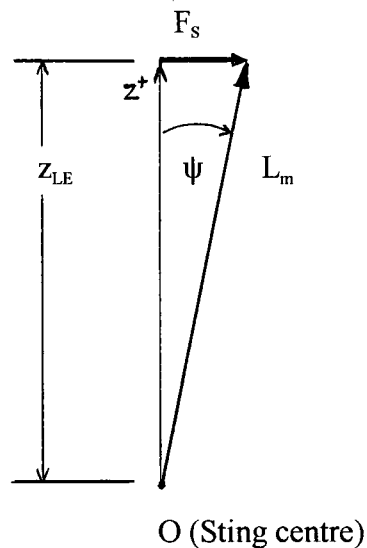


Figure 3.4: Angle-of-Lean of the Model Mount

In order to further investigate this speculation, Table 3.7 displays the ratio of side force-to-lift force for all reference points. If the inherent side force is solely a component of the lift force, the angle ψ (given by $\sin^{-1}(F_s/L)$) should be reasonably constant throughout the readings, assuming the mount is rigid enough.

F_s/L			
ZPOS/c_m	α_m = 6.2 deg	α_m = 9.8 deg	α_m = 12.3 deg
-1.30	0.077	0.044	0.043
-0.51	0.086	0.054	0.058
0	0.086	0.055	0.058
+0.51	0.077	0.063	0.061
+1.30	0.074	0.059	0.060
avg	0.080	0.054	0.055
ψ_{min} (deg)	4.2	2.5	2.5
ψ_{max} (deg)	4.9	3.6	3.5
ψ_{avg} (deg)	4.6	3.1	3.2

Table 3.7: Side Force-to-Lift Ratio (for Reference Data)

Table 3.7 shows that while the I'_{typ} and I'_{max} cases agree particularly well with each other, the I'_{min} case displays side force-to-lift ratios (and corresponding angles-of-lean) that are almost 50% larger than for the other two cases. The general agreement of the numbers within each case suggests that the angle-of-lean was the principal instigator of the inherent side force.

Although physically valid, the angle-of-lean hypothesis is unlikely since an angle of three degrees over the length of the model mount is visible to the naked eye, and thus this

error would have been corrected. A more likely explanation is that an equivalent angle-of-twist existed between the supporting structure and the sensor housing of the Sting (possibly as a result of previous damage or of frequent dismantling and re-assembly), causing an interaction between the Sting's channels and yielding the same results. The magnitude of this angle will be further investigated in section 3.1.3.

The non-superposition of the I_{min} reference side force curve with the other two curves reflects that of the I_{min} reference lift curve (refer to section 3.1.1), which reinforces the hypothesis of the link between the side and lift forces.

As shown in Figure 3.4, the vertical location of the side force w.r.t. the Sting central position is actually z_{LE} and not $ZPOS$ (as a result of α_m), which will affect the rolling moment reading since the data acquisition program subtracts the effect of the side force as if it were located at $ZPOS$. This will be discussed further in section 3.1.3.

Interaction Data

The interaction data is compared to the reference data in order to determine the direction of the vortex-induced side force. Accordingly, a side force of lesser magnitude than its corresponding reference force is considered negative (i.e., leftwards) while one of greater magnitude than its corresponding reference force is considered positive (i.e., rightwards). Plots 4.1 to 4.3 show the induced side forces. All curves from plots 4.2 and 4.3 are very similar in shape and value, the side force direction (inferred from its sign) usually being in agreement between any two corresponding points, except for

$ZPOS/c_m=+1.3$. Side force values displayed in plot 4.1, however, are generally of lesser magnitude (and often of different sign) than those in plots 4.2 and 4.3, indicating that the vortex impacted the model differently for the Γ_{min} case.

The magnitude of the induced side force is generally within the maximum load estimations, with the exception of a few points which show greater than predicted maximum side force values (up to 143% greater in one case). For the Γ_{typ} and Γ_{max} cases, the largest induced side forces (both negative and positive) were obtained for $YPOS=0$, confirming the intuitive speculation that a horizontally centred vortex placed either directly above or directly below the model will produce the greatest side forces⁸. In order to confirm the vertical position of the vortex core, an analysis of horizontally-centred points (points for which $YPOS=0$) was conducted. Looking at consecutive $ZPOS$ points between which the direction of the induced side force reverses (and bearing in mind that a ccw vortex with its core located above the model's side area centre of pressure⁹ ($(cp)_s$) will yield a positive (induced) side force while one with its core located below the model's $(cp)_s$ will yield a negative (induced) side force) it is possible to determine a vertical range for the vortex core.

Comparing the three cases for $YPOS=0$ (the case for which there are no net wall effects along the z -axis), one can infer the observations listed in Table 3.8 by looking at the

⁸ Incidentally, for both cases, the largest negative force was obtained when $ZPOS/c_m=0$, while the largest positive force was obtained when $ZPOS/c_m=-1.3$, confirming that the vortex core is always located somewhere between these points.

⁹ The location of the longitudinal centre of pressure is not known nor is it easily determinable due to the complex shape of the model. A simple surface estimation yields that the $(cp)_s$ vertical location is very near the wing's MAC leading edge, which we will thus use as our reference for $(cp)_s$.

change in direction of the induced side force. Note that, according to this analysis, the vortex core is to be located below z_{LE} for which the side force is positive ($z_{LE} (F_S^+)$) and above z_{LE} for which the side force is negative ($z_{LE} (F_S^-)$).

Case	ZPOS/ c_m (F_S^+)	ZPOS/ c_m (F_S^-)	$z_{LE} (F_S^+)$	$z_{LE} (F_S^-)$
Γ_{min}	-0.50	0	-0.05 m	+0.10 m
Γ_{typ}	-0.50	0	+0.01 m	+0.16 m
Γ_{max}	-1.3	-0.50	-0.18 m	+0.05 m

Table 3.8: Side Force Direction Reversal Ranges for $YPOS=0$

Using the common reference z_{LE} , Table 3.8 clearly shows that the location of the vortex core (at the generating wing) is somewhere in the interval $+0.01 \text{ m} \leq z_{LE} \leq +0.05 \text{ m}$. This observation suggests that the vortex core is located between 1 cm and 5 cm above the location estimated in section 3.0 (i.e., between 83 cm and 87 cm from the BLWT floor). Accordingly, z_{CL} (at the generating wing) is located between $0.91b_{GW}$ and $0.96b_{GW}$. Note that for cases other than $YPOS=0$, the position of the vortex core will be moved (up or down) along the z -axis, as described in Table 3.4.

For $ZPOS/c_m=-1.3$ and for all three cases, the induced side force is always positive (rightward) except when $YPOS=-0.61 \text{ m}$. The (relatively small) negative side forces obtained for $YPOS=-0.61 \text{ m}$, though not intuitive, are a consistent trend for the three cases. When the model is located directly below the vortex core ($YPOS=0$ and $ZPOS/c_m=-1.3$), the side forces are observed to increase with α_m as any increase in α_m shifts the model towards

the vortex core, subjecting it to higher tangential flow velocities and thus increasing the side force. The sudden increase in side force between the Γ_{min} and the Γ_{typ} cases suggests that the earlier prediction of the vortex core location was reasonably accurate.

As for the induced lift force, it is essential to determine the minimal and maximal variations in the side force with model vertical and lateral movement in order to establish least and most position-sensitive regions of the generated vortex for the side force. This is accomplished by looking at variations in normalized side force for constant $YPOS$ and for constant $ZPOS$. The results are displayed in Table 3.9 (the symbol $((\Delta F'_S)_{max} - (\Delta F'_S)_{min})$ indicates the maximum variation of normalized induced side force for each case).

	$((\Delta F'_S)_{max} - (\Delta F'_S)_{min})_{\Gamma_{min}}$	$((\Delta F'_S)_{max} - (\Delta F'_S)_{min})_{\Gamma_{typ}}$	$((\Delta F'_S)_{max} - (\Delta F'_S)_{min})_{\Gamma_{max}}$
$YPOS = -0.61$ m	0.33	0.27	0.20
$YPOS = -0.305$ m	0.15	0.25	0.23
$YPOS = 0$	0.27	0.68	0.71
$YPOS = +0.305$ m	0.16	0.26	0.32
$YPOS = +0.61$ m	0.17	0.12	0.11
$ZPOS/c_m = 1.3$	0.20	0.50	0.50
$ZPOS/c_m = -0.5$	0.29	0.26	0.16
$ZPOS/c_m = 0$	0.18	0.37	0.37
$ZPOS/c_m = +0.5$	0.16	0.42	0.29
$ZPOS/c_m = +1.3$	0.24	0.18	0.13

Table 3.9: Induced Side Force Variation With Position

Although the trends often differ for the Γ_{min} case, the Γ_{typ} and the Γ_{max} cases are

indeed consistent with each other. Table 3.9 shows that there is generally less vortex-induced side force variation as the model is moved up or down when $YPOS=+0.61$ m, while large vortex-induced side force variations occur for $YPOS=0$. The least vortex-induced side force variation for lateral movement seems to occur for $ZPOS \cdot c_m = +1.3$, while the largest vortex-induced side force variation is when $ZPOS/c_m = -1.3$. It is thus reasonable to conclude that the region of the vortex for which the side force is least position-sensitive is to the left and far above the vortex core, while the region of the vortex for which the side force is most “position-sensitive” is horizontally centred and far below the vortex core. Figure 3.5 illustrates the least and most position-sensitive regions observed for the side force on the model.

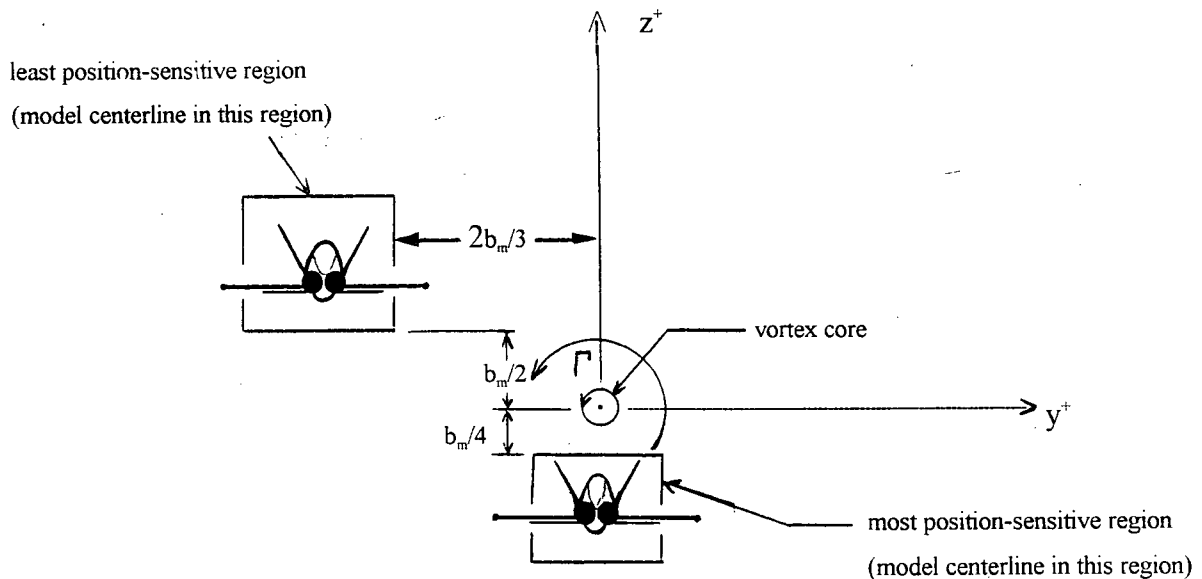


Figure 3.5: Least and Most “Position-Sensitive” Regions for the Side Force

The complexity of the flow around the model makes it very difficult to predict the direction of the side force for $YPOS \neq 0$, especially when the model is significantly above or

below the vortex core. Consequently, many of the side force results obtained are not intuitive, although some qualitative patterns have been observed between points of similar relative position. For example, the four conditions for which $+0.161 \text{ m} \leq z_{LE} \leq +0.311 \text{ m}$ ($ZPOS/c_m=0$ for the Γ_{typ} and Γ_{max} cases, and $ZPOS/c_m=+0.5$ for the Γ_{min} and Γ_{typ} cases), have side forces of the same direction for all corresponding points (i.e., for points with same $YPOS$ values). The same is true for the three conditions for which $-0.278 \text{ m} \leq z_{LE} \leq -0.178 \text{ m}$ (i.e., $ZPOS/c_m=-1.3$ for all three cases). These trends will be further discussed in Chapter 4.

In a last attempt to explain some of the discrepancies associated with the side forces, the side force induced by the vortex flow on the model mounting plate was estimated using a force and moment summation program calculating the impact of the dynamic pressure from the tangential flow component. The results indicate that the maximum side force on the model mounting plate (assuming an undisturbed vortex flow¹⁰) is approximately $\pm 0.001 \text{ N}$ when $YPOS=\pm 0.61 \text{ m}$, respectively. This inconsequential result is due to fact that the vortex core is approximately centred with the centre of the mounting plate¹¹, and thus most side forces cancel out. The effect of the vortex flow on the model mounting plate can thus be neglected for the side force analysis.

¹⁰ Although the assumption of undisturbed vortex flow aft of the model is not realistic, it provides a worst case scenario of the vortex impact on the mounting plate.

¹¹ The vortex core is centred with the centre of the mounting plate when $YPOS=0$, but shifts up or down for $YPOS \neq 0$, which induces a net side force on the mounting plate.

3.1.3 Rolling Moment

In like fashion to the lift and side forces, rolling moment data for the model was plotted against $ZPOS$ for all $YPOS$ and for the three AAR conditions investigated. Rolling moments are non-dimensionalized when divided by $\Gamma_{GW}\rho U_m c_m^2$. Plots 5.1 to 5.3 display the non-dimensional rolling moment (and corresponding reference data) as a function of $ZPOS$ for five relative horizontal positions. Plots 6.1 to 6.3 show the variation of induced non-dimensional rolling moment for the same relative positions, while plot 6.4 is a comparison between non-dimensional reference data for the three AAR cases. As for the lift and side forces, the reference rolling moments are non-dimensionalized by the circulation related to their specific case, although the reference data was obtained without the generating wing.

Reference Data

Although no significant rolling moment reading was expected in the reference data, reference plots show the existence of inherent rolling moments on the model. Plot 6.4 shows how the Γ -normalized rolling moment reference curves for the Γ_{typ} and the Γ_{max} cases are again neatly superimposed, while the reference curve representing Γ_{min} displays larger values (but a similar shape). A general trend of rolling moment increase (i.e., becoming more ccw) with increasing $ZPOS$ can be observed.

The curves all show negative (clockwise) reference moments for $ZPOS/c_m < 0$, and positive (ccw) reference moments for $ZPOS/c_m \geq 0$. The transducer's angle-of-twist (equivalent to the angle-of-lean ψ) discussed in section 3.1.2 provides a suitable explanation

to this observation. More precisely, the angle-of-twist causes a component of the model's weight to exert a rolling moment w.r.t. the Sting. This moment was "zeroed-out" using the amplifier prior to the BLWT fan being turned on. With the addition of the free-stream, the weight of the model was alleviated by the lift force (and increasingly with $ZPOS$ increasing), thus creating an "apparent" moment of opposite sign for the Sting. This apparent moment is positive (for a cw ψ) when $z_{LE} > 0$ and negative for $z_{LE} < 0$, as illustrated in plot 6.4. The inherent rolling moment due to lift ($(M_R)_L$) is given by the equation:

$$(M_R)_L = L z_{LE} \sin\psi \quad (3.7)$$

Furthermore, inherent side forces created by the angle-of-twist act at z_{LE} from the Sting central position, while the data acquisition program subtracts the moment created by a side force acting at $ZPOS$ in order to obtain the pure rolling moment about the model's axis (as previously discussed in section 3.1.2). This results in a negative inherent rolling moment reading ($(M_R)_{Fs}$), given by:

$$(M_R)_{Fs} = F_s (ZPOS - z_{LE}) \quad (3.8)$$

Equations (3.7) and (3.8) are added to obtain the total inherent rolling moment caused by the angle-of-twist ($(M_R)_\psi$), or:

$$(M_R)_\psi = L z_{LE} \sin\psi + F_s (ZPOS - z_{LE}) \quad (3.9)$$

In order to verify the accuracy of Equation (3.9), all points for the Γ_{typ} and Γ_{max} cases are investigated around $\psi=3$ degrees. An optimization method (calculating the least sum of

$(\Delta M_R - \Delta M_R)^2$ for all cases ¹²) yields that the most likely magnitude for the angle-of-twist is approximately 3.5 degrees. The optimized results are displayed in Table 3.10.

Case	ZPOS (m)	z _{LE} (m)	L (N)	F _s (N)	(M _R) _ψ [*] (N·m)	(M _R) _{data} (N·m)	Δ(M _R) (N·m)
Γ _{typ}	-0.38	-0.22	+49.0	+2.13	-1.00	-0.64	+0.36
Γ _{typ}	-0.15	+0.01	+54.1	+2.90	-0.43	-0.27	+0.16
Γ _{typ}	0	+0.16	+53.6	+2.96	+0.05	+0.22	+0.17
Γ _{typ}	+0.15	+0.31	+62.1	+3.91	+0.55	+0.82	+0.27
Γ _{typ}	+0.38	+0.54	+71.0	+4.18	+1.67	+1.97	+0.30
Γ _{max}	-0.38	-0.18	+64.1	+2.76	-1.26	-0.80	+0.46
Γ _{max}	-0.15	+0.05	+69.0	+4.00	-0.59	-0.38	+0.21
Γ _{max}	0	+0.20	+67.5	+3.95	+0.03	+0.39	+0.36
Γ _{max}	+0.15	+0.35	+79.2	+4.86	+0.72	+1.10	+0.38
Γ _{max}	+0.38	+0.58	+89.6	+5.37	+2.10	+2.44	+0.34

* From equation (3.9)

Table 3.10: Calculated and Obtained Inherent Rolling Moments Values ($\psi=3.5$ degrees)

Table 3.10 shows that the inherent rolling moment obtained in the data $(M_R)_{data}$ is consistently larger (i.e., less negative) than $(M_R)_{\psi}$, which suggests the presence of at least another inherent positive moment component (of the order of +0.30 N·m). This component could be the result of asymmetric lift on the model's wings or tail, stemming either from an asymmetry in the construction or from the possible inherent yaw discussed in section 3.1.2, or from a combination of both.

¹² Note that $\Delta(M_R)$ is the difference between M_R obtained in the data and $(M_R)_{\psi}$ (calculated).

Interaction Data

The interaction data displays similar trends of rolling moment for all cases. Firstly, it can be observed that the induced rolling moment is generally positive when $YPOS < \pm b_m/2$ (i.e., within the model's wingspan), the only exceptions occurring when the model's wings are significantly below the vortex core (yielding weak negative moments for $z_{LE} \leq -b_m/5$). This is in agreement with the direction of the circulation from the vortex and with mathematical predictions estimating the forces and moments from the vortex on the surfaces of the model. The rolling moment is also positive when the model's wings are significantly above the vortex core (i.e., when $z_{LE} \geq +b_m/5$) for all cases, which is also intuitive when considering the vortex flow patterns at larger distances from the core (the cases for which $YPOS = \pm 0.61$ m are not, however, so intuitive and thus required further analysis¹³). Negative rolling moments are observed when the vortex core is located outside of the model's span and near or above wing level (i.e., for $YPOS = \pm 0.61$ m and $-b_m/3 \leq z_{LE} < +b_m/5$), with the most negative moments occurring when the vortex is nearest to wing level and either below the wing (for $YPOS = -0.61$ m - the upwash case) or above the wing (for $YPOS = +0.61$ m - the downwash case), which are intuitive results. The rolling moment gradually becomes less negative as the vortex core moves away from the wing level, shifting to positive moments for $|z_{LE}| > b_m/3$. Note that the rolling moment is always largest in the horizontally-centred position ($YPOS = 0$), which is also an intuitive result since

¹³ Mathematical predictions based on pressure coefficient data and vortex velocity distribution all yield weak negative or positive rolling moments for these cases, suggesting that the rolling moment was near zero for these points.

it is where the vortex flow is estimated have opposite directions over the left and the right wings.

In order to investigate some points where rolling moment is counter-intuitive, a mathematical prediction was performed using the vortex flow velocity profile over the model. Outside of the vortex core, the tangential flow velocity decreases with radial distance (refer to Equation (1.11)). The mathematical approximations based on velocity distribution of the generated vortex estimate the vortical flow-induced dynamic pressure on 21 sub-areas of the model wings and on the vertical stabilators. The effect of the vortex flow on the horizontal stabilators and the LEX are estimated as a percentage of the effect on the wings, based on area ratios and on centre-of-pressure locations. The mathematical approximations were found to be consistent with intuitive data in terms of the direction (i.e., the sign) of forces and moments, but failed to accurately estimate their magnitudes¹⁴. Furthermore, the approximations generally disagreed with non-intuitive data, suggesting either that the vortex flow did not always behave in a predictable manner (perhaps due to wall effects) or that the rolling moment data is inaccurate because of its relation to the side force.

Three similar cases were investigated in an attempt to explain some of the observed data discrepancy. These cases are described in Table 3.11 below, while Figure 3.6 provides a schematic for the analysis (cell shading indicates a non-intuitive result).

¹⁴ The approximations yielded much lower magnitudes than the actual force and moment data. This was expected as effects on the wing boundary layer and those on the opposite surface are not accounted for in the approximations.

Case	YPOS (m)	ZPOS/ c_m	y_w (m)	z_w (m)	ΔL (N)	ΔF_s (N)	ΔM_R (Nm)
Γ_{\min}	-0.61	+0.50	+0.62	+0.29	+10.7	+0.2	+0.2
Γ_{typ}	-0.61	0	+0.63	+0.24	+18.9	+2.0	+0.15
Γ_{\max}	-0.61	0	+0.64	+0.30	+29.3	+1.7	-0.5

Table 3.11: Induced Forces and Rolling Moments for Three Similar Cases

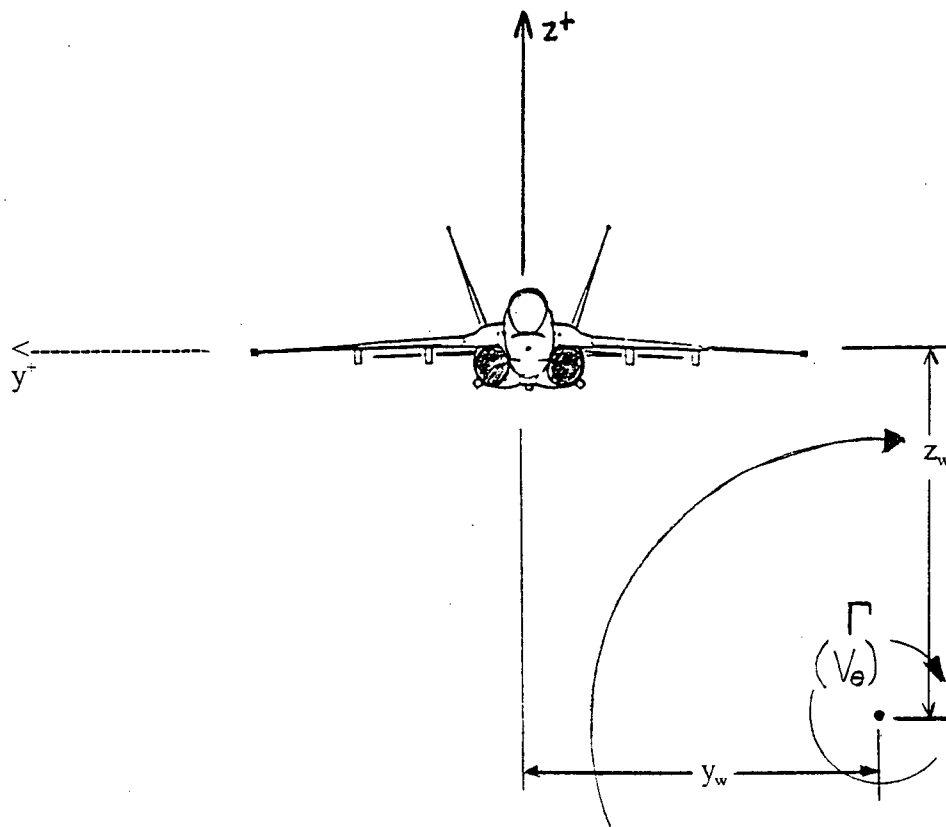


Figure 3.6: Schematic for the Analysis of Three Similar Cases

Because of the similarity of these three cases, some consistency is expected in the

force and moment data obtained (i.e., consistent directions of forces and moments between cases, relative magnitude of the readings, etc.) Referring to Table 3.11 and to Figure 3.6, the induced lift forces for all three cases are intuitive when considering the position of the model and the direction of the tangential flow. The relative magnitude of the lift forces reflects that of the circulation from the generating wing. The side forces, however, are not intuitive nor are they related to the lift forces or to the circulation from the generating wing. The rolling moment for the I_{max} case, although intuitive, is not consistent with the other two (non-intuitive) cases. The rolling moments are not apparently related to the lift or side forces, nor to the circulation from the generating wing. This could be interpreted as erroneous side force and rolling moment data ¹⁴, which nevertheless seems unlikely considering the intuitively-correct data obtained using the very same equipment and method. Other potential causes of error for these unexplained cases will be discussed in section 3.3.

As for the induced lift and side forces, it is once again practical to determine the minimal and maximal variations in the rolling moment with model vertical and lateral movement in order to establish regions of the vortex where the rolling moment on the model is least and most position-sensitive. The results of this analysis are displayed in Table 3.12, where the symbol $((\Delta M_R')_{max} - (\Delta M_R')_{min})$ indicates the range of normalized induced rolling moment for each case.

¹⁴ Note that any discrepancy in side force data will affect the rolling moment data, as rolling moment readings are mathematically related to those of the side force by the data acquisition program (refer to section 3.1.2).

	$((\Delta M_R')_{\max} - (\Delta M_R')_{\min})$	$((\Delta M_R')_{\max} - (\Delta M_R')_{\min})$	$((\Delta M_R')_{\max} - (\Delta M_R')_{\min})$
<i>YPOS</i> = -0.61 m	0.78	0.71	0.47
<i>YPOS</i> = -0.305 m	0.31	0.66	0.38
<i>YPOS</i> = 0	0.33	0.39	0.30
<i>YPOS</i> = +0.305 m	0.49	0.52	0.41
<i>YPOS</i> = +0.61 m	0.53	0.49	0.47
<i>ZPOS/c_m</i> = -1.3	0.22	0.42	0.25
<i>ZPOS/c_m</i> = -0.5	0.76	0.74	0.75
<i>ZPOS/c_m</i> = 0	0.24	0.66	0.60
<i>ZPOS/c_m</i> = +0.5	0.39	0.46	0.45
<i>ZPOS/c_m</i> = +1.3	0.12	0.29	0.25

Table 3.12: Induced Rolling Moment Variation With Position

Table 3.12 shows consistent trends among the three cases. The least and most vortex-induced rolling moment variations as the model is moved vertically are observed for *YPOS*=0 and *YPOS*=-0.61 m, respectively. For lateral movement of the model, Table 3.12 shows that the least and most vortex-induced rolling moment variation occur for *ZPOS/c_m*=+1.3 and *ZPOS/c_m*=-0.5, respectively. It is thus reasonable to conclude that, according to the force data, the region of the vortex for which the rolling moment is least position-sensitive is the central lateral position and far above the vortex core, while the region of the vortex for which the rolling moment is most position-sensitive is level with and to the left of the vortex core. Figure 3.7 illustrates the least and most position-sensitive regions observed for the rolling moment on the model.

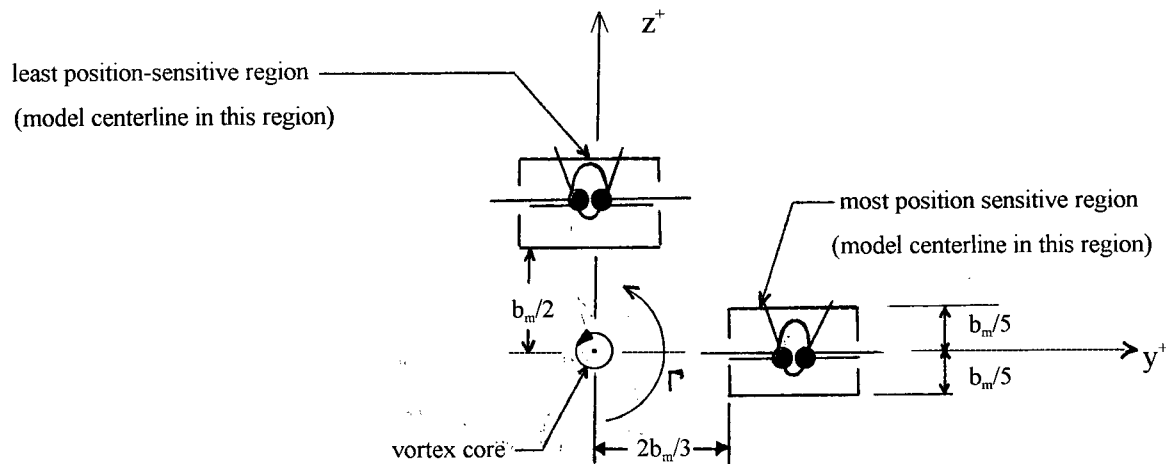


Figure 3.7: Least and Most “Position-Sensitive” Regions for the Rolling Moment

As for the side force, the rolling moment induced by the vortex flow on the model mounting plate was estimated using the force and moment summation program. The results indicate that the maximum rolling moment on the model mounting plate is approximately $+0.02 \text{ N} \cdot \text{m}$ when $YPOS=0$, and negligible otherwise. These results increase the (already positive) rolling moment for $YPOS=0$ by up to 2.5 percent. The effect of the vortex on the model mounting plate are thus reasonably negligible in the rolling moment analysis.

3.1.4 Reynolds Number Effects

In order to investigate the effects of performing wind tunnel testing at Reynolds numbers (Re) much lower than those characterizing actual AAR flight, the reference tests as well as some interaction tests were repeated at half the maximum free stream velocity (i.e., at 8.4 m/s). This data, although limited in its validity for predictions beyond the BLWT

capabilities¹⁶, will nonetheless provide a gross estimate of the effects of Re on aerodynamic forces and pressures.

Plots 7.1 to 7.3 show the actual lift, side forces and rolling moments obtained from the Sting balance (as a function of α_m) for reference and interaction data, while plots 8.1 to 8.3 display the non-dimensional version of the same data¹⁷. Note that all reference data (labelled “ref”) was obtained for $ZPOS/c_m=0$, while all interaction data (labelled “int”) was obtained for $YPOS=ZPOS/c_m=0$.

In theory, the model and generating wing lift forces for $V_\infty = 8.4$ m/s (which will be referred to as the “half Re case”) are $\frac{1}{4}$ those generated for $V_\infty = 16.8$ m/s (referred to as the “full Re case”). Accordingly, the generating wing circulation for the half Re case is half that generated for the full Re case¹⁸.

Lift force : Plot 7.1 shows the reference lift forces for the half Re case to be consistently $\frac{1}{4}$ that of the full Re case (within a 2 percent error margin), while the interaction lift forces display approximately the same ratio within a 14 percent error margin, which could be attributable to the position of the generated vortex (recall from section 3.0 that due to

¹⁶ AAR is performed at Reynolds numbers typically 100 times greater than those obtainable with a 1/12 scale model in the UBC BLWT. The extrapolation required to relate wind tunnel Re -effects results to full scale AAR is, at best, a rough approximation.

¹⁷ The Reynolds number data has been non-dimensionalized in a like fashion than described in section 3.1.1, accounting for variations in free stream velocity and generated circulation.

¹⁸ Refer to Appendix A, equations (A.1) and (A.12). Thus, the non-dimensionalizing factor for the full Re case is four times greater than that of the half Re case.

BLWT wall effects, the position of the generated vortex varies with vortex strength).

Accordingly, plot 8.1 shows great similitude between the reference lift curves, suggesting negligible Re effects on the lift force. Furthermore, note that the non-dimensional lift force is proportional to the ratio α_m/α_{GW} (using *absolute* AOA's), which *decreases* as α_m increases, explaining the negative slope of the non-dimensional reference lift curves.

Pressure data integration over the model's wings and LEX's (for both the half Re and the full Re cases) yields lift values that are consistently 27 to 31 percent less than those obtained in the force data, which is attributable to the lift generated by the model's horizontal tail and fuselage (this will be discussed further in section 3.2). It is thus reasonable to conclude that Re effects were also negligible for the pressure data.

Side force : Plot 7.2 shows the reference side forces for the half Re case to be approximately $\frac{1}{4}$ that of the full Re case within an 11 percent error margin. As previously noted, the reference side force is likely proportional to the reference lift force (refer to the angle-of-twist discussion, section 3.1.2), thus justifying this trend despite the fact that no side force should occur in reference data. The half Re data confirms the linear relation between reference lift and side forces, as well as the presence of another side force component on the model (due to model yaw or to misalignment of vertical tail surfaces, as discussed in section 3.1.2). Plot 8.2 shows significant agreement between the non-dimensional side force reference curves, and reasonable agreement between the interaction curves. It can be observed that the interaction side forces for the half Re case are approximately $\frac{1}{2}$ those of the full Re case (within a 12 percent error margin), suggesting that

the side force is proportional to I_{GW} , and thus to V_θ ¹⁹. However, this is simply a combination of the inherent side force (a positive force) and of the vortex-induced side force (a negative force), which coincidentally yields this result. Since the reference data is the only accurate means of estimating Re effects, it can be concluded that Re effects are insignificant for the side force data.

Rolling moment : Plot 7.3 shows the reference rolling moment for the half Re case to have no consistent relation with that of the full Re case. As previously discussed in section 3.1.3, the reference rolling moments are likely related to both the lift and side forces, thus making their analysis rather complex. Despite the fact that no rolling moments are expected in the reference data, near-constant rolling moments are observed at both Reynolds number (note that the half Re case displays almost negligible inherent rolling moments, while the moments observed for the full Re case are more substantial). Pressure data integration over the model's wings and LEX's confirms the (positive) direction of the rolling moments and shows reasonable agreement with the force data-obtained rolling moments, except for the reference half Re case, for which pressure data predicts larger magnitudes (roughly triple) than that obtained with the Sting balance. This is likely due to the very small rolling moments observed for this case (i.e., +0.03 N·m in observed in the force data and +0.08 N·m estimated by the pressure data), for which the Sting's inherent uncertainty creates a relatively large error (refer to section 3.3.4 for Sting balance uncertainty analysis). Plot 8.3 shows the non-dimensional reference rolling moment for the half Re case to be less than

¹⁹ According to theory, the side force should be proportional to V_θ^2 .

that of the full Re case, indicating that the model's inherent rolling moment is Re -sensitive. However, considering the low magnitude of the reference rolling moments observed for the half Re case (i.e., between 0.03 N·m and 0.07 N·m), it is possible that this discrepancy is attributable to error margins in the lift and side forces, or to the uncertainty of the Sting balance.

Accordingly, it can be concluded that observed Re effects are null or insignificant for the lift and side forces, while questionably significant for the rolling moment. These observations suggest that the BLWT modelling of AAR interaction provides a reasonable prediction of the full-scale effects, although this is a gross extrapolation and further testing (at much larger Reynolds number) should be performed in order to confirm these results.

3.2 Pressure Data

As stated in section 2.2.3, static pressure was recorded at 74 locations on the model's wings and LEX for each condition tested, including the reference data. Due to limited applicability and of the quantity of data involved, pressure data was processed for the typical AAR case (Γ_{typ}) only. The data acquisition program was used to convert the pressure readings into pressure coefficients. The results were interpolated using a Kriegering interpolation and plotted as pressure contour lines (using Tecplot software) for visualization purposes (reference plots *A.1-1* to *A.1-5*, *A.2-1* and *B.2-1*, as well as interaction plots *B.1(i)-1* to *B.1(v)-5*, in Appendix B). The pressure distribution over the model's wings and LEX

was used to estimate the lift force and the rolling moment using a summation program ²⁰. The area of action for each pressure tap was determined by considering the local chord length and the spanwise distance between pressure tap rows. A diagram displaying pressure tap locations as well as their areas of action is included in Appendix C. In order to account for the trailing edge areas of the wings ²¹, a linear interpolation was performed to add a pressure reading at 94 percent of the chord length on the wings' suction surface in order to cover the aft 12 percent of the wing ²². Similarly, an interpolation was performed over the suction surface of the model LEX ²³, adding a pressure reading at approximately 12 percent of the LEX, where large pressure gradients are expected.

3.2.1 Reference Data

The reference pressure plots reflect the trends observed in the force data. Accordingly, a general increase in pressure differential (i.e., the pressure difference between the wings' top and bottom surfaces) can be observed as *ZPOS* increases, corroborating the lift force pattern noted in section 3.1.1. It can also be noticed that the right wing pressure differential is always larger than that of the left wing, indicating an inherent positive rolling

²⁰ Unfortunately, the side force could not be estimated using the summation program since all pressure taps are located on horizontal surfaces of the model.

²¹ Because of wing thickness restrictions, the aftmost pressure taps were installed at 75% of the chord length on the top (suction) surface of the wing, and at 70% of the chord length on the bottom (pressure) surface.

²² The pressure surface did not require such an interpolation since pressure distributions vary very little over the aft portion of the chord.

²³ Incidentally, no pressure taps were installed on the LEX pressure surfaces because of thickness restrictions.

moment trend (thus supporting the argument that the negative inherent rolling moment trend observed in the force data is linked to the inherent side force on the model).

Mathematical approximations using the pressure data confirm the trends of lift force and rolling moment increases with $ZPOS$ (accentuated for $ZPOS/c_m > 0$). The approximations yield lift forces roughly 30% less in magnitude than those obtained in the force data, the difference being attributable to horizontal tail and fuselage lift components (which are not included in the approximations), and to the LEX bottom surface being approximated by $C_p = 0$ (when in actual case $C_p > 0$). Rolling moments obtained from the approximations are in agreement with the force data rolling moments for $ZPOS/c_m = 0$ only, when the effects from the inherent side force are very small due to the short moment arm at that position.

A closer observation of the pressure contour lines over the model's wings reveals a slightly higher suction peak as well as a somewhat higher bottom surface pressure on the right wing, suggesting that the right wing is set at a slightly larger incidence angle than the left wing (thus explaining the inherently positive rolling moment). Furthermore, an extended suction peak region is observed near the right wing leading edge (within the range $15 \text{ cm} < Y < 24 \text{ cm}$, where Y refers to the pressure plots' axes), indicating a slightly thicker wing in that area and accounting for the higher lift experienced on the right wing. These patterns are also observed throughout the interaction data and are likely due to model construction discrepancies.

The LEX reference pressure curves (refer to the LEX plots, Appendix B) show great similitude between right and left LEX pressure coefficients, with the left LEX suction pressure slightly higher than the that of the right LEX (thus partly offsetting the inherent positive rolling moment created by the wings). All plots show suction peaks to occur around 80 percent of the LEX length, and, like for the wings, suction pressure on the LEX top surfaces is observed to increase with increasing ZPOS.

Overall, the pressure reference data confirms the findings and hypotheses of section 3.1.

3.2.2 Interaction Data

Interaction pressure data was obtained for each of the 25 I'_{typ} case positions. Mathematical estimations of the lift force and rolling moment were carried out for critical points, including all areas where the force data results were non-intuitive. All lift estimations carried out were in general agreement with lift values obtained in the force data, although magnitudes for corresponding points often differed (by as much as 60 percent). This is once again attributable to the action of the generated vortex on untapped surfaces of the model (i.e., LEX bottom, horizontal tail and fuselage). Rolling moment estimations were often in disagreement with values obtained in the force data, which is attributable to the side force readings corrupting the rolling moments in the force data (side forces are in turn linked to the lift forces, and thus are likely inaccurate as well).

The effects of the generated vortex on the wings' pressure distributions will be

investigated for two major cases: the first when the vortex core is *inboard* of the model wing tips, and the second when it is *outboard* of the model wing tips, each case looking into considerations such as vortex positions above/ below the model's wings and left/ right of the model's centerline.

1) Vortex core is outboard of model wing tips: ($YPOS=\pm 0.61$ m)

These cases are characterized by the vortex flow creating an upwash or a downwash over the entire model.

Pressure plots *B.1(i)-1* to *B.1(i)-5* (Appendix B) illustrate the pressure contour lines for a vortex core located to the right of the model, which produces a downwash flow over the model. The general trends for such a vortex location is a decrease in model lift force (as evidenced by the force data and confirmed by pressure force mathematical estimations), as well as weak rolling moments that are positive when the vortex core is below wing level and negative when it is above. The vortex is observed to reduce the suction pressure on both wings while increasing the lower surface pressure. The increased pressure on the bottom surface of the wings, although a consistent occurrence, is counter-intuitive when considering the vortex-induced downwash flow over the wings. The effect of the impinging vortex flow on the right wing's top surface is evident when the vortex core is above or near level with the wings ($ZPOS/c_m < 0$), creating a distortion in the pressure contour lines. This effect becomes more prominent on the left wing when the vortex is located below the model. The nearly-identical effect of the outboard-located vortex on both wings indicates that the wing

tip is well out of the vortex core nearfield.

Pressure plots $B.1(v)-1$ to $B.1(v)-5$ illustrate the pressure contour lines for a vortex core located to the *left* of the model, thus producing an upwash flow over the model. The general trends for such a vortex location is a substantial increase in model lift (as evidenced by the force data and confirmed by pressure force mathematical estimations). As evidenced by the pressure plots, the bottom surfaces of the wings play a larger role than the top surfaces in generating the increased lift, especially when the vortex core is much above or much below the wings. As for the rightward outboard vortex, the induced rolling moments are small, attesting to the fact that the left wing tip is once again well out of the vortex core near field.

The LEX pressure plots for $YPOS=\pm 0.61$ m (plots B-9 and B-11) reveal little variation between the left and right LEX. Plots 9.1 to 9.3 ($YPOS=+0.61$ m) show considerable decreases in LEX suction pressure w.r.t. the respective reference data, attributable to vortex downwash over the model. The trend of suction pressure increase with $ZPOS$ is also present, like for the wings. Plots 11.1 to 11.3 ($YPOS=-0.61$ m) indicate rather moderate increases in LEX suction pressure w.r.t. the reference data for $ZPOS/c_m=\pm 1.3$, the effect of the overall upwash being more noticeable for $ZPOS/c_m=0$. Once again, these results are consistent with the pressure data obtained for the wings for each specific case.

Comparing the magnitude of the induced lift between the downwash and upwash

flow scenarios, the following conclusions can be drawn:

i) lift increases generated by the upwash flow cases are significantly larger than lift reductions generated by the downwash flow cases, which indicates that the vortex flow has a general tendency to increase lift on the model; and,

ii) the impact of the vortex flow is maximal when the vortex core is located slightly above wing level for a downwash flow, and slightly below wing level for an upwash flow.

2) Vortex core is inboard of model wing tips: ($-0.305 \text{ m} \leq YPOS \leq +0.305 \text{ m}$)

These cases are characterized by the vortex flow creating an upwash over part of the model and a downwash over another part.

Pressure plots *B.1(ii)-1* to *B.1(ii)-5* show the vortex core above and below the midspan (approximately) of the right wing. Plots *B.1(ii)-1* and *B.1(ii)-2* show cases where the vortex core lies above the right wing, resulting in a general reduction in suction pressure on the top surface of both wings (i.e., a loss of lift) and a mild increase in bottom surface pressure, more pronounced on the right wing. Note that as the vortex core gets closer to the wing's top surface, a higher suction pressure develops around the area where the vortex flow direction is "away" from the wing surface, while higher pressure characterizes the area where the vortex flow direction is "towards" the wing surface. This observation holds true for all spanwise position of the vortex core, and is especially visible on plot *B.1(ii)-2* (where

a new suction area has formed to the right of the vortex core) and on plot *B.1(iii)-1* (where the entire right wing top surface displays increased suction while the left wing top surface shows reduced suction). This pattern is consistent with observations from [10], explaining the formation of a higher pressure zone where the vortex flow “attaches” itself to a surface (i.e., the top surface of the left wing) and of a reduced pressure zone in the region where a vortex flow “separates” from a surface²⁴. Once again, the (although minor) increase in pressure on the bottom surface of a wing subjected to a vortex flow downwash (such as the left wing for plots *B.1(ii)-1* and *B.1(iii)-1*) is counter-intuitive considering the vortex flow downwash over the left wing.

When the vortex core is below the wings, the bottom surfaces of the wings experience a surge in pressure on the vortex “attachment” side and a mild decrease in pressure on the vortex “separation” side, which can be explained as in the previous paragraph. As the vortex moves farther below the wings, the pressure increases approximately equally over the bottom surfaces (presumably to a point where the effects of the vortex begin to diminish, which was not reached in these tests). The wings’ top surfaces experience either an upwash (to the right of the vortex core) or a downwash (to the left of the vortex core), which is reflected in suction pressure increases or decreases, respectively. Note that the suction pressure coefficients do not seem to be affected by the vertical distance between the wing and the vortex core (presumably to a certain point, which was not

²⁴ This explains the *spanwise drift* of a vortex (over a surface of interaction) in the direction of the pressure gradient created, which can equally be explained by the presence of an image vortex below the surface of interaction.

reached). Accordingly, the vortex flow induces a *reduction* in lift force when the vortex is above or below the right wing (as for $YPOS=+0.305$ m), and a lift *increase* whenever the vortex is above or below the left wing (as for $YPOS=-0.305$ m). The pressure data yields positive rolling moments for these cases, which is consistent with the force data results ²⁵.

When the vortex core is approximately vertically aligned with the model's fuselage (i.e., for $YPOS=0$), the result is a lift increase, in agreement with the earlier observation that the vortex flow has a general tendency to increase lift on the model. These cases also produce the largest (positive) rolling moments, as suggested by the LEX pressure plots (refer to plots 10.1 to 10.3) and confirmed by the Sting rolling moment data.

The LEX pressure plots for $YPOS=0$ (plots 10.1 to 10.3) all show larger suction pressures for the right LEX than for the left LEX, confirming the ever positive rolling moment contribution of the LEX when the ccw vortex is centred with the model's fuselage. The LEX plots indicate that the induced rolling moment from the LEX decreases as $ZPOS$ increases (the largest pressure differential between the two LEX occurs for $ZPOS/c_m=-1.3$). Incidentally, while the left LEX's suction pressure is consistently weaker than its reference pressure, the right LEX's suction pressure is larger than its reference for $ZPOS/c_m \leq 0$, but becomes less than its reference for $ZPOS/c_m = +1.3$ (although never less than the left LEX's suction pressure). The LEX-induced rolling moment trend with $ZPOS$ seems opposite to the observed trend of rolling moment magnitude (i.e., rolling moments have been observed to

²⁵ Note that Sting reading indicates a negative rolling moment for plot $B.I(iv)-I$, likely the result of an erroneous side force reading.

generally increase with $ZPOS$ in the force data), but is consistent with the pressure data on the model's wings. This last observation suggests that the rolling moment from the force data is inaccurate for $ZPOS/c_m \neq 0$, as it is tainted by erroneous side forces. The pressure data over the model's wings and LEX attest that the strongest rolling moment indeed occurred at $YPOS=ZPOS/c_m=0$.

Overall, the pressure data lift force estimations are somewhat in concordance with the lift force data obtained with Sting balance, while the rolling moment estimations are only agree for $YPOS=0$ as a result of the erroneous side force readings in the force data. Furthermore, it can be concluded from the data that the induced lift force on the model "shifts" from negative to positive when the vortex core is located somewhere between the midspan and the root of the right wing. Finally, it is worth mentioning that the pressure data is consistent with the position of the vortex core estimated in section 3.0.

3.3 Uncertainty Analysis

As with all experimental results, the data obtained during AAR interaction scale testing in the BLWT carry a certain level of uncertainty. The significant experimental uncertainties involved for this project stem from the following factors:

- 1) BLWT wind velocity measurement;
- 2) model geometry (i.e., construction) uncertainties;
- 3) generating wing uncertainties;

- 4) Sting balance uncertainties (setting of α_m and force transducer inherent uncertainties);
- 5) inherent uncertainty in the pressure transducers; and,
- 6) calculation round-ups in the data processing.

The uncertainty involved with each of these factors will be assessed in order to obtain a “data certainty” figure for the lift force, side force, rolling moment and pressure readings.

3.3.1 BLWT Uncertainties

Wind velocity readings in the BLWT are obtained by means of a pitot-static probe/ alcohol manometer combination. Manometer readings carry 0.5% uncertainty for maximum velocity tests ($V_\infty=16.8$ m/s) and 2% uncertainty for half-velocity tests ($V_\infty=8.4$ m/s), corresponding to half of the smallest division on the manometer tube divided by the manometer reading for each velocity. The uncertainty on the given manometer fluid specific density is 0.7%, while that on the manometer tube inclination angle is 1%. Accordingly, the BLWT velocity readings carry 2.2% and 3.7% uncertainties for the maximum velocity cases and the half-velocity cases, respectively, which translate into lift force uncertainties of 4.4% and 7.4%, respectively (the lift force being proportional to the square of the free stream velocity).

Furthermore, the uncertainty in the free-stream velocity yield pressure coefficient

uncertainties of 4.4% and 7.4%, respectively, since C_p is also proportional to V_∞^2 .

3.3.2 Model Geometry Uncertainties

Due to a lack of specified dimensions and to “blended” surfaces, most dimensions used in the design of the model were measured from 1/100 scale drawings provided by McDonnell Aircraft Co., with a measurement uncertainty of ± 0.5 mm. The measurements were converted to the model’s 1/12 scale, which implies an inherent uncertainty of ± 4.2 mm in the model plans. The model builder’s (self-proclaimed) error margin is $\pm 1/16$ inch (or ± 1.6 mm), which yields a total uncertainty of ± 5.8 mm in the model construction. The effects from such an error would be most felt if perpetrated on lifting surfaces such as the model’s wings, LEX and (vertical and horizontal) stabilators. In order to estimate the largest possible uncertainty associated with model dimension errors, it is necessary to add the effects from the maximum uncertainty over all lifting surfaces of the model, assuming they all act in the same direction (i.e., that they do not cancel each other) ²⁶.

Given the maximum possible error in wing chord alignment ²⁷, leading edges could be 5.8 mm above or below their prescribed locations (using the trailing edges as references), which, over a mean chord of 293 mm, induces respective incidence angle (α_m) variations of ± 1.1 degree. This translates into lift coefficient variations of the order of ± 0.08 , resulting in

²⁶ This is however a very unlikely case, as some of the errors are undoubtedly less than maximum and likely cancel each other to a certain point, but it must be considered in determining limits of certainty for the data.

²⁷ As stated in section 3.2.1, a higher incidence angle is likely on the right wing of the model.

a maximum lift uncertainty (at $V_\infty=16.8$ m/s) of ± 3.6 N if both leading edges are misplaced either up or down, and a rolling moment uncertainty of ± 1.4 N·m if leading edges are misplaced in opposite directions. The same analysis yields lift and rolling moment uncertainties of ± 0.9 N and ± 0.35 N·m, respectively, for the half-*Re* cases ($V_\infty=8.4$ m/s). Note that these figures are based on the model's reference lift surface area, which includes the LEX.

The same analysis applied to the horizontal stabilators ($c_H=159$ mm and $S_H=0.057$ m²) yield AOA uncertainties of ± 2.1 degrees, lift coefficient uncertainties of ± 0.13 and maximum lift and rolling moment uncertainties of ± 1.3 N and ± 0.21 N·m, respectively, for $V_\infty=16.8$ m/s (± 0.33 N and ± 0.05 N·m for $V_\infty=8.4$ m/s).

The vertical stabilators ($c_V=178$ mm and $S_V=0.065$ m²) are inclined 20 degrees from the vertical, which yields a combination of lift and side forces. The analysis yields AOA uncertainties of ± 1.9 degrees, lift coefficient uncertainties of ± 0.078 , and thus a maximum perpendicular force uncertainty of ± 0.88 N. At a 20 degree inclination, this results in lift force uncertainties of ± 0.30 N, side force uncertainties of ± 0.83 N, and rolling moment uncertainties of ± 0.14 N·m for $V_\infty=16.8$ m/s (and lift, side force and rolling moment uncertainties of ± 0.08 N, ± 0.21 N and ± 0.04 N·m, respectively, for $V_\infty=8.4$ m/s). Table 3.13 summarizes the force uncertainties on the model for $V_\infty=16.8$ m/s.

Surface	Lift Force Uncertainty (N) @16.8 m/s / @8.4 m/s	Side Force Uncertainty(N) @16.8 m/s / @8.4 m/s	Rolling Moment Uncertainty(N·m) @16.8 m/s / @8.4 m/s
Wings	±3.6 / ±0.9	0 / 0	±1.4 / ±0.35
H-Stabilators	±1.3 / ±0.33	0 / 0	±0.21 / ±0.05
V-Stabilators	±0.3 / ±0.08	±0.83 / ±0.21	±0.14 / ±0.04
TOTAL	±5.2 / ± 1.3	±0.83 / ±0.21	±1.8 / ±0.44

Table 3.13: Aerodynamic Forces Uncertainties Due to Model

Similarly, ±3.6 N / ±0.9 N lift force uncertainties (for the wings) translate into average pressure uncertainties of ±7 Pa/ ±1.8 Pa over both surfaces of the wings, or into a ±0.04 average pressure coefficient uncertainty over both surfaces ²⁸.

3.3.3 Generating Wing Uncertainties

The generating wing's AOA was set using the adjustment plate attached to the wing's lower tip. The adjustment plate's smallest division was 0.5 degree, yielding a ±0.25 degree uncertainty for the generating wing, which translates into ±6%, ±3% and ±2.3% AOA uncertainties for the Γ_{min} , Γ_{typ} and Γ_{max} cases, respectively. This in turn yields circulation uncertainties of ±6%, ±3% and ±2.3% as well. For the model, this means tangential velocity uncertainties of the same relative magnitudes, resulting in maximum anticipated uncertainties of ±4% in lift and side forces, and ± 8% uncertainties in rolling

²⁸ The uncertainty estimation on C_p for these cases is only an average, since both wing surfaces are independently involved in producing lift, and thus the pressure variation may not be the same for both surfaces.

moment ²⁹.

As for the previous section, a $\pm 4\%$ lift force uncertainty translates into an average pressure coefficient uncertainty of $\pm 4\%$ as well (over both surfaces of the wings).

3.3.4 Sting Balance Uncertainties

The Sting balance induces three types of uncertainties: the setting of α_m through the Sting mount assembly, the inherent force transducer uncertainty (related to the accuracy of the gauges), and the uncertainty due to channel interaction.

The uncertainty in setting α_m results from the smallest division on the Sting pitch adjustment scale, which is 1 degree. Accordingly, the maximum model AOA uncertainty is ± 0.5 degree, which translates into a maximum lift uncertainty of ± 1.6 N on the model's wings, ± 0.31 N on the horizontal stabilators, and ± 0.08 N on the vertical stabilators ³⁰, for a total of ± 2.0 N for $V_\infty = 16.8$ m/s (± 0.5 N for $V_\infty = 8.4$ m/s). There are no implications of this α_m setting uncertainty for both the side force and the rolling moment measurements.

The Sting inherent transducer uncertainty (as determined by the manufacturer) is $\pm 0.1\%$ for the lift and side force channels, and $\pm 0.06\%$ for the rolling moment channel.

These uncertainties are indeed much smaller than those obtained during the Sting

²⁹ Maximum force and moment uncertainties were estimated by considering the largest observed ratio of force (or moment) to circulation increase between similar Γ_{min} and Γ_{max} cases. The validity of this approximation is however questionable.

³⁰ Refer to the analysis carried out in section 3.3.2.

calibration performed prior to the testing, which yielded uncertainties of $\pm 0.8\%$ for the lift force channel, $\pm 1.1\%$ for the side force channel, and $\pm 0.7\%$ for the rolling moment channel. Consequently, the more recent calibration figures shall be used in the uncertainty analysis.

Finally, the Sting cross-channel interference was almost eliminated by the elimination of the axial channel (which was welded in place due to previous damage). According to manufacturer's specifications, the only interaction other than that caused by the axial channel is the interaction from the rolling moment channel on the side force channels ($S1$ and $S2$). The interaction is specified as being $\pm 0.6\%$ on $S1$ and $\pm 0.3\%$ on $S2$, which results in an additional $\pm 0.9\%$ uncertainty in side force readings. Table 3.14 summarizes the Sting-induced uncertainties for $V_\infty = 16.8$ m/s and $V_\infty = 8.4$ m/s.

Factor	Lift Force Uncertainty @16.8 m/s / @8.4 m/s	Side Force Uncertainty @16.8 m/s / @8.4 m/s	Rolling Moment Uncertainty @16.8 m/s / @8.4 m/s
α_m setting	± 2.0 N / ± 0.5 N	0	0
Inherent	$\pm 0.8\%$ / $\pm 0.8\%$	$\pm 1.1\%$ / $\pm 1.1\%$	$\pm 0.7\%$ / $\pm 0.7\%$
Channel interaction	0	$\pm 0.9\%$ / $\pm 0.9\%$	0
TOTAL	$\pm(2N+0.8\%) /$ $\pm(0.5N+0.8\%)$	$\pm 2\%$ / $\pm 2\%$	$\pm 0.7\%$ / $\pm 0.7\%$

Table 3.14: Sting-Induced Force Uncertainties on the Model

3.3.5 Pressure Transducers Uncertainties

The four 160 PC low pressure sensors used for this experiment carry a manufacturer-

specified output voltage uncertainty of ± 0.05 volt (which is equivalent to ± 25 Pa).

Accordingly, the uncertainty on pressure coefficient readings is approximately ± 0.14 for $V_\infty = 16.8$ m/s, and ± 0.58 for $V_\infty = 8.4$ m/s (which is a relatively large error, considering that pressure coefficients for the tests were in the range: $-2.5 \leq C_p \leq +1.0$).

3.3.6 Calculations Uncertainties

The lift force, side force and rolling moment are calculated from Sting voltage readings which were amplified and digitized using the A/D converter. Uncertainties carried by the amplifier and the A/D converter are much smaller than that of the Sting (in the order of 100 and 1000 times smaller, respectively), and thus they can be neglected. In the analysis, the force data was rounded to three (3) significant digits, thus inducing a $\pm 0.5\%$ maximum uncertainty on all force and rolling moment readings.

The pressure readings were not amplified but were also digitized using the A/D converter. As for the force data, the pressure data was rounded to three (3) significant digits, thus inducing a $\pm 0.5\%$ maximum uncertainty on all pressure readings (uncertainties carried by the A/D converter are much smaller and are once again neglected).

Table 3.15 provides a summary of the uncertainties discussed in this section for $V_\infty = 16.8$ m/s and $V_\infty = 8.4$ m/s.

Uncertainty Factor	Estimated Impact On ... (@16.8 m/s / @8.4 m/s)			
	Lift Force	Side Force	Rolling Moment	Pressure Coefficient
BLWT (V_∞)	$\pm 4.4/\pm 7.4 \%$	0	0	$\pm 4.4/\pm 7.4 \%$
Model (dimensions)	$\pm 5.2/\pm 1.3 \text{ N}$	$\pm 0.83/\pm 0.21 \text{ N}$	$\pm 1.8/\pm 0.44 \text{ N}\cdot\text{m}$	$\pm 0.04/\pm 0.04$
Generating wing (Γ_{GW})	$\pm 4/\pm 4 \%$	$\pm 4/\pm 4 \%$	$\pm 8/\pm 8 \%$	$\pm 4/\pm 4 \%$
Sting balance	$\pm(2 \text{ N}+0.8\%)/$ $\pm(0.5 \text{ N}+0.8\%)$	$\pm 2/\pm 2\%$	$\pm 0.7/\pm 0.7\%$	0
Pressure transducers	0	0	0	$\pm 0.14/\pm 0.58$
Calculations	$\pm 0.5/\pm 0.5 \%$	$\pm 0.5/\pm 0.5 \%$	$\pm 0.5/\pm 0.5 \%$	$\pm 0.5/\pm 0.5 \%$
TOTAL	$\pm(7.2\text{N}+9.7\%)/$ $\pm(1.8\text{N}+13\%)$	$\pm(0.83\text{N}+6.5\%)/$ $\pm(0.21\text{N}+6.5\%)$	$\pm(1.8\text{Nm}+9.2\%)/$ $\pm(0.44\text{Nm}+9.2\%)$	$\pm(0.18+8.9\%)/$ $\pm(0.62+12\%)$

Table 3.15: Summary of Uncertainties for Wind Tunnel Tests

Since the numbers in Table 3.15 are a mix of absolute and relative uncertainties, consideration of specific cases is required in order to assess the uncertainty of a reading. Absolute uncertainties mainly stem from the model and constitute the largest source of error in the readings. The uncertainty on the generating wing circulation is the next largest source of uncertainty in the readings, although the accuracy of this estimation is dubious. Uncertainties are larger for the half-speed case ($V_\infty=8.4 \text{ m/s}$), reducing the significance of the readings.

There are other sources of uncertainty that cannot be accurately estimated, such as the possibility of an uneven velocity profile or turbulence caused by irregularities on the walls in the BLWT. There is also the questionable reliability of the Sting force transducer,

which has been previously dropped and broken, and was repaired by welding the axial channel "off" (which could have implications on other channels). Although the Sting force transducer was tested prior to data acquisition, there could be some residual permanent damage to the other strain gauges due to breakage and/ or to welding.

CHAPTER 4

DISCUSSION

The sizeable amount of data analysed in Chapter 3 calls for a synthesis of the observations made. This chapter will provide a recapitulation of the findings made in Chapter 3 in an attempt to explain the patterns observed and to provide some insight on the AAR interaction problem.

4.1 Force Data

4.1.1 Lift Force

The force data results showed both the reference and the interaction lift forces to exceed the predicted maximum lift force ¹ for the model. This was in part due to the absence of variable-pitch horizontal stabilators on the model. More precisely, the CF-18A aircraft possesses horizontal stabilators for which the AOA varies depending on current flight conditions. In flight, the horizontal stabilators keep a slightly negative AOA, generating a negative lift in order to ensure the stability of the aircraft ². Since the model was designed with constant-pitch stabilators ³ (set at the same AOA as the wings), the horizontal stabilators

¹ As estimated in Appendix A.

² The CF-18A, like most aircraft, has a c of g located slightly forward of the wings' centre of pressure, thus requiring negative lift on the tail to balance the inherent pitching moment.

³ This discrepancy was overlooked in the design, much to the author's dismay, although it would have likely been impractical to incorporate to the design.

generate a positive lift for all testing conditions in the BLWT. Based on lift surface ratios, the fixed stabilator are estimated to produce almost 20% of the model's total lift. When taking into consideration the effect of negative tail lift on the full-scale CF-18A⁴, the discrepancy in the model design could account for lift forces 25% to 40% larger than predicted. Ground effect (estimated to increase lift by up to 35%) and formation effect (estimated to produce a steady 9% lift increase) due to BLWT wall image vortices are likely the only other significant factors contributing to higher-than-expected lift on the model. In light of the significant ground effect observed for $ZPOS/c_m=1.3$ (for all three AAR cases), the interaction results obtained for this position are highly doubtful and thus will not be considered "valid" data.

The general trend of lift increase with increasing $ZPOS$ is also likely due to ground effect as the model approaches the BLWT floor or ceiling. According to Figure 9.10 of [3], ground effect is significant (i.e., increases lift by more than 5 percent) for $h/b_m < 0.5$, where h is the distance between the aircraft wings' MAC and a BLWT boundary. The "dip" observed in the inherent lift curves ($ZPOS/c_m=0$) is likely due to a misalignment between the model mounting plate slots, yielding a lesser α_m when the T-brackets bolts are not both in the same slot.

The non-conformity of the normalized reference lift curve for the I_{min} case is attributable to the full-scale AAR conditions chosen. As explained in section 3.1.1 (*Reference Data*), the full-scale conditions simulated differ in altitude, airspeed and tanker weight, yielding a different value of normalized lift for each case. While the full-scale I_{typ} case's normalized

⁴ Incidentally, the tail lift becomes more negative as the aircraft's AOA increases, compensating for an increasing forward pitching moment.

lift value is (coincidentally) very near that of the full-scale Γ_{max} case, the full-scale Γ_{min} case yields a normalized lift value that is roughly 20% larger than that of the full-scale Γ_{max} case, which is also observed in the BLWT data (plot 2.4). The congruence between wind tunnel and full-scale non-dimensional lift values (within 6% difference, attributable to BLWT wall effects) indicates that circulation scaling was successfully accomplished with the generating wing in the BLWT.

The effect of the generated vortex is a general lift increase when the model is positioned to the right of the (ccw) vortex core (and thus subjected to an upwash) or centred with the core, while a reduction in lift characterizes a leftward position of the model w.r.t. the vortex core (as the model is subjected to downwash). Exceptions to this trend occur for the Γ_{min} case only (for $YPOS > 0$ and $ZPOS/c_m > 0$), where lift increases are observed as the model is in a (presumed) downwash vortex flow. It is possible that a weaker vortex located below the wings could only significantly affect the wings' and LEX's bottom surfaces⁵, thus increasing lift. Because of their inconsistency, these cases remain unexplained.

The program used throughout the analysis to estimate the vortex flow-induced lift forces and rolling moments on the model did so by calculating the effect of the added dynamic pressure induced by the tangential flow component (i.e., the flow component perpendicular to the wings). Although providing suitable predictions for the direction and relative magnitude of the aerodynamic forces, the approximations yielded values that were much lower than those

⁵ Supporting this hypothesis, the pressure data shows that a moderate downwash flow over the model's wings increases the pressure on their bottom surfaces.

obtained in the force data, indicating that the effect of the vortex flow is far beyond that of its tangential flow dynamic pressure alone.

For $YPOS \leq 0$, it was observed that the vortex has a greater impact on the model when it is located below the model's wings than when it is located at an equivalent distance above the model's wings. It was also observed that ΔL is larger for $YPOS = -0.61$ m than for $YPOS = -0.305$ m when the vortex core is below the model's wings, while ΔL for the two positions is roughly even or slightly larger for $YPOS = -0.305$ m when the vortex core is above the model's wings. The vortex flow downwash cases ($YPOS > 0$), however, do not clearly display any such trends, as ΔL does not vary much between the cases where $YPOS = +0.305$ m and $YPOS = +0.61$ m (attesting to the lesser impact of a downwash flow on the model's lift). The pressure data does not always distinctly illustrate these observations, which are more prominent for the I_{max} case. Nonetheless, the pressure data shows that a vortex core located outboard of and below the model's wing (thus creating an upwash flow over the model) will significantly increase the pressure on both wings' bottom surfaces, while a similar inboard-located vortex core (as for $YPOS = -0.305$ m) will only significantly increase the pressure on the far wing's bottom surface, consequently generating less lift.

The interference of the BLWT ceiling with the vortex flow above the model's wings for $ZPOS/c_m = +1.3$ is a plausible explanation for the lift patterns observed for $ZPOS/c_m > 0$ and $YPOS > 0$ (a larger negative induced lift is expected for $YPOS = +0.305$ m for all cases), indicating that better ceiling "clearance" is likely required for this type of experiment.

Another significant observation is that vortex strength has the least impact on the model's lift for $YPOS=-0.305$ m, and the greatest impact for $YPOS=+0.61$ m. For ccw vortex of constant strength (as is the case in AAR), it was observed in section 3.1.1 that induced lift variations due to model positional changes were least for the extreme bottom area to the left of the vortex core (i.e., for $ZPOS/c_m=-1.3$ and $YPOS=+0.61$ m; refer to Figure 3.3). Conversely, the induced lift variations due to model positional changes were greatest for the area just above and to the right of the vortex core (i.e., for $ZPOS/c_m=0$ or $ZPOS/c_m=-0.50$, and $YPOS=-0.61$ m). Accordingly, the least "position-sensitive" regions of the tanker's right wing tip vortex (and thus the preferred region for AAR approach, based on lift variations only) is $\frac{2}{3}$ of a receiver wingspan inboard of and in excess of half a wingspan below the right wing-tip vortex core.

The spanwise location of the fully rolled-up tip vortex core for the CC-130H(T) is roughly 95% of the half-wing span (i.e., roughly 1.0 m inboard of the wing tip - refer to section 1.2.4). The vertical location of the vortex core is affected by the left wing tip vortex and thus varies with trailing distance and with tip vortex strength. In the "pre-contact position"⁶, the receiver aircraft's MAC leading edge is approximately 40 m downstream of the tanker's wing tip trailing edge. Table 4.1 displays the CC-130H(T)'s estimated tip vortex vertical location for the three AAR conditions investigated. Note that d_v is the distance between the tanker's two trailing vortices and is required in calculating V_θ the downwards velocity imparted on the right tip vortex by the left tip vortex flow (using Equation (A.7)), and z_v is the vertical location of

⁶ This corresponds to the position of the refuelling basket for a fully extended refuelling drogue, where the receiver aircraft is able to make contact with the basket.

the trailing vortex below the tanker's wing.

AAR case	Γ (m ² /s)	d_v (m)	V_θ (m/s)	V_∞ (m/s)	z_{tv} (m)
Γ_{\min}	-95.7	31.7	0.48	124	0.16
Γ_{typ}	-189	31.7	0.95	134	0.29
Γ_{\max}	-286	31.7	1.44	156	0.37

Table 4.1: CC-130H(T)'s Tip Vortex Vertical Location in the AAR Pre-Contact Position

Table 4.1 indicates that the tip vortex in the AAR pre-contact position is just slightly below wing level for all cases. Because z_v is small compared with b_{18} , the trailing vortex can be estimated to be approximately at wing level in the AAR pre-contact position. Accordingly, in order to be in the least position-sensitive zones, the receiver aircraft's centerline must be roughly 8.6 m to 14 m inboard of the tanker's right wing tip (which corresponds to roughly $\frac{1}{4}$ to $\frac{1}{2}$ of the right wing's half-span from the tanker's centerline) and in excess of 6 m below the tanker wing level. As stated in Chapter 1, the present location of the AAR pod is 6.25 m inboard of the right wing tip. Refuelling drogue position tests [12] have shown that the refuelling basket trails between 7.4 m (at 240 KEAS) and 10.3 m (at 180 KEAS) below the CC-130H(T)'s wing trailing edge ⁷. This indicates that the receiver aircraft must currently fly outside of the least position-sensitive region observed, although the lower AAR position

⁷ The refuelling basket trails between 5.9 m and 8.8 m below the AAR pod reference, which is located 1.45 m below the CC-130H(T)'s wing trailing edge.

(relative to the tanker wing tip vortex) may compensate for the non-optimal lateral position.

Conversely, the receiver aircraft pilot should avoid approaching the tanker from directly outboard of its wing tip (more precisely, in the region 6.5 m to 12 m outboard of and less than 4.5 m above the right wing tip), where the effects of the tip vortex are the most position-sensitive for the lift force.

4.1.2 Side Force

The inherent side force pattern observed in the reference data (and its similarity to the reference lift force pattern) suggests that the reference side force was induced by the lift force as a result of Sting channel interaction. As stated in section 3.1.2, this interaction is likely the result of improper alignment between the Sting sensor housing and its supporting structure. Furthermore, side force-to-lift ratios indicate that the angle of misalignment (also previously referred to as the “angle-of-twist”) was approximately 3.5 degrees. Another possible cause of inherent side force is inherent yaw of the model (caused by a misalignment of the Sting or of the model w.r.t. the Sting). Since the surface area of the model’s vertical tails is $\frac{1}{4}$ that of the wings, a yaw angle of approximately $\alpha_m/5$ would also cause the observed side force-to-lift ratio ($F_y/L \approx 0.05$). For the typical AAR case, this corresponds to a misalignment of the model of less than two degrees. This is a strong possibility, given the method used to align the model in the BLWT. Finally, inherent side forces may have originated from the misalignment of a vertical stabilator(s) which, according to the uncertainty analysis, could induce side forces up to ± 0.83 N (refer to

section 3.3.2).

The higher-than-predicted magnitude of some of the induced side forces is undoubtedly linked to higher-than-predicted lift forces observed for many cases (refer to section 4.1.1), through the angle-of-twist hypothesis. Induced side forces were generally largest (in the intuitive direction) for $YPOS=0$ and when the vortex core was clearly above or below the model. This is an expected result as it is the position for which the vortex core is nearest to the model's fuselage and vertical tail, the surfaces playing the largest role in creating the side force. Furthermore, the reversal in induced side force direction for $YPOS=0$ attests that the estimated initial vertical position of the vortex core was between $0.91 b_{GW}$ and $0.96 b_{GW}$ (or between 83 cm and 88 cm above the BLWT floor). The estimated location of the vortex core at the model position (taking wall effects into consideration) is evidently reasonably accurate, as it generally concurs with the force data.

Intuitively, a ccw vortex core located well above the model's MAC leading edge ($d_z < -b_m/5$) should induce a positive (rightward) side force on the model, regardless of the y-location of the vortex w.r.t. the model. Conversely, a ccw vortex core located well below the model's MAC leading edge ($d_z > +b_m/3$) should result in a negative (leftward) side force on the model, regardless of the y-location of the vortex w.r.t. the model. However, there is a possibility that, when $YPOS$ is great enough ($-b_m/2 > YPOS > +b_m/2$), the flow impacts the wing of the model and "fountains" on it, creating flows of opposite spanwise directions which will impact the body of the model on one side, and run out the wing tip on the other side, creating a non-intuitive side force (refer to Figure 4.1).

Side force qualitative patterns observed between the three cases (i.e., matching side force directions for all $YPOS$ values between all cases when $+0.161 \text{ m} \leq z_{LE} \leq +0.311 \text{ m}$ and for $-0.278 \text{ m} \leq z_{LE} \leq -0.178 \text{ m}$) can be attributed to similarities in the vortex flow over the model. Noting that these ranges represent regions where the vortex core is “well clear” of the model, yet within $b_m/3$ of it (one region being above the model, the other below), it is reasonable to expect similarities in the vortex flow for each of these regions. It is thus not surprising to observe similar side force patterns develop for all laterally-corresponding points within these regions.

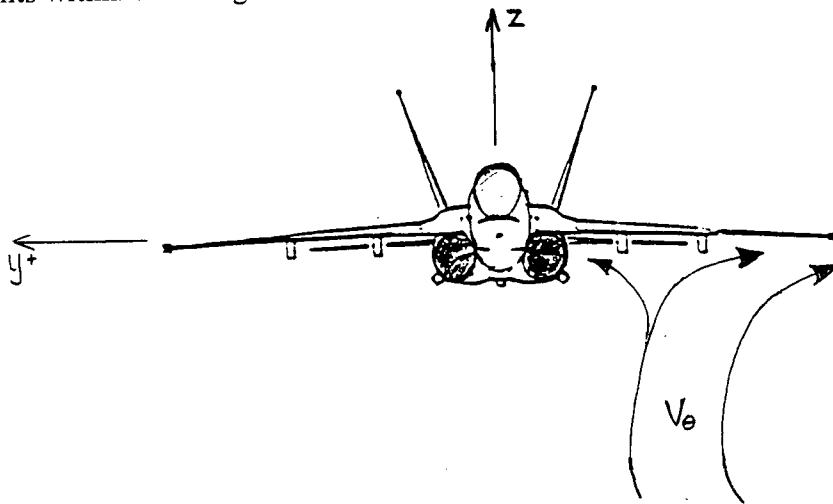


Figure 4.1: Hypothetical Flow Pattern Explaining Non-Intuitive Side Forces

Some of the interaction side forces remain unexplained but show consistent trends, such as the negative side forces observed for $YPOS = -0.61 \text{ m}$ and $ZPOS/c_m = -1.3$ (for all three cases), which all become positive for $YPOS = -0.305 \text{ m}$. It is also worth pointing out the non-congruence of plot 4.1 (i.e., the Γ_{min} case) with side force plots 4.2 and 4.3, likely related by the angle-of-twist to the dissimilarities in the induced lift force plots.

The estimation of the vortex flow-induced side force on the model mount (through a summation program calculating the impact of the dynamic pressure from the tangential flow component) yielded negligible resultant side forces due to the position of the mount w.r.t. the vortex core (i.e., the side forces on the upper half of the mount cancel those on the lower half of the mount). Accordingly, the effect of the vortex flow on the model mounting plate can be neglected for the side force analysis. It would be desirable, however, to verify the accuracy of this estimation prior to any future testing. This could be accomplished by conducting interaction tests with only the model mount installed on the Sting balance, for various *YPOS* values.

As for the induced lift force, an analysis of side force least and most "position-sensitive" areas of the vortex was conducted. Section 3.1.2 states that induced side force variations due to model positional changes were least for the top left area of the vortex core (i.e., $YPOS=+0.61$ m and $ZPOS/c_m=+1.3$; refer to Figure 3.5)⁸. Conversely, the induced side force variations due to model positional changes were greatest for the area just below and centred with the vortex core (i.e., $YPOS=0$ and $ZPOS/c_m=-1.3$). It can be inferred from these observations that, for the side force, the least position-sensitive region of the tanker's right wing tip vortex is $\frac{2}{3}$ of a receiver wingspan inboard of and at least half a receiver wingspan above the right wing tip vortex core, while the most position-sensitive region of the tanker's tip vortex is $\frac{1}{4}$ to $\frac{1}{2}$ of a receiver aircraft wingspan directly below the tip vortex core.

⁸ Note that this region is neither position-sensitive for the lift force, as shown in Table 3.6.

Since the CC-130H(T)'s wing tip trailing vortex core can be estimated to be 1.0 m inboard of the tip and at wing level for the AAR contact position (refer to section 4.1.1), the receiver aircraft must fly with its centerline roughly 8.6 m to 14 m inboard of the tanker's right wing tip (i.e., roughly $\frac{1}{4}$ to $\frac{1}{2}$ of the right wing's half-span from the tanker's centerline) and in excess of 6 m above the tanker's wing level in order to be in the least (side force) position-sensitive zone. This is not however a practical region in which to approach the tanker: since the refuelling drogue lies much below the tanker's wing level, this approach requires the receiver aircraft subsequently to descend through the vortex level and risk experiencing large variations in induced lift, side force and rolling moment while flying in a precarious position. Accordingly, it is more practical for the receiver to approach the tanker from the bottom left region of the trailing vortex (the least position-sensitive region for the lift), where (side force) position-sensitivity is moderate.

Conversely, the most (side force) position-sensitive region of the vortex (as defined in section 3.1.2) is $\frac{1}{4}$ to $\frac{1}{2}$ of a receiver wingspan directly below the tip vortex core. Accordingly, the receiver aircraft pilot approaching the tanker from below its wing level should avoid the region roughly 6.7 m inboard to 4.7 m outboard of the tanker wing tip, and 2.8 m to 5.7 m below it.

4.1.3 Rolling Moment

The inherent rolling moments observed on the model (i.e., in the reference data) are also attributable to the angle-of-twist and thus to the inherent lift and side force (refer to

section 3.1.3). The angle-of-twist (ψ) was estimated at 3.5 degrees through an optimization method. The angle-of-twist analysis suggests that another positive component of rolling moment (of the order of +0.30 N·m) acts on the model, in agreement with the wings' positive inherent rolling moment observed in the pressure data ⁹.

The induced rolling moment was observed to be mostly positive, which was expected considering the (ccw) direction of the vortex flow. Most negative rolling moments were observed for $YPOS=\pm 0.61$ m and when the vortex core was near wing level, where one wing is much nearer to the core than the other. The rolling moments for the outboard vortex cases ($YPOS=\pm 0.61$ m) are mostly non-intuitive and in disagreement with rolling moment estimation program and mathematical predictions based on pressure data. This is attributable to the large induced lift forces observed for these cases, inducing large erroneous side forces (through the angle-of-twist), and thus inaccurate rolling moment readings.

As for the induced lift and side forces, an analysis of least and most (rolling moment) position-sensitive areas of the vortex was conducted. Section 3.1.3 states that induced rolling moment variations due to model positional changes were least for the top central area of the vortex core (i.e., $YPOS=0$ and $ZPOS/c_m=+1.3$; refer to Figure 3.7), while induced rolling moment variations due to model positional changes were greatest for the area to the right and level with the vortex core (i.e., $YPOS=-0.61$ m and $ZPOS/c_m=0$).

⁹ Incidentally, the pressure data estimations yield inherent rolling moments between +0.23 N·m and +0.48 N·m (and averaging +0.33 N·m) resulting from asymmetries in the model's wings and LEX's.

Considering the location of the CC-130H(T)'s tip vortex core (refer to section 4.1.1), the receiver aircraft must fly with its centerline roughly between 6.7 m inboard and 4.7 m outboard of the tanker wing tip, and at least 5.5 m above it in order to be in the least (rolling moment) position sensitive region. As for the side force, this is not a practical region in which to approach the tanker since the receiver aircraft will be required to descend through the vortex core in order to reach the refuelling probe contact position. Accordingly, it is more practical for the receiver to approach the tanker from the bottom left region of the trailing vortex (inboard of and below the tanker wing tip), a region with average (rolling moment) position-sensitivity.

Conversely, the most (rolling moment) position-sensitive region of the vortex is outboard of and approximately level with the right wing tip. Therefore, the receiver aircraft pilot should avoid approaching the tanker in the region roughly 6.5 m to 12 m outboard of the wing tip and nearly level with it (i.e., ± 2 m from wing level).

Finally, the estimation of the vortex flow effect on the model mount (using the dynamic pressure from the tangential flow component) indicates that the mounting plate will produce maximum rolling moments of +0.02 N. It is wise to note, however, that dynamic pressure estimations on the model have yielded rolling moments typically 10 to 40 times smaller than those from pressure data estimations. A more accurate estimation can be obtained by recognizing that the mounting plate's lateral surface is approximately 10% that of the model's lifting surfaces combined, and sits approximately 15% farther from the

vortex core than the weighted surface average for the model ¹⁰. Since the induced rolling moment is proportional to the surface area and inversely proportional to the distance from the vortex core, the mounting plate is estimated to produce rolling moments roughly 9% those produced by the model at $ZPOS/c_m=0$ (the condition for which the rolling moment is relatively unaffected by the side force). Nevertheless, tests should be performed to determine the actual contribution of the model mount to the rolling moment (this could be done by performing tests with the generating wing and only the mount installed on the Sting balance).

4.1.4 AAR Considerations

Since the least and most position-sensitive regions do not coincide for the lift force, side force and rolling moment, it is necessary to determine the region(s) which provides minimal position-sensitivity for all three force components, as well as to identify the region providing the most overall position-sensitivity.

Assuming that each force component has equal importance during AAR, the all-around least position-sensitive pre-contact region (for the CF-18A aircraft) would be the top left region of the tanker right wing tip vortex (more precisely, when the CF-18A's centerline is in the region roughly 8.6 m to 14 m inboard of and more than 6 m above the tanker wing tip). This region combines optimal side force position-sensitivity with near-optimal lift

¹⁰ The weighted surface average is obtained by summing the products of each of the model's control surface area (i.e., the wings', LEX's, and the vertical and horizontal stabilators') by its respective moment arm (from the centre of pressure), and dividing by the summation by the total combined area for the model.

position-sensitivity and better-than-average rolling moment position-sensitivity. This is however not a practical pre-contact region as the CF-18A would have to subsequently descend below tanker wing level and shift towards the wing tip in order to contact the refuelling drogue (a de-stabilizing move, to say the least). Accordingly, the only practical alternatives are approach regions that are below the vortex core (i.e., roughly below tanker wing level) and inboard of the right wing tip, since it is the only true possible location of the trailing refuelling basket (from a right wing mounted pod). Taking this new constraint into consideration, the new optimal pre-contact region is the left lower region of the vortex (in excess of 6 m below and 8.6 m to 14 m inboard of the right wing tip). This region is characterized by optimal lift position-sensitivity, better-than-average side force position-sensitivity and average rolling moment position-sensitivity, thus avoiding the most position-sensitive region for each force parameter and offering a position that is compatible with that of the present refuelling drogue.

Similarly, the worse (most position-sensitive) pre-contact region for the CF-18A would be outboard of and roughly level with the tanker right wing (i.e., approximately 6.5 m to 12 m outboard of the right wing tip and less than 3 m above or below wing level). This region is most position-sensitive for the lift and side forces, and a fairly position-sensitive region for the rolling moment, making it an area to avoid when approaching the tanker from behind in order to reach the AAR contact position. Furthermore, it would be wise of the receiver aircraft's pilot to avoid flying in the region of the tanker aircraft's tip vortex core near field (especially the upwash region), for this is a region characterized by large

tangential flow velocities acting in different directions on localized regions of the receiver aircraft. Figure 4.2 is a schematic of the overall best and worst AAR pre-contact positions w.r.t. the tanker's right wing tip, as determined by the BLWT tests.

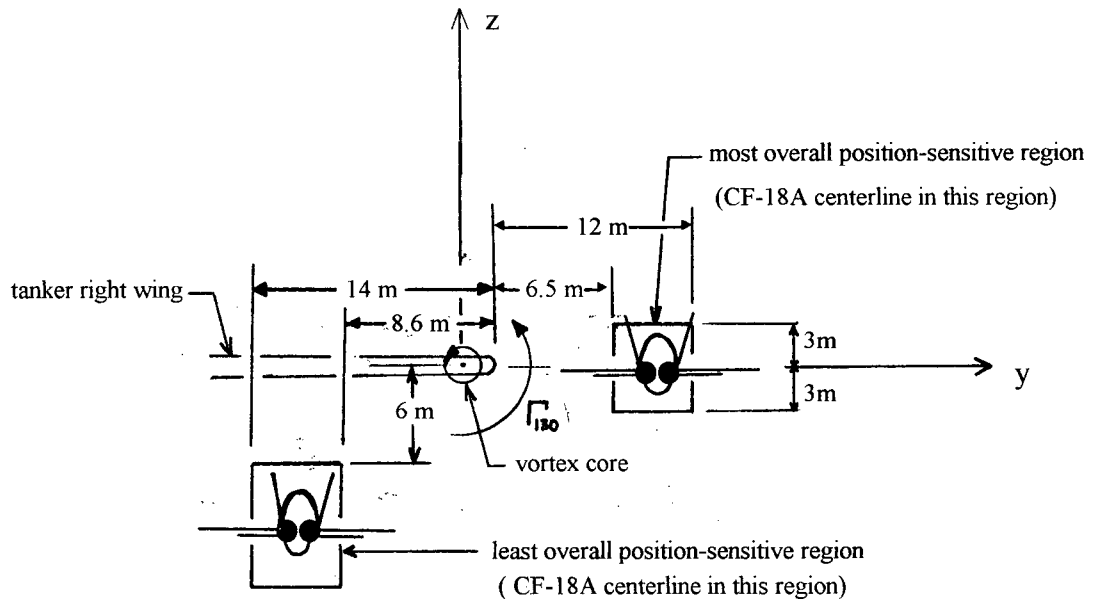


Figure 4.2: Least and Most Overall Position-Sensitive AAR Pre-Contact Regions

The current position of the refuelling drogue (6.25 m inboard of the wing tip and 7.4 m to 10.3 m below wing level, depending on airspeed) is approximately 1.4 m to 4.3 m lower than and 2.3 m outboard of the optimal pre-contact position, a region that could not be tested in the BLWT due to space limitations with the equipment used. It is suspected, however, that the lower pre-contact position dictated by that of the refuelling drogue basket will put the receiver aircraft in an even less position-sensitive region for all force components, despite the non-ideal lateral position of the drogue.

Ultimately, the current AAR pre-contact position is not estimated to be position-

sensitive, although it was not tested in the BLWT ¹¹. The data obtained during BLWT tests suggests that shifting the position of the refuelling drogue inboard would reduce the position-sensitivity of the receiver aircraft during AAR, although the analysis does not take into consideration the tanker fuselage vortices, which become more noticeable as the receiver gets closer to the wing root ¹².

4.1.5 Reynolds Number Effects

The Reynolds number effects between the half *Re* case and the full *Re* case have been found to be insignificant for the lift and side forces, and questionably significant for the rolling moment. These conclusions were mainly based on reference data comparisons, as interaction data involves more uncertainties such as the effects of halving the circulation of the vortex flow on the model's control surfaces, wall effects related to vortex strength, etc. Nonetheless, the non-dimensional lift force interaction data displayed a relatively low disparity (14% or less) between the half *Re* case and the full *Re* case, a result that was verified by the pressure data over the model's wings and LEX.

The side force reference data for the half *Re* case confirmed the linear relation between side force and lift force (i.e., the angle-of-twist hypothesis) as well as the presence of another side force on the model (likely due to model yaw or to model design

¹¹ As stated in Chapter 1, flight testing had already established that tanker-induced turbulence around the pre-contact position was "acceptable".

¹² Reference [1] reports that tanker fuselage vortices were quite strong during the AAR flight tests.

uncertainties).

The effect of Reynolds number on the Sting-measured rolling moment was found to be significant as shown by the non-superposition of the half *Re* case and full *Re* case reference curves. However, this is a questionable result since the magnitude of the rolling moments for the half *Re* case are much less than the model design induced uncertainty (which is ± 0.44 N·m) and since the rolling moment has been linked to both the lift and side forces, which also carry error margins. Furthermore, the pressure data approximations yield a $\frac{1}{4}$ ratio between the half *Re* case and the full *Re* case (reference and interaction) rolling moments, which implies that the non-dimensional curves would superimpose for both the reference and interaction data, and thus corroborating that errors exist in the force data rolling moment readings. In light of these observations, it is reasonable to conclude that the effect of Reynolds number on the rolling moment data is also insignificant.

Ultimately, no significant Reynolds number effects were observed between the half *Re* case and the full *Re* case for all force components, which could be an indication that the BLWT modelling of AAR interaction provides reasonable insight into the full-scale AAR interaction problem. It is essential to point out, however, that this last statement involves a large extrapolation of *Re* effects to Reynolds numbers approximately 100 times larger than those obtainable in the UBC BLWT, and thus that further testing at much higher Reynolds number would be required to confirm the validity of these results.

4.2 Pressure Data

4.2.1 Reference Data

The reference pressure data displays significant agreement with reference lift force data, consistently yielding lift estimations that are roughly 30 percent less than the values obtained with the Sting transducer. This (consistent) discrepancy is attributed to the lift generated by untapped lifting surfaces such as the LEX's bottom surface and the horizontal stabilators. Pressure data approximations also show that minor model design flaws (well within the design uncertainties) cause the model's wings to generate an inherent positive rolling moment, partially offset by the LEX's inherent negative rolling moment¹³. The relation between the rolling moment, the side force and the lift force (due to the angle-of-twist) proscribes the Sting-measured rolling moments to be in agreement with pressure data-estimated rolling moments for all conditions except $ZPOS/c_m=0$, where the "corrupting" effect of the side force (on the rolling moment) is negligible due to its short moment arm. Accordingly, the pressure-estimated rolling moments are deemed more accurate than the force data rolling moments¹⁴.

¹³ The direction and magnitude of the resulting moments are in agreement with the force data rolling moments when taking into consideration the angle-of-twist hypothesis, as stated in section 4.1.3.

¹⁴ These approximations were mostly carried out for the non-intuitive points (i.e., $YPOS=\pm 0.61$ m), and the predictions were also usually in agreement with intuitive results.

4.2.2 Interaction Data

Due to the unsteadiness of the vortex flow, pressure data estimations for the interaction tests tend to diverge more from the force data than estimations performed for the reference tests. Unlike the reference data, interaction pressure data estimations sometimes yielded lift forces that were greater than the corresponding lift force data, while most estimations yielded lesser lift forces (up to 60% less) than the force data. Unlike the force data, the pressure data estimations were always in agreement with intuitive speculation regarding the direction of the vortex-induced rolling moments, suggesting once again that rolling moments obtained in the force data are inaccurate (for $ZPOS/c_m \neq 0$) due to the tainted side force readings.

When the vortex core is located outboard of the model's wing tip, it was observed that an upwash flow over the entire model (i.e., when $YPOS = -0.61$ m) increases both the wings' suction pressure and the lower surfaces' pressure, while a downwash flow over the entire model (i.e., when $YPOS = +0.61$ m) reduces the wings' suction pressure but increases the lower surfaces' pressure. The result is a significant lift increase when the model is subjected to an upwash flow, and a comparatively small decline in lift when the model is subjected to a downwash flow. These observations lead to the conclusion that an upwash tangential flow over the model has a stronger effect than an equivalent downwash flow. Extended to full-scale AAR, this result concurs with force data observations (section 4.1) that the receiver aircraft would experience less tanker wing tip vortex effects by flying inboard of the tanker's wing tip (in the downwash area of the tip vortex) than if it were

flying outboard of the tanker's wing tip (in the upwash area). Note however that rolling moments are relatively weak when the vortex core is clearly outboard of the model's wing tips, suggesting that both the far upwash and the far downwash regions of the tanker's wing tip vortex are rolling moment-stable ¹⁵.

Another significant observation from these cases is that the bottom surfaces of the wings generally play a larger part than the top surfaces in generating vortex-induced lift, especially when the vortex core is much above or much below the model's wings. This could explain the lift force discrepancies noted for $YPOS > 0$ and $ZPOS/c_m > 0$ in the Γ_{min} case (refer to section 4.1.1, footnote [5]). Conversely, the impact of the tangential flow is greatest when the vortex core is near wing level (slightly above wing level for a downwash flow, and slightly below wing level for an upwash flow).

When the vortex core is located inboard of the model's wing tip and relatively near the wing level (i.e., within approximately one-third of the model's span), high pressure areas develop where the vortex flow "attaches" itself to the wing surface, while low pressure areas develop where the vortex flow "separates" from the wing surface. These observations are consistent with those from [10]. This effect is most critical when the model or receiver aircraft's centerline is laterally aligned with the vortex core (with the wings either slightly above or below it), creating strong rolling moments by sharply increasing lift on the right wing and LEX, and simultaneously decreasing it on the left wing and LEX. The inboard

¹⁵ Intuitively, the effect of the vortex flow on each of the model's wings becomes more similar as the model moves away (laterally) from the vortex core, thus decreasing the rolling moment on the model.

vortex core cases confirm that vortex-induced downwash over a wing increases the pressure on the bottom surface of the wing (as it was observed for the outboard vortex core cases). Accordingly, the force data shows that cases for which the model and the vortex core are laterally aligned (i.e., $YPOS=0$) invariably yield positive induced lift and the strongest rolling moments.

It is thus possible to conclude that while the pressure data estimations and the force data are usually in agreement in terms of the relative magnitude and direction of the lift force, the same is not true for the rolling moment (except for the cases where $ZPOS/c_m=0$). Because of the consistency and of the intuitive value of the pressure data (and in light of the previous explanation provided for the discrepancies in the force rolling moment data), the rolling moments obtained in the force data are believed to be inaccurate for $ZPOS/c_m \neq 0$.

Within the restrictions pertaining to Reynolds number extrapolations, the pressure data and the force data suggest that the induced lift shifts from positive to negative when the vortex core is somewhere between the midspan and the root of the model's right wing, moving rightwards.

4.2.3 Pressure Data Estimation Program Uncertainties

The pressure data estimation program uses pressure data over the model's wings and LEX to estimate the lift force and rolling moment on the model. All estimations carried out have pressure uncertainties of ± 25 Pa (refer to section 3.3.5), which, over the wings and LEX surfaces, result in a ± 13 N lift uncertainty and a ± 5 N·m rolling moment uncertainty

for $V_\infty = 16.8$ m/s. Furthermore, the estimations do not account for lift and rolling moments induced by other surfaces such as the model's vertical and horizontal stabilators, as well as the fuselage. From relative area and moment arm ratios, these omissions could account for as much as 26% of the lift force and 24% of the rolling moment. It is thus not surprising that lift forces obtained with the prediction program are considerably less than those obtained with the Sting. Nevertheless, the pressure data estimations of lift forces and rolling moments are consistent among themselves and, despite their relatively large uncertainties, they have provided the author with analytical tools and a means to compare several AAR conditions.

The four pressure transducers used for the experiments have operating limits of $-7.24 \leq C_p \leq +7.24$ (which corresponds to the pressure induced by a water column ± 5 inches). At full range (i.e., for $C_p = \pm 7.24$), the inherent relative uncertainty on C_p from the pressure transducers is $\pm 1.9\%$. However, for the BLWT tests conducted, the pressure coefficient range was $-2.5 \leq C_p \leq +1.0$, inducing a much larger relative uncertainty, especially for the half Re case. More precisely, the uncertainty on C_p is no less than $\pm 6\%$ for the full Re case, and no less than $\pm 23\%$ for the half Re case¹⁶. Accordingly, the 160PC pressure transducers are not the best suited pressure sensors for AAR testing in the UBC BLWT; they would be best suited for applications where pressure fluctuations are much higher than those obtained, such as a higher velocity wind tunnel.

¹⁶ The relative uncertainty increases for lesser values of C_p , and thus the maximum relative uncertainty occurs for $C_p = 0$.

CHAPTER 5

CONCLUSIONS AND RECOMMENDATIONS

This Chapter is divided into two parts: the first is a summary of the key findings, observations and conclusions, while the second lists recommendations pertaining to AAR and to further testing of this type.

5.1 Conclusions

The object of the research was to investigate the aerodynamic interaction between the CC-130H(T) aircraft (a tanker) and the CF-18A (a fighter) during air-to-air refuelling (AAR). More precisely, the wind tunnel test program aimed to assess the impact of the CC-130H(T)'s right wing tip vortex on the CF-18A in the AAR pre-contact position. A force transducer - the Sting balance - was used to measure the lift force, side force and rolling moment on a 1/12 scale model of the CF-18A subjected to a vortex flow. Simultaneously, pressure transducers were used to record the pressure over the model's wings and LEX. Three AAR conditions were investigated, each for 25 model positions w.r.t. the vortex centerline. The leading results are presented in three sub-sections: force data, pressure data and validity of results.

5.1.1 Force Data

The congruence between wind tunnel non-dimensional lift and full-scale non-dimensional lift values indicate that circulation scaling was successfully accomplished in the BLWT.

The absence of variable pitch horizontal stabilators on the model combined with BLWT wall effects contributed to higher-than-predicted lift on the model. The force data suggest that inherent side forces are components of the lift force, imputable to the misalignment of the model w.r.t the Sting, or of the Sting transducer w.r.t. its support (i.e., an “angle-of-twist”, estimated at 3.5 degrees). Similarly, inherent rolling moments observed in the force data most likely result from the angle-of-twist effect and from the wrongful estimation of the side force location in the data acquisition program (refer to section 3.1.3). An additional (positive) rolling moment component on the model is thought to be caused by an asymmetry in the model construction, as evidenced by the pressure data. Consequently, the side force and rolling moment data obtained with the Sting balance are often counter-intuitive and are deemed less accurate than the pressure data estimations.

The aerodynamic forces on the model are more substantial in the upwash region of the vortex flow than in the downwash region. Furthermore, the upwash flow has the greatest impact on the model when it is located below the model’s wings.

Although the regions of least and most position-sensitivity did not always coincide for the lift force, the side force and the rolling moment on the model, the overall least position-sensitive region (i.e., the best compromise) was found to be the top left region of the vortex, or $YPOS = +0.61$ m and $ZPOS/c_m = +1.3$. For full scale AAR, this corresponds to the receiver aircraft’s centerline being roughly between 8.6 m and 14 m inboard of and at least 5.5 m above the tanker’s right wing tip. This is however not a practical pre-contact position since the current tanker’s refuelling drogue lies below its wing level. The alternate least position-

sensitive position for the model is the lower left region of the vortex (i.e., $YPOS=+0.61$ m and $ZPOS/c_m=-1.3$), which corresponds to the receiver aircraft's centerline being roughly between 8.6 m and 14 m inboard of and at least 6 m below the tanker's right wing tip for full-scale AAR.

Conversely, the overall most position-sensitive region was found to be the right central region of the vortex (i.e., $YPOS=-0.61$ m and $-1.3 \leq ZPOS/c_m \leq 0$), which corresponds to the position outboard of and roughly level with the tanker aircraft's wing tip (more precisely, 6.5 m to 12 m outboard of the wing tip and roughly less than 3 m above or below it). Furthermore, the region of the tanker aircraft's tip vortex core near field (especially the upwash region) is equally a position-sensitive region and should be avoided by the CF-18A pilot.

The actual pre-contact position for full-scale AAR could not be modelled in the BLWT due to space limitations. Nevertheless, extrapolations on the BLWT test results indicate that the current AAR pre-contact position is relatively insensitive to (receiver aircraft) positional changes. BLWT test results suggest that shifting the current refuelling pod's location farther inboard of the tanker's wing tip would further reduce the receiver aircraft's position-sensitivity in the AAR pre-contact position.

Estimations of the vortex flow impact on the model mount yielded negligible side forces and relatively small rolling moments (refer to sections 4.1.2 and 4.1.3). A more accurate estimation (comparing the exposed surface of the mounting plate to that of the model) revealed that the mounting plate could produce rolling moments of the order of 9% of those produced by the model. However, it would be desirable to verify the accuracy of these estimations prior

to any future testing. This could be accomplished by conducting interaction tests with only the model mount installed on the Sting balance, for various *YPOS* values.

Finally, the location of the vortex core was fairly accurately estimated, as evidenced by the direction reversal in the side force for *YPOS*=0. A better way of determining the position of the vortex core at the model would be to inject a vertical trail of smoke just upstream of the generating wing.

5.1.2 Pressure Data

Pressure data results have shown that an upwash or a downwash tangential flow over the model increases the pressure on the bottom surface of its wings. This observation explains the stronger overall lifting effect of the upwash tangential flow (since the upper surface of the wings show increased lift for an upwash flow and decreased lift for a downwash flow). The pressure data also shows that the lower surface of the model's wings play a larger role than the upper surface in generating the vortex-induced lift, especially when the model is significantly above or below the vortex core.

In the pressure data plots, it was possible to observe the formation of high pressure areas where the vortex "attaches" itself to the model's wing, and low pressure areas where the vortex "separates" from the wing (as predicted in [10]), explaining the occurrence of strong rolling moments for cases where *YPOS*=0.

Estimations based on pressure and force data confirmed that the induced lift on the

model “shifts” from positive to negative when the vortex core is between the midspan and the root of the model’s right wing (moving rightwards). Finally, pressure data estimations of the rolling moment confirmed the inaccuracy of the rolling moments obtained with the Sting balance due to their relation with the side force readings (refer to section 3.1.3).

5.1.3 Validity and Significance of Results

The uncertainty analysis reveals that relatively large uncertainties exist for the lift force, side force and rolling moment data (refer to section 3.3 for details). The largest source of uncertainty is the model’s design, followed by the generating wing and the BLWT itself. The force data uncertainties are large enough to cover all measurement discrepancies observed.

In the case of pressure data, significant data uncertainty also exists, the largest source being the pressure transducers used. The lift and rolling moment estimations from the pressure data, although found to be consistent among themselves, carry large uncertainties due to the pressure transducers’ inherent uncertainty and to untapped lifting surfaces on the model.

Reynolds number effects have been found insignificant for all force data between the half Re tests and the full Re tests. Although this is an encouraging result, it is a gross extrapolation to extend the BLWT tests results to full scale AAR, which involves Reynolds numbers roughly 100 times larger. Accordingly, it can only be concluded that the BLWT tests results are possibly applicable to full scale AAR.

5.2 Recommendations

The following recommendations stem from the BLWT tests results and can be classified into two sub-sections: recommendations pertaining to AAR, and recommendations about future testing of a similar nature to that performed in the UBC BLWT.

5.2.1 AAR Recommendations

It is recommended that the receiver aircraft's pilot approach the tanker from the lower, inboard wing position. Conversely, it is recommended that the receiver aircraft's pilot avoid the outboard, wing-level region of the tanker's wing tip, as well as the region near the tanker's tip vortex core.

It is recommended that flight tests be conducted to assess AAR pre-contact stability characteristics when the refuelling pod is located farther inboard of the tanker's wing tip, and to assess the effects of the tanker's fuselage vortices at these locations.

5.2.2 Recommendations for Future Testing

Since the main cause of uncertainty is the CF-18A model itself, a more accurately built model would greatly improve the accuracy and the significance of the results. Accordingly, it is recommended that a more accurately built model be used for future testing.

If this experiment were repeated using the same model, great care should be taken to ensure that the model mount sits perfectly vertical on the Sting sleeve, as the slightest angle-of-lean will affect forces and moments in all directions. Similarly, great care should be taken to ensure no model yaw, and that the model is aligned w.r.t. the Sting. Tests should be performed

to confirm the absence of side forces or rolling moments in the reference data.

Tests should be conducted in order to determine the actual side force centre of pressure on the model as well as a lateral drag coefficient. This new centre of pressure location should be used as a reference to determine the z-location of the model w.r.t. the Sting.

Tests should be conducted to estimate the flexibility of the model mount under aerodynamic loading in two directions.

The impact of the vortex flow on the model mount should be measured. This could be accomplished by conducting interaction tests with only the model mount installed on the Sting, for various I^* s and $YPOS$ values.

The Sting balance should be calibrated with the mount and model installed. Cross-channel interaction should be eliminated as much as possible by ensuring that the Sting force transducer is properly aligned. Any remaining cross-channel interaction should be recorded.

Care should be taken to ensure sufficient tunnel wall clearance for all positions of the model (i.e., $h/b_m \geq 0.5$, where h is the floor or ceiling clearance distance).

In order to determine the exact position of the vortex core at the model, a vertical trail of smoke should be injected just upstream of the generating wing.

Pressure transducers that are better suited for the BLWT air velocity (i.e., with a lesser pressure range) should be used in order to reduce the uncertainty of the pressure readings for such experiments.

REFERENCES

- [1] Captains Marris JM, Reif A. and Matthewson C.S., *CC-130H(T) Tactical Transport Tanker Development and Acceptance Test Program*, AETE Report 91/19, pp.2-60, (1993).
- [2] NATO Advisory Group for Aerospace Research and Development, *The Need for Large Wind Tunnels in Europe*, AGARD Advisory Report No.60, pp.3-6, (1972).
- [3] Shevell R.S., *Fundamentals of Flight*, Second Edition, Prentice-Hall, (1989)
- [4] Bertin J.J. & Smith M.L., *Aerodynamics for Engineers*, Second Edition, Prentice Hall, (1989), pp.69-73 and 235-244.
- [5] Chow J.S., Zilliac G.G. and Bradshaw P., *Initial Roll-Up of a Wing Tip Vortex*, Proceedings of the Aircraft Wake Vortices conference, Vol.2, No.35, pp.2-8, (1991).
- [6] Staffman P.G., *The Velocity of Viscous Vortex Rings*, pp.9-10
- [7] Gerhart P.M. & Gross R.J., *Fundamentals of Fluid Mechanics*, Addison-Westley Printing Co., (1985).
- [8] Green S.I., *Fluid Vortices*, Kluwer Academic Publishers (1995), Chapter 10: *Wing Tip Vortices*.
- [9] Von Mises R., *Theory of Flight*, Dover Publications, (1945).
- [10] Seath D.D. and Wilson D.R., *Vortex-Airfoil Interaction Tests*, AIAA 24th Aerospace Sciences Meeting (AIAA-86-0354), Reno, NV, 1986.
- [11] Meier G.E.A. and Timm R., *Unsteady Vortex Airfoil Interaction*, Fluid Dynamics and Flight Mechanics Panels, NATO AGARD-CP-386, Neuilly-Sur-Seine, France, 1985, pp.16-1 to 16-10.
- [12] Lockheed Aerospace, *130-(3)-xi/27-0108-1*, CC-130H(T) Specifications, 1991.

APPENDIX A

1. DETERMINATION OF AAR CONDITIONS TO BE INVESTIGATED

The AAR flight envelope as determined in [1] and shown in Appendix C is delimited by airspeeds between 170 KIAS and 240 KIAS and pressure altitudes between 500 ft and 35,000 ft Aircraft AAR weights are 31,300 lbs to 40,000 lbs¹ and 130,000 lbs to 155,000 lbs for the CF-18A and the CC-130H(T), respectively. Other limiting factors (such as CF-18A pilots' poor visibility of the refuelling drogue above 12 degrees AOA) further restricted the AAR envelope and contributed to the determination of the flight conditions to investigate. Because of the extensive amount of data to be collected and analyzed for each flight condition investigated, three conditions were deemed adequate: a maximum circulation case (Γ_{max}), a minimum circulation case (Γ_{min}) and a typical circulation case at representative flight conditions (Γ_{typ}). Since we are modelling the right wing of the CC-130H(T), the circulation is always ccw (and by convention negative), which will be conserved in the BLWT. Notwithstanding this convention, Γ will be estimated *maximum* when its absolute value is maximized.

1.1 Parameter relationships:

Since AAR is always performed in steady, level, 1g flight, lift is always equal to aircraft weight. Lift (or weight) and mean wing circulation are related by equation (1.1), or:

¹ Because the effect of varying α_g on the CF-18A is to be investigated in this report, all wind tunnel testing was conducted assuming a CF-18A typical weight of 33,500 lbs in order to eliminate the undesirable weight variable.

$$-\Gamma = \frac{L}{\rho V_{\infty} b} \quad (\text{A.1})$$

Furthermore, lift and AOA are related through the lift coefficient (C_L) by:

$$C_L = \frac{2L}{\rho V_{\infty}^2 S} = \frac{2\pi AR \alpha_a}{(AR+2)} \quad (\text{A.2})$$

where: $\alpha_a = \alpha_g - \alpha_0$

The different α 's represent the wings' absolute, geometric and zero-lift AOA, respectively.

The parameter V_{∞} in equations (A.1) and (A.2) is the *true* airspeed (V_T), which is related to *indicated* airspeed (V_I) by the square root of the density ratio, or:

$$\frac{V_T}{V_I} = \sqrt{\frac{\rho_0}{\rho}} \quad (\text{A.3})$$

The scaled circulation required by the generating wing inside the BLWT (Γ_{GW}) is calculated from equation (1.13) (refer to section 1.3.2) using a mean aerodynamic chord ratio of 1/12 (i.e. the scale of model).

$$\Gamma_{GW} = \Gamma_a \left(\frac{1}{12}\right) \left(\frac{V_m}{V_{aT}}\right) \quad (\text{A.4})$$

Finally, the geometric AOA of the generating wing $((\alpha_g)_{GW})$ is related to Γ_{GW} through equations (A.1) and (A.2), yielding:

$$(\alpha_g)_{GW} = \frac{-\Gamma_{GW} (AR+2)}{\pi AR V_m \bar{c}_{GW}} + \alpha_0 \quad (\text{A.5})$$

1.2 Γ_{max} case:

According to equation (A.1), Γ_{max} for the CC-130H(T) aircraft will occur when the lift is maximum and the product $\rho(V_{dT})$ is minimized, which occurs at minimum indicated airspeed and maximum altitude (i.e. 170 KIAS and 35,000 ft). The wing span (b) of the CC130H(T) is 40.4 m and its wing area (S) is 162 m². Thus, for $L_{max}=155,000$ lbs=691,000 N:

$$\text{at 35,000ft (=10,670 m):} \quad \rho = 0.384 \text{ kg/m}^3$$

$$\text{equation (A.3) yields:} \quad (V_a)_T = 304 \text{ KTAS} = 156 \text{ m/s}$$

$$\text{equation (A.1) yields:} \quad \Gamma_{max} = -286 \text{ m}^2/\text{s}$$

The CF-18A has wings with $AR=3.5$, $S=37.2$ m² and $\alpha_0=0$, and so for the same flight conditions (i.e. $(V_{dT})=156$ m/s and $\rho=0.384$ kg/m³) and $L_{18}=33,500$ lbs=149,000 N:

equation (A.2) yields: $(C_L)_{18} = 0.857$

and: $(\alpha_a)_{18} = (\alpha_g)_{18} = 0.214 \text{ rads} = 12.3 \text{ deg.}$

which is approximately equal to the AAR limit restricted by pilot visibility and thus a realistic flight condition.

In the BLWT, $(\alpha_g)_m$ must match $(\alpha_g)_{18}$ (refer to section 1.3.1), so:

$$(\alpha_g)_m = 12.3 \text{ deg}$$

For the generating wing, $(\Gamma_{max})_{GW}$ is obtained from equation (A.4). With $\Gamma_{max} = -286 \text{ m}^2/\text{s}$, $V_m = 16.8 \text{ m/s}$ and $(V_d)_T = 156 \text{ m/s}$, we obtain:

$$(\Gamma_{max})_{GW} = -2.57 \text{ m}^2/\text{s}$$

Finally, equation (A.5) yields the required generating wing AOA. For the generating wing, $c = 0.609 \text{ m}$, $AR = 1.49$, and $\alpha_0 = -3.0 \text{ deg}$, which yields:

$$(\alpha_g)_{GW} = 7.7 \text{ deg}$$

1.3 Γ_{min} case:

Γ_{min} for the CC-130H(T) aircraft will occur when the lift is minimum and the product $\rho(V_d)_T$ is maximized, which occurs at maximum indicated airspeed and minimum altitude (i.e. 240 KIAS and 500 ft), and consequently, for $L_{min} = 130,000 \text{ lbs} = 580,000 \text{ N}$:

at 500ft (= 152 m): $\rho = 1.21 \text{ kg/m}^3$

equation (A.3) yields: $(V_a)_T = 241 \text{ KTAS} = 124 \text{ m/s}$

equation (A.1) yields: $\Gamma_{\min} = -95.7 \text{ m}^2/\text{s}$.

For the CF-18A in the same flight conditions (i.e. $V_{aT}=124 \text{ m/s}$ and $\rho=1.21 \text{ kg/m}^3$) and $L_{18}=33,500 \text{ lbs}=149,000 \text{ N}$

equation (A.2) yields: $(C_L)_{18} = 0.431$ and $(\alpha_g)_{18} = 0.108 \text{ rads} = 6.19 \text{ deg}$.

thus: $(\alpha_g)_m = 6.19 \text{ deg}$.

equation (A.4) yields: $(\Gamma_{\min})_{GW} = -1.08 \text{ m}^2/\text{s}$.

equation (A.5) yields: $(\alpha_g)_{GW} = 1.51 \text{ deg}$

1.4 Γ_{typ} case:

Γ_{typ} was chosen as a typical AAR condition, where $W_{18}=33,500 \text{ lbs}$, $W_{130}=150,000 \text{ lbs}$ and $V_a=190 \text{ KIAS}$, at an altitude of 20,000 ft, yielding:

at 20,000ft (=6098 m): $\rho = 0.653 \text{ kg/m}^3$

equation (A.3) yields: $(V_a)_T = 260 \text{ KTAS} = 134 \text{ m/s}$

equation (A.1) yields: $\Gamma_{\text{typ}} = -189 \text{ m}^2/\text{s}$.

For the CF-18A in the same flight conditions (i.e., $(V_a)_T=134 \text{ m/s}$ and $\rho=0.653 \text{ kg/m}^3$)

and $L_{18}=149,000$ N:

equation (A.2) yields: $(C_L)_{18} = 0.685$ and $(\alpha_g)_{18} = 0.171$ rads = 9.81 deg.

Thus: $(\alpha_g)_m = 9.81$ deg.

equation (A.4) yields: $(\Gamma_{typ})_{GW} = -1.97$ m²/s.

equation (A.5) yields: $(\alpha_g)_{GW} = 5.23$ deg.

Table A1 summarizes the AAR conditions to be investigated.

Flight Condition	Γ_{130} (m ² /s)	V_a (KIAS)	PA (10 ³ ft)	W_{130} (10 ³ lbs)	W_{18} (10 ³ lbs)	α_{18} (deg)	Γ_{GW} (m ² /s)	α_m (deg)	$(\alpha_g)_{GW}$ (deg)
Γ_{max}	-286	170	35	155	33.5	12.3	2.57	12.3	7.71
Γ_{typ}	-189	190	20	150	33.5	9.81	1.97	9.81	5.23
Γ_{min}	-95.7	240	0.5	130	33.5	6.19	1.08	6.19	1.51

Table A1: Summary of AAR Conditions Investigated

2. ESTIMATION OF AERODYNAMIC FORCES ON CF-18A MODEL

The estimation of the maximum anticipated aerodynamic loading on the CF-18A model, though theoretical, is critical to the determination of appropriate ranges for the calibration of the Sting force transducer. In order to carry out this analysis, some trivial and some less trivial assumptions must be made, and some specific AAR conditions must be considered (refer to section 1 of this Appendix for the determination of these conditions).

2.1 Side Force:

Side forces on the model are the direct result of the tangential velocity (V_θ) induced by the generating wing and can be estimated from the equation:

$$F_{s_m} = \frac{1}{2} \rho V_\theta^2 C_{D_s} S_S \quad (\text{A.6})$$

where: i)
$$V_\theta = \frac{-\Gamma_{GW}}{2\pi r} \quad (\text{A.7})$$

Accordingly, $(V_\theta)_{\max}$ will occur at $(\Gamma_{GW})_{\max}$ and for r_{\min} . $(\Gamma_{GW})_{\max}$ is readily available from parameter scaling (refer to Table A1), while r_{\min} is the radius for which the mean tangential velocity has a magnitude of $(V_\theta)_{\max}$, which is approximately equal to half of the model's average height (h_{avg}) (i.e., in the vertical direction). This dimension was in turn difficult to determine because of the irregular side profile of the model, but was estimated at 0.18 m, which implies $r_{\min} = \frac{1}{2} h_{\text{avg}} \approx 0.09$ m. Equation (A.7) with $(\Gamma_{GW})_{\max} = -2.57$ m²/s (Table A1) and $r_{\min} = 0.09$ m yields:

$$(V_\theta)_{\max} = 4.5 \text{ m/s.}$$

ii) C_{D_s} is the lateral drag coefficient for the model (i.e. flow along the Y-axis). Since the fuselage of the model is roughly elliptic (with the long axis in the vertical (Z) direction), C_{D_s} can be approximated, in a worst-case scenario, by the drag coefficient of a cylinder having a diameter (d) equal to the small axis of the ellipse (C_D decreases

with increasing diameter for a given Re). C_D of a cylinder is *also* Re -dependent, and thus Re is calculated as follows:

$$Re = \frac{\rho V_{\theta} d}{\mu} \quad (\text{A.8})$$

Using $V_{\theta}=(V_{\theta})_{\max}=4.5$ m/s, $\rho=1.225$ kg/m³, $d=0.13$ m (approximated) and $\mu=1.789 \times 10^{-5}$ N·s/m², equation (A.8) yields $Re \approx 40,000$, which in turn yields $C_{D_s} \approx 1.0$ (fig. 8.10 of [7]).

iii) S_s is the lateral surface area, which can be approximated by the product of h_{avg} and the model's length ($l_m=1.43$ m), thus:

$$S_s \approx h_{\text{avg}} l_m = 0.24 \text{ m}^2.$$

Equation (A.6) yields the estimated maximum side force on the model (located approximately at the center fuselage). Because of the variation in the relative position between the generating wing and the model, it is also estimated that the side force could act in either direction along the Y -axis, and thus it could bear a positive or a negative sign². Accordingly:

$$(F_s)_{\max} = \pm 3.0 \text{ N}$$

or:
$$-3.0 \text{ N} \leq (F_s)_m \leq +3.0 \text{ N}$$

² A rightward side force is defined as positive.

2.2 Rolling Moment:

The rolling moment is also an effect attributed exclusively to the generated vortex flow. More specifically, the rolling force is induced by an asymmetrical change in effective AOA on the model's wings, thus causing asymmetrical lift.

Assuming the aerodynamic flow over the model's wings is accurately scaled from the CF-18A, the center of pressure on the model's wings is located along the axes $Y=\pm 0.24\text{m}$ (just short of the midspan). The circulation generated inside the BLWT is always negative and, accordingly, the maximum rolling moment will also be ccw (but positive, by convention). With $(\Gamma_{GW})_{max}=-2.57\text{m}^2/\text{s}$ and the generated vortex dead-on the nose of the model, V_θ can be calculated at a radius of $r_{cp}=\pm 0.24\text{m}$ from the model centerline. Using equation (A.7):

$$(V_\theta)_{cp} = \pm 1.7 \text{ m/s}$$

Because a positive rolling moment is by definition ccw, a positive (ccw) V_θ at $YPOS=0$ results in an upwards flow on the model's right wing and a downwards flow on the left wing. The change in effective AOA (ϵ) is calculated by:

$$\epsilon = \tan^{-1}\left(\frac{V_\theta}{V_\infty}\right) \quad (\text{A.9})$$

Note that even though this value of ϵ is only exact at the specified radius (i.e. at r_{cp}), it is assumed to represent an average ϵ for the wing because of its location along the span and

of vortex tangential velocity distribution (refer to section 1.2.5). The rolling moment about the model centerline axis (M_m) is given by:

$$M_m = (L_R - L_L) |r_{cp}| \quad (\text{A.10})$$

where L_R and L_L is the lift force on the right and left wing, respectively. Susting lift equations into equation (A.10) and re-arranging, we get:

$$M_m = \frac{\pi AR \rho V_\infty^2 S_m |r_{cp}| \epsilon}{(AR+2)} \quad (\text{A.11})$$

With $\rho = \rho_0$, $AR = 3.5$, $S_m = 0.258 \text{ m}^2$, $(V_\theta)_{\max} = 1.7 \text{ m/s}$ and $V_\infty = 16.8 \text{ m/s}$, equations (A.9) and (A.11) yield:

$$\epsilon = 0.101 \text{ rads} = 5.78 \text{ deg}$$

and: $(M_m)_{\max} = +4.3 \text{ N}\cdot\text{m}$

Note that for calibration purposes, since the R-channel is symmetrical (i.e. same input/output scale in both the cw and ccw direction), the value used for $(M_m)_{\min}$ will be the mirrored value of $(M_m)_{\max}$, though in reality $(M_m)_{\min}$ is likely much smaller. Thus:

$$-4.3 \text{ N}\cdot\text{m} \leq (M_m) \leq +4.3 \text{ N}\cdot\text{m}$$

2.3 Lift Force

Lift is given by the equation:

$$L = \frac{1}{2} \rho_a V_\infty^2 C_L S_w \quad (\text{A.12})$$

Inside the BLWT, $\rho \approx \rho_0$, and thus for a given freestream velocity (V_∞), the lift force on the model is only dependant on C_L , which in turn is a function of α_e (the *effective* AOA). α_e is obtained by adding the generating wing's upwash (or downwash) (ϵ) to the absolute AOA, or:

$$\alpha_e = \alpha_a + \epsilon \quad (\text{A.13})$$

For the model, $(\alpha_a)_{max} = 12.3$ degrees. Calculation of ϵ_{max} requires knowledge of $(V_\theta)_{max}$ which is in turn derived from $(\Gamma_{GW})_{max}$ at a given radius from the vortex centerline. Knowing that the circulation generated inside the BLWT is always negative and assuming, in a worst-case scenario, that the vortex centerline coincides with the left wing tip axis of the model (thus creating an *upwash* flow around the entire model), $(V_\theta)_{avg}$ is estimated to occur at the model centerline, or at $r \approx b/2 = 0.513$ m. Equation (A.7) with $(\Gamma_{GW})_{max} = -2.57$ m²/s and $r = 0.513$ m yields:

$$(V_\theta)_{avg} \approx 0.80 \text{ m/s.}$$

Equation (A.9) with this last result and $V_\infty = 16.8$ m/s yields:

$$\epsilon_{max} = 0.047 \text{ rads} = 2.7 \text{ deg.}$$

Equation (A.13) yields: $(\alpha_e)_{max} = 0.262 \text{ rads} = 15.0 \text{ deg}$

Because of the complex lifting surfaces on the CF-18A, equation (A.2) cannot be used to predict $(C_L)_{18}$. Instead, a trimmed lift characteristic table is used to find $(C_L)_{18}$ as a function of (α_e) for a given Mach number. Using the $M=0.2$ curve (the lowest charted Mach curve), the lift coefficient at $(\alpha_e)_{max}=15.0$ degrees can be estimated. The chart yields:

$$(C_L)_m \approx 1.27$$

Equation (A.12) with $S_w=0.258 \text{ m}^2$, $\rho=1.225 \text{ kg/m}^3$, $V_\infty=16.8 \text{ m/s}$, yields:

$$(L_m)_{max} = 56.6 \text{ N}$$

Since the model will always be tested at positive α_e , it will always develop a positive lift when subjected to the freestream flow, and thus the minimum lift case will be the zero-lift condition (i.e. when there is no freestream flow). For calibration purposes, we can summarize the lift envelope on the model as follows:

$$0 \leq L_M \leq 56.6 \text{ N}$$

3. ESTIMATION OF MAXIMUM LOADS ON STING BALANCE

3.1. Normal Forces (N1, N2 channels)

The moments with respect to points N1 and N2 (M_{N1} and M_{N2} , respectively) are calculated by considering model and mount weight as well as model lift force in the BLWT. The maximum *upward* load on the Sting balance will occur when the lift force on the model is greatest. Conversely, the maximum *downward* load on the Sting balance will occur when the model is not developing any lift (ie. when the BLWT wind velocity is zero). Figure A2 is a schematic of the normal forces and of their relative positions along the X-axis. Point "O" is referred to as the *electric center* of the Sting balance and is located halfway between points N1 and N2.

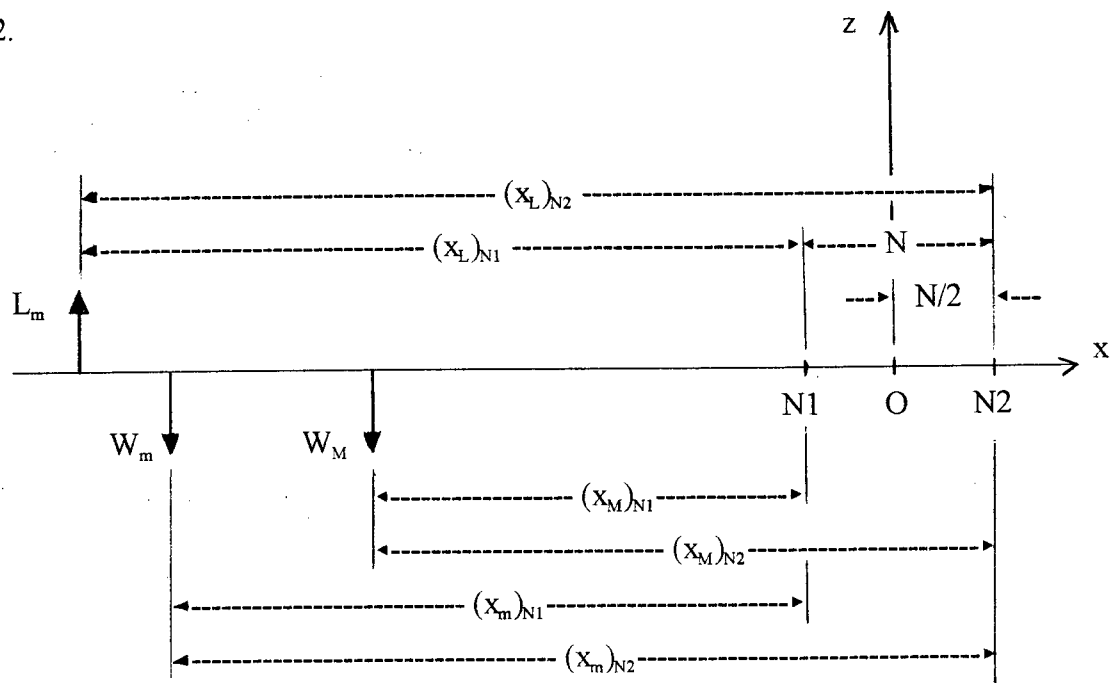


Figure A2: Schematic of Forces Acting on the Sting *Normal Force* Channels

The Sting's output voltage for the $N1$ and $N2$ channels is proportional to the moments with respect to points $N1$ and $N2$. The X -location is measured along the X -axis with respect to point O (the electrical center). Two moment equations can be written (i.e., one with respect to each point $N1$ and $N2$). During the testing, the unknowns are L_m and x_L , which can be determined by using the two moment equations³. The lift force is obtained by measuring the respective changes in M_{N1} and M_{N2} (symbolized as ΔM_{N1} and ΔM_{N2} , respectively) due to the addition of the freestream velocity in the BLWT. Since an upwards Normal Force is defined as being positive, the lift force on the model is given by the equation:

$$L_m = \frac{\Delta M_{N1} + \Delta M_{N2}}{N} \quad (\text{A.14})$$

and the X -location of the lift force $(x_L)_o$ is given by:

$$(x_L)_o = \frac{\Delta M_{N1}}{L_m} - \frac{N}{2} \quad (\text{A.15})$$

For the maximum and minimum loads estimation on the Sting, we shall use values of L_m derived from the aerodynamics forces analysis (refer to section 2.3 of this Appendix) and assume that the lift force on the model acts at the wings' center of pressure (i.e. at 25% MAC), and thus:

³ Note that by design of the Sting balance, M_{N1} yields a positive voltage reading when a downward force is applied to the model, while M_{N2} has the reverse sign convention (i.e. M_{N2} yields a positive reading with an upward force to the model).

$$x_L = -34.4 \text{ in} = -0.874 \text{ m}$$

Table A2 summarizes the maximum and minimum Normal Forces with their respective locations along the X-axis, distances to points N1 and N2 ($(x)_{N1}$ and $(x)_{N2}$ respectively) as well as the resulting moments at these points.

Component	Force (N)	X-location (m)	$(x)_{N1}$ (m)	M_{N1} (N·m)	$(x)_{N2}$ (m)	M_{N2} (N·m)
Model (weight) ⁴	-90.7	-0.716	0.618	-56.1	0.814	-73.8
Mount (weight)	-62.3	-0.114	0.016	-1.0	0.212	-13.2
Max. lift force	+56.6	-0.874	0.776	43.9	0.972	55.0
SUM(L_{max} case)	-96.4			-13.1		-32.0
Min. lift force	0	-0.874	0.776	0.0	0.972	0.0
SUM (L_{min} case)	-153			-57.0		-87.0

Table A2: Estimated Maximum and Minimum Normal Forces on the Sting Balance.

Finally, note that the largest estimated Normal Force (i.e., -153 N=-34.3 lbs) and the maximum estimated Normal Moment (i.e., -87.0 N·m = -767 lb·in) are well within the prescribed Sting balance's limits (refer to section 2.1.2).

3.2 Side Forces (S1, S2 channels)

The Sting's output voltage for the S1 and S2 channels is proportional to the moment generated by the Side Force on the model with respect to points S1 and S2 (M_{S1} and

⁴ The weight of the model includes half the weight of the tygon tubing protruding from the model's exhaust, the other half being supported by the Sting balance mount.

M_{S2} , respectively) The maximum side load on the Sting balance will occur when the side force on the model is greatest⁵. The *Side Force* channels are independent of the weight of the model and of its mount. Figure A3 is a schematic of the side forces and of their relative positions along the X-axis. Point "O" is the electric center of the Sting balance, located halfway between points S1 and S2.

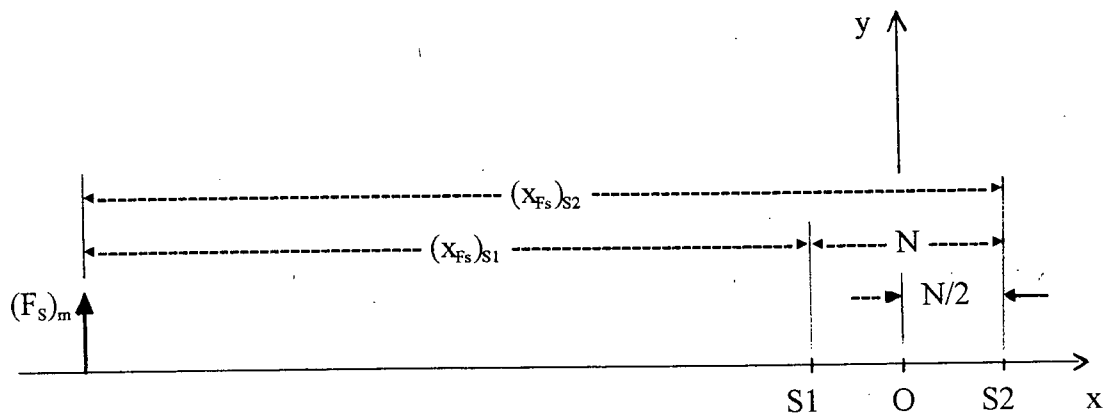


Figure A3: Schematic of Forces Acting on the Sting *Side Force* Channels

Points S1 and S2 correspond to points N1 and N2. The *X-location* is measured along the X-axis with respect to point O. Similarly to the Normal Forces, two moment equations can be written⁶ (i.e., one for each point S1 and S2). During the testing, the unknowns are $(F_s)_m$ and x_{Fs} , which can be determined using the two moment equations. The Side Force is

⁵ As determined in section 2.3, the maximum Side Forces on the model are estimated to be the same in both spanwise directions (i.e. along the Y-axis).

⁶ By design of the Sting, both side moments M_{S1} and M_{S2} yield positive voltage readings when the model is subjected to a *leftward* force (i.e. for a *negative* Side Force).

obtained by measuring the respective changes in M_{S1} and M_{S2} (symbolized as ΔM_{S1} and ΔM_{S2} , respectively) due to the addition of the tangential velocity in the BLWT. Since a *rightwards* Side Force is defined as being positive, the Side Force is given by:

$$(F_S)_m = \frac{\Delta M_{S1} - \Delta M_{S2}}{N} \quad (\text{A.16})$$

and the X-location of the Side Force $(x_{Fs})_o$ is given by:

$$(x_{Fs})_o = \frac{\Delta M_{S1}}{F_S} - \frac{N}{2} \quad (\text{A.17})$$

For the maximum and minimum loads estimation on the Sting, we shall use values of $(F_S)_m$ derived from the aerodynamics forces analysis (section 2.1 of this Appendix) and assume that the Side Force on the model acts approximately at center of the model's fuselage, and thus:

$$(x)_{Fs} \approx 41.3 \text{ in} = -1.05 \text{ m}$$

Table A3 displays the maximum/ minimum expected Side Forces, their location along the X-axis, the distances to points S1 and S2 ($(x)_{S1}$ and $(x)_{S2}$, respectively) as well as the resulting moments at these points.

Component	Force (N)	X-location (m)	(x) _{s1} (m)	M _{s1} (N·m)	(x) _{s2} (m)	M _{s2} (N·m)
Max. side force	±3.0	-1.05	0.952	±2.86	1.148	±3.44

Table A3: Estimated Range of Side Forces on the Sting Balance.

Evidently, the largest estimated Side Force (i.e., ±3.0 N=±0.67 lbs) and Side Moment (±3.44 N·m=±30.4 lb·in) are well within the prescribed Sting balance's limits (refer to section 2.1.2).

3.2 Rolling Moment (R channel)

The Rolling Moment "felt" by the Sting (M_R) is the sum of the actual rolling moment about the model's centerline axis (M_m) and of the moment of the Side Force about the Sting's centerline. Figure A4 is a schematic of the forces and distances involved in calculating the Rolling Moment.

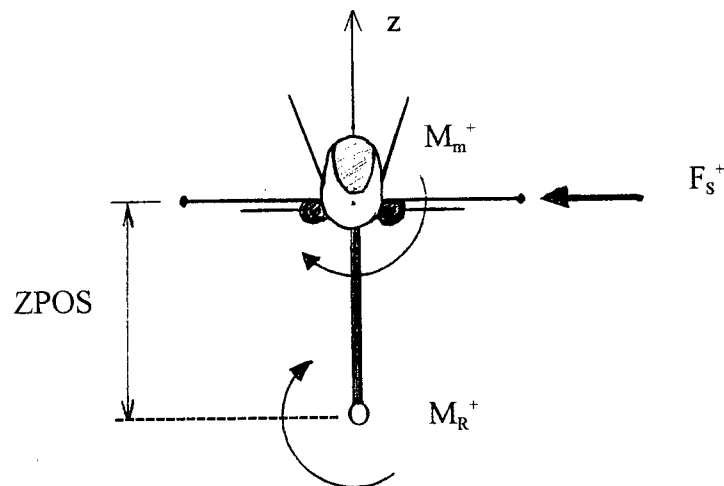


Figure A4: Schematic of Forces Acting on the Sting *Rolling Moment* Channel

Taking the summation of the moments about the Sting (point "O"), we get:

$$M_R = M_m - F_s \cdot ZPOS \quad (\text{A.18})$$

Thus, in order to obtain M_m , one must de-couple the moments by subtracting the Side Force component from M_R , which implies that the Side Force value must be known prior to solving for the Rolling Moment⁷. The equation then becomes:

$$M_m = M_R + F_s \cdot ZPOS \quad (\text{A.19})$$

The largest estimated Rolling Moment felt by the Sting can be calculated using a combination of the largest positive M_m and maximum negative F_s for $ZPOS=+0.38$ m.

Using $M_m=+4.3$ N·m and $F_s=-3.0$ N, equation (A.18) yields:

$$(M_m)_{\max} = \pm 5.44 \text{ N}\cdot\text{m}$$

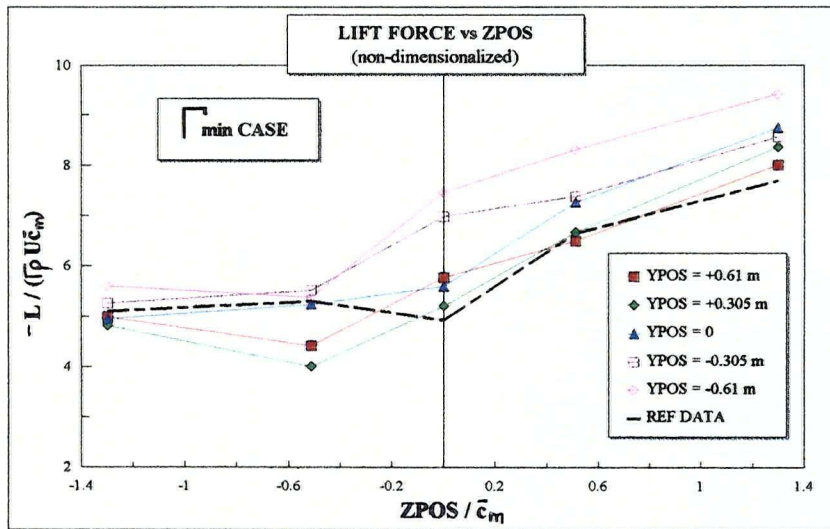
This figure is well within the prescribed Sting balance's limit of ± 1000 lb·in (± 113 N·m).

⁷ The data acquisition program solves for F_y and F_s first, allowing for the subsequent computation of M_m in the program.

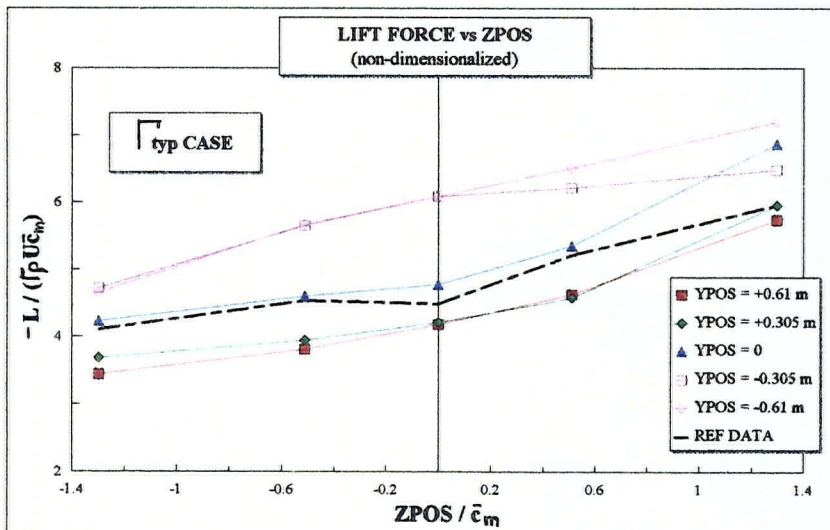
APPENDIX B
FORCE AND PRESSURE PLOTS

NON-DIMENSIONAL LIFT FORCE

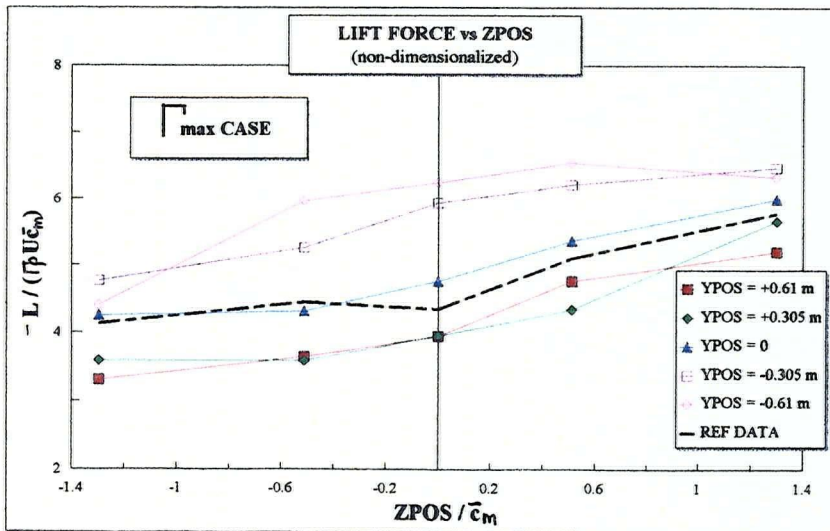
Plot 1.1



Plot 1.2

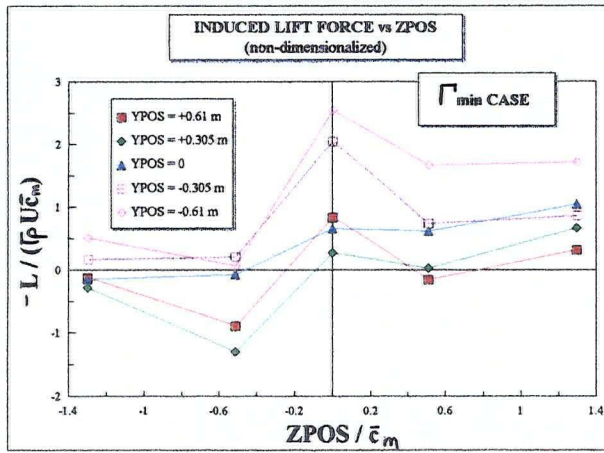


Plot 1.3

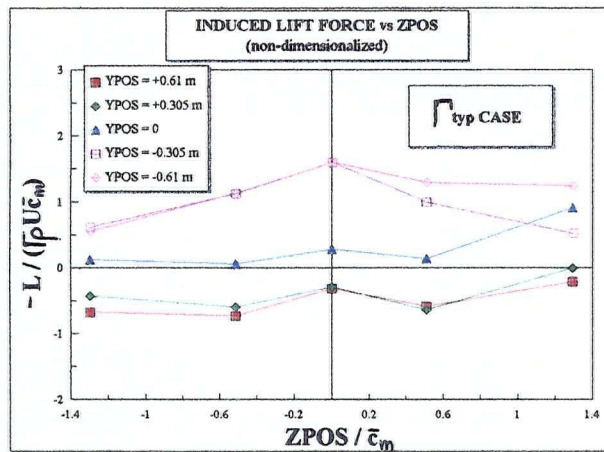


NON-DIMENSIONAL INDUCED LIFT FORCE

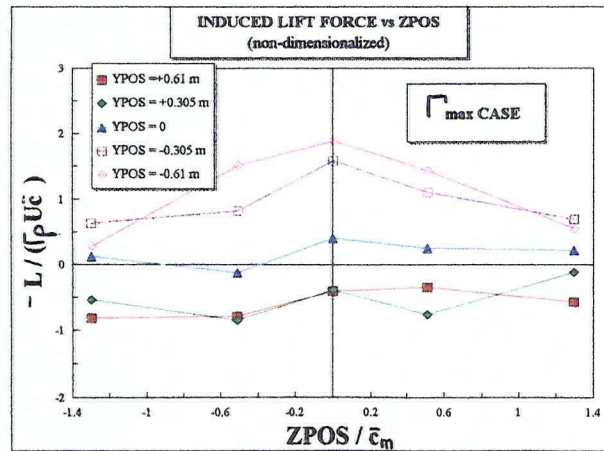
Plot 2.1



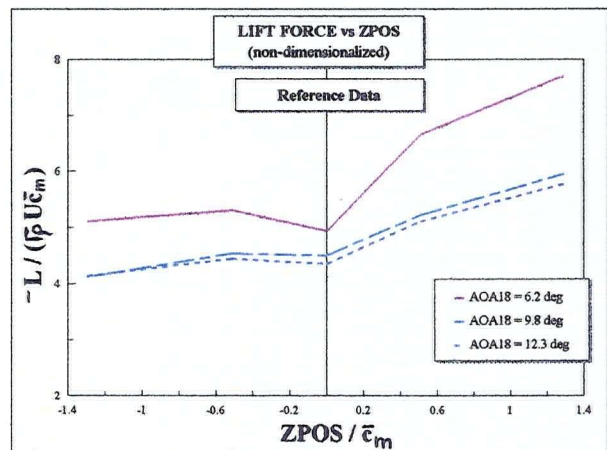
Plot 2.2



Plot 2.3

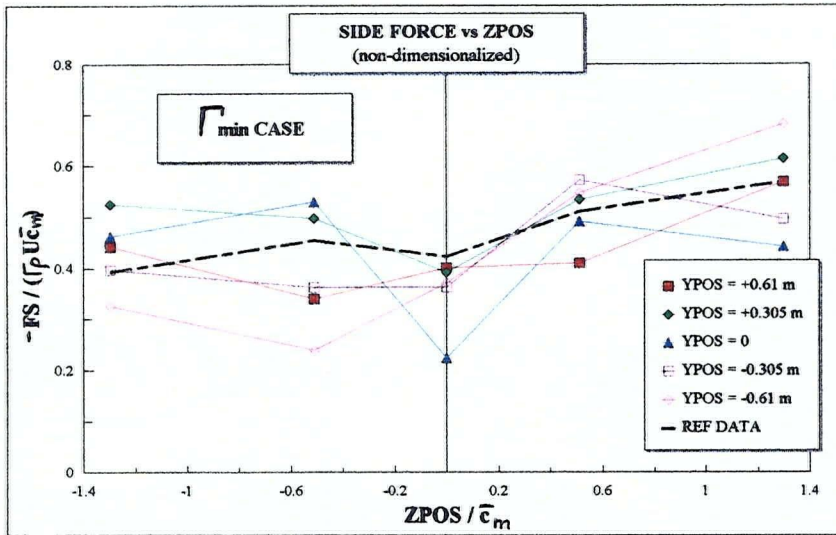


Plot 2.4

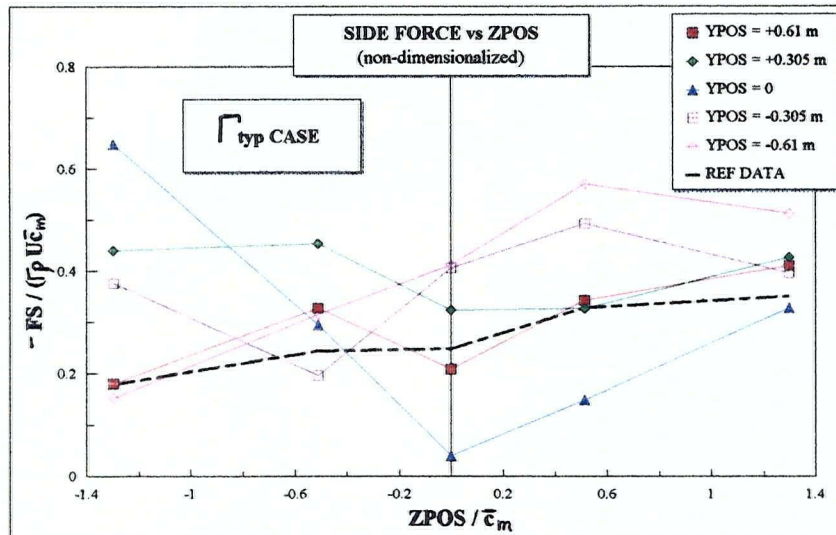


NON-DIMENSIONAL SIDE FORCE

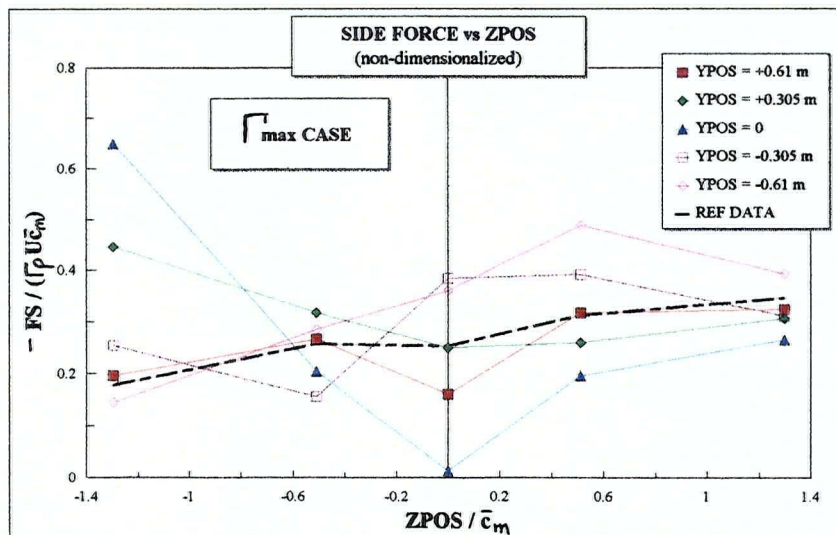
Plot 3.1



Plot 3.2

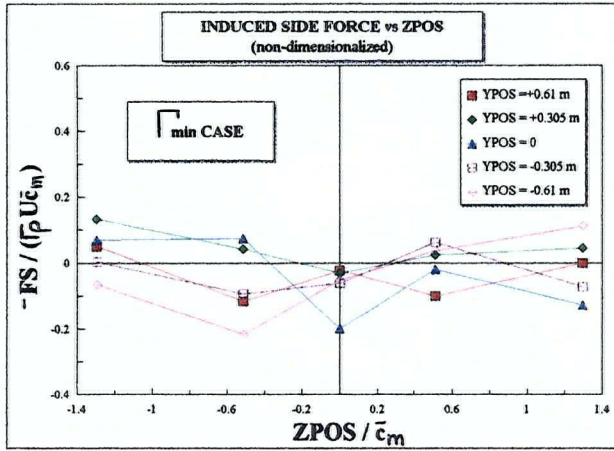


Plot 3.3

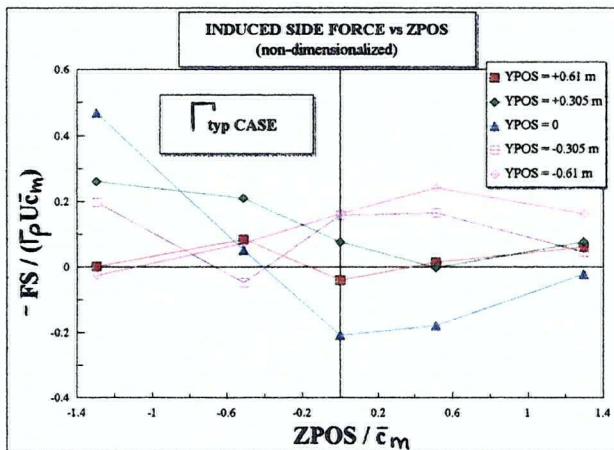


NON-DIMENSIONAL INDUCED SIDE FORCE

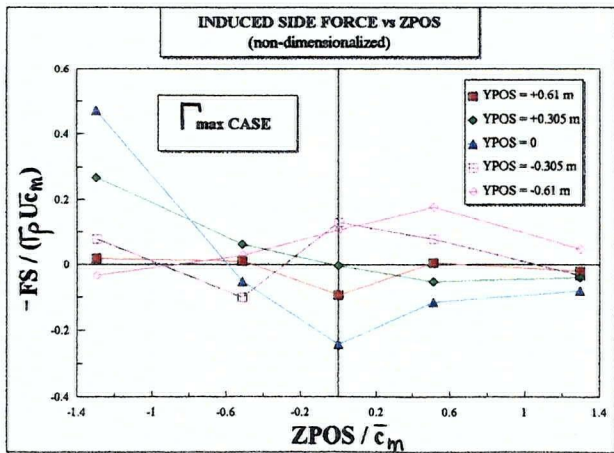
Plot 4.1



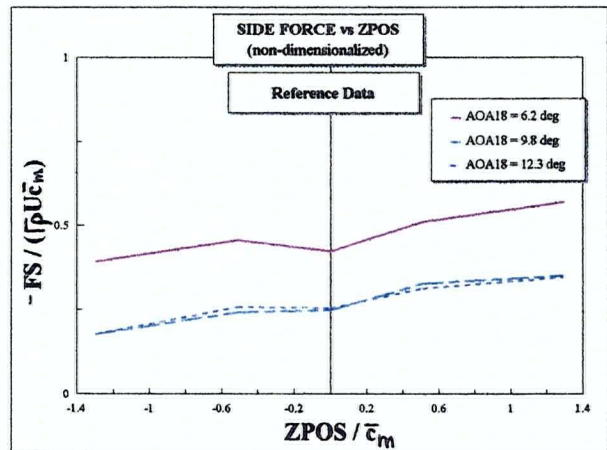
Plot 4.2



Plot 4.3

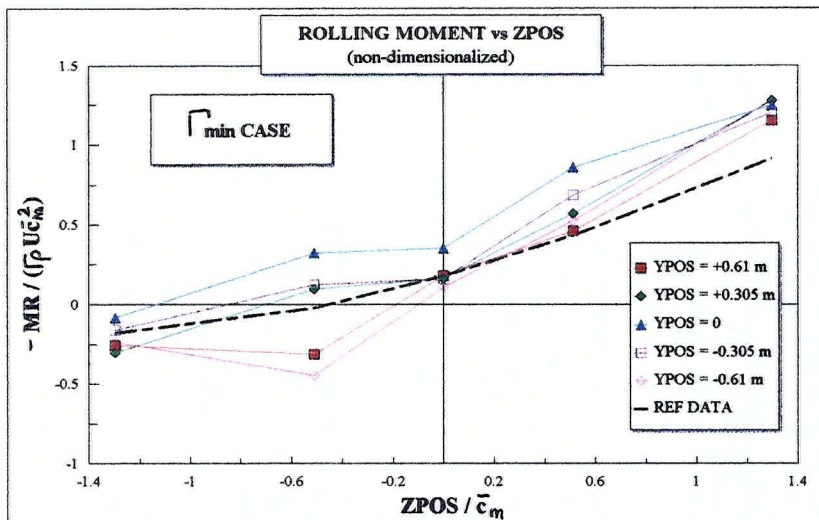


Plot 4.4

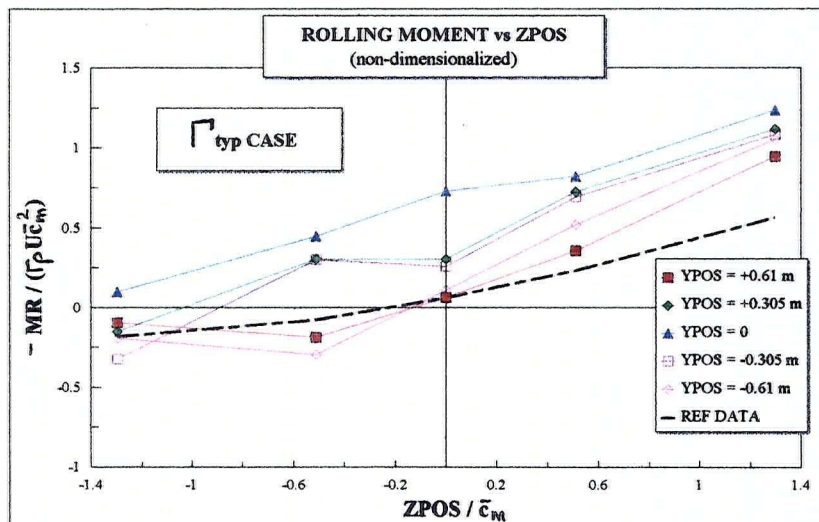


NON-DIMENSIONAL ROLLING MOMENT

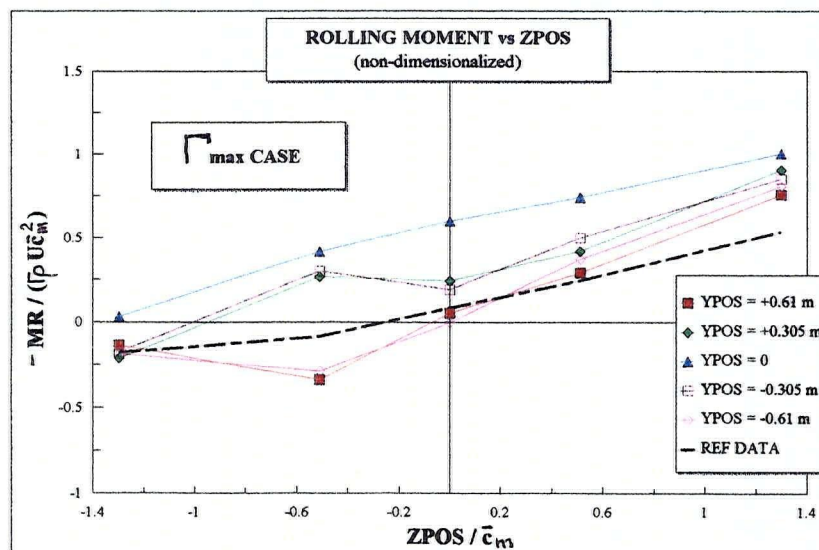
Plot 5.1



Plot 5.2

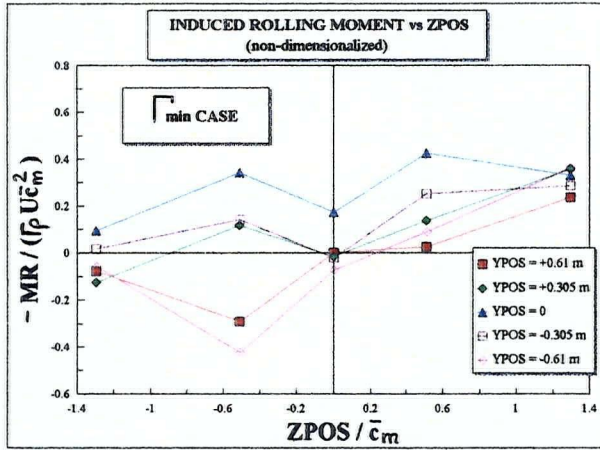


Plot 5.3

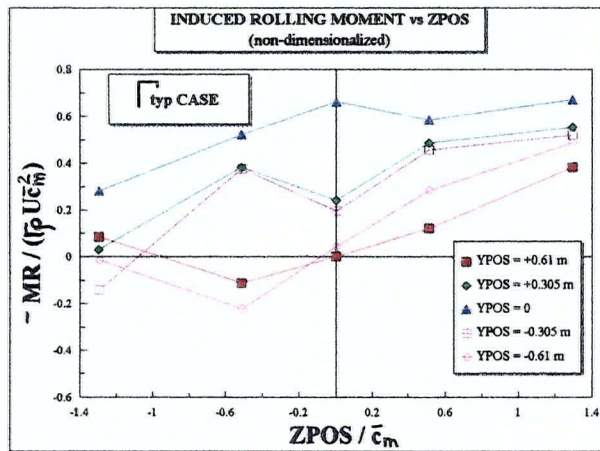


NON-DIMENSIONAL INDUCED ROLLING MOMENT

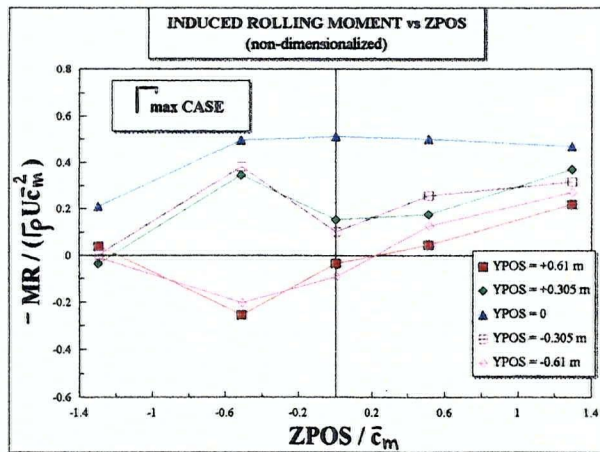
Plot 6.1



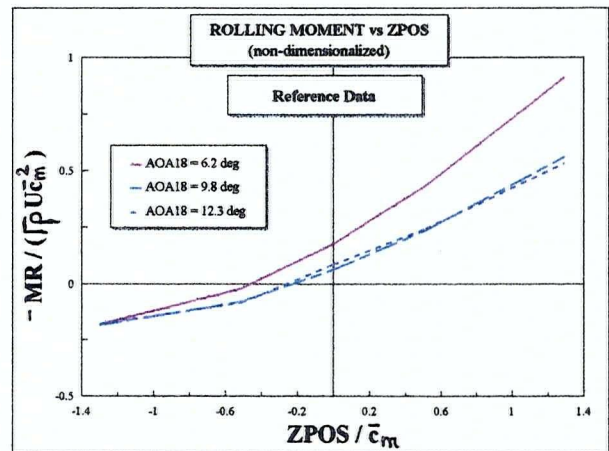
Plot 6.2



Plot 6.3



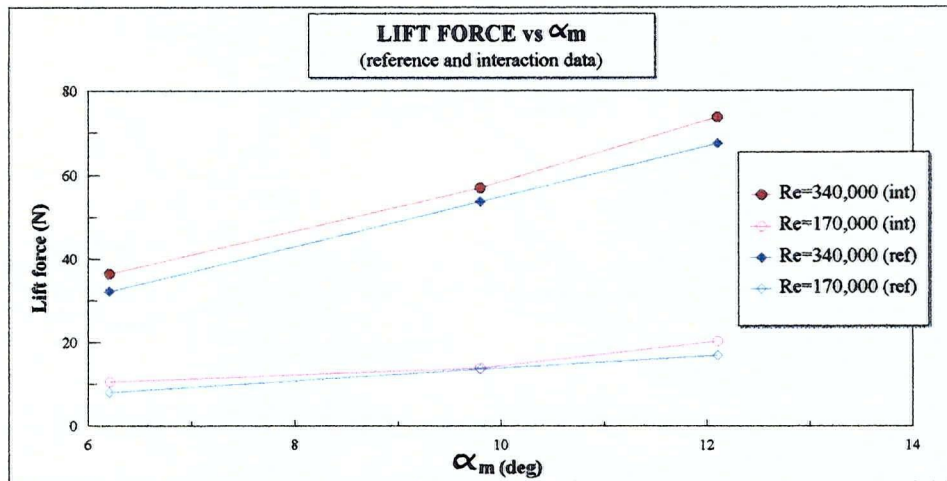
Plot 6.4



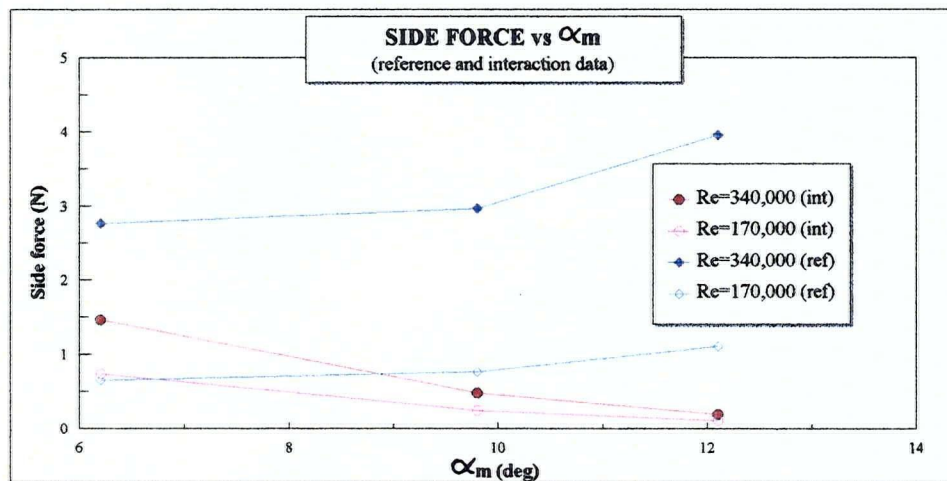
REYNOLDS NUMBER EFFECTS

(FORCES AND ROLLING MOMENTS FOR YPOS=0 AND ZPOS/c =0)

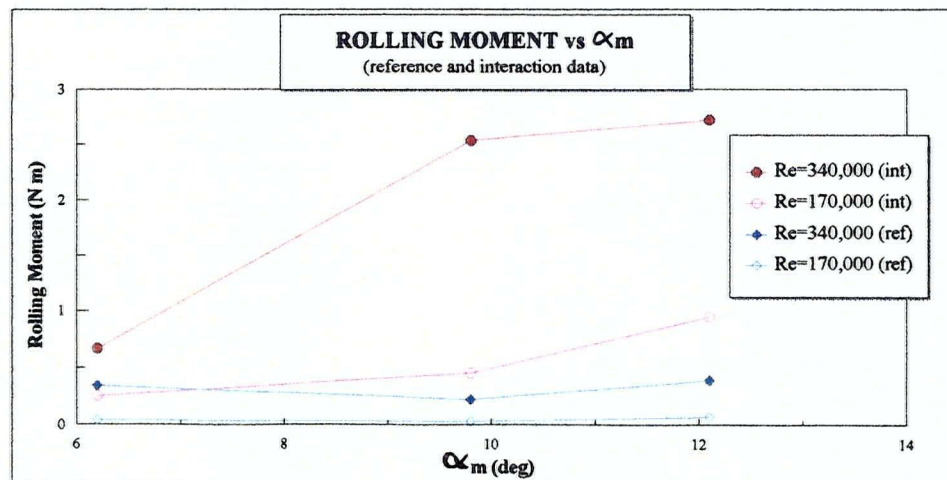
Plot 7.1



Plot 7.2



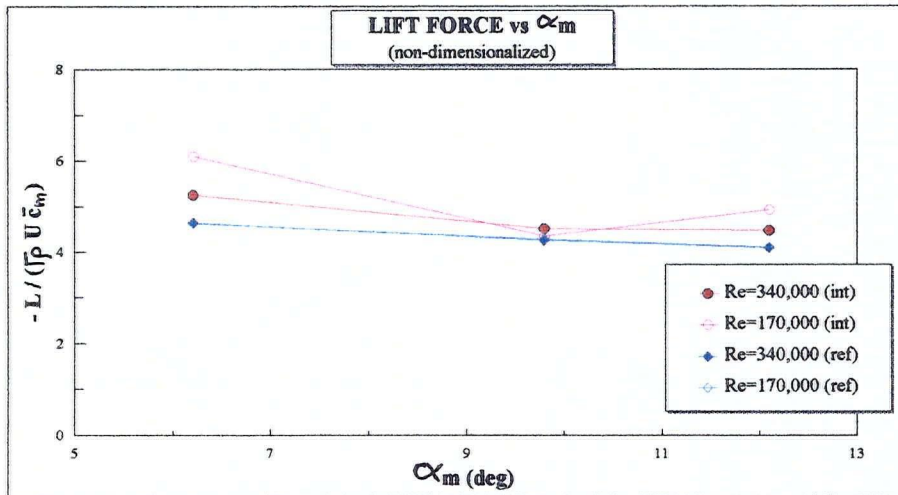
Plot 7.3



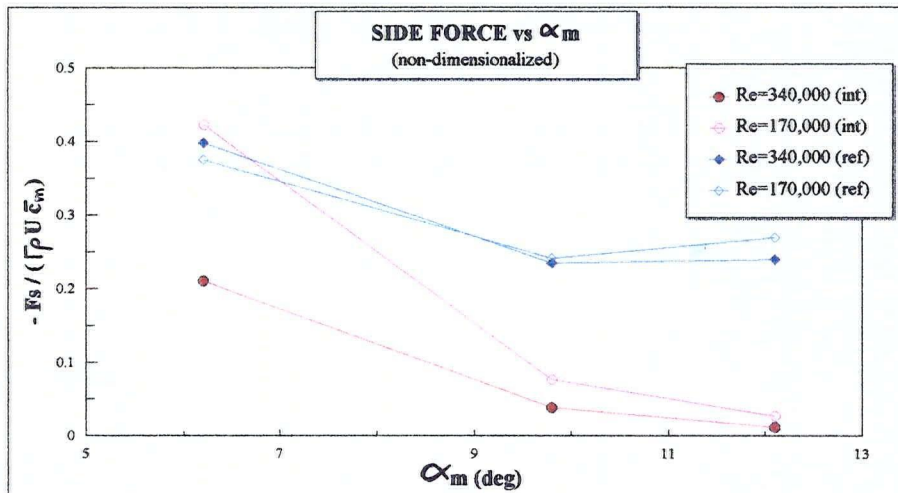
NON-DIMENSIONAL REYNOLDS NUMBER EFFECTS

(NON-DIMENSIONAL FORCES AND ROLLING MOMENTS FOR $Y_{POS}=0$ AND $Z_{POS}/c = 0$)

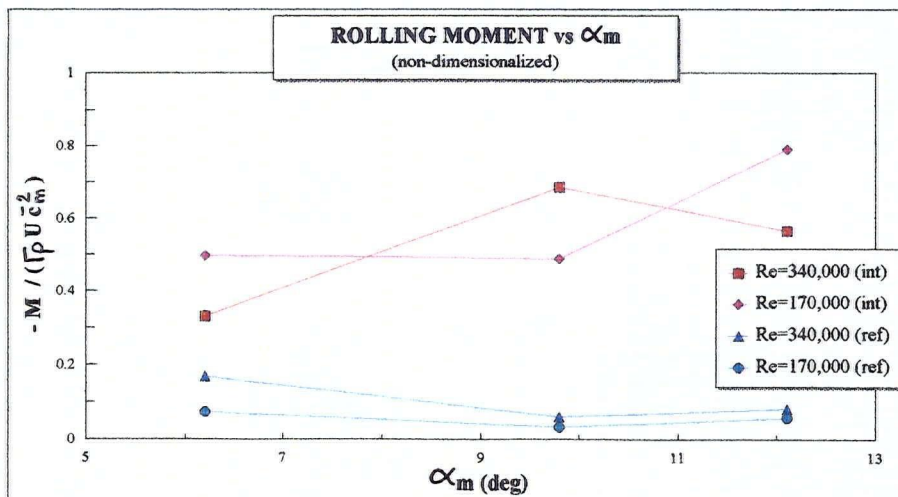
Plot 8.1



Plot 8.2



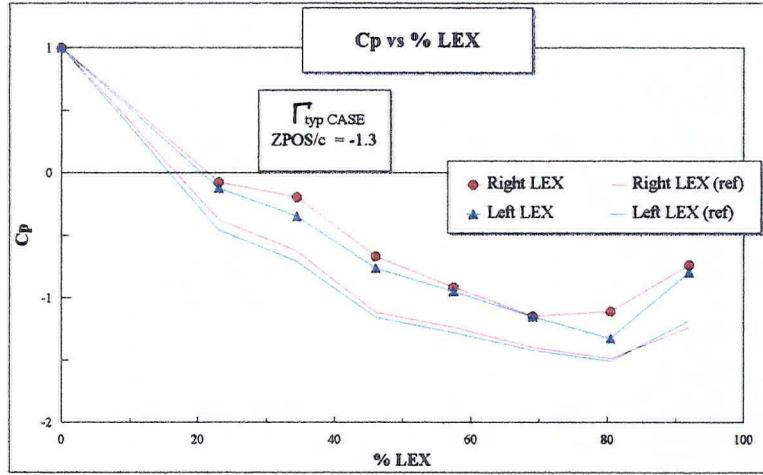
Plot 8.3



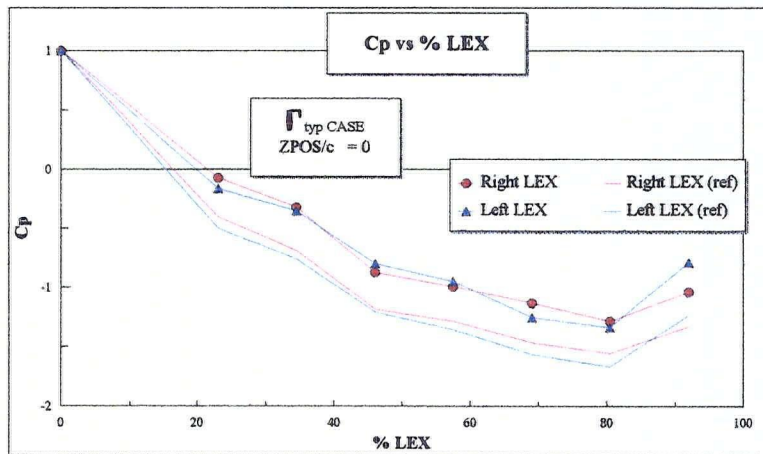
PRESSURE COEFFICIENT ON LEX

Comparing Interaction and Reference Data for YPOS=+0.61 m

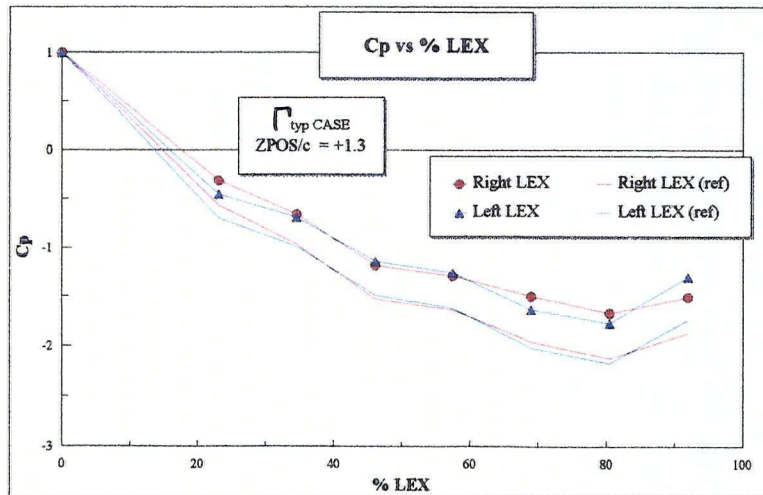
Plot 9.1



Plot 9.2



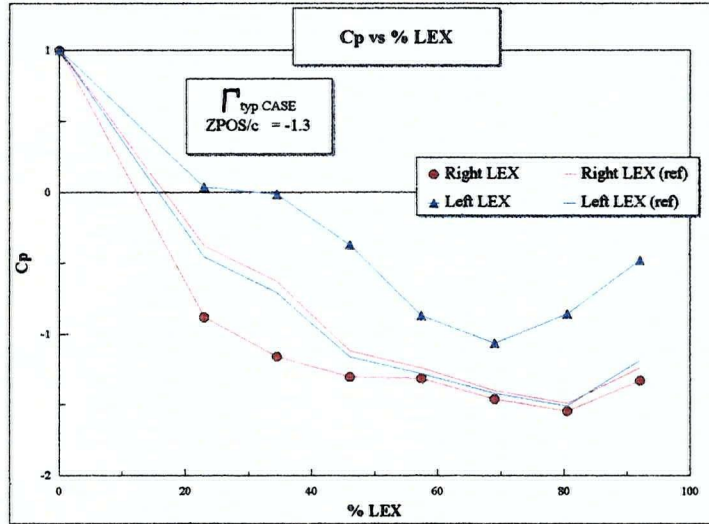
Plot 9.3



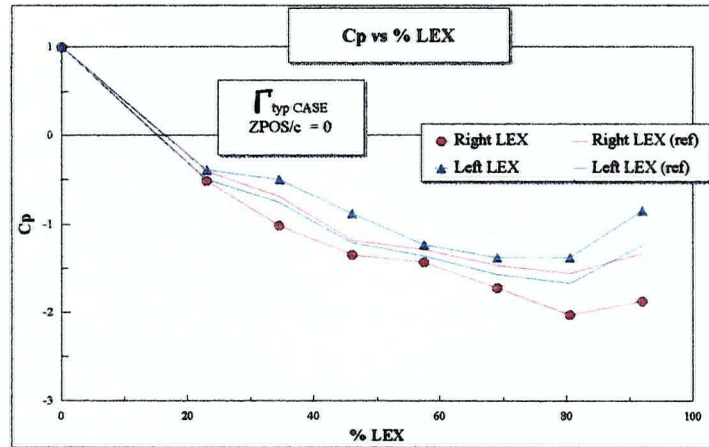
PRESSURE COEFFICIENT ON LEX

Comparing Interaction and Reference Data for YPOS=0

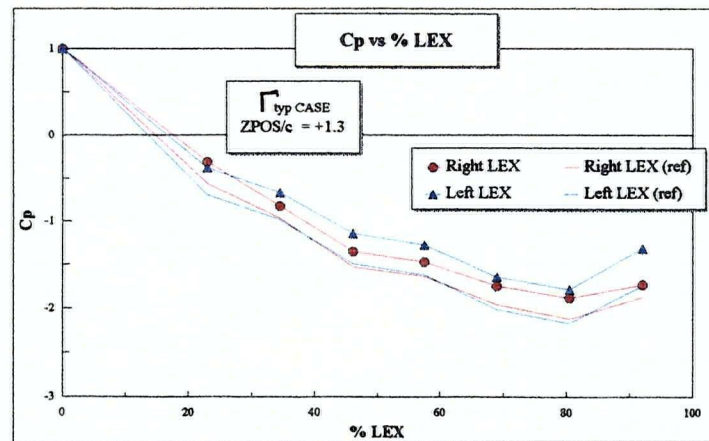
Plot 10.1



Plot 10.2



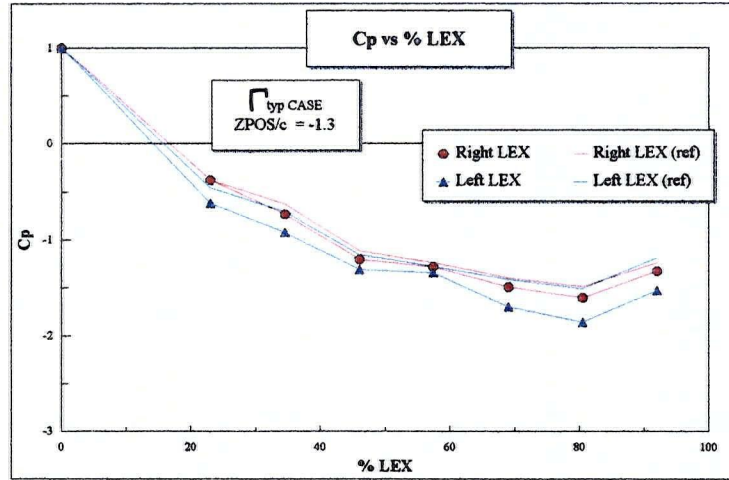
Plot 10.3



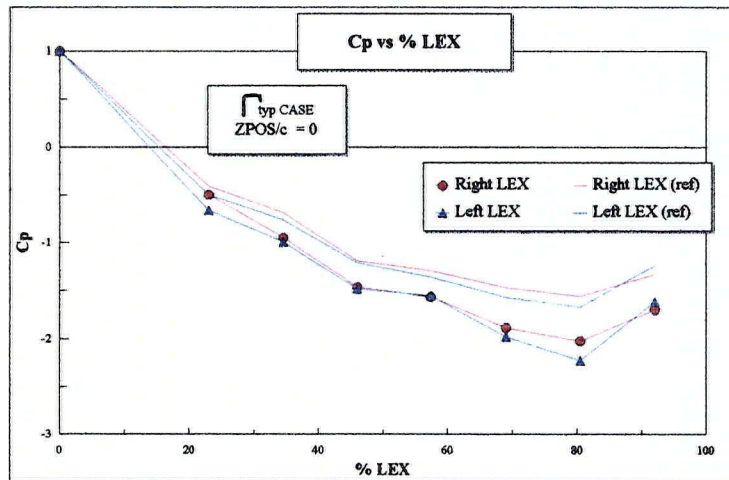
PRESSURE COEFFICIENT ON LEX

Comparing Interaction and Reference Data for YPOS=-0.61 m

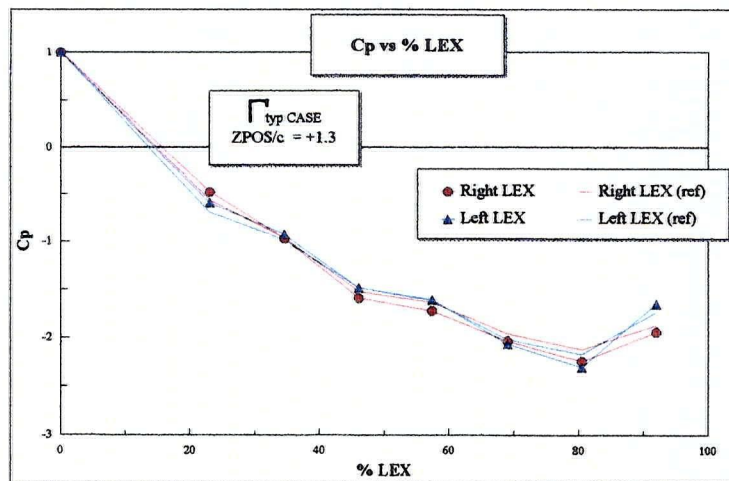
Plot 11.1

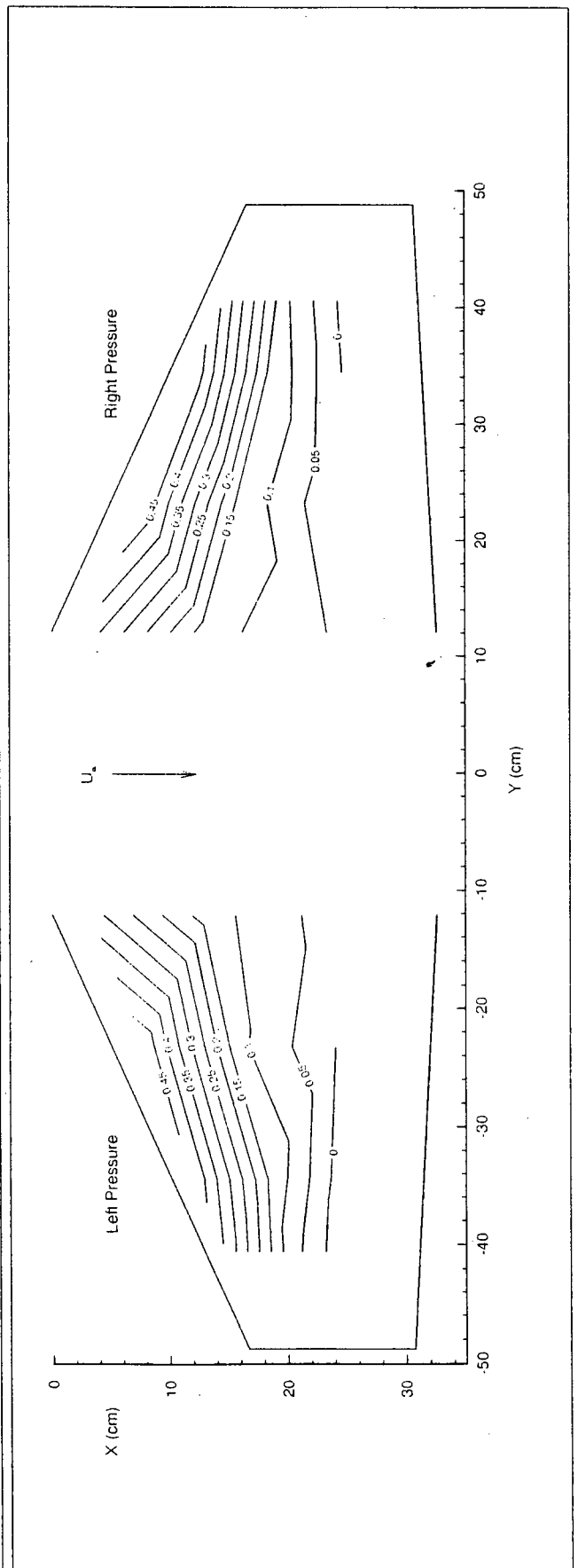
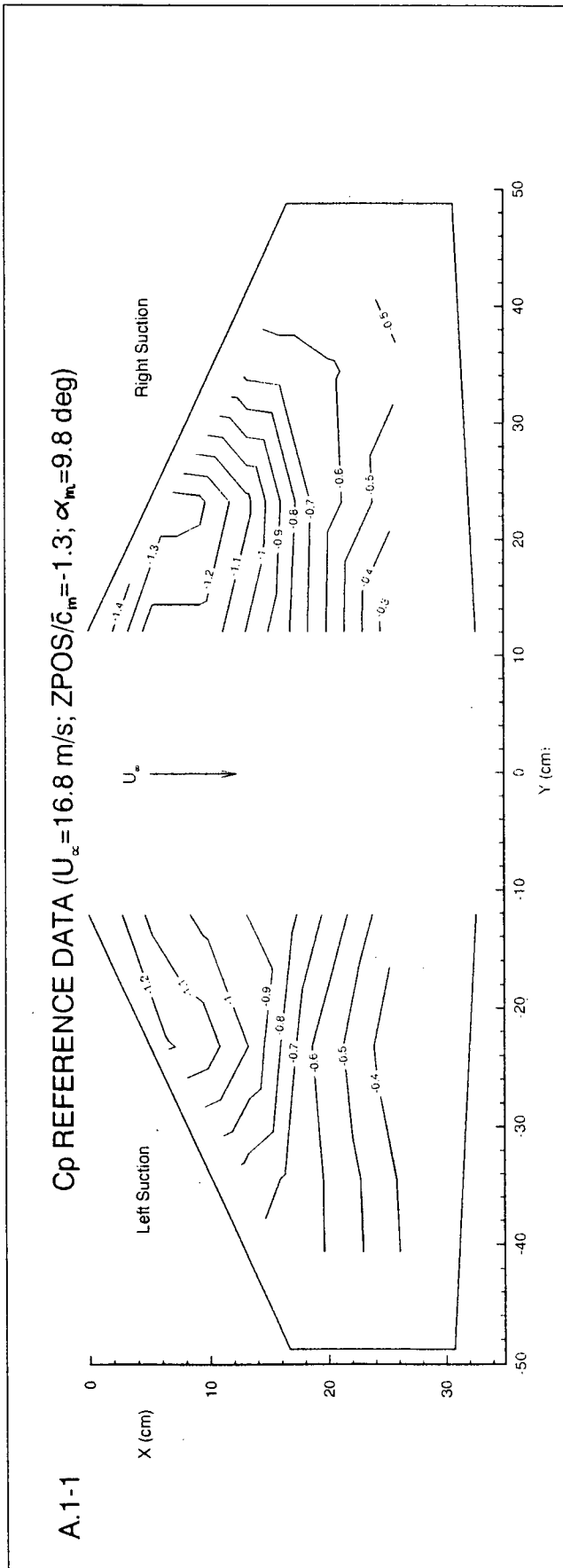


Plot 11.2



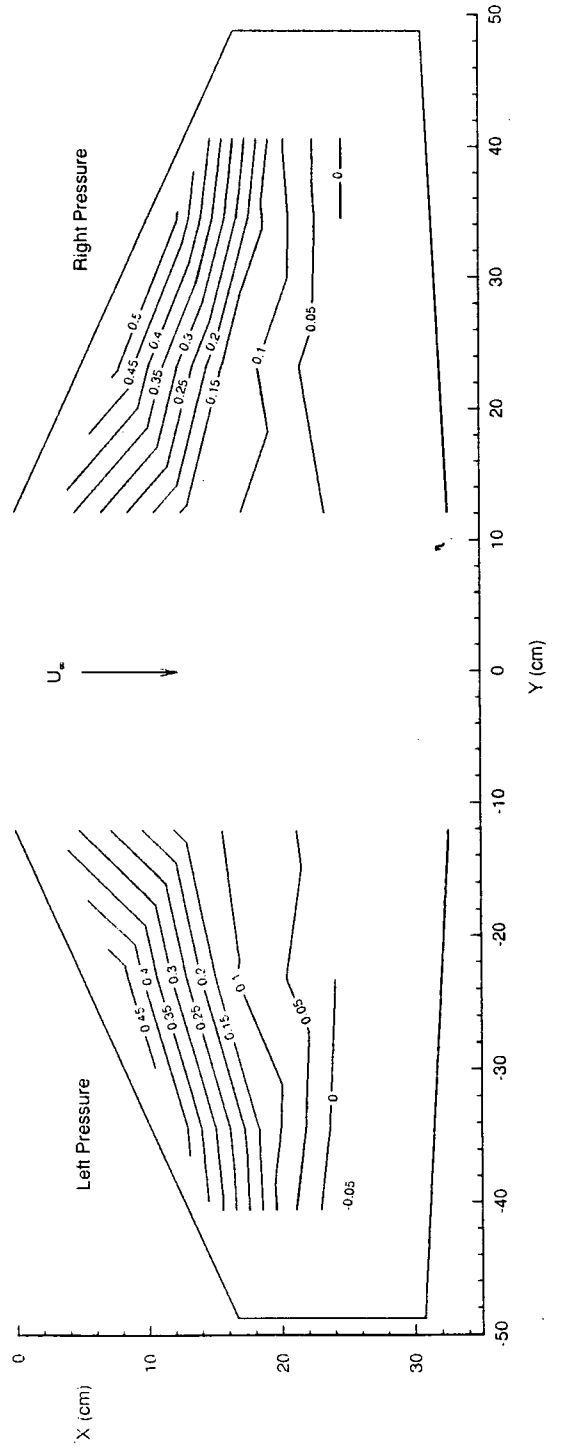
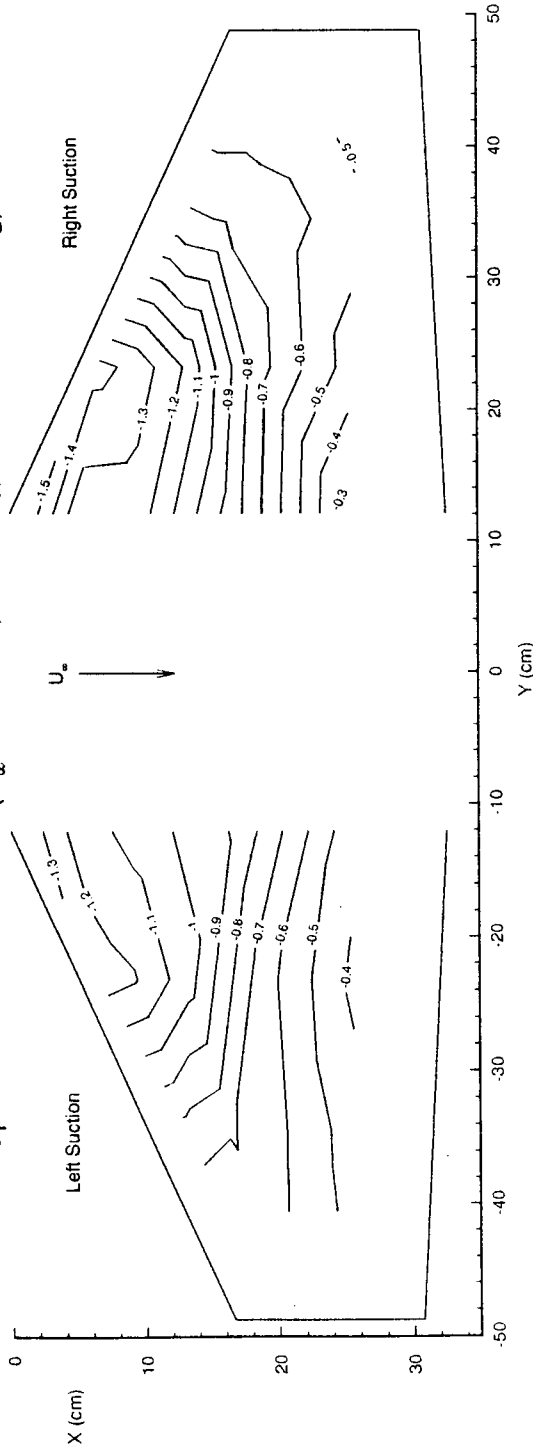
Plot 11.3



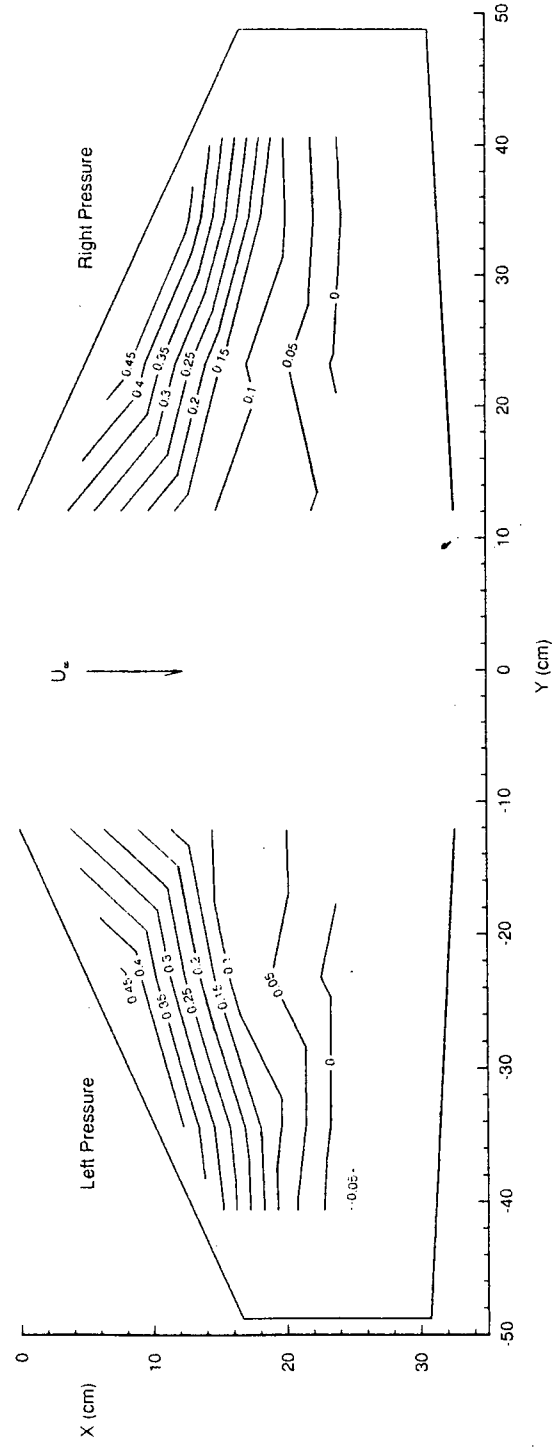
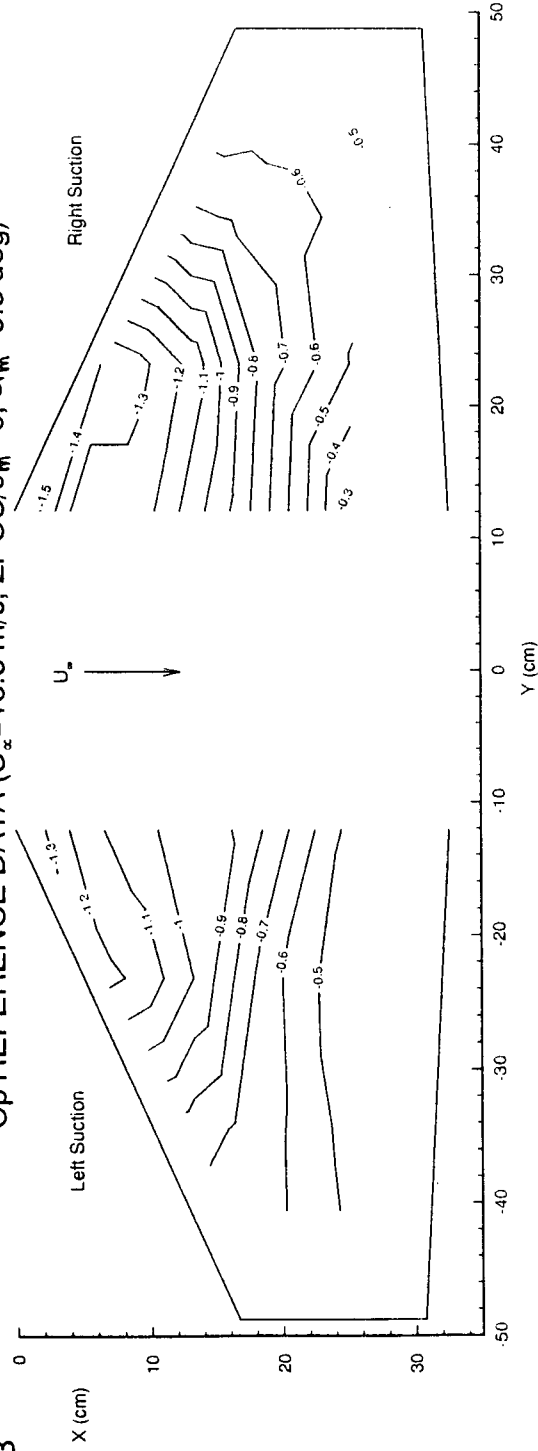


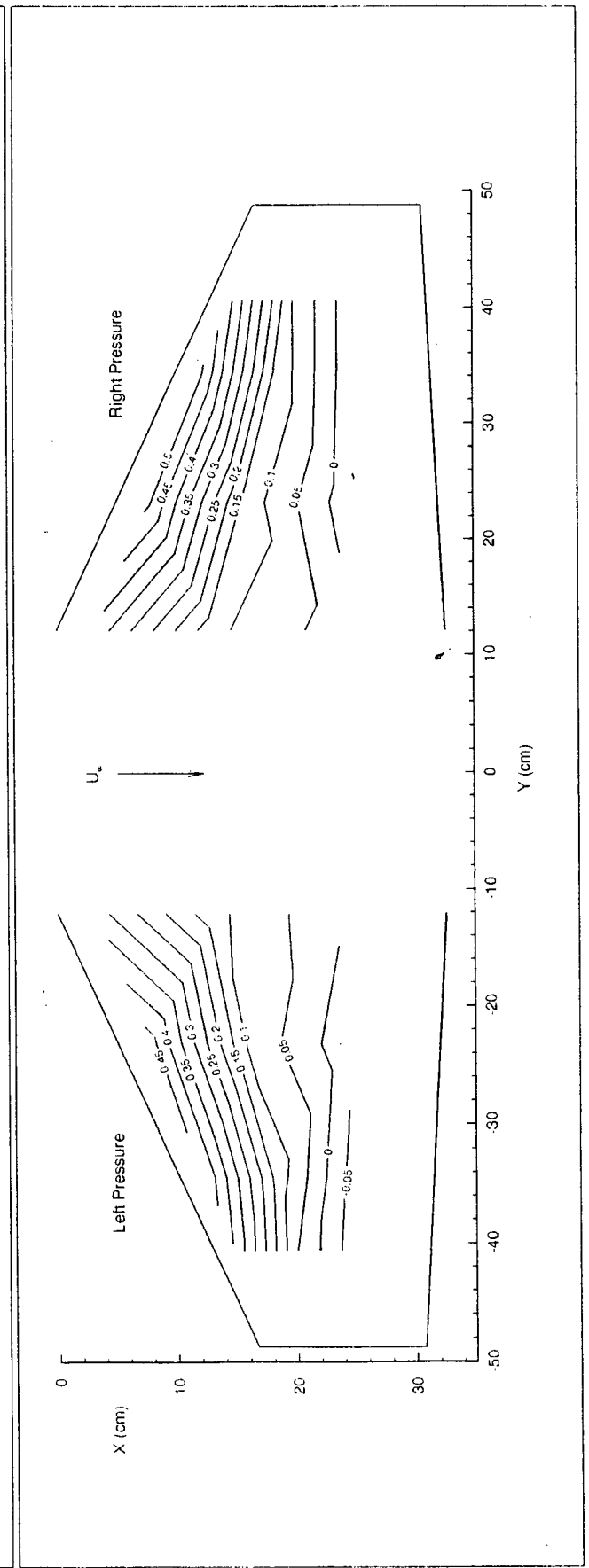
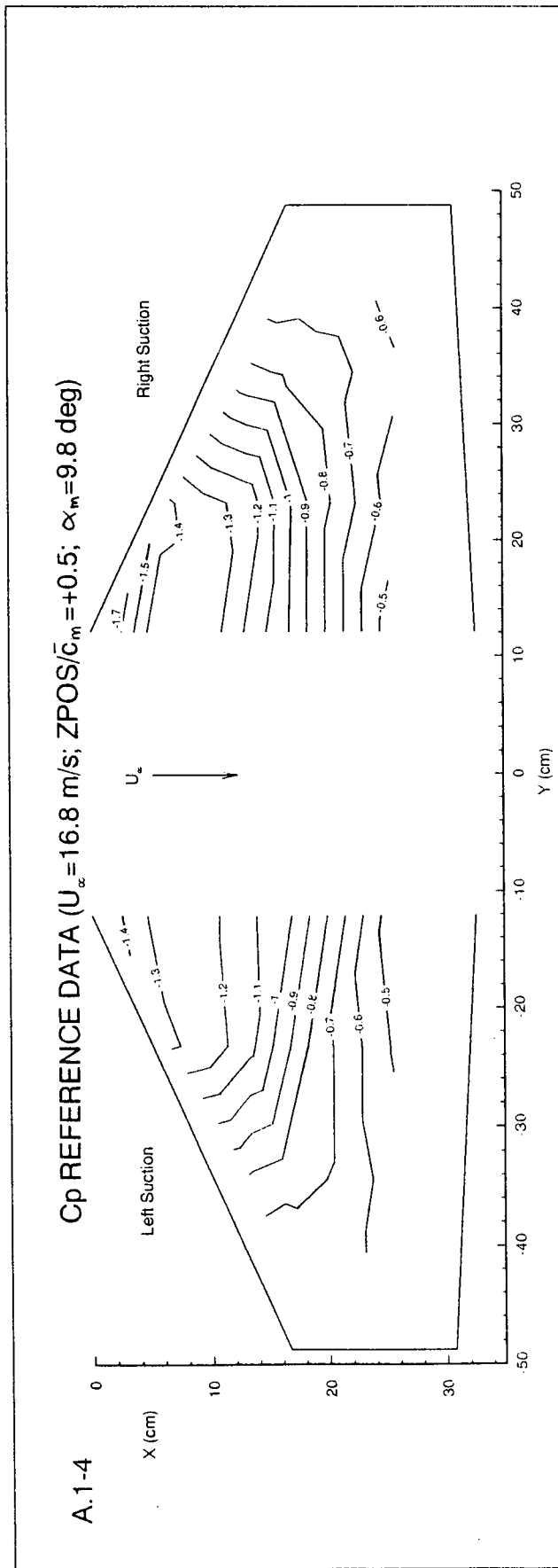
A.1-2

Cp REFERENCE DATA ($U_\infty = 16.8$ m/s; $ZPOS/\bar{C}_m = -0.5$; $\alpha_m = 9.8$ deg)

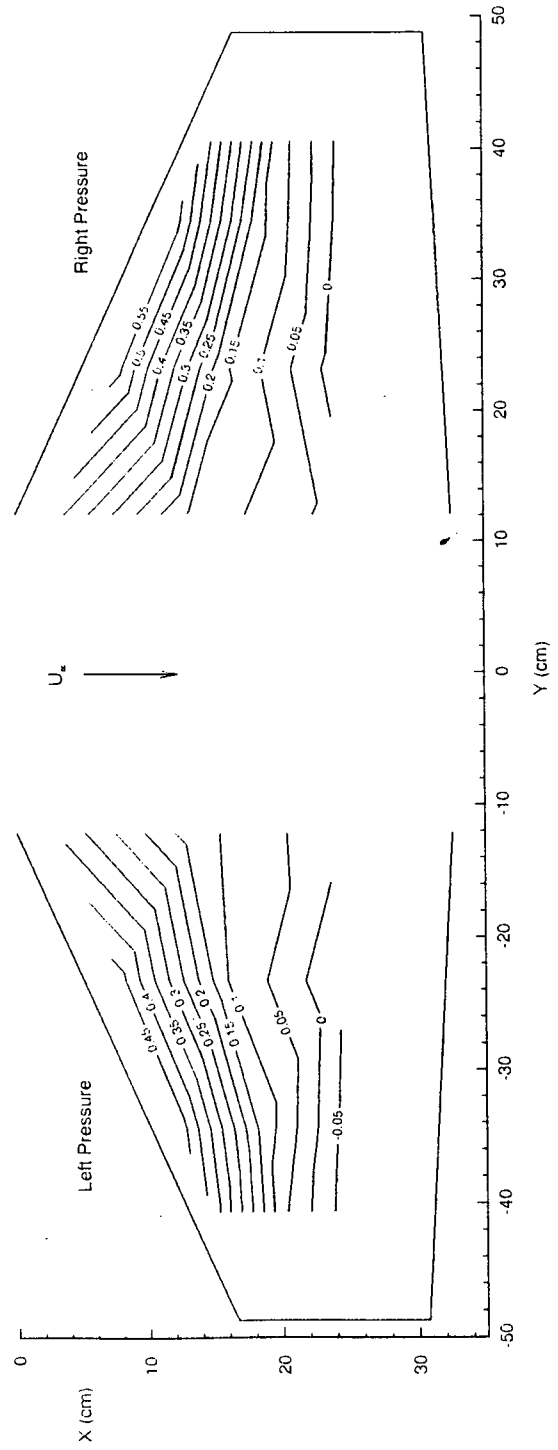
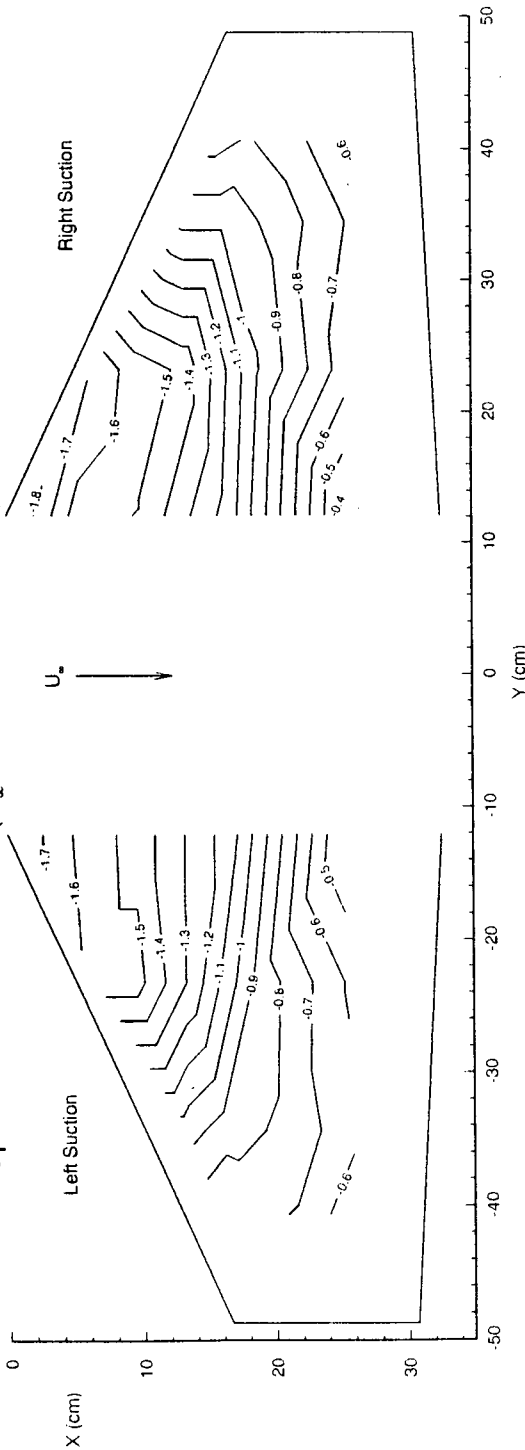


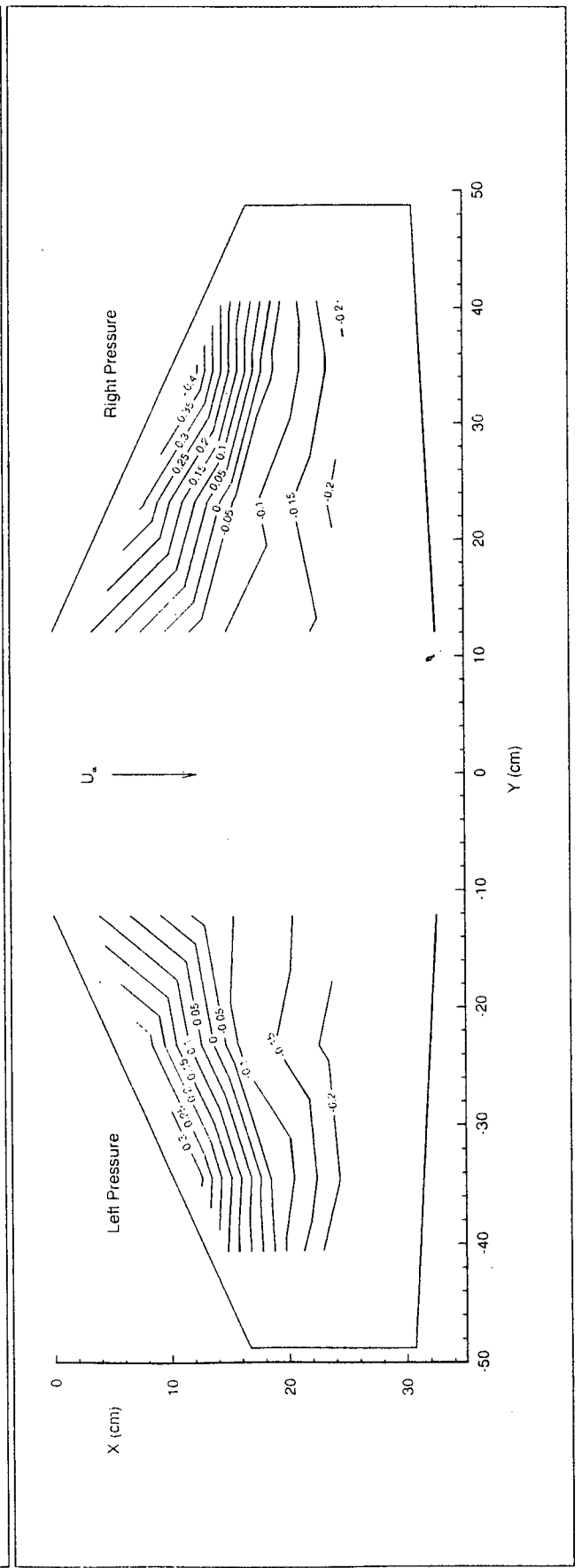
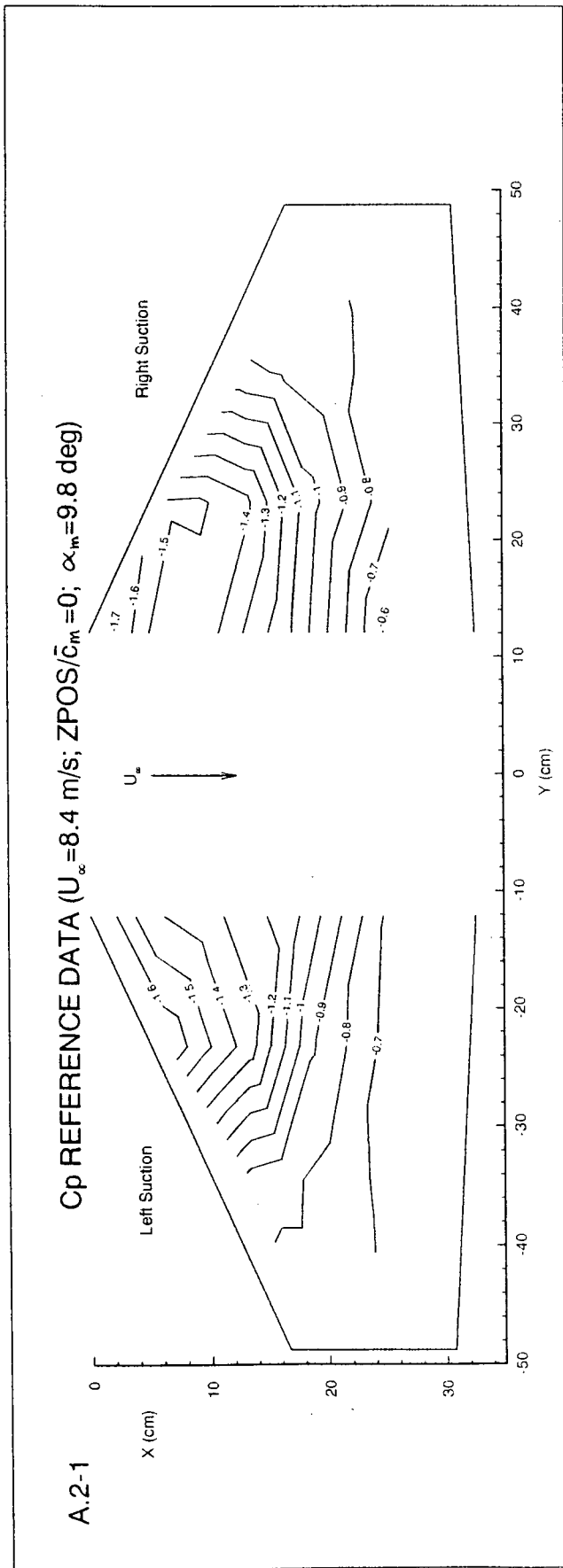
A.1-3 Cp REFERENCE DATA ($U_\infty = 16.8 \text{ m/s}$; $Z_{POS}/\bar{c}_m = 0$; $\alpha_m = 9.8 \text{ deg}$)

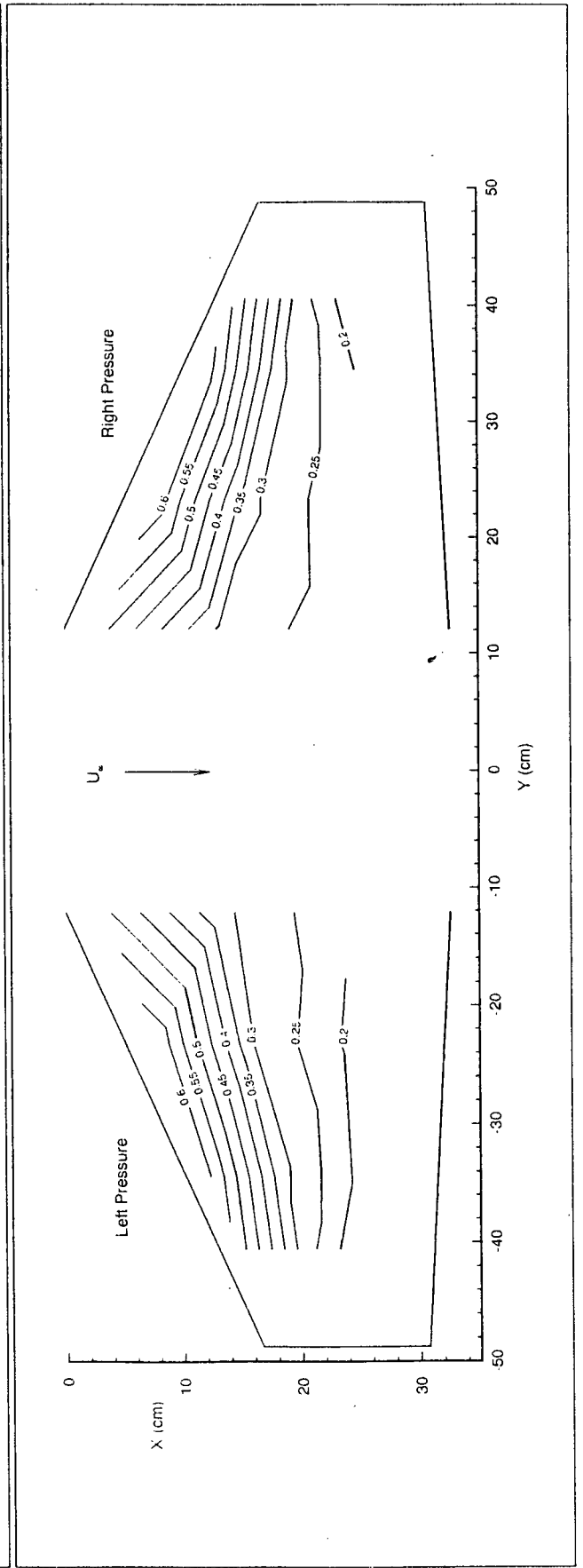
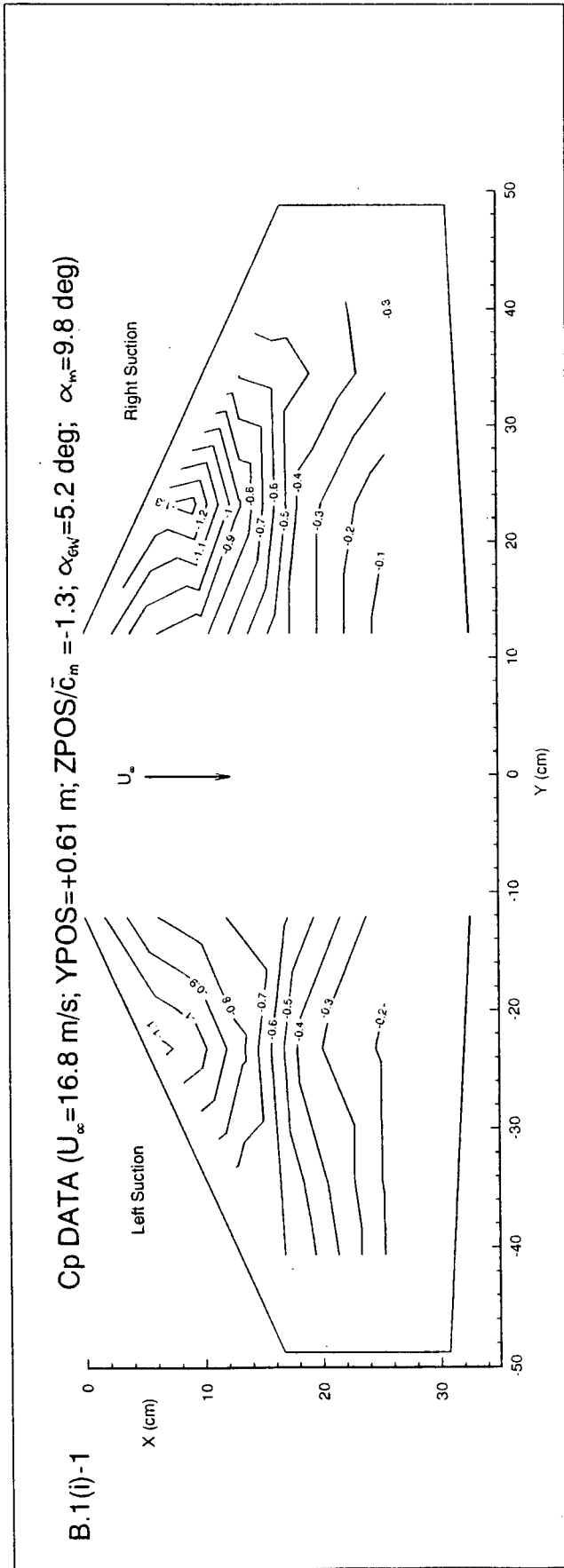




A.1-5 Cp REFERENCE DATA ($U_x = 16.8$ m/s; $ZPOS/\bar{c}_m = +1.3$; $\alpha_m = 9.8$ deg)

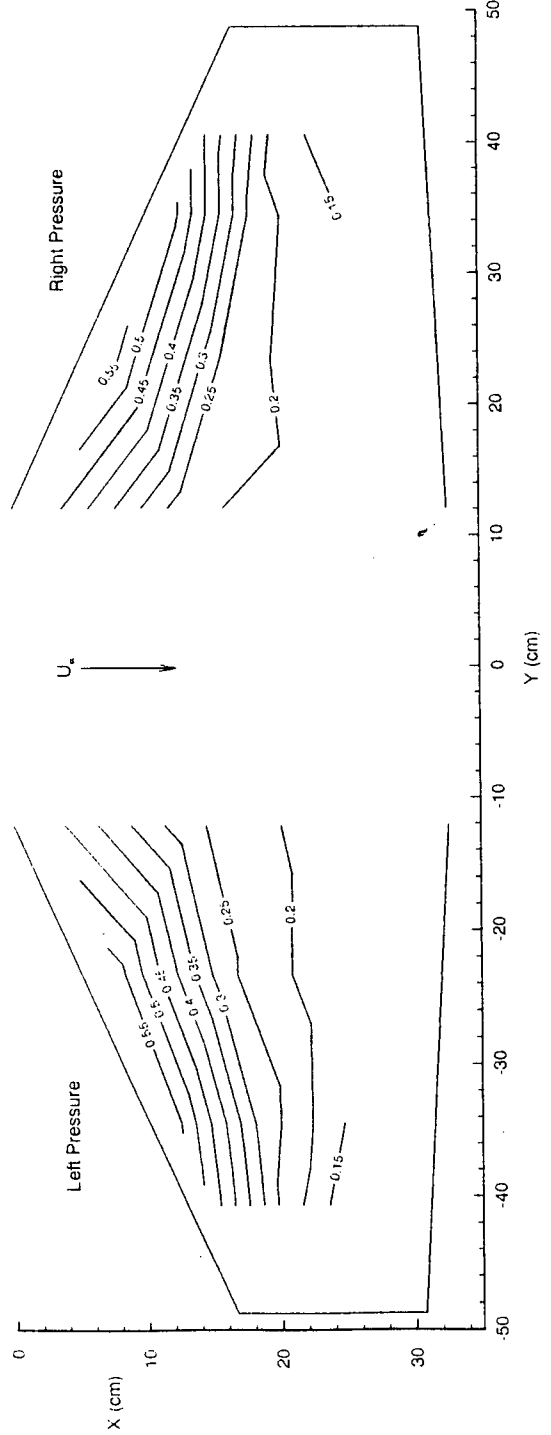
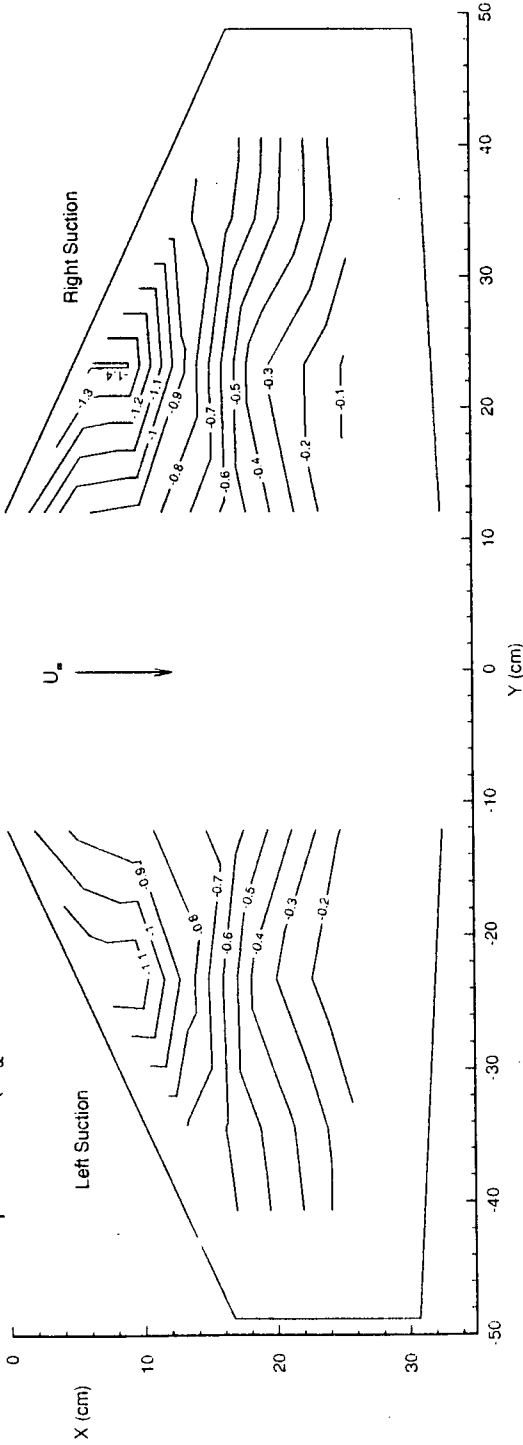






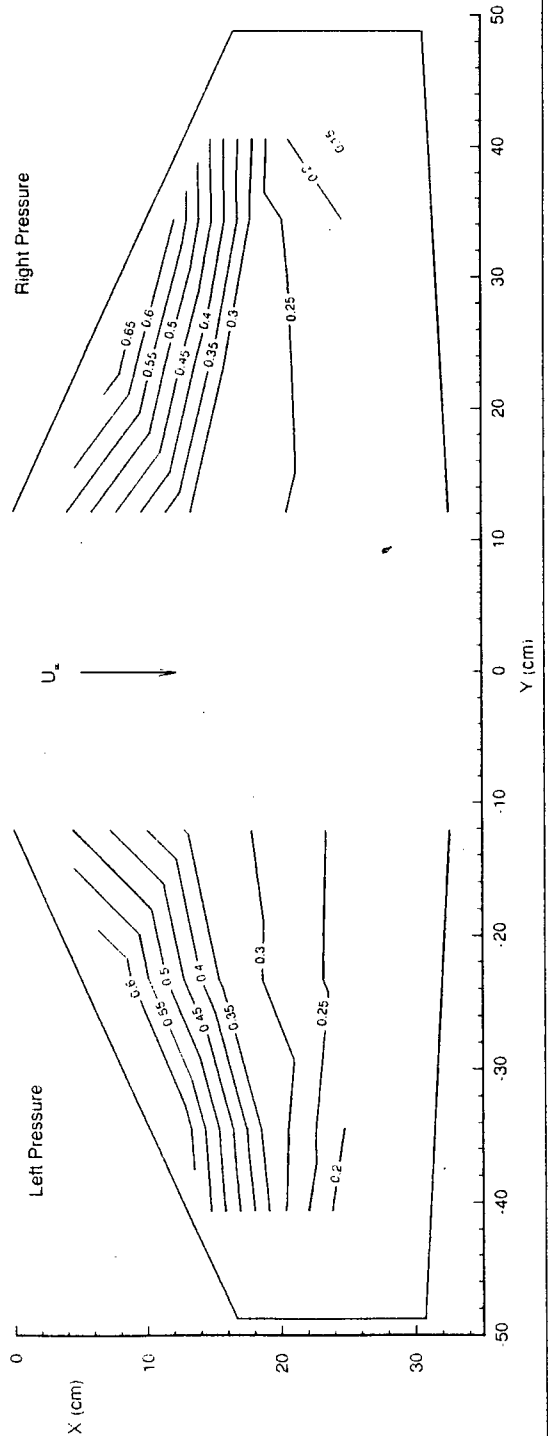
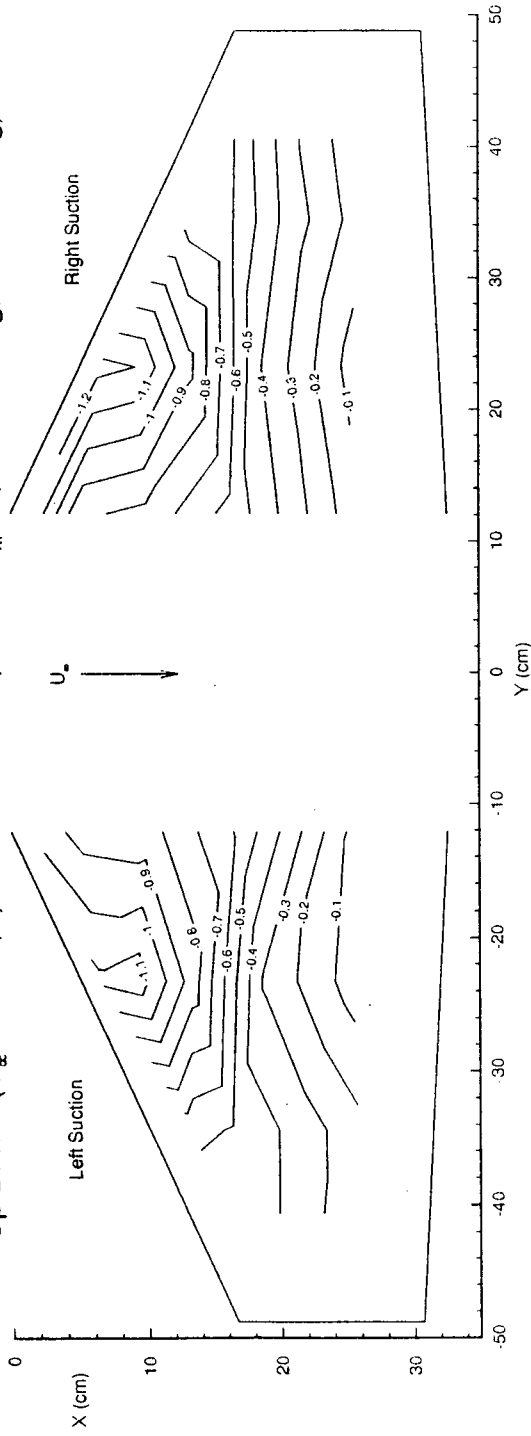
B.1(i)-2

Cp DATA ($U_\infty = 16.8$ m/s; YPOS = +0.61 m; ZPOS = +0.61 m; $\alpha_{eff} = 5.2$ deg; $\alpha_m = 9.8$ deg)



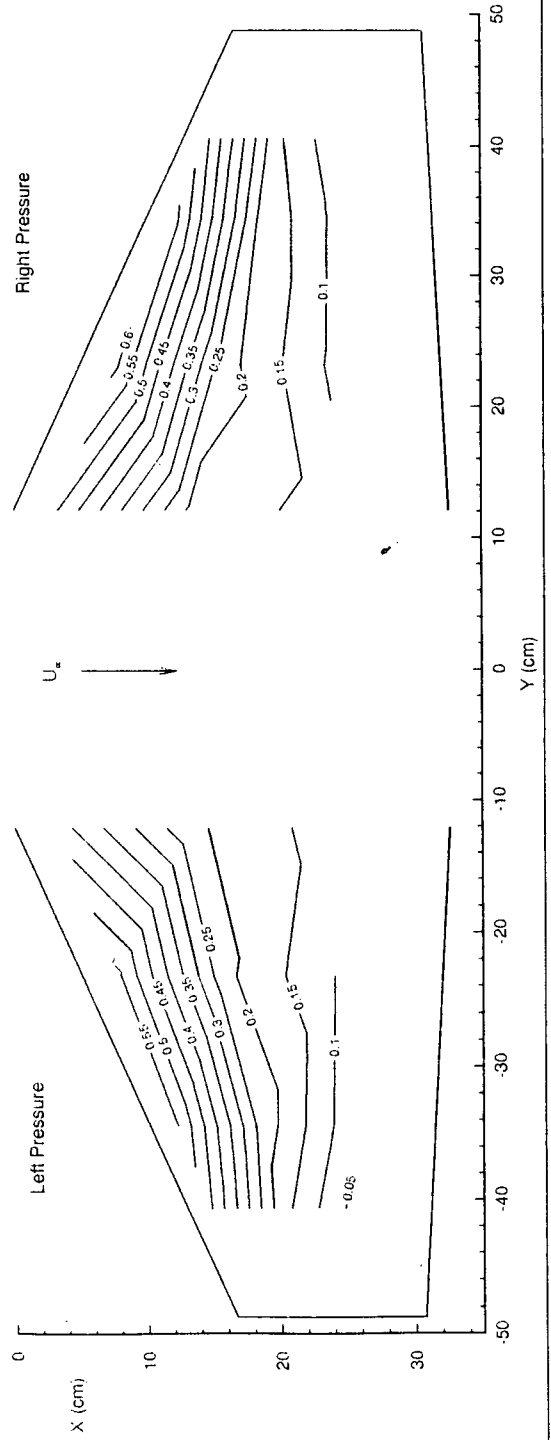
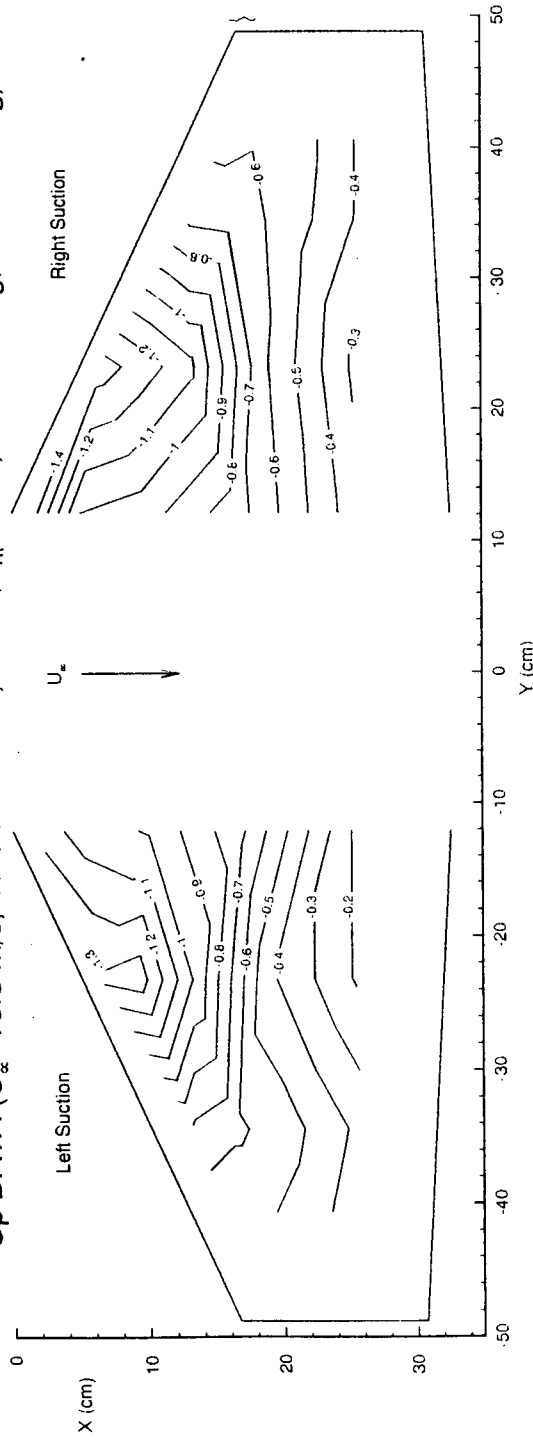
B.1(i)-3

Cp DATA ($U_\infty = 16.8$ m/s; $YPOS = +0.61$ m; $ZPOS = 0$; $\alpha_{6W} = 5.2$ deg; $\alpha_m = 9.8$ deg)

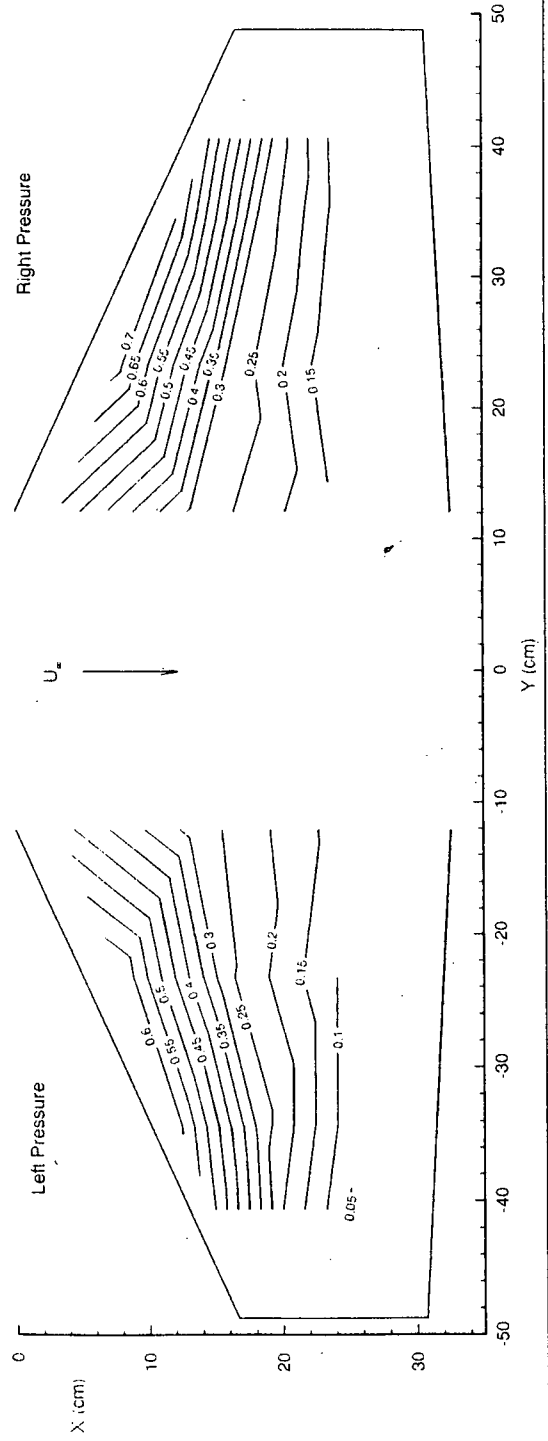
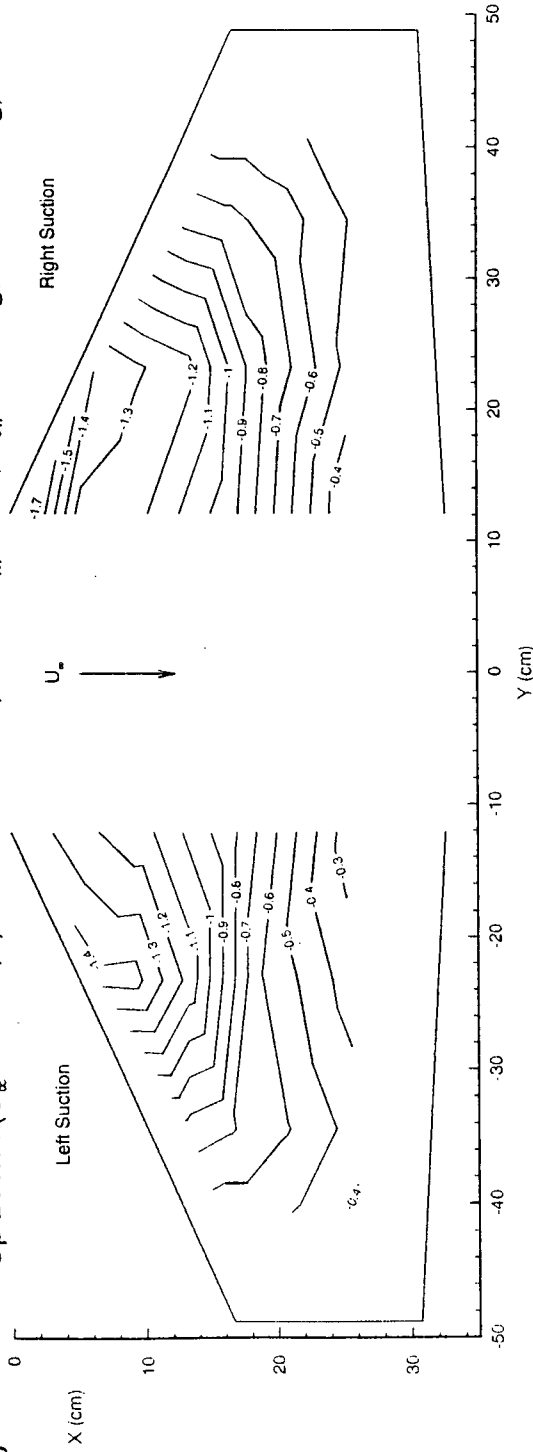


B.1(i)-4

Cp DATA ($U_\infty = 16.8$ m/s; $YPOS = -0.61$ m; $ZPOS/\bar{C}_m = +0.5$; $\alpha_{6H} = 5.2$ deg; $\alpha_m = 9.8$ deg)

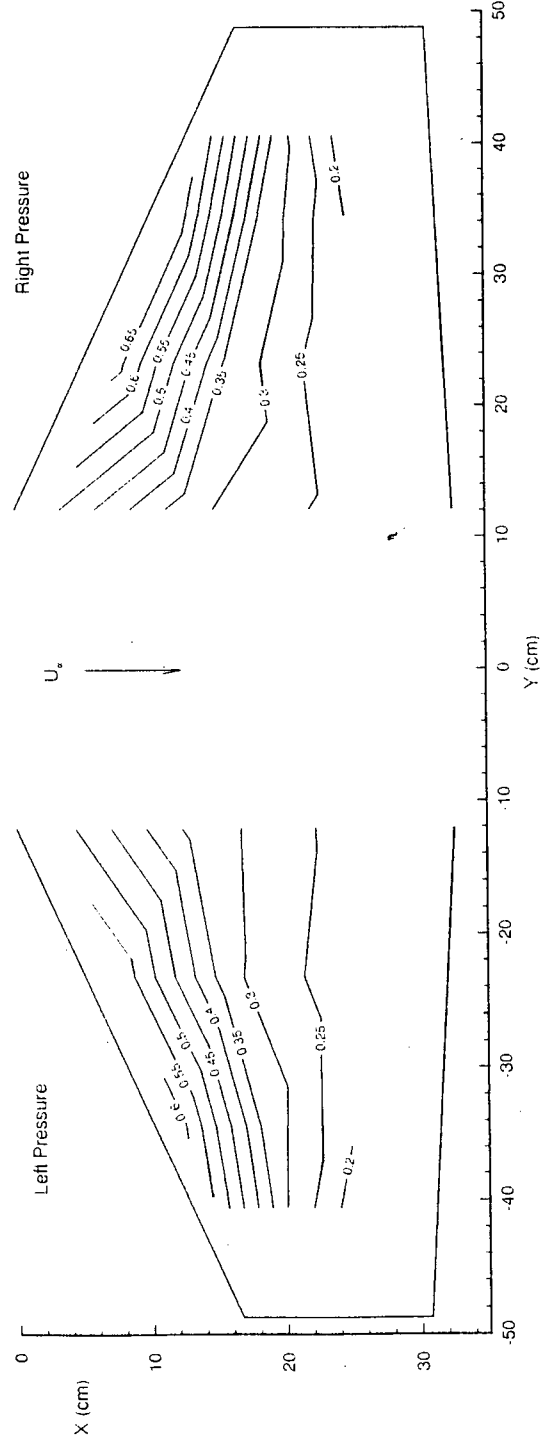
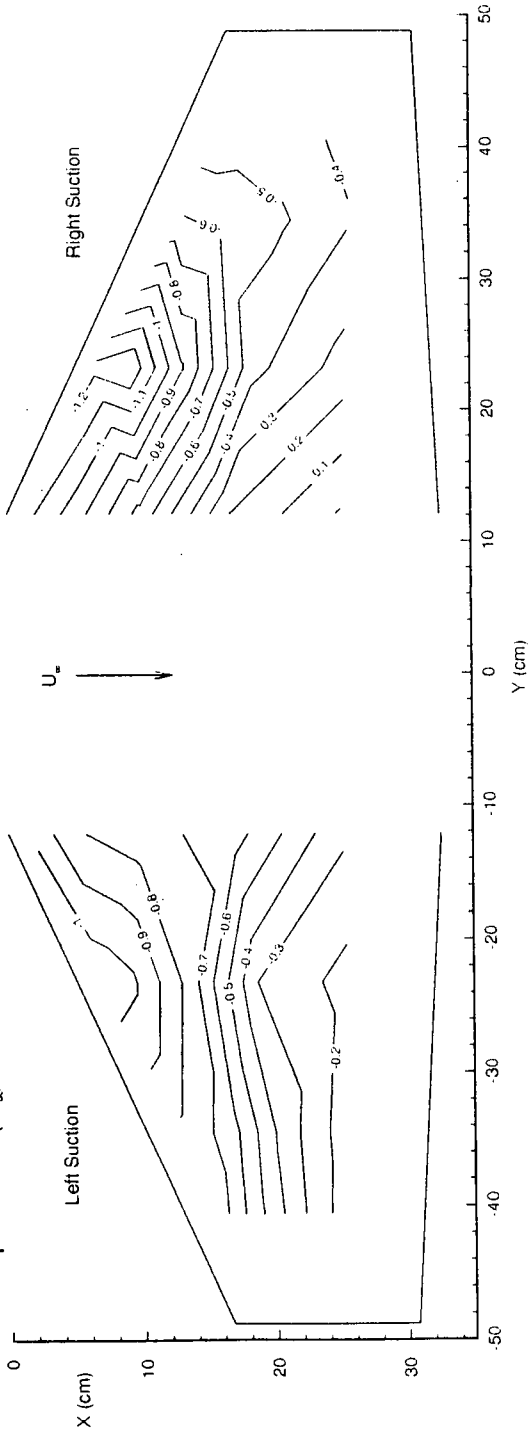


B.1(i)-5 Cp DATA ($U_\alpha = 16.4$ m/s; $YPOS = +0.61$ m; $ZPOS/\bar{c}_m = +1.3$; $\alpha_{6W} = 5.2$ deg; $\alpha_m = 9.8$ deg)

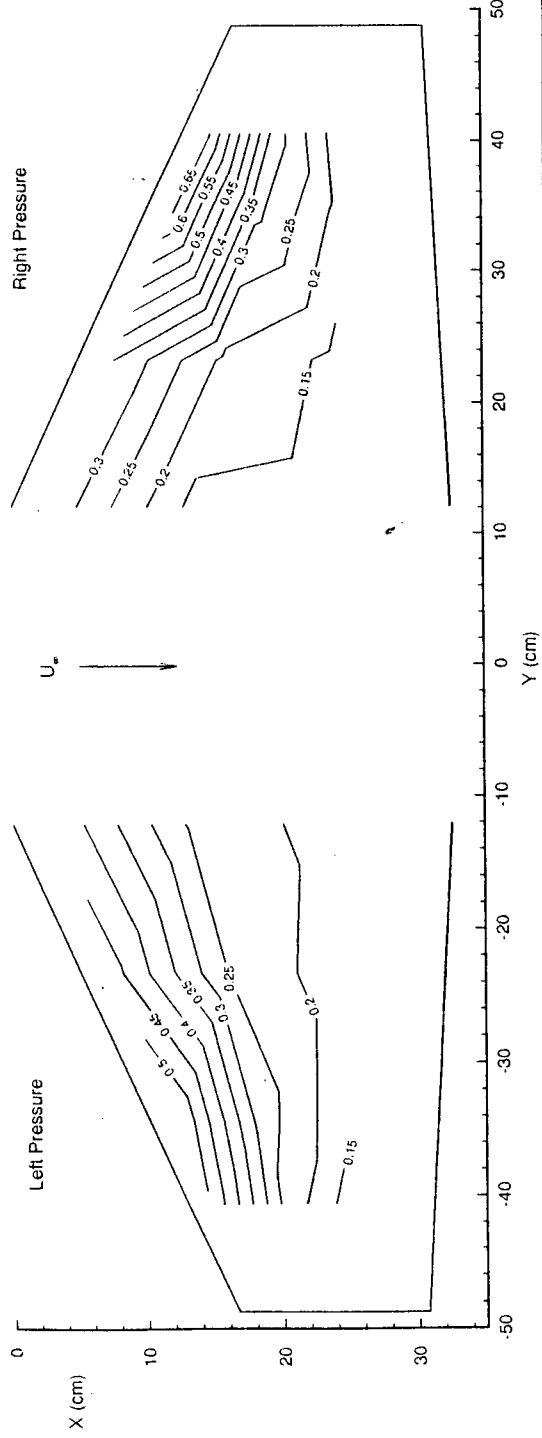
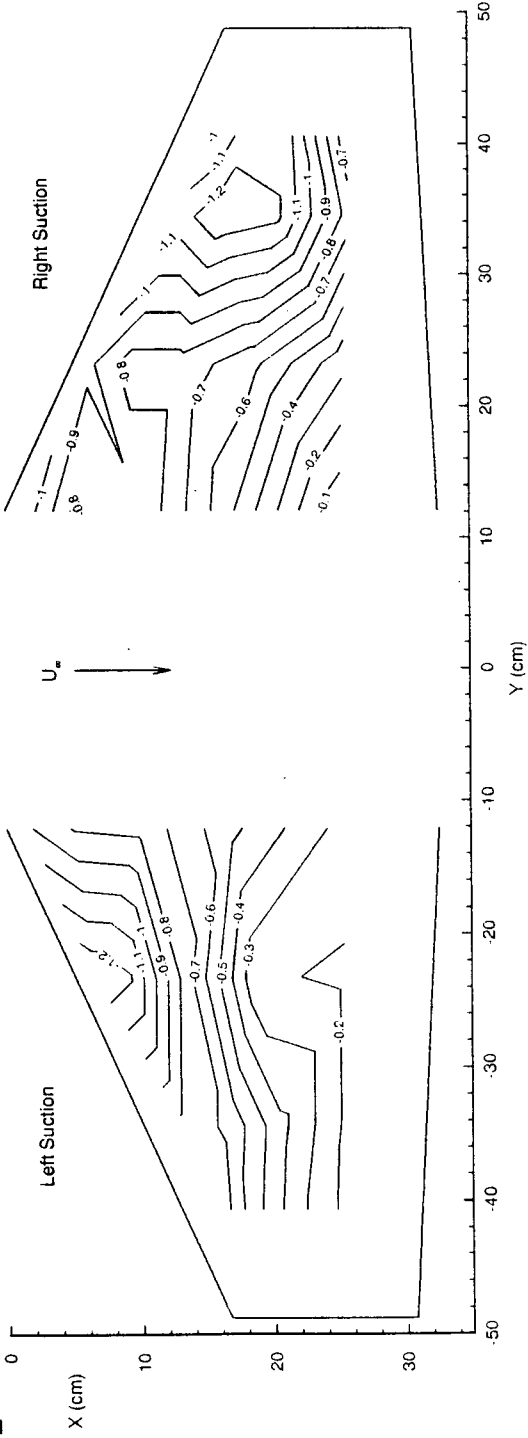


B.1(ii)-1

Cp DATA ($U_\infty = 16.8$ m/s; $YPOS = +0.305$ m; $ZPOS = -1.3$; $\alpha_{6M} = 5.2$ deg; $\alpha_m = 9.8$ deg)

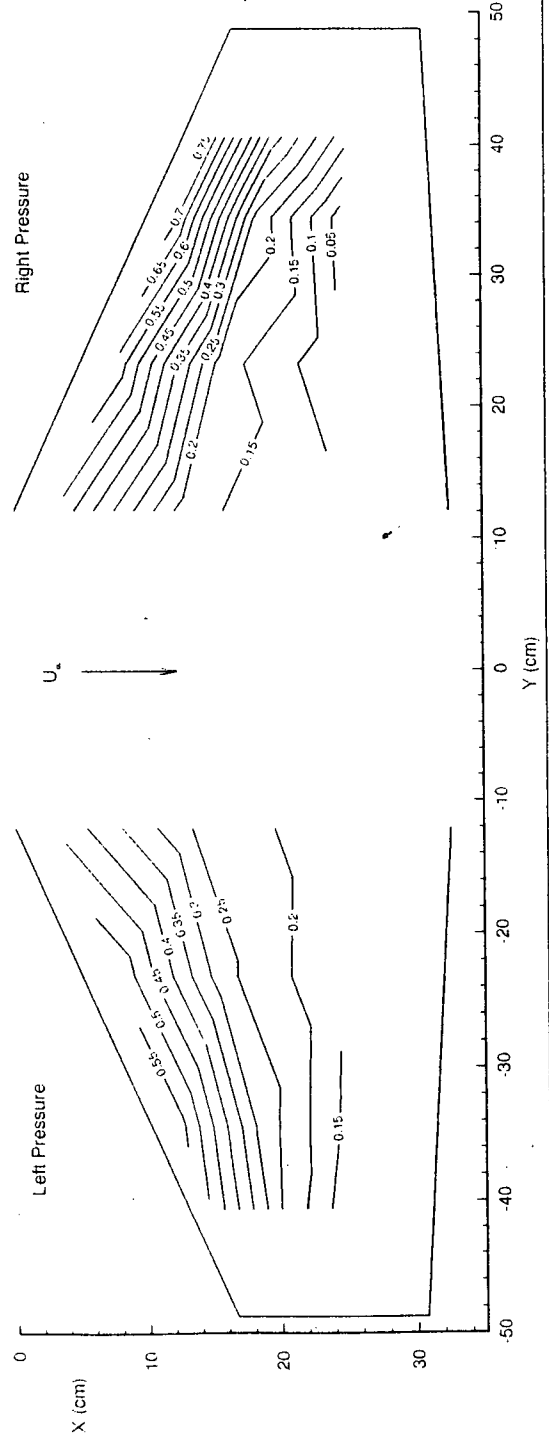
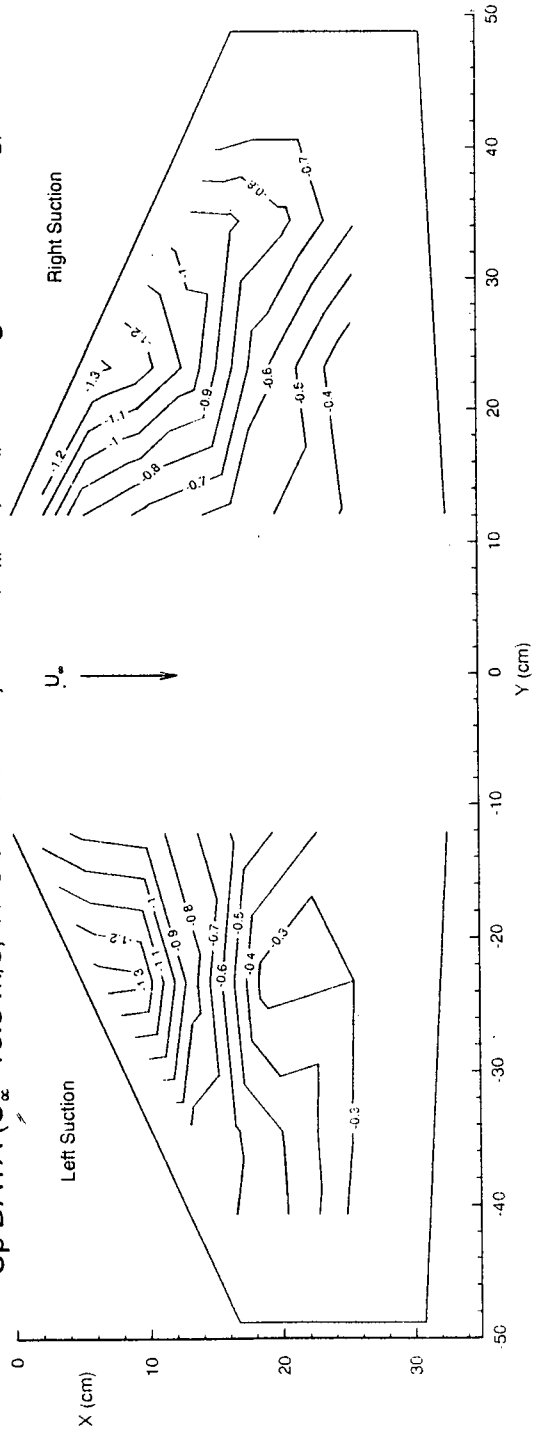


B.1(ii)-2 Cp DATA ($U_\infty = 16.8$ m/s; $YPOS = +0.305$ m; $ZPOS/\bar{c}_m = -0.5$; $\alpha_{GW} = 5.2$ deg; $\alpha_m = 9.8$ deg)

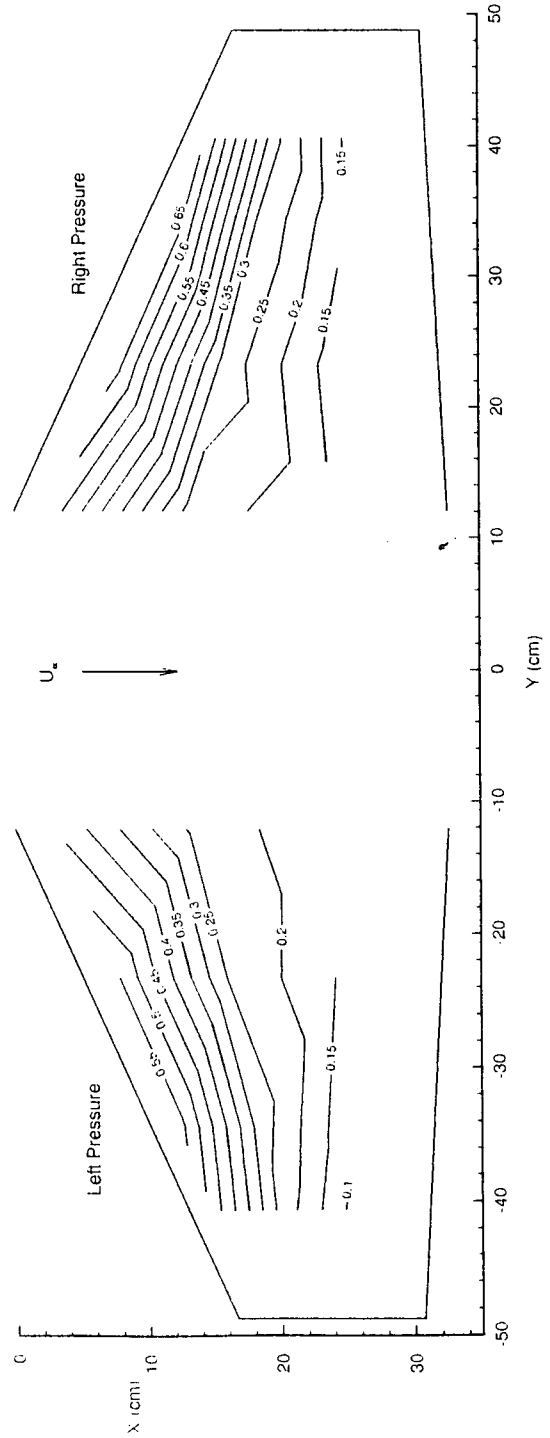
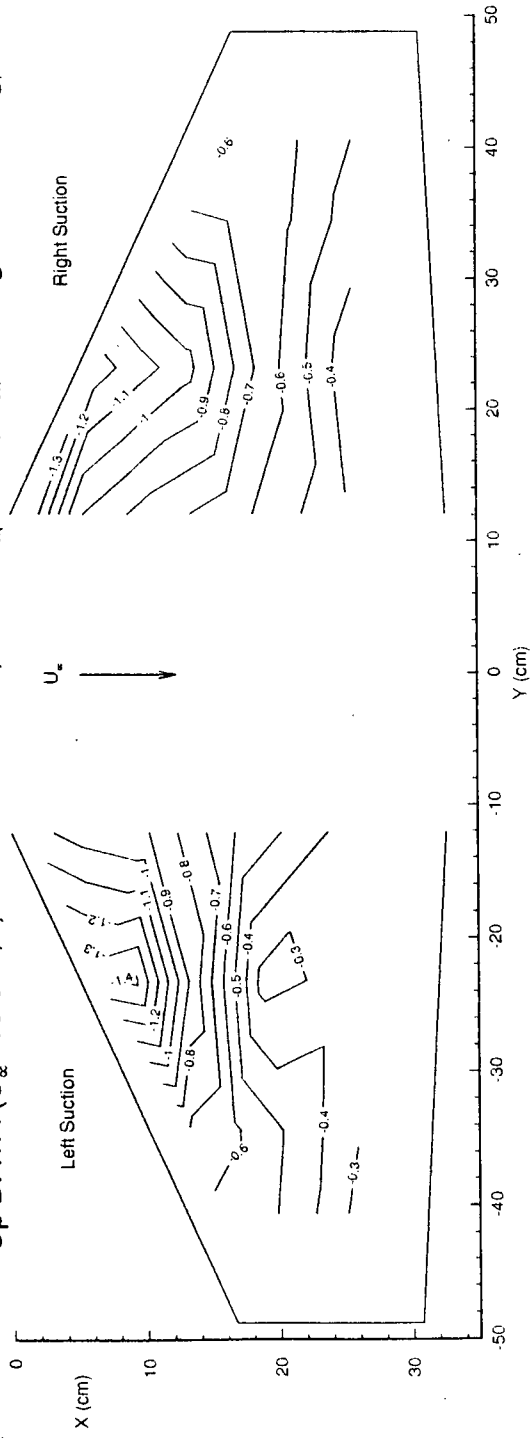


B.1 (ii)-3

Cp DATA ($U_\infty = 16.8$ m/s; $YPOS = +0.305$ m; $ZPOS = 0$; $\alpha_{SM} = 5.2$ deg; $\alpha_m = 9.8$ deg)

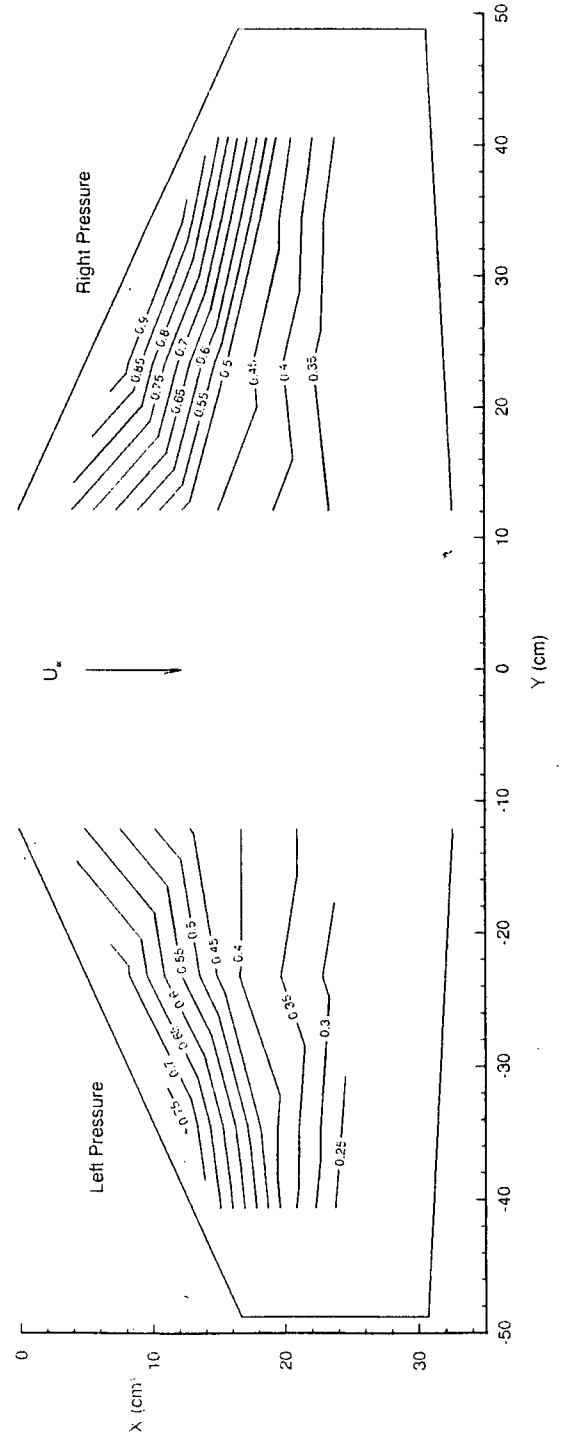
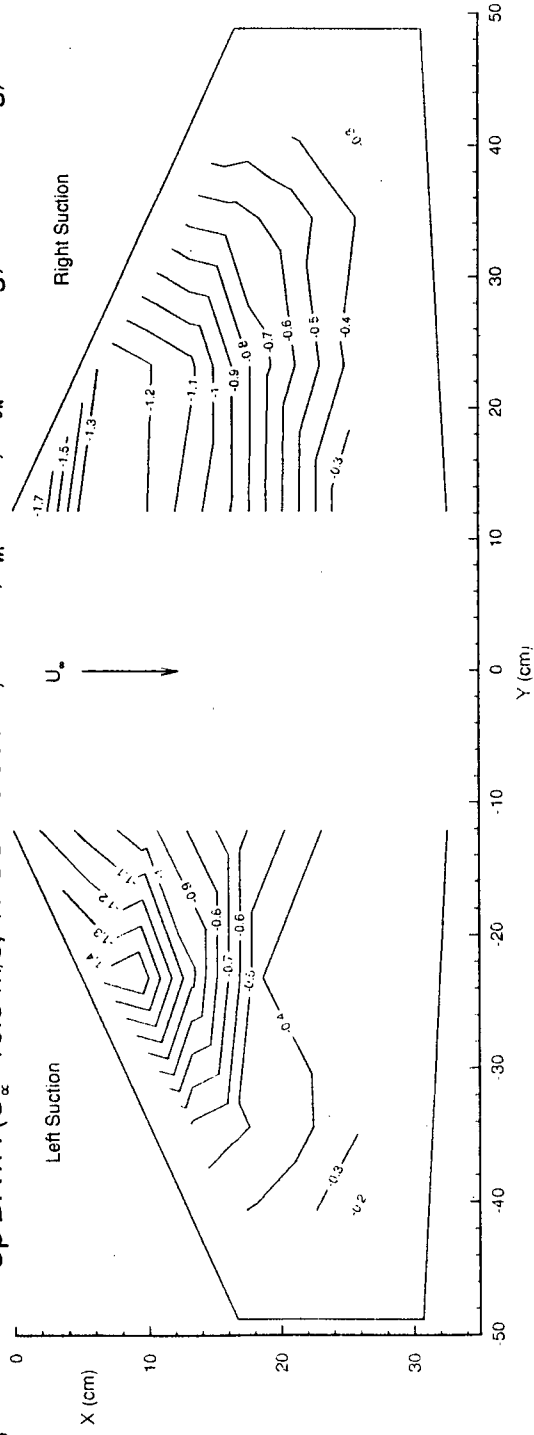


B.1(ii)-4 Cp DATA ($U_\infty = 16.8$ m/s; $YPOS = +0.305$ m; $ZPOS/\bar{C}_m = +0.5$; $\alpha_{6.1} = 5.2$ deg; $\alpha_m = 9.8$ deg)



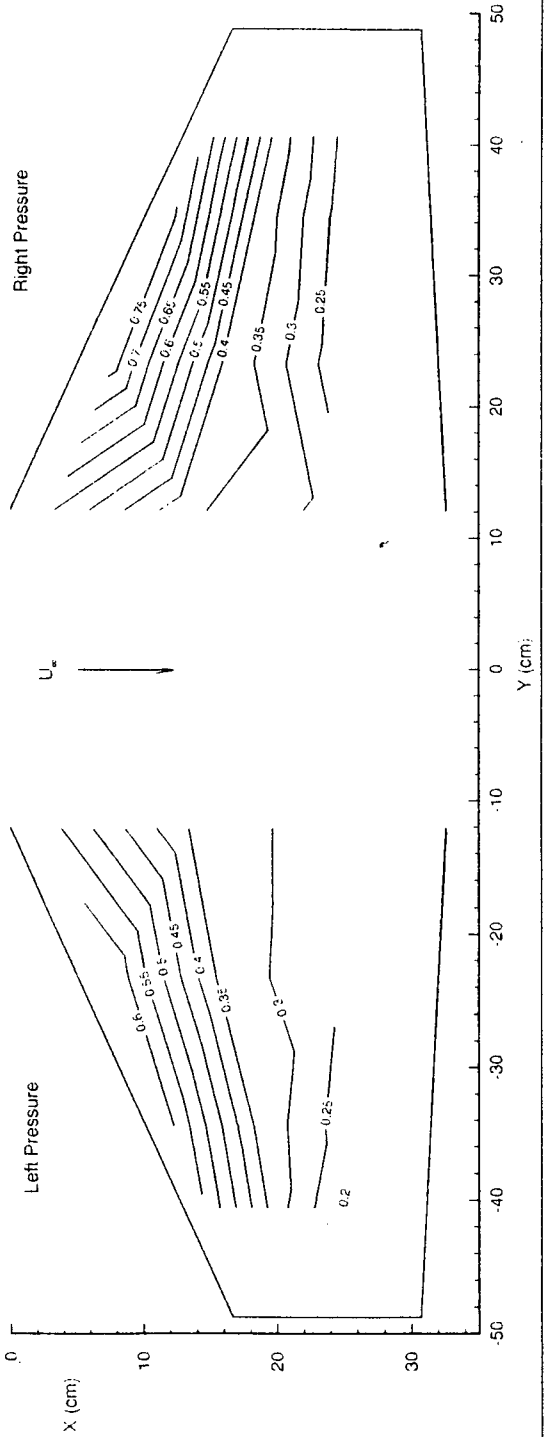
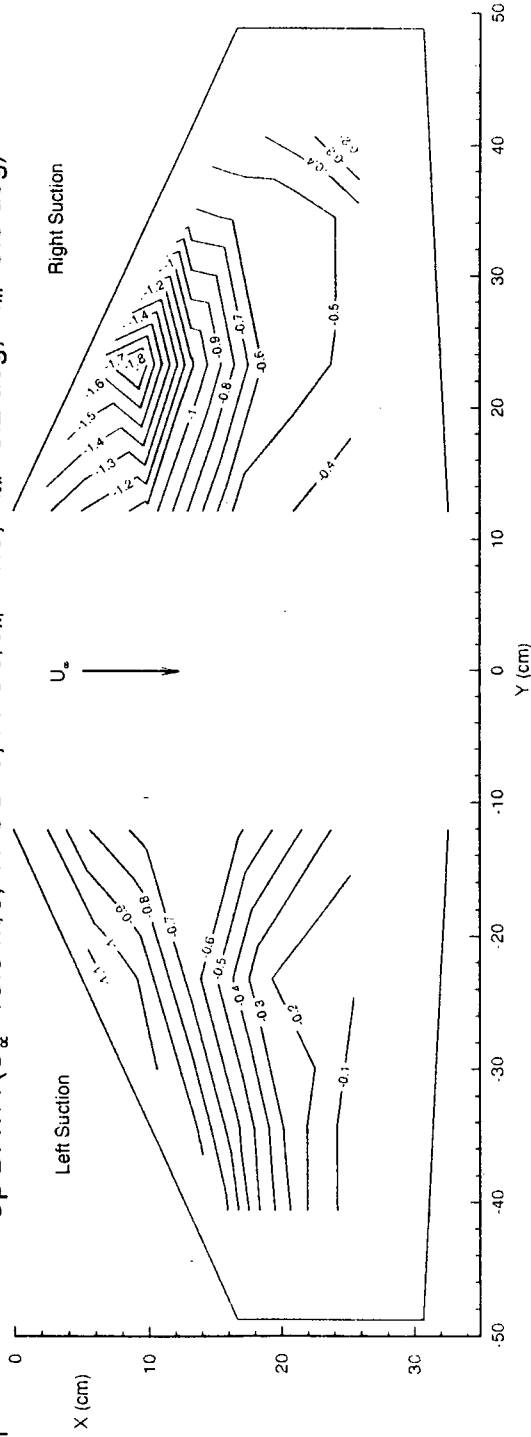
B.1(ii)-5

Cp DATA ($U_\infty = 16.8$ m/s; $YPOS = +0.305$ m; $ZPOS/\bar{c}_m = +1.3$; $\alpha_{6N} = 5.2$ deg; $\alpha_m = 9.8$ deg)



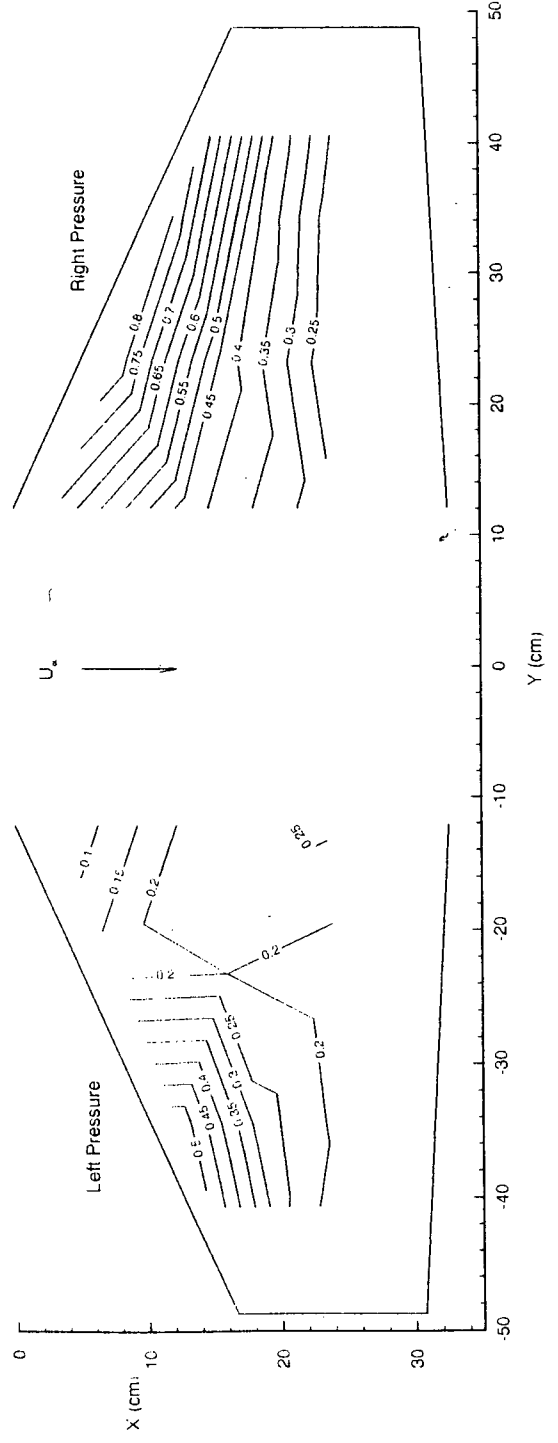
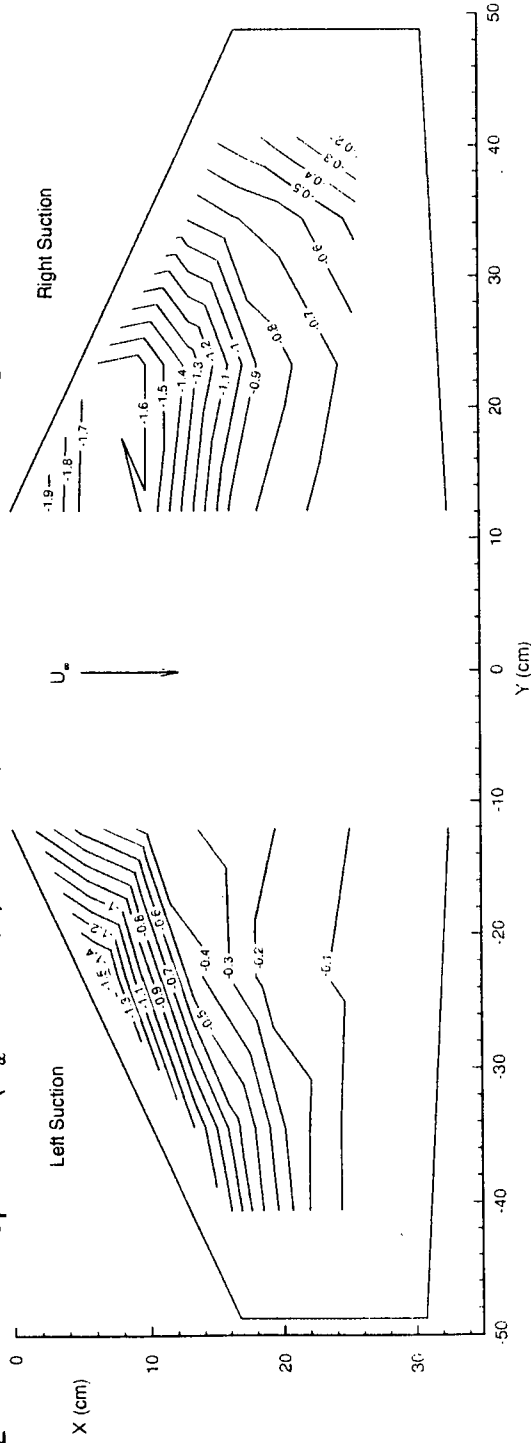
B.1 (iii) -1

Cp DATA ($U_\infty = 16.8$ m/s; $YPOS=0$; $ZPOS=0$; $ZPOS/c_m = -1.3$; $\alpha_{64} = 5.2$ deg; $\alpha_m = 9.8$ deg)



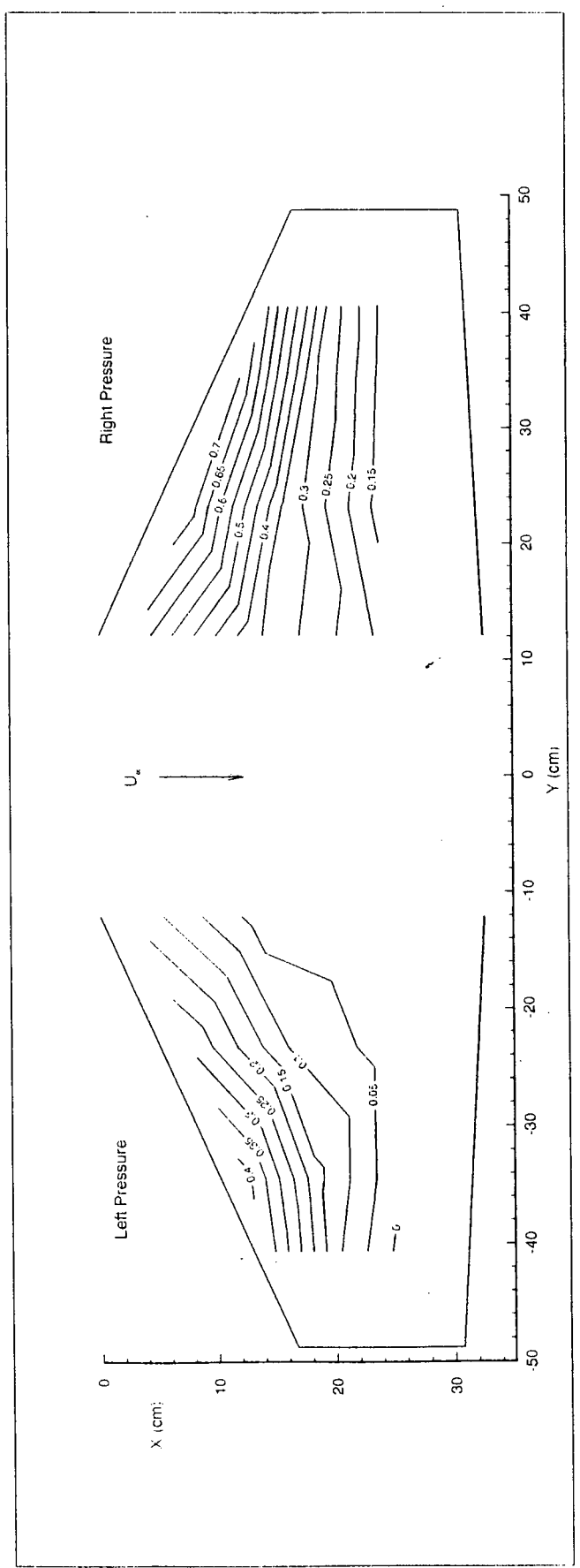
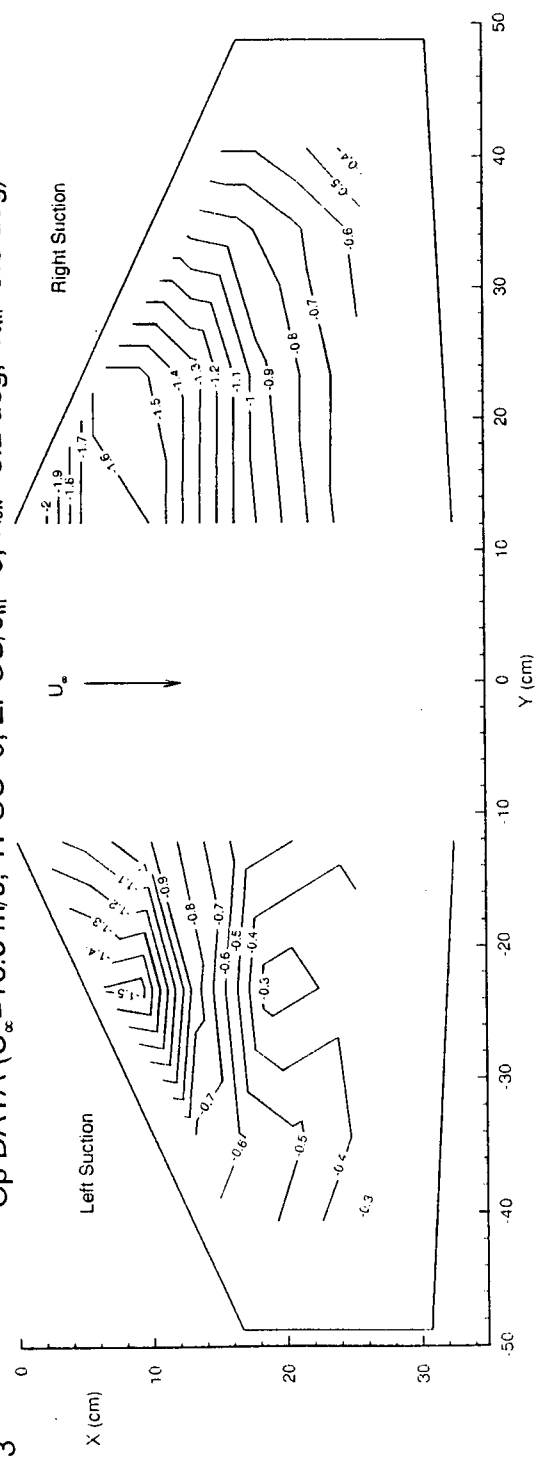
B.1(iii)-2

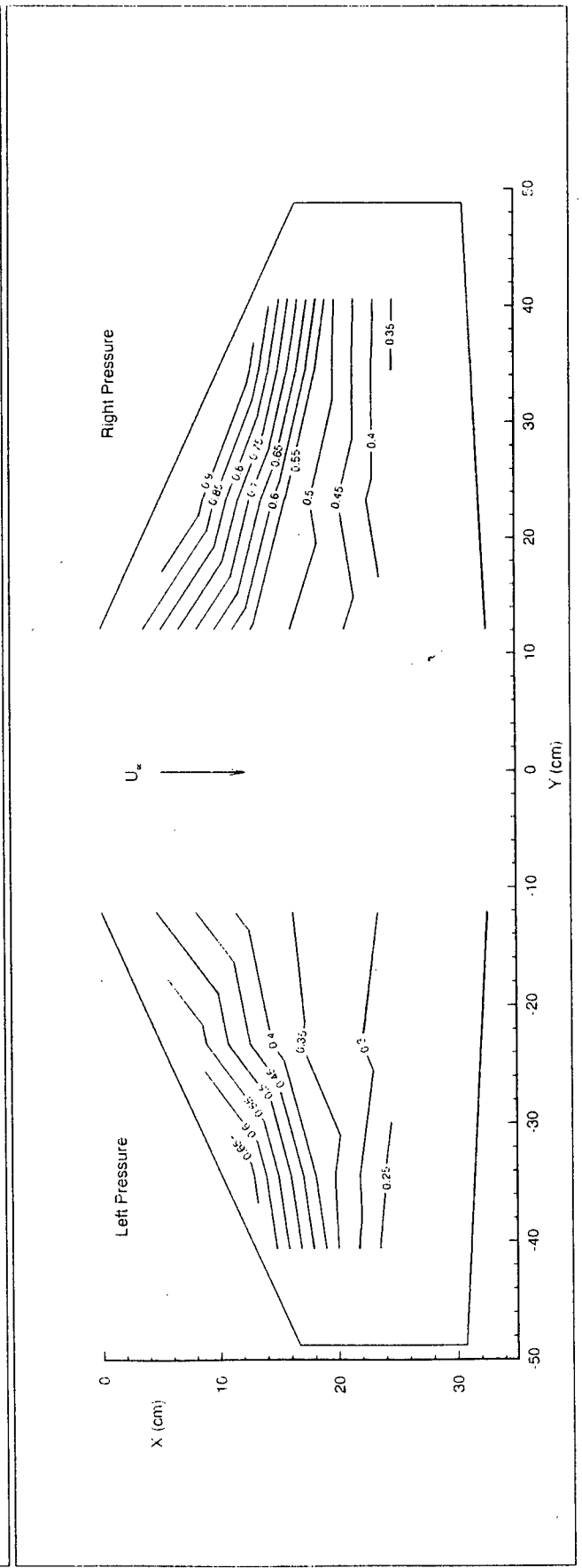
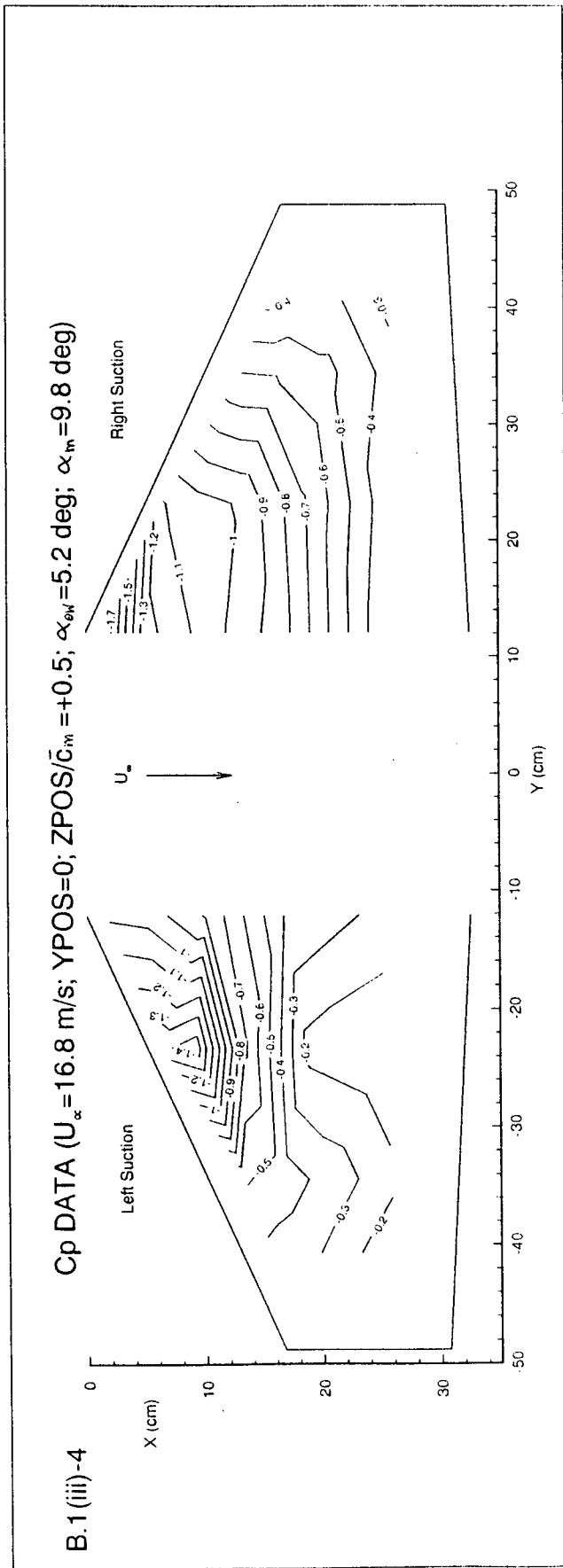
Cp DATA ($U_\infty = 16.8$ m/s; $Y_{POS} = 0$; $Z_{POS} = 0$; $\alpha_{EM} = -0.5$; $\alpha_{EW} = 5.2$ deg; $\alpha_m = 9.8$ deg)



Cp DATA ($U_\infty = 16.8$ m/s; $YPOS=0$; $ZPOS=0$; $\alpha_{GM} = 5.2$ deg; $\alpha_m = 9.8$ deg)

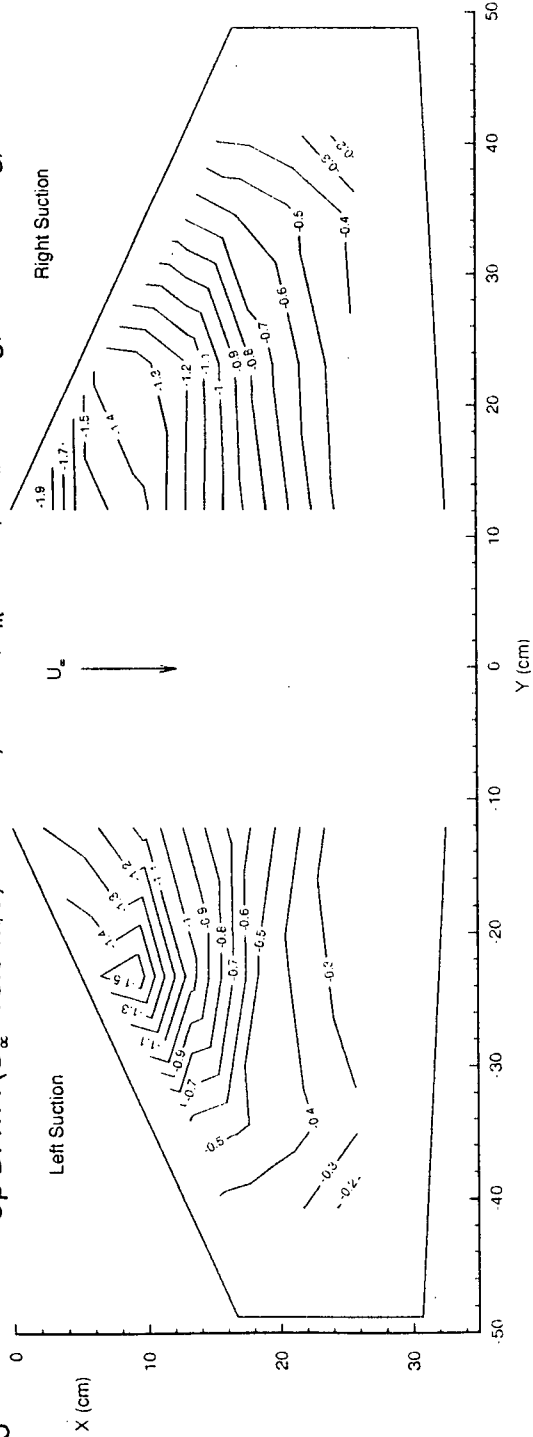
B.1 (iii) -3



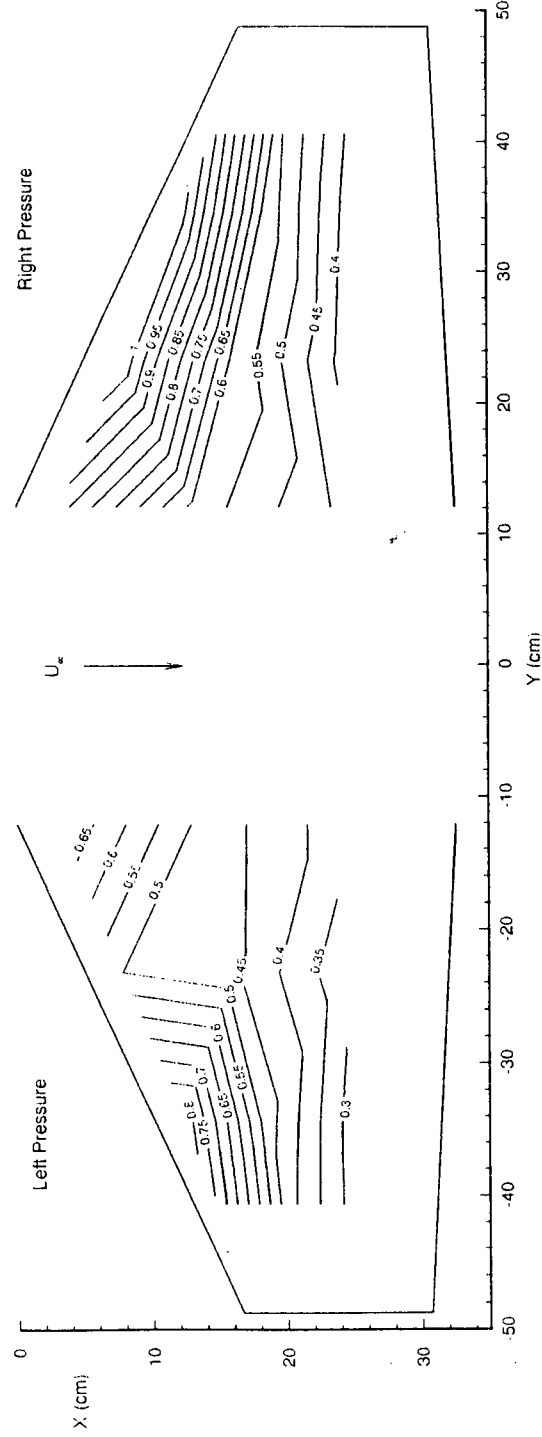


B.1 (iii) -5

Cp DATA ($U_\infty = 16.8$ m/s; $YPOS = 0$; $ZPOS = 0$; $\alpha_{eff} = 5.2$ deg; $\alpha_m = 9.8$ deg)

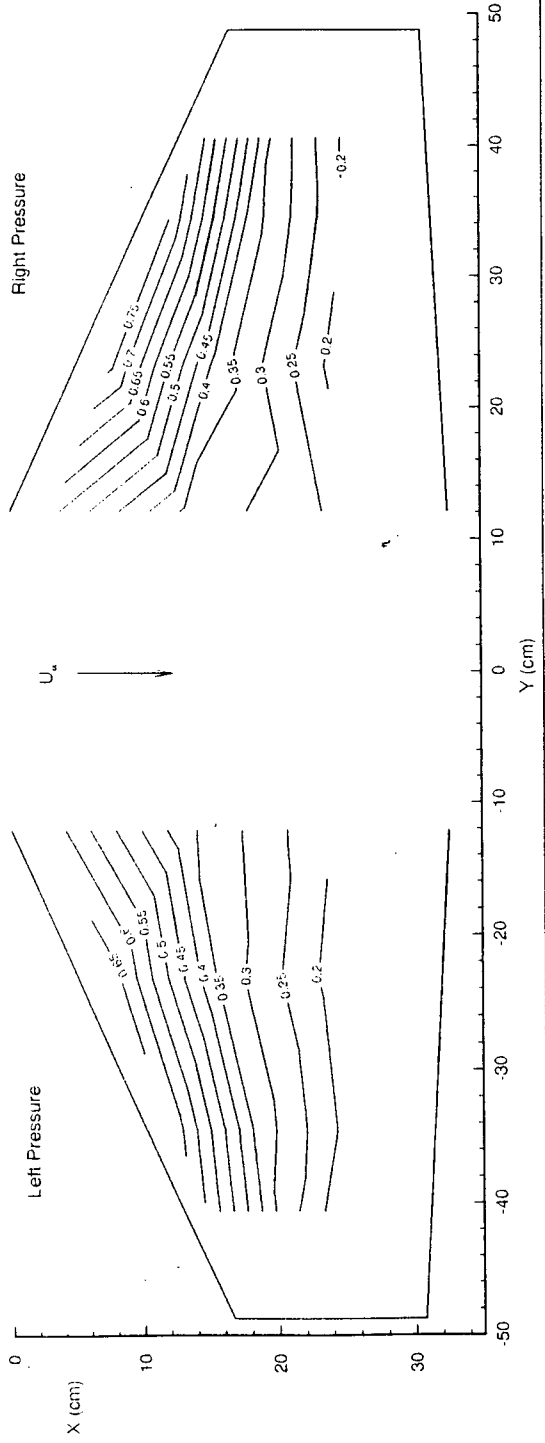
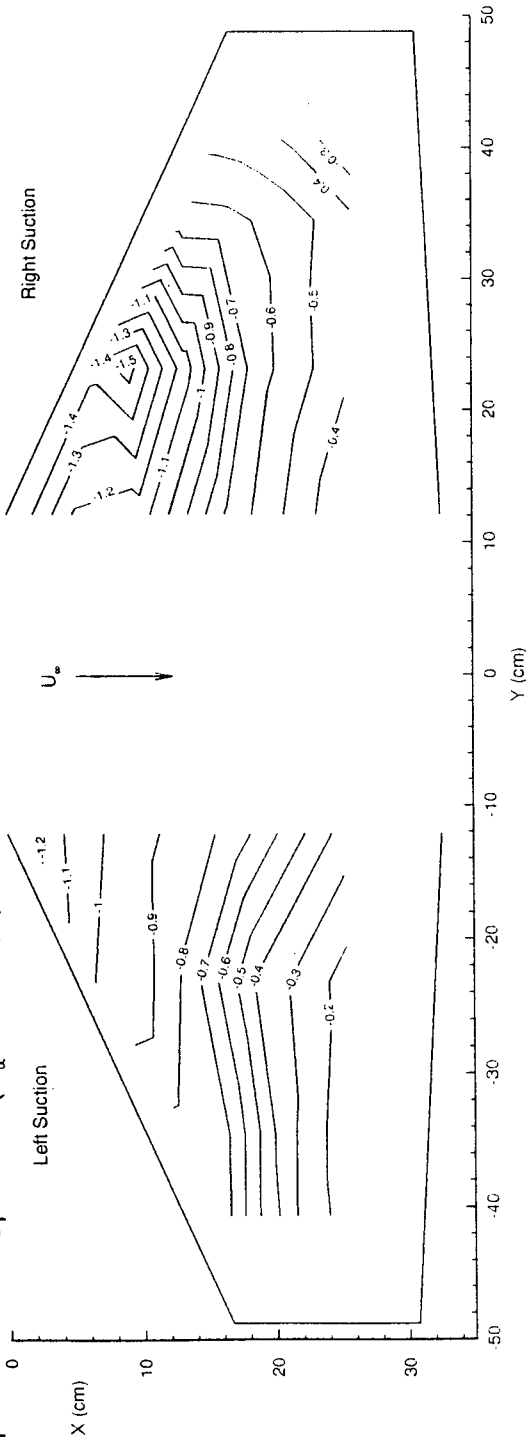


Left Pressure

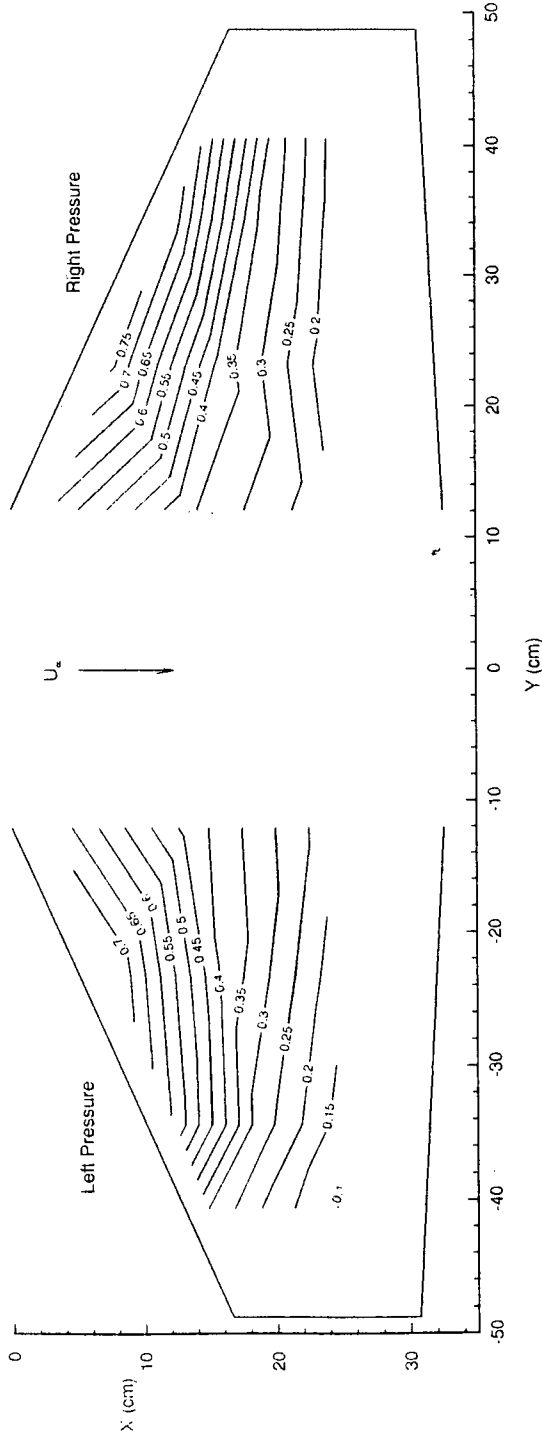
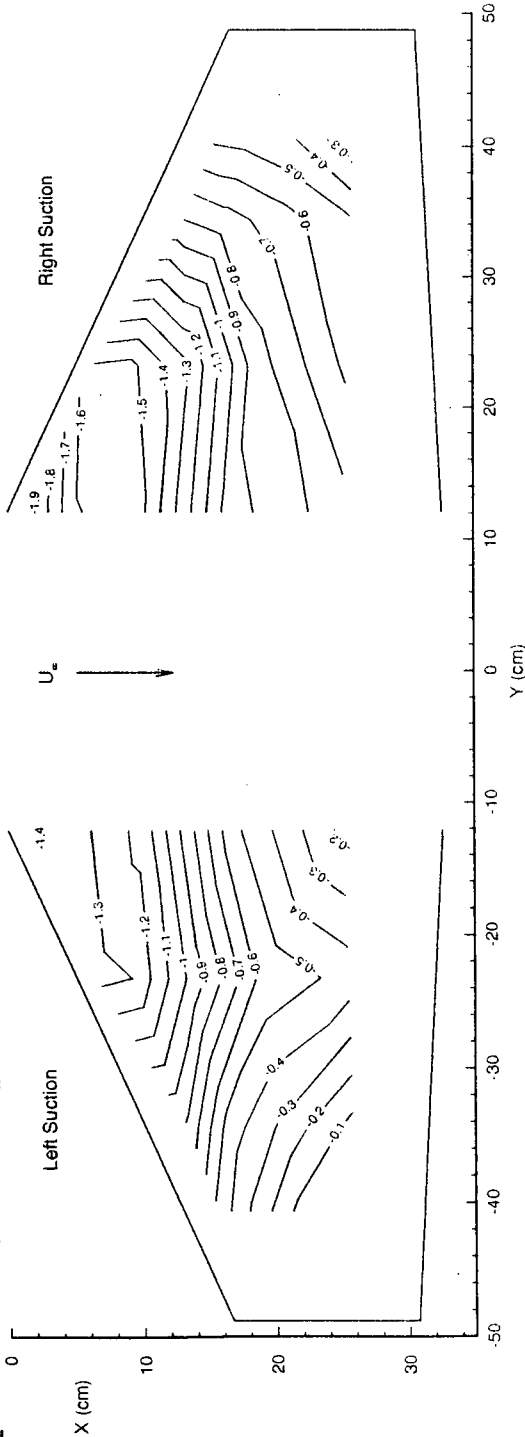


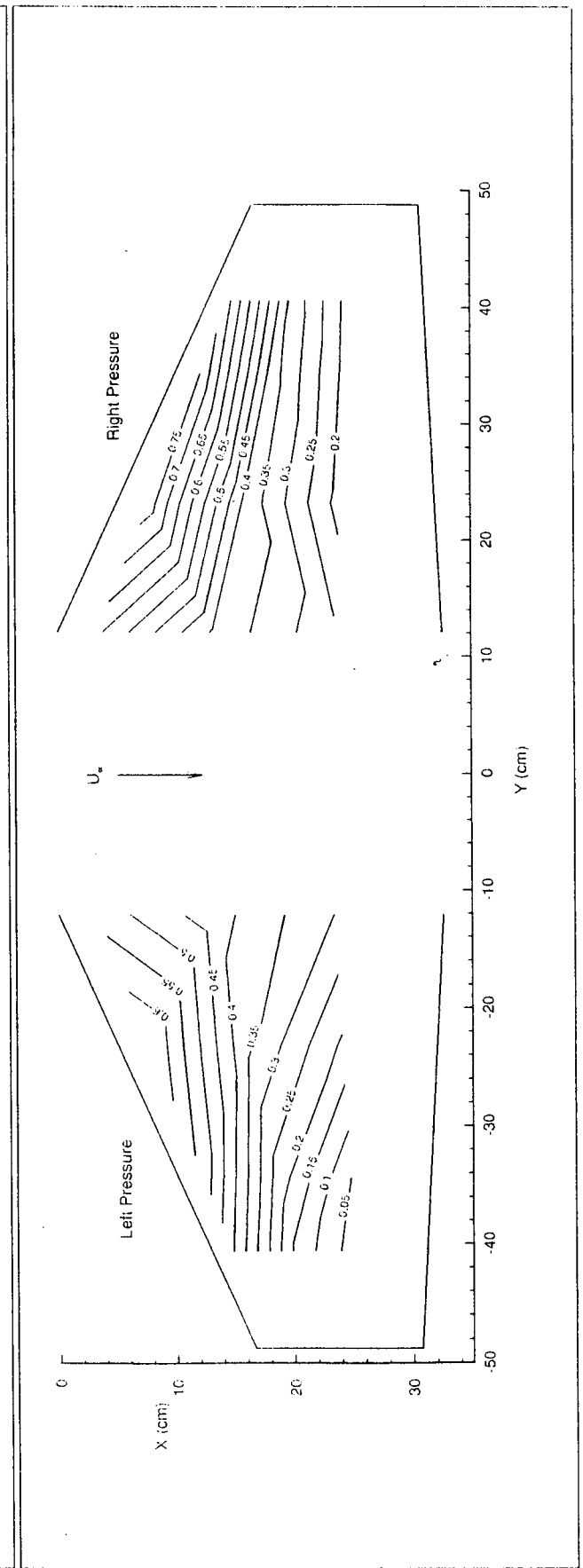
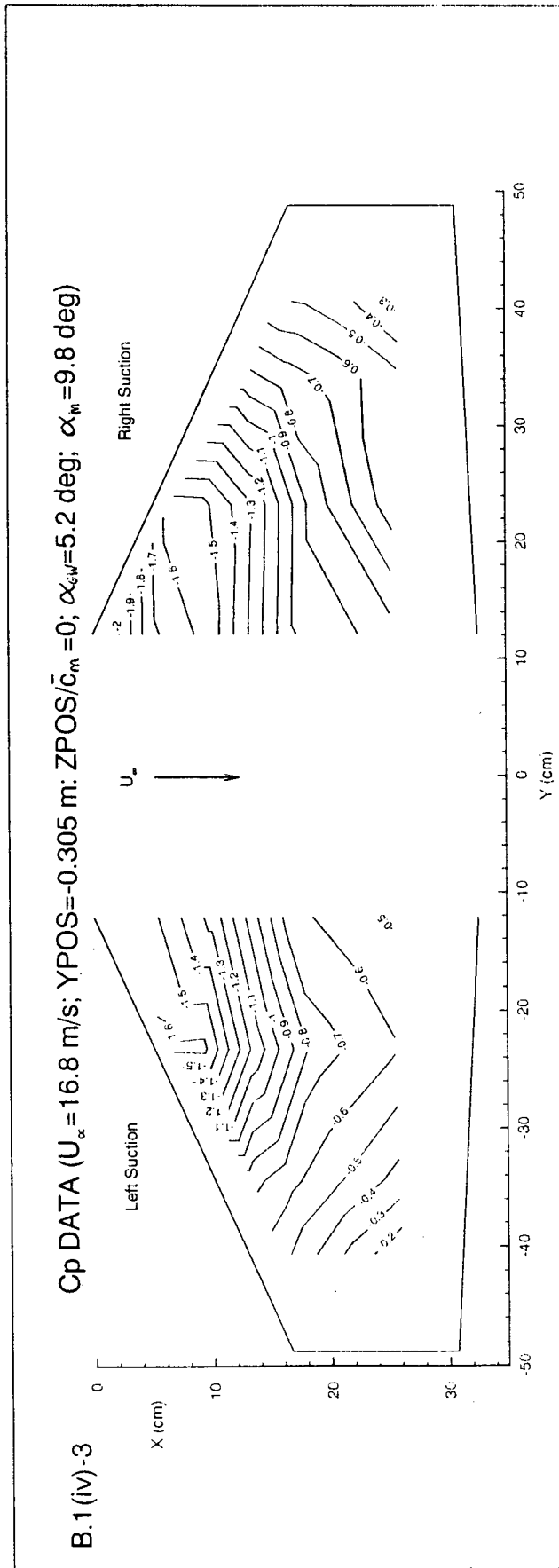
B.1(iv)-1

Cp DATA ($U_\infty = 16.8$ m/s; $YPOS = -0.305$ m; $ZPOS = -1.3$; $\alpha_{cav} = 5.2$ deg; $\alpha_m = 9.8$ deg)



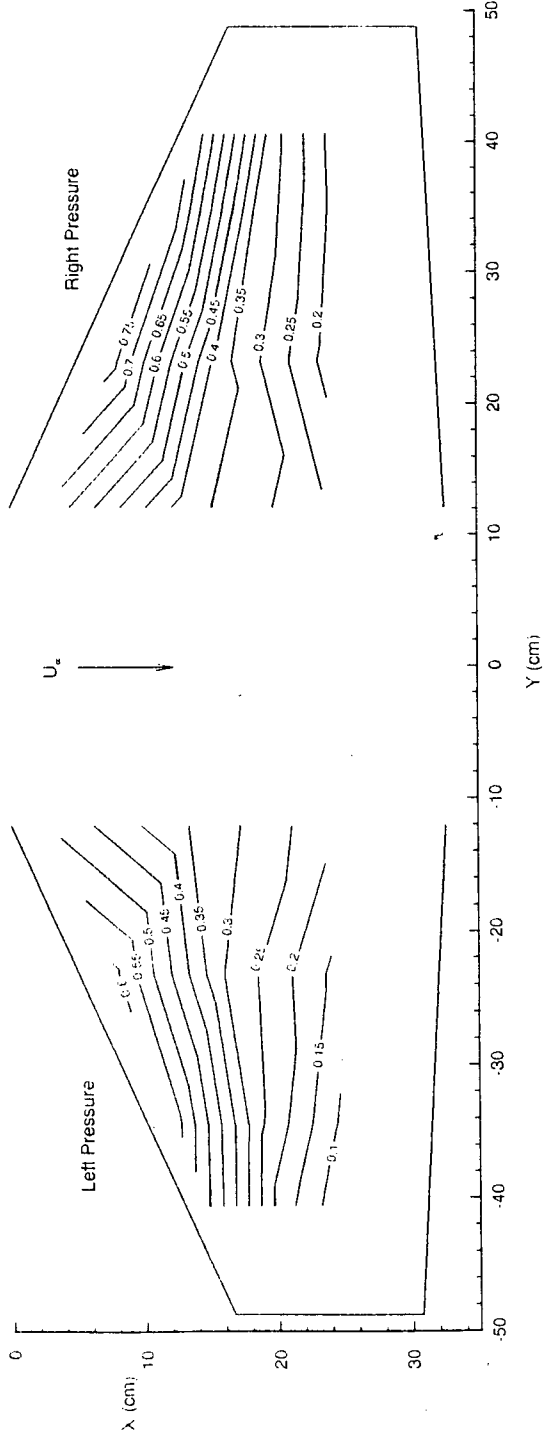
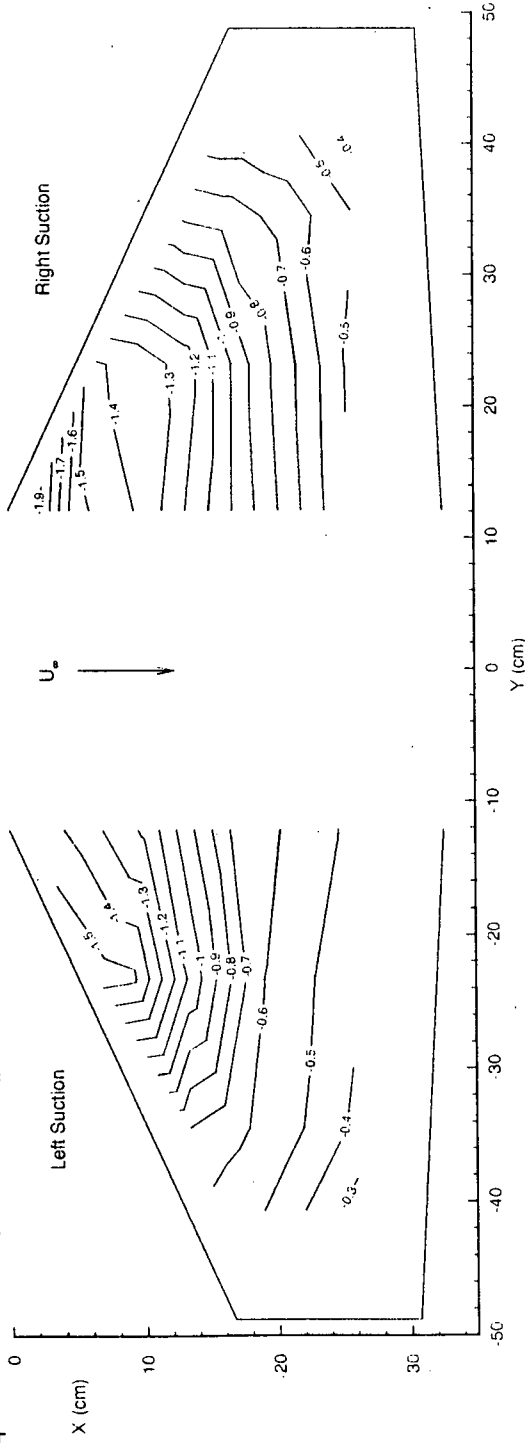
B.1 (iv)-2 Cp DATA ($U_\infty = 16.8$ m/s; $YPOS = -0.305$ m; $ZPOS/\bar{c}_m = -0.5$; $\alpha_{6W} = 5.2$ deg; $\alpha_{m1} = 9.8$ deg)



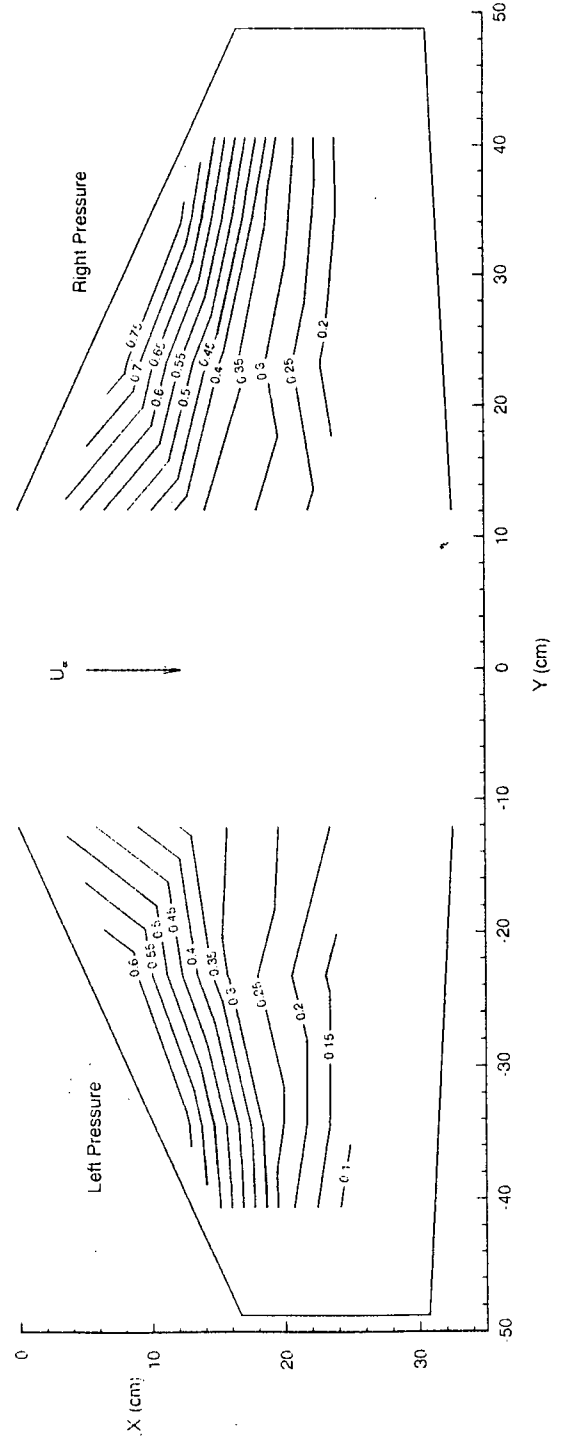
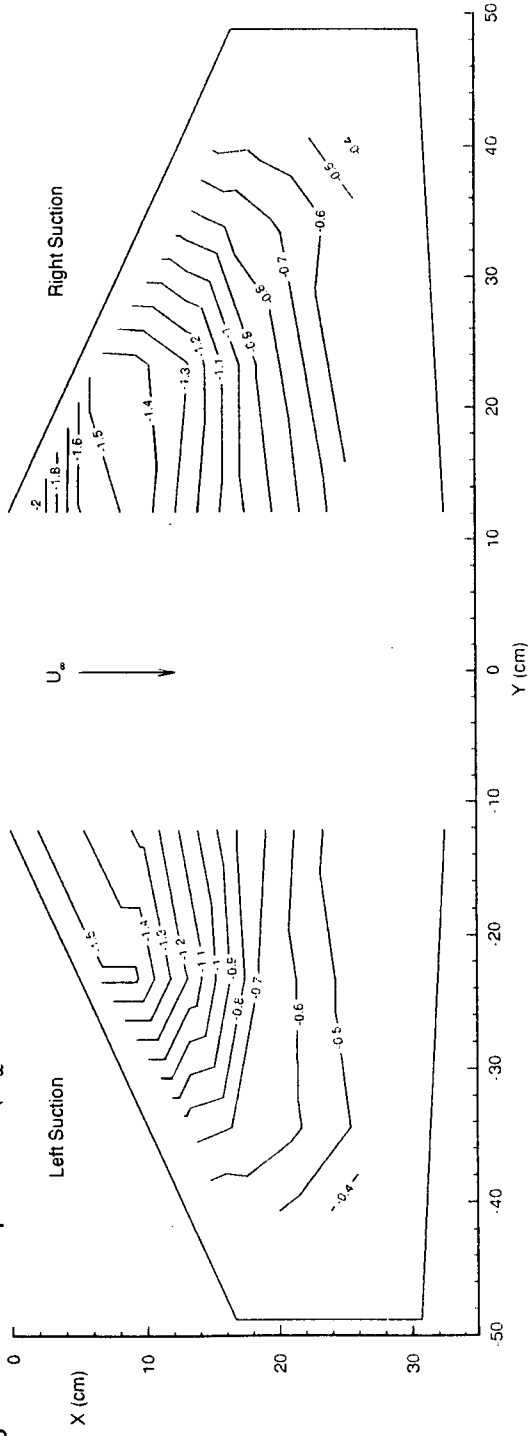


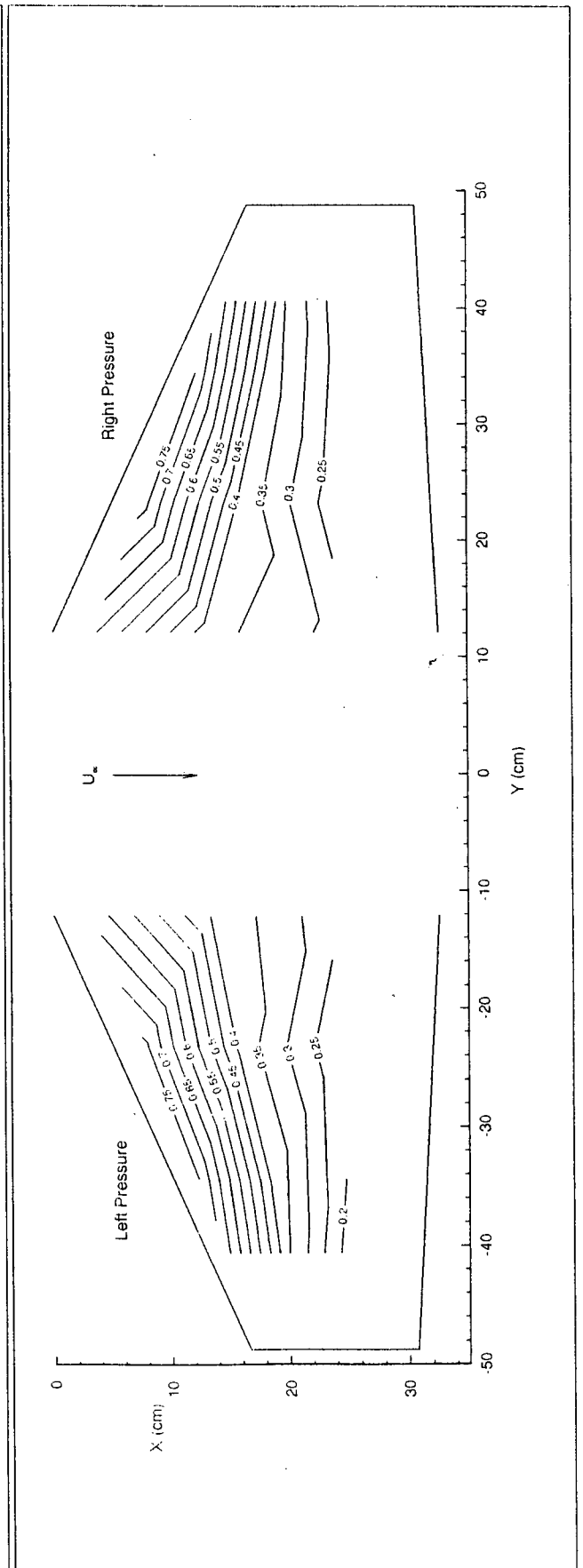
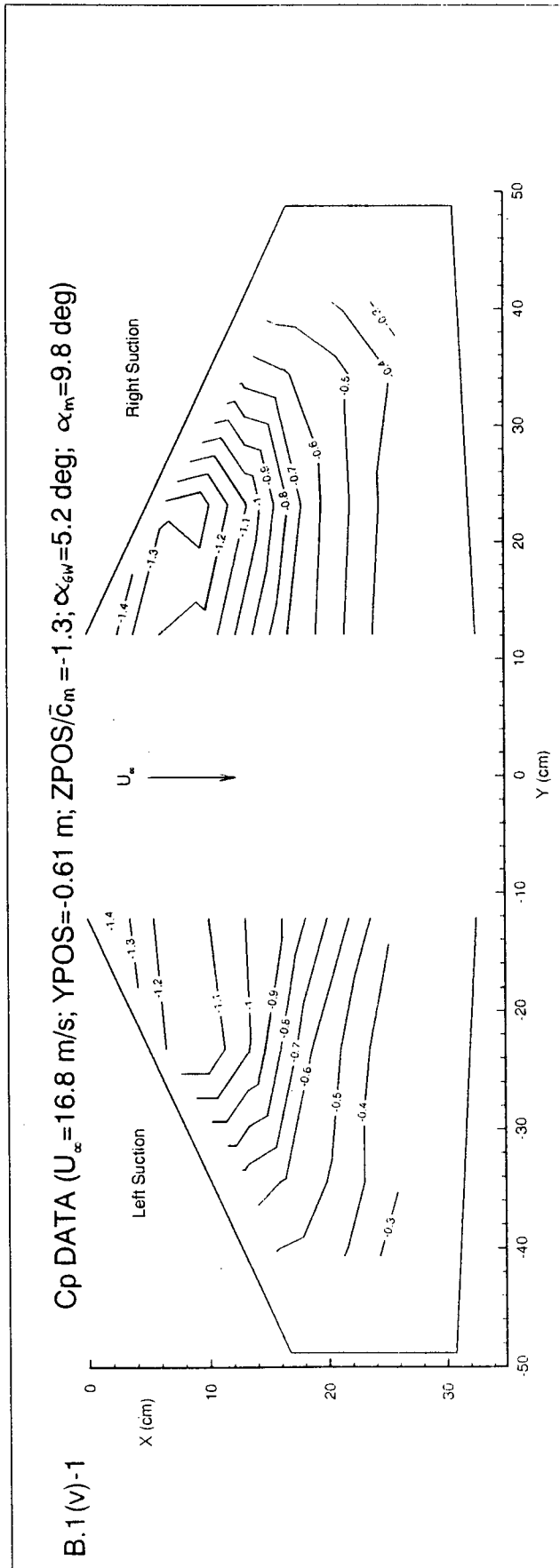
B.1(iv)-4

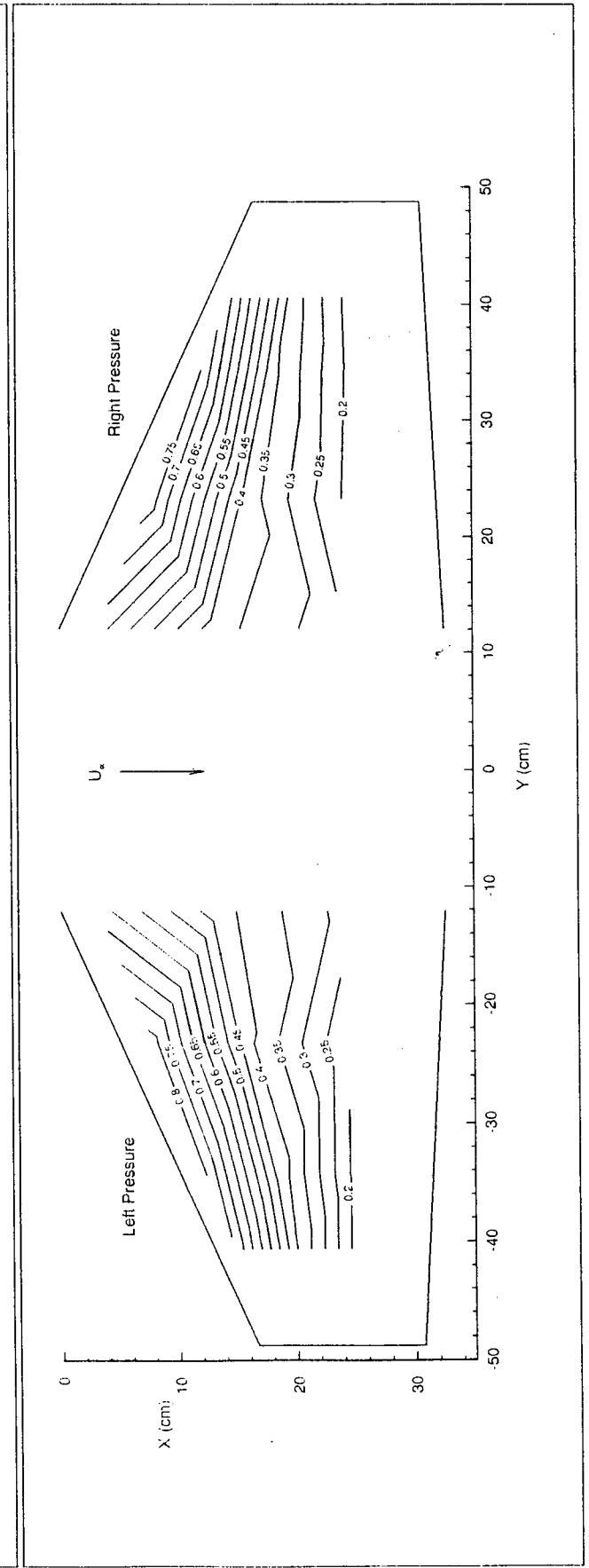
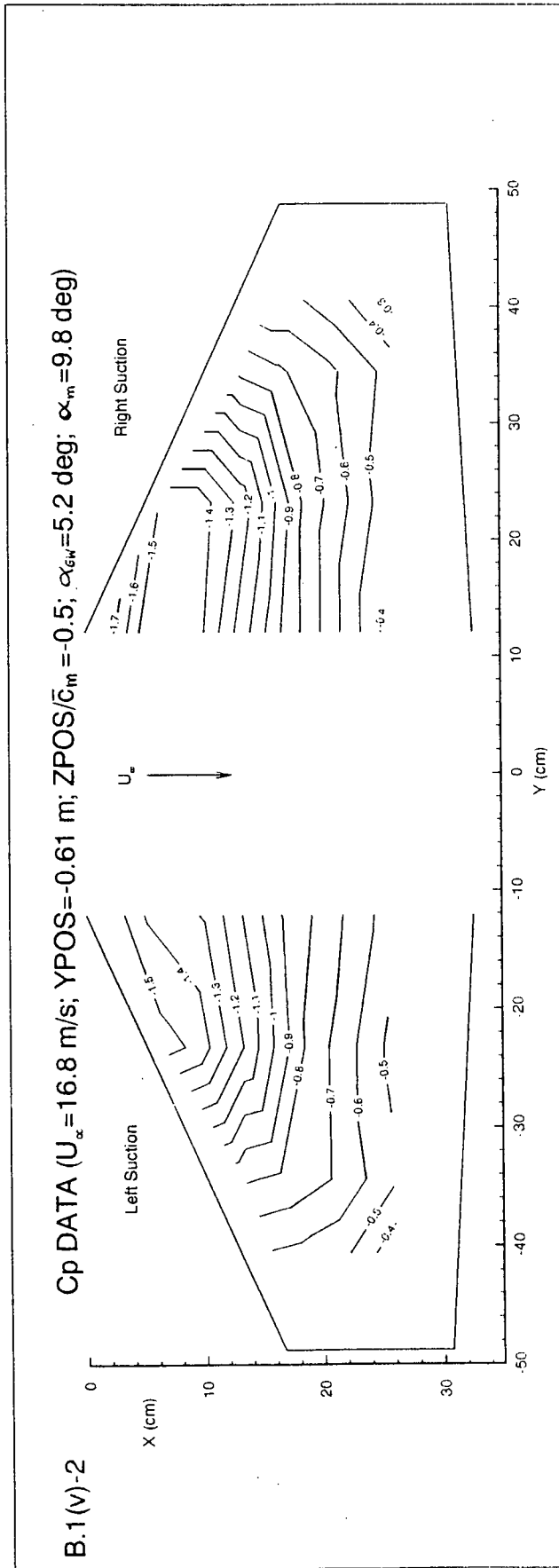
Cp DATA ($U_{\infty} = 16.8$ m/s; $YPOS = -0.305$ m; $ZPOS/\bar{c}_m = +0.5$; $\alpha_{GW} = 5.2$ deg; $\alpha_m = 9.8$ deg)



B.1(iv)-5 Cp DATA ($U_\infty = 16.8$ m/s; $YPOS = -0.305$ m; $ZPOS/\bar{c}_m = +1.3$; $\alpha_{eW} = 5.2$ deg; $\alpha_m = 9.8$ deg)

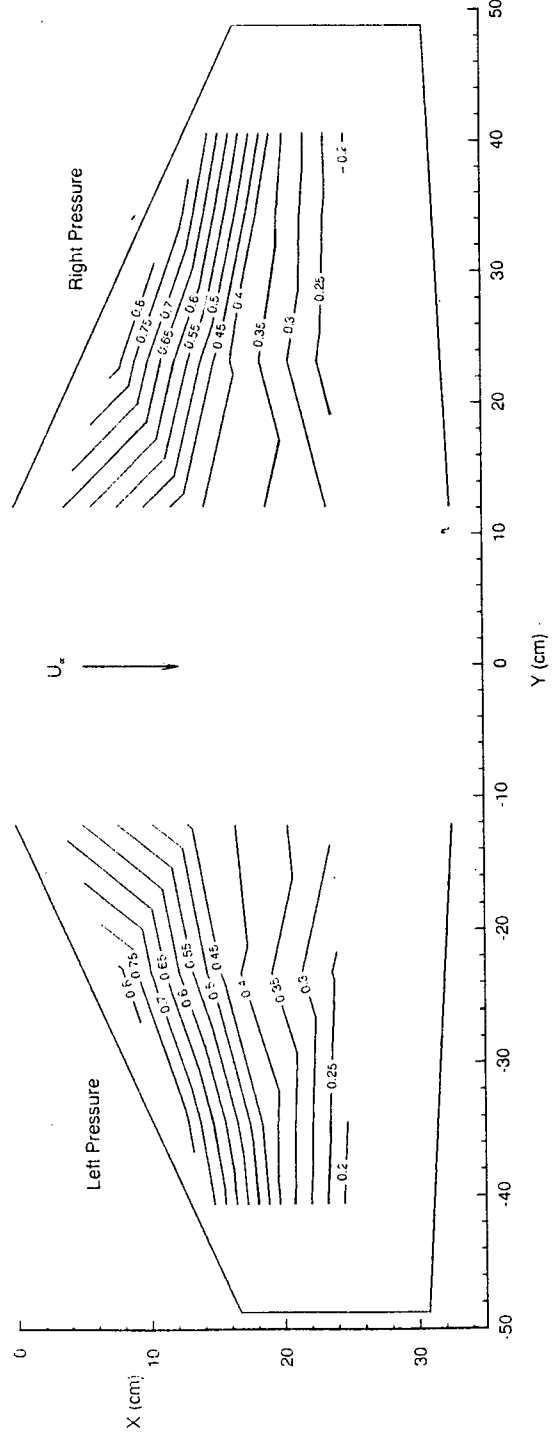
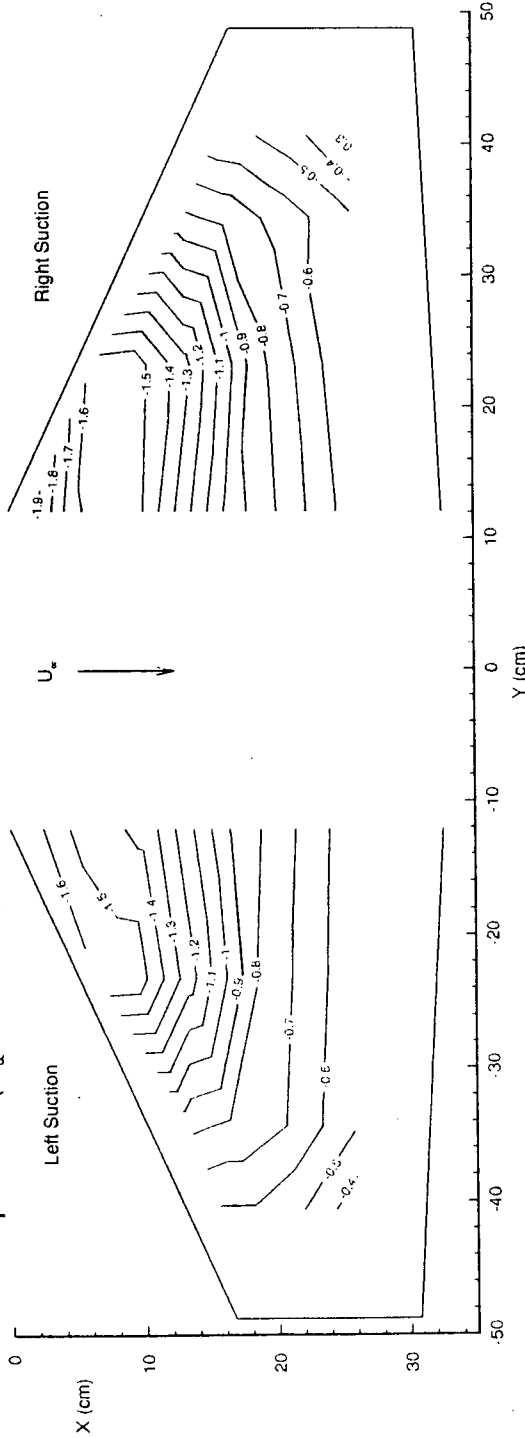






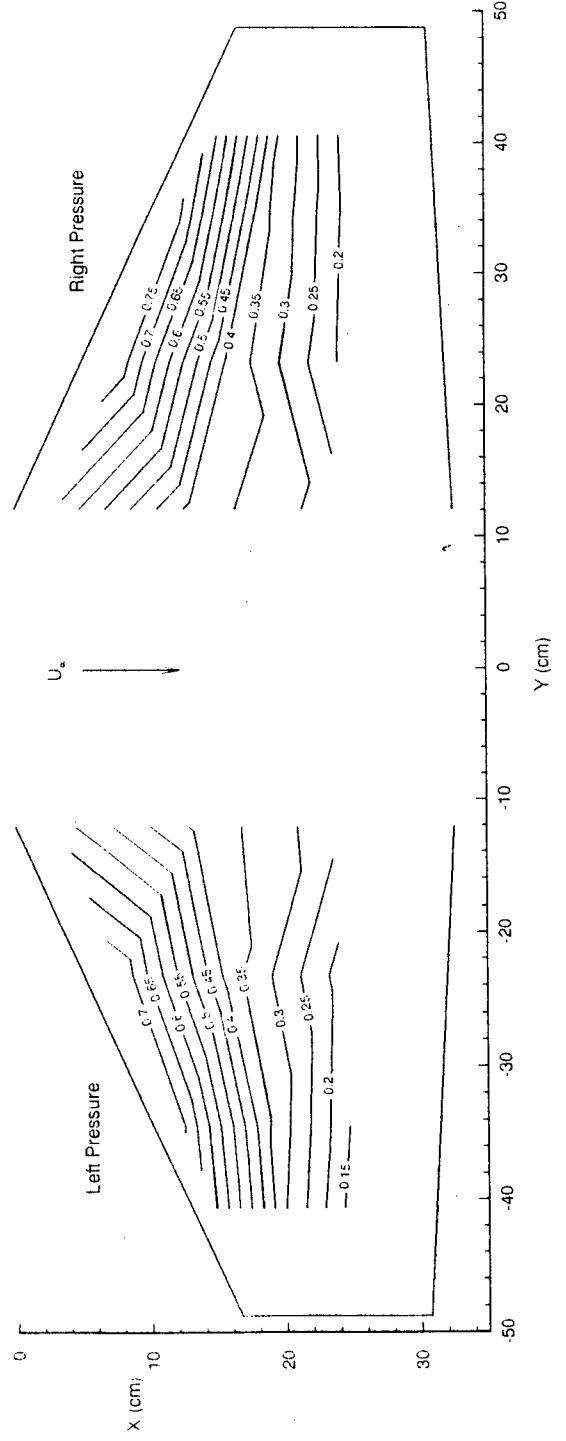
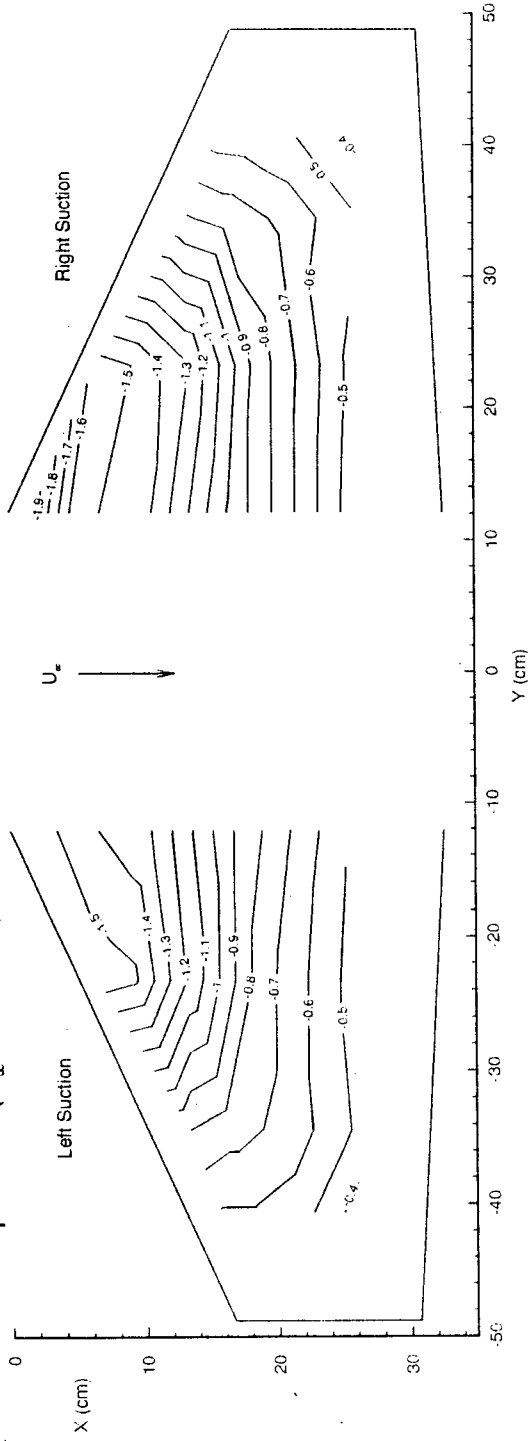
B.1(V)-3

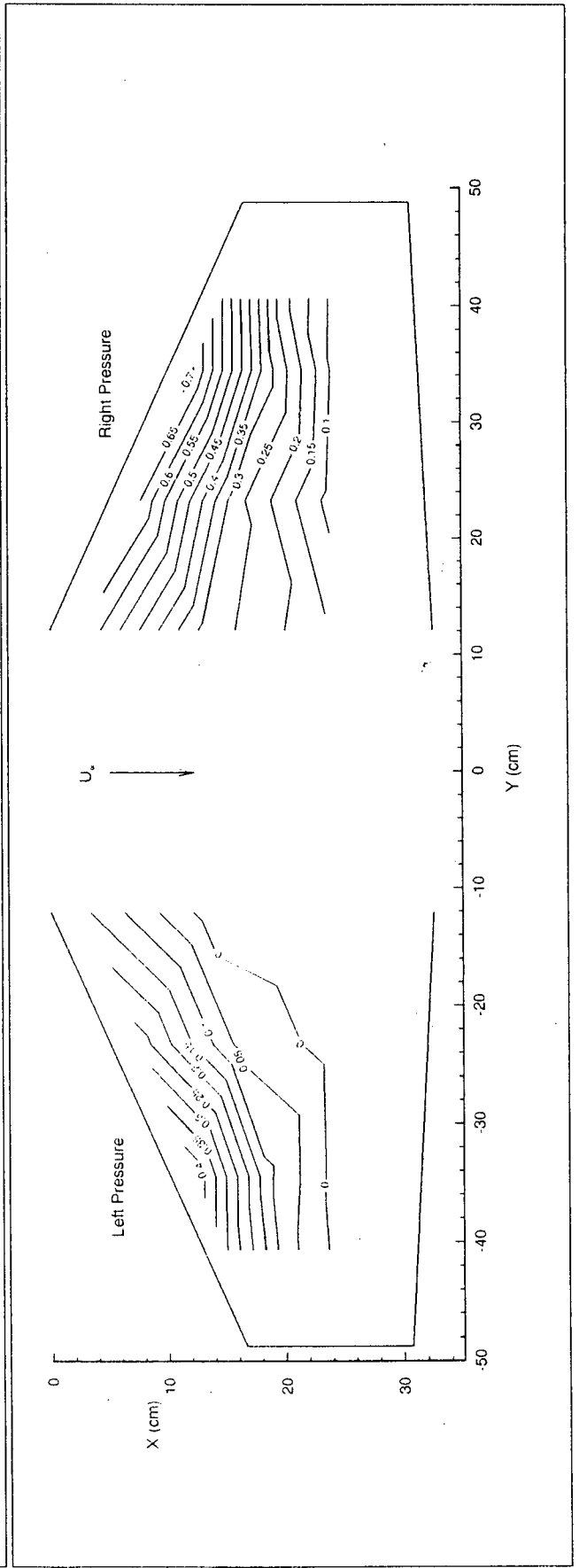
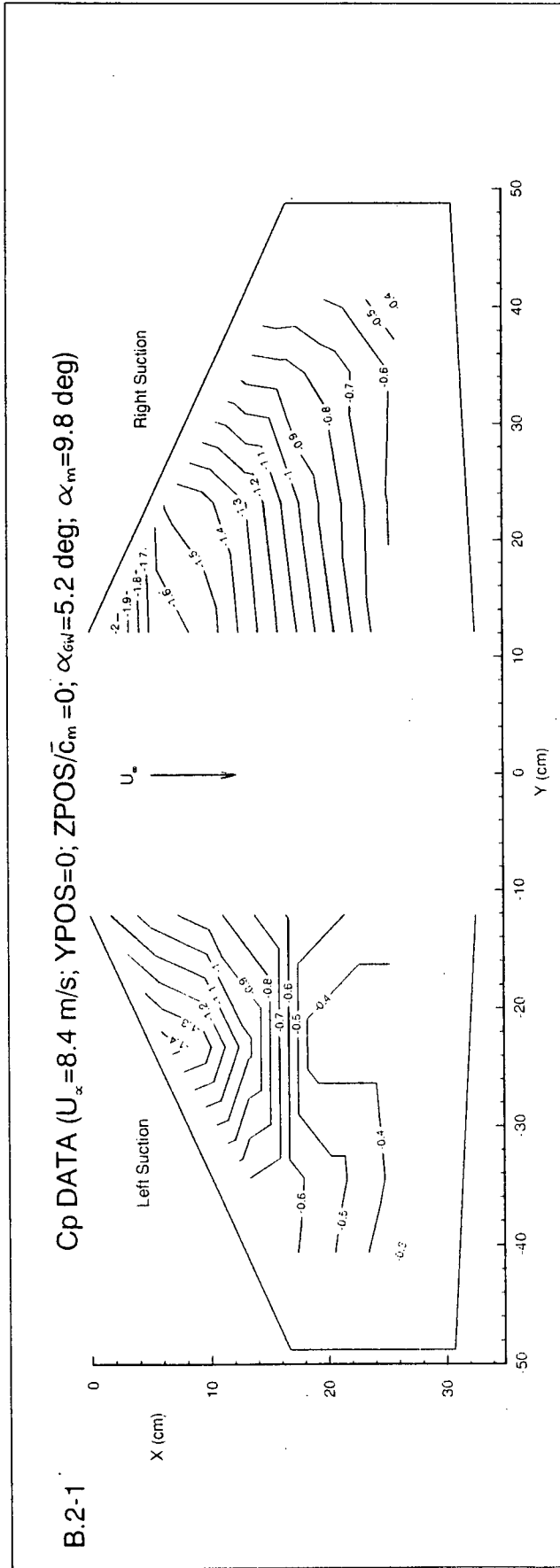
Cp DATA ($U_\infty = 16.8$ m/s; $YPOS = -0.61$ m; $ZPOS = 0$; $\alpha_{GW} = 5.2$ deg; $\alpha_m = 9.8$ deg)



B.1(V)-4

Cp DATA ($U_\infty = 16.8$ m/s; $YPOS = -0.61$ m; $ZPOS/\bar{c}_m = +0.5$; $\alpha_{eff} = 5.2$ deg; $\alpha_m = 9.8$ deg)





APPENDIX C
CODE LISTING AND SPECIFICATIONS

```

outportb(794,64); /* Scannivalve go home */
delay(1000); /* Wait for valve to reach position #1 */
outportb(794,0); /* Connect IRQ3 to post trigger delay timeout */

/**** Get the Scannivalve data ****/
printf("... Scannivalve Data ***\n\n");
printf(out, "..... Scannivalve Data *****\n");
for(step=1; step<=Scani_pos; ++step)
{
    printf("\nSTEP %2d Volts Cp\n", step);
    printf(out, "\nStep %2d Volts Cp\n", step);

    Def_Scani_Chan();
    delay(100);
    Initialize_AD_Scani();
    delay(100);
    Enable_Scani();
    delay(5000);
    Read_Scani_Buffer();
    delay(100);
    if(step != 24)
    {
        outportb(794,0);
        delay(100);
        outportb(794,32); /* Scannivalve step */
        delay(5000); /* Pressure tap settle time */
        outportb(794,0); /* Connect IRQ3 to post trigger delay timeout */
    } /* End for */
    printf("\n");
    printf(out, "\n");
    printf("End of Scannivalve Data\n\n");
    printf(out, "***** End of Scannivalve Data *****\n\n");
}

/**** Get force data ****/
printf("... Force Transducer Data ***\n\n");
printf(out, "..... Force Transducer Data *****\n");

Def_Force_Chan();
Printf("Initializing AD...\n\n");
delay(100);
Printf("Size of Force()");
Printf("Collecting force data...\n");
Delay(100);
Delay(100);
Printf("Force Data()");
Printf("Size of Force()");
Printf("Reading force buffer...\n\n");
Delay(100);
Printf("Force Buffer()");

printf("... End of force data ***\n");
printf(out, "***** End of force data *****\n");
}

/**** Assign channels to multiplexer ram ****/
chmux[0]=chmux[4]=chmux[8]=chmux[12]=0;
chmux[1]=chmux[5]=chmux[9]=chmux[13]=2;
chmux[2]=chmux[6]=chmux[10]=chmux[14]=4;
chmux[3]=chmux[7]=chmux[11]=chmux[15]=6;

/**** Write Mux RAM (LS nibble) out to the board ****/
for(i=0; i<15; ++i)
{
    outportb(794,chmux[i]);
} /* end for */

} /* End of Def_Scani_Char */

```

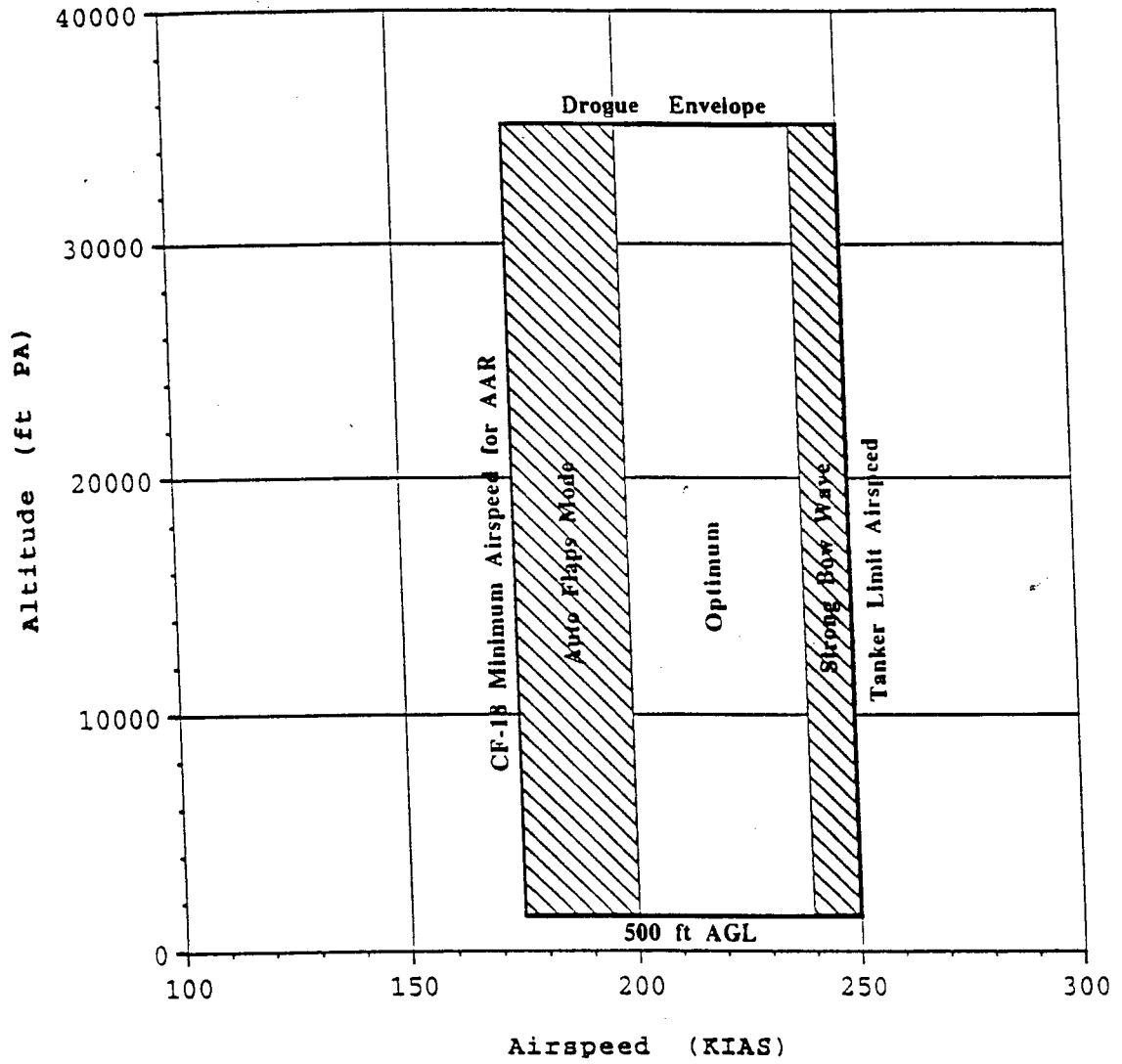
outportb(794,64); /* This may not be needed */


```

/**** Subroutine Read_Force_Buffer *****/
/*****
Read_Force_Buffer()
{
    int i, j, k, l, sign, data[force_samples][force_chan];
    float fdata[force_samples][force_chan];
    float M1,M2,M3,M4,M5,M6,H,FN,DH1,DS,DS1,DS2,DS3,DS4,MR,CL1B;
    float sum[force_chan], avg[force_chan];
    outputb(788,0); /* select bank k, Manual bank switching */
    outputb(795,4); /* ...and reset bank k start address */
    N = 0.1953; /* distance between N1 & N2 axes */
    for(k=0; k<force_samples; ++k)
    {
        for(i=0; i<force_chan; ++i)
        {
            sign = peekb(0x0000,0);
            if(sign < 0) sign = 256 + sign;
            data[k][i] = (float) (data[k][i]-2048)*0.004883;
            /* print out "data[k][i] = %f %d\n", fdata[k][i],k); */
            /* fprintf(out,"%i ",i); */
        }
        fprintf(out,"\n"); /* endfor "k" */
    }
    /* output force data to specified file */
    printf("Chan# Output(volt)\n\n");
    fprintf(out,"Chan# Output(volt)\n\n");
    for(j=0; j<force_chan; ++j)
    {
        sum[j]=0.0;
        avg[j]=0.0;
        for(i=0; i<force_samples; ++i)
        {
            sum[j] += fdata[i][j];
        }
        avg[j] = sum[j]/((float) force_samples);
        fprintf(out,"%3d %f\n",j,avg[j]);
        printf("%3d %f\n",j,avg[j]);
    } /* endfor "j" */
}
/**** CONVERSION OF OUTPUT DATA TO FORCES AND DISTANCES ****
**** ) conversion from volts to Newton-meters ****
****
**** 2) solving for forces and distances... ****
**** Pitching Axis ****
FN=(H1-H2)/H; /* in Newtons */
DH=(H1-FN)/184; /* both in meters */
CL1B=0.328*FN/(U_INF*U_INF); /* CFIE lift coefficient */
**** Yawing Axis ****
FS=(M5-M4)/H; /* in Newtons */
DS=M4/FS; /* both in meters */
DS1=0.1184;
**** Rolling Axis ****
MR=M6-(FS*Y_pos);
printf("M6 = %f N-m ; M2 = %f N-m\n",M1,M2); /*
printf("FN = %f Newtons\n",FN);
printf(out,"FN = %f Newtons\n",FN);
printf("DH = %f meters\n",DH);
printf(out,"DH = %f meters\n",DH);
printf("CL1B = %f\n",CL1B);
printf(out,"CL1B = %f\n",CL1B);
printf("FS = %f Newtons\n",FS);

```

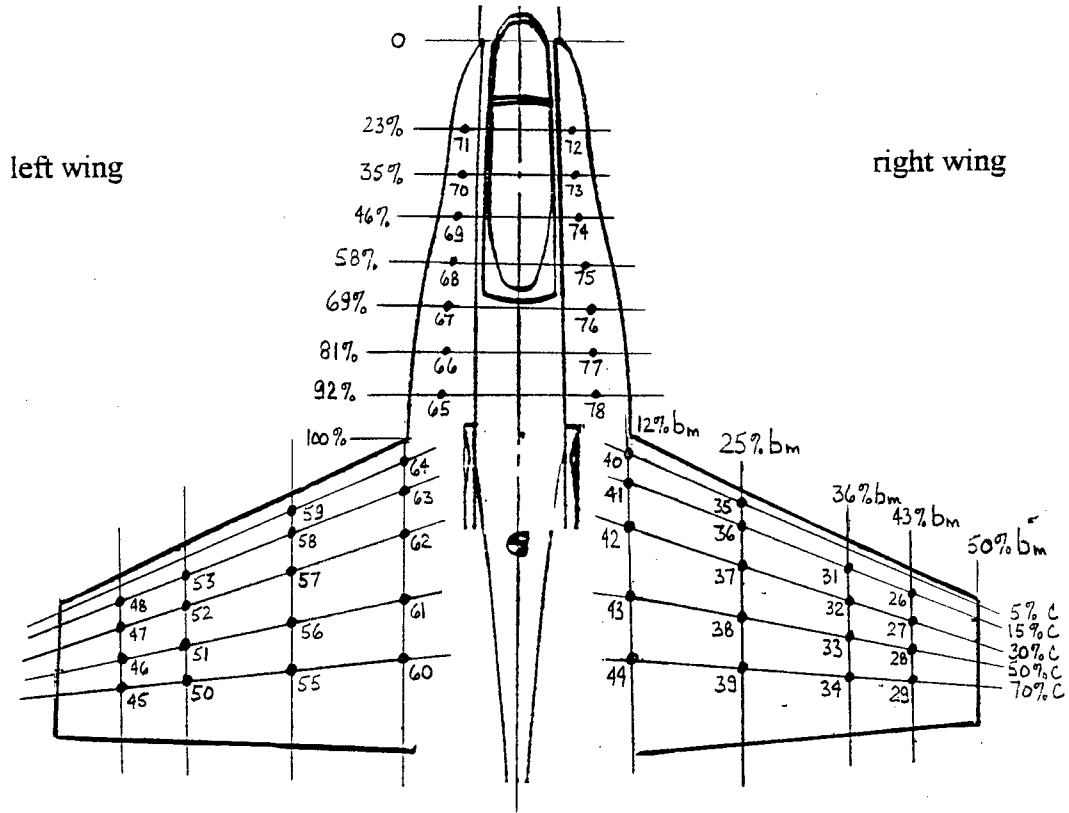
AAR ENVELOPE: CC-130H(T) AND CF-18A AIRCRAFT



CF-188 AAR Envelope with the CC-130H(T)

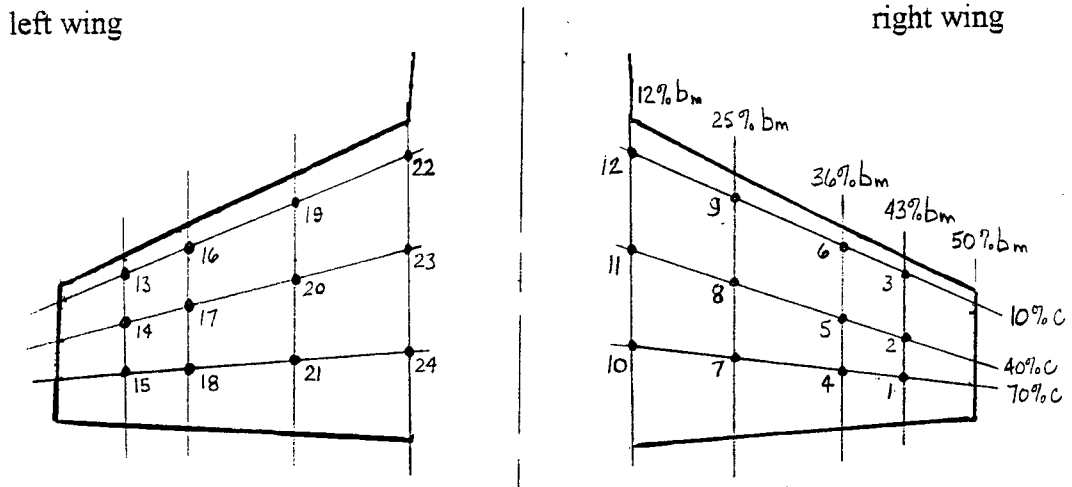
MAP OF THE MODEL PRESSURE TAPS
 (taps are symmetrically located on both sides of the model centerline)

TOP SURFACE



BOTTOM SURFACE

(no pressure taps on the LEX bottom surfaces)



APPENDIX D

GENERATING WING DOWNWASH VELOCITY ANALYSIS

The purpose of this analysis is to compare the BLWT wall effects on the generated vortex for two scenarios:

- i) a vertically-mounted generating wing (as used for the experiment); and
- ii) a horizontally-mounted generating wing.

This is accomplished by vectorially summing the effects of each principal image-vortex at three model locations, along the lateral (y) and vertical (z) axis and for three generating wing positions. Since the ratio of induced velocities (between a vertically-mounted and a horizontally-mounted generating wing will be identical for all AAR cases, the investigation is carried out for the Γ_{vp} case only.

I) Vertically-Mounted Generating Wing

This portion of the analysis was conducted in section 3.0; the results are displayed in Table D.1, where w_y and w_z represent the resultant image-induced “downwash” velocity at the model along the y and z axis, respectively ¹.

	ZPOS/ $c_m = -1.3$		ZPOS/ $c_m = 0$		ZPOS/ $c_m = +1.3$	
YPOS	w_y (m/s)	w_z (m/s)	w_y (m/s)	w_z (m/s)	w_y (m/s)	w_z (m/s)
-0.61 m	+0.083	-0.078	-0.037	-0.078	-0.17	-0.078
0	+0.077	0	-0.035	0	-0.16	0
+0.61 m	+0.083	+0.078	-0.037	+0.078	-0.17	+0.078

Table D.1: Wall-Induced Downwash Velocity for a Vertically-Mounted Generating Wing

¹ The individual contributions of each image vortex are displayed in pages 220 (for a vertically-mounted wing) and 221 (for a horizontally-mounted wing).

The tangential flow velocity components at the model from the generated vortex (V_{θ_y} and V_{θ_z}) vary with the relative position of the model. However, for comparison purpose: $|V_{\theta_y}| \geq 0.95$ m/s and $|V_{\theta_z}| \geq 0.6$ m/s, which indicates that the image-induced downwash velocities account for less than 15% of the total tangential velocity components.

ii) Horizontally-Mounted Generating Wing

Figure D.1 illustrates the principal images associated with the horizontal mounting of the vortex-generating wing in the BLWT. Note that the analysis is performed for a fixed, horizontally-mounted generating wing installed 0.82 m above the BLWT floor. The model would thus have to be moved laterally to vary $YPOS$.

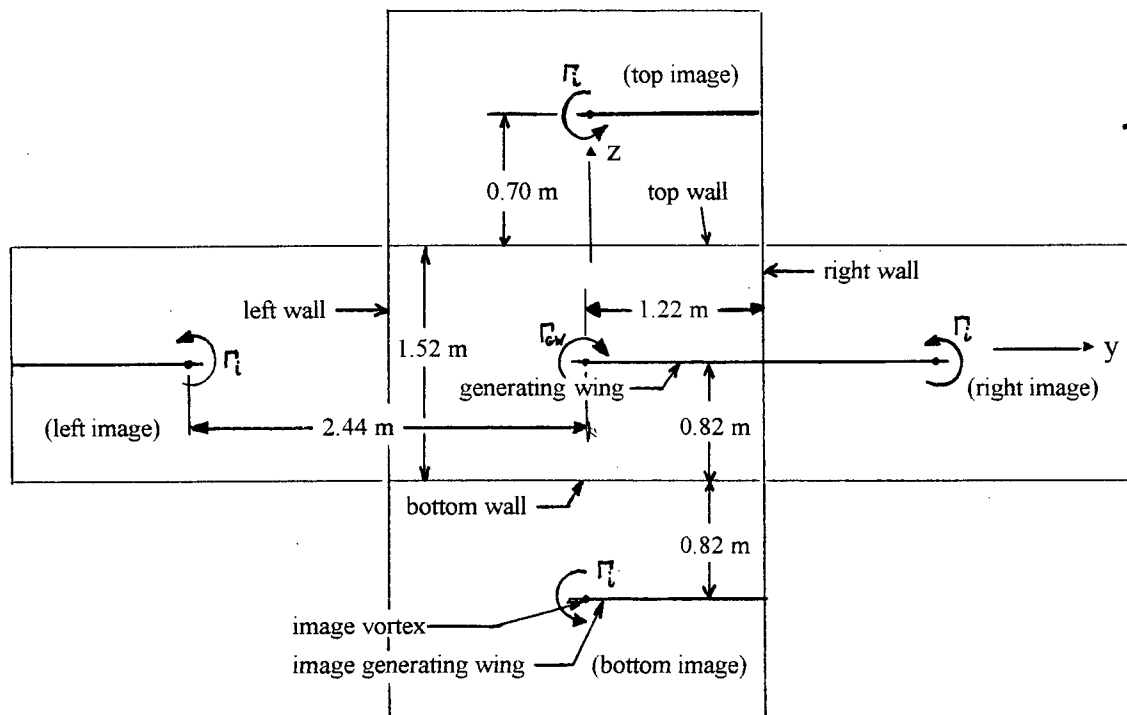


Figure D.1: Principal Image Vortices for a Horizontally-Mounted Generating Wing

The horizontally-mounted generating wing produces a vortex for which the ground effects and the formation effects are constant, increasing the vortex strength by 10% and 5%, respectively. Accordingly, the Γ_{yp} case, with a “no-wall” vortex strength of 1.97 m²/s, would produce a “wall-effect” vortex of 2.27 m²/s for all model positions.

The results are displayed in Table D.2, where w_y and w_z represent the resultant image-

induced “downwash” velocity at the model along the y and z axis, respectively.

	ZPOS/ $c_m = -1.3$		ZPOS/ $c_m = 0$		ZPOS/ $c_m = +1.3$	
YPOS	w_y (m/s)	w_z (m/s)	w_y (m/s)	w_z (m/s)	w_y (m/s)	w_z (m/s)
-0.61 m	-0.084	-0.079	+0.038	-0.079	+0.18	-0.079
0	-0.084	0	+0.038	0	+0.18	0
+0.61 m	-0.084	+0.079	+0.038	+0.079	+0.18	+0.079

Table D.2: Wall-Induced Downwash Velocity for a Horizontally-Mounted Generating Wing

Tables D.1 and D.2 show that while the magnitude of the downwash velocity components is practically identical for the vertically-mounted and the horizontally-mounted generating wings, the direction of the horizontal velocity (w_y) is always reversed. This result is intuitive, considering the reverse direction of the top and bottom images between the two scenarios. Comparing the downwash velocity components to the freestream velocity in the BLWT yields the horizontal and the vertical downwash angles (ϵ_y and ϵ_z , respectively). Accordingly, ϵ_z is roughly identical for both scenarios ($-0.3 \text{ deg} < \epsilon_z < +0.3 \text{ deg}$), while ϵ_y is reversed between the two scenarios ($-0.3 \text{ deg} < \epsilon_y < +0.6 \text{ deg}$).

Overall, a horizontally-mounted generating wing (although impractical for our application) would not significantly change the magnitude of the generating wing downwash velocity components and would induce only minor changes in the side force due to the reversal of the horizontal downwash angle. Since the only significant ϵ_y occurs for ZPOS/ $c_m = +1.3$ and that the readings for this model position have been discarded (refer to section 4.1), it is reasonable to conclude that the effect of mounting the generating wing vertically (instead of horizontally) in the BLWT has no significant effect on the downwash velocity. Furthermore, the effect of reversing ϵ_y (between the two scenarios) on the model side force is less than the uncertainty in the model dimensions.

**BLWT WALL EFFECTS (DOWNWASH FROM IMAGE VORTICES)
(GENERATING WING MOUNTED VERTICALLY)**

Gamma = -1.97 m²/s

i) $ZPOS/\bar{c}_m = -1.3$

Effect at ...	From...				Total horiz. velocity (m/s)	Total vert. velocity (m/s)
	top (along y-axis) (m/s)	bottom (along y-axis) (m/s)	y+ side (along z-axis) (m/s)	y- side (along z-axis) (m/s)		
YPOS=-0.61	-0.200	0.283	0.117	-0.195	0.083	-0.078
YPOS= 0	-0.187	0.264	0.136	-0.136	0.077	0.000
YPOS=+0.61	-0.200	0.283	0.195	-0.117	0.083	0.078

ii) $ZPOS/\bar{c}_m = 0$

Effect at ...	From...				Total horiz. velocity (m/s)	Total vert. velocity (m/s)
	top (along y-axis) (m/s)	bottom (along y-axis) (m/s)	y+ side (along z-axis) (m/s)	y- side (along z-axis) (m/s)		
YPOS=-0.61	-0.255	0.217	0.117	-0.195	-0.037	-0.078
YPOS= 0	-0.238	0.203	0.136	-0.136	-0.035	0.000
YPOS=+0.61	-0.255	0.217	0.195	-0.117	-0.037	0.078

iii) $ZPOS/\bar{c}_m = +1.3$

Effect at ...	From...				Total horiz. velocity (m/s)	Total vert. velocity (m/s)
	top (along y-axis) (m/s)	bottom (along y-axis) (m/s)	y+ side (along z-axis) (m/s)	y- side (along z-axis) (m/s)		
YPOS=-0.61	-0.350	0.176	0.117	-0.195	-0.173	-0.078
YPOS= 0	-0.326	0.165	0.136	-0.136	-0.161	0.000
YPOS=+0.61	-0.350	0.176	0.195	-0.117	-0.173	0.078

**BLWT WALL EFFECTS (DOWNWASH FROM IMAGE VORTICES)
(GENERATING WING MOUNTED HORIZONTALLY)**

$\Gamma = -1.97 \quad \text{m}^2/\text{s}$

i) $ZPOS/\bar{c}_m = -1.3$

Effect at ...	From...				Total horiz. velocity (m/s)	Total vert. velocity (m/s)
	top (along y-axis) (m/s)	bottom (along y-axis) (m/s)	y+ side (along z-axis) (m/s)	y- side (along z-axis) (m/s)		
YPOS=-0.61	0.203	-0.287	-0.197	0.119	-0.084	-0.079
YPOS= 0	0.203	-0.287	-0.148	0.148	-0.084	0.000
YPOS=+0.61	0.203	-0.287	-0.119	0.197	-0.084	0.079

ii) $ZPOS/\bar{c}_m = 0$

Effect at ...	From...				Total horiz. velocity (m/s)	Total vert. velocity (m/s)
	top (along y-axis) (m/s)	bottom (along y-axis) (m/s)	y+ side (along z-axis) (m/s)	y- side (along z-axis) (m/s)		
YPOS=-0.61	0.258	-0.220	-0.197	0.119	0.038	-0.079
YPOS= 0	0.258	-0.220	-0.148	0.148	0.038	0.000
YPOS=+0.61	0.258	-0.220	-0.119	0.197	0.038	0.079

iii) $ZPOS/\bar{c}_m = +1.3$

Effect at ...	From...				Total horiz. velocity (m/s)	Total vert. velocity (m/s)
	top (along y-axis) (m/s)	bottom (along y-axis) (m/s)	y+ side (along z-axis) (m/s)	y- side (along z-axis) (m/s)		
YPOS=-0.61	0.354	-0.179	-0.197	0.119	0.175	-0.079
YPOS= 0	0.354	-0.179	-0.148	0.148	0.175	0.000
YPOS=+0.61	0.354	-0.179	-0.119	0.197	0.175	0.079